Probing Biological Redox Chemistry with Fourier Transformed ac Voltammetry

Hope Adamson

PhD

University of York

Chemistry

April 2017

Abstract

Biological electron transfer is fundamental to life on earth. Photosynthesis, respiration and many other biological processes are underpinned by electron transfer between redox proteins and catalysis by redox enzymes. Fully understanding the mechanisms of redox biology is crucial to understanding life and inspiration for chemical, biomedical and future energy technologies can be taken from Nature's fine example. Developments in techniques and data analysis are required to gain a deeper understanding of biological electron transfer and redox catalysis. Protein film electrochemistry has enabled mechanistic insight into protein redox chemistry but has distinct limitations in the study of non-catalytic electron transfer as opposed to catalytic reactions. This thesis outlines the insight into biological redox chemistry gained through development of Fourier Transformed ac Voltammetry and associated analysis, in combination with spectroscopic, biochemical and molecular biology approaches. Novel pyranopterin ligand redox chemistry is proposed to control catalysis in a molybdoenzyme YedY, reversible disulphide bond redox chemistry is confirmed in a [NiFe]-hydrogenase maturation protein and an iron-sulphur cluster relay site distant from the active site is shown to influence the key catalytic properties of overpotential and bias in an O_2-tolerant [NiFe]-hydrogenase.

Contents

List of Tables

List of Figures

5   Analysis of HypD Disulfide Redox Chemistry via Optimization of Fourier Transformed ac Voltammetric Data

7   Control of Catalytic Bias and Overpotential by the Electron Entry/exit Site in a [NiFe]-hydrogenase

Preface

This thesis utilises Fourier Transformed ac Voltammetry (FTacV) to characterise previously ambiguous aspects of biological redox chemistry in metalloproteins. It is presented in the alternative format, comprising papers in referred journals and integrative chapters to describe the context, theory, methods and conclusions of the work as a whole. Chapter 1 presents a broad introduction to redox proteins and techniques used in their study, with a final focus on electrochemical techniques and the history of FTacV of redox proteins prior to this thesis. Chapter 2 describes the theory underpinning electrochemistry and FTacV and Chapter 3 details the experimental methods utilised. The experimental results of this thesis are reported in Chapters 4 to 7. Chapter 4 describes the use of FTacV to discover novel redox chemistry in the molybdoenzyme YedY, which is ascribed to the pyranopterin ligand and provides explanation for ambiguities in the catalytic mechanism. It is reproduced from the journal Proceedings of the National Academy of Sciences (Adamson, H., et al., *Electrochemical evidence that pyranopterin redox chemistry controls the catalysis of YedY, a mononuclear Mo enzyme.* Proceedings of the National Academy of Sciences, 2015. **112**(47): p. 14506-14511). Chapter 5 characterises disulphide bond redox chemistry in the maturation protein HypD, using FTacV and advances in data optimisation, in support of its proposed redox role in hydrogenase active site construction. It is reproduced from the journal Analytical Chemistry (Adamson, H., et al., *Analysis of HypD Disulfide Redox Chemistry via Optimization of Fourier Transformed ac Voltammetric Data.* Analytical Chemistry, 2017. **89**(3): p. 1565–1573). Chapter 6 describes the molecular biology and protein purification used to produce variants of *Escherichia coli* hydrogenase-1 for use in Chapter 7. Chapter 7 describes the use of FTacV to measure electron transfer in and out of a hydrogenase simulataneously with catalysis and probes how this controls the crucial properties of catalytic bias and overpotential. It is a paper that has been submitted to the journal Nature Chemical Biology. Chapter 8 summarises the conclusions and perspectives of the work as a whole. The integrative Chapters 1, 2, 3 and 8 are referenced collectively at the end of the thesis and the results Chapters 4 to 7 are referenced separately within each chapter.

Acknowledgements

Declaration

I declare that this thesis is a presentation of original work and I am the sole author, except where explicitly stated in the declaration prior to each Chapter that is reproduced from a paper. The declaration for each of these Chapters gives the full reference of the paper and explicitly states the contribution from all co-authors, which is confirmed by the second and corresponding authors. This work has not previously been presented for an award at this, or any other, University. All sources are acknowledged as References.

Chapter 1

Introduction

1.1 Redox proteins

1.1.1 Biological function

Redox active proteins and electron transfer reactions are at the heart of many biological processes.[1-3] The energy transduction pathways of photosynthesis and respiration, as well as many metabolic, signalling and biosynthesis reactions, are all unpinned by redox chemistry.[4-6] Redox cofactors within proteins can be electron transfer centres for charge transport or catalytic sites for reactions.[6, 7]

Photosynthesis converts light to chemical energy, via a series of electron transfer reactions and provides most of the energy required for life on Earth.[8] In the light-dependent reactions of photosynthesis, the chlorophyll of photosystem II is excited by light and the electrons passed through a protein electron transport chain to photosystem I. This provides energy for the chemiosmotic synthesis of ATP, the energy currency of life, by ATP-synthase. Light excites the chlorophyll of photosystem I and electrons are passed along a chain of electron acceptors to NADP reductase, which reduces NADP to NADPH. This is a strong reducing agent and source of energetic electrons for other cellular reactions, such as sugar synthesis in the dark reactions of photosynthesis.[9-11] The ultimate source of these electrons is H_2O, which is oxidised to O_2 by the oxygen evolving complex of photosystem II.[12-14] The series of electron transfers are shown in Figure 1.1 A.

A great many organisms use O_2 and sugar in aerobic cellular respiration to release energy. Reducing equivalents from NADH, produced during glycolysis or the citric acid cycle, enter the mitochondrial electron transport chain and are passed via a series of electron transfer steps (Figure 1.1 B) to cytochrome c oxidase, which reduces the terminal electron acceptor O_2 to H_2O.[15, 16] Proton pumping accompanies the electron transfer steps and generates a proton gradient used to drive ATP synthesis.[17] Aerobic respiration of sugar is just one example of cellular respiration and many combinations of electron donating fuels and terminal electron acceptors are known to be used by organisms for generation of ATP.[6, 18] For example, in the facultative anaerobe *Escherichia coli* (*E. coli*), hydrogen oxidation catalysed by a hydrogenase (Chapters 6 and

7) is coupled to enzyme-catalysed fumarate reduction, via the quinone pool, in an energy releasing respiratory chain.[19]
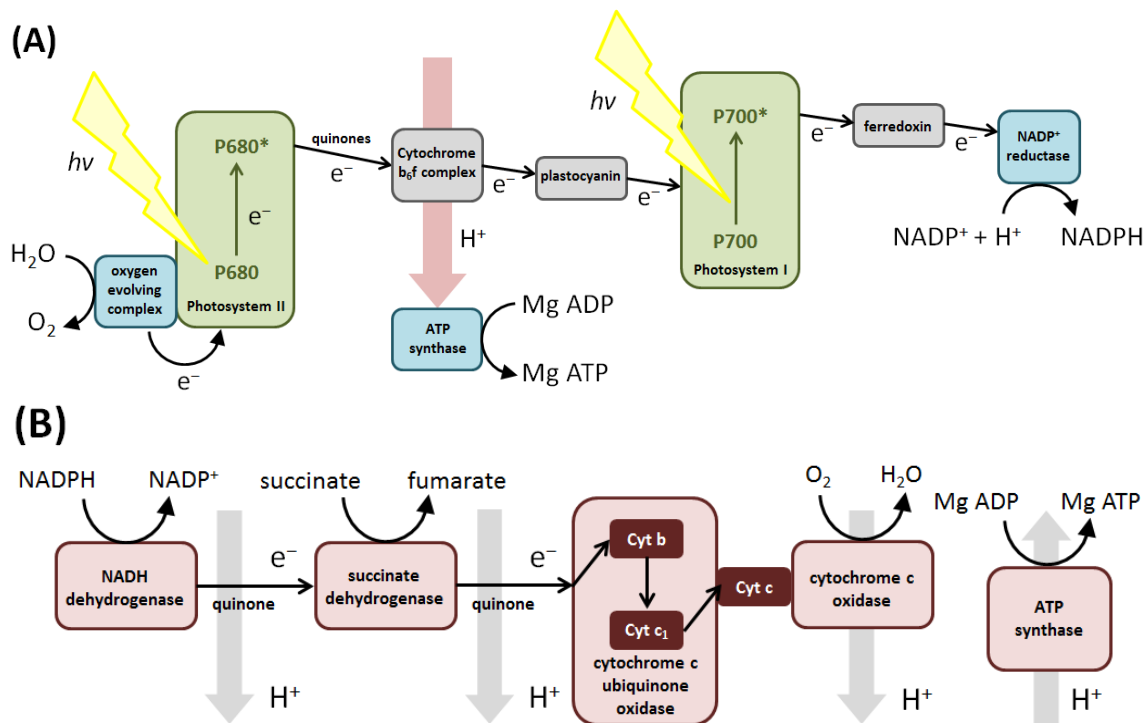
Figure 1.1 Biological electron transfer in (A) Photosynthesis and (B) Respiration

Redox proteins also catalyse a whole host of vital metabolic reactions. For example, cytochrome P450 Fe-heme proteins perform monoxygenation in steroid and hormone biosynthesis, vitamin processing and drug metabolism.[20] Cobalt containing methyl transferases are used in amino acid synthesis and molybdoenzymes are involved in detoxification metabolism, such as sulphite and xanthine oxidation, to name just a few important examples.[21, 22]

Biological electron transfer is also involved in cell signalling and sensing. Thiol redox signalling, via reduction and oxidation of redox active cysteine, is a major mechanism by which the presence of oxidants is transduced into cellular signalling pathways.[23, 24] Iron-sulphur (FeS) cluster proteins are also involved in regulation, for example the fumarate nitrate regulator senses oxygen and regulates transcription of enzymes for aerobic or anaerobic respiration in *E. coli*.[6, 25]

Biosynthesis and repair of macromolecules can also be carried out by redox proteins. For example, the redox active cysteine-disulphide containing enzyme HypD (Chapter 5) is the scaffold for reductive insertion of cyanide ligands into

the active site of NiFe-hydrogenases (Chapters 6 and 7).[26] Molybdoenzyme YedY had unknown biological function at the time of writing Chapter 4, but is now known to be a methionine sulfoxide reductase and reduces oxidised methionine to repair oxidative damage in proteins.[27, 28] FeS cluster proteins are involved in both DNA synthesis and repair.[29]

As outlined, redox reactions are essential for sustaining life and such biochemistry is demonstrably widespread. In order to facilitate this, numerous redox active structures have evolved within proteins, from metal centres, to organic cofactors and amino acids themselves, and a brief introduction is provided below.

1.1.2 Metalloproteins

This thesis will focus on metalloproteins, which make up a third of all known proteins.[1-3] Redox activity is a property of only a subset of biological metallocentres. S-block metal protein centres, as well as the stable d-block metal ion Zn^{2+} centres, generally perform structural, signalling and acid-base catalysis roles.[6] In contrast, redox active metalloproteins contain transition metals, from across the first row and Mo/W from the second and third row (Figure 1.2).[2, 6]

1																	18
H	2											13	14	15	16	17	He
Li	Be											B	C	N	O	F	Ne
Na	Mg	3	4	5	6	7	8	9	10	11	12	Al	Si	P	S	Cl	Ar
K	Ca	Sc	Ti	V	Cr	Mn	Fe	Co	Ni	Cu	Zn	Ga	Ge	As	Se	Br	Kr
Rb	Sr	Y	Zr	Nb	Mo	Tc	Ru	Rh	Pd	Ag	Cd	In	Sn	Sb	Te	I	Xe
Cs	Ba	La	Hf	Ta	W	Re	Os	Ir	Pt	Au	Hg	Tl	Pb	Te	Po	At	Rn
Fr	Ra	Ac															

Figure 1.2 Biological periodic table. Periodic table of the elements with elements commonly known to be essential for life highlighted in blue (non-metals), green (d-block metals) and yellow (s-block metals). Lanthanides, actinides and the elements beyond are not shown. Adapted from Reference [2].

Transition metals are ideally suited to redox reactions, as they exhibit facile interconversion between a number of oxidation states. They also make excellent catalytic sites due to their stability in a number of geometries and coordination numbers, relative lability to bind and exchange substrate / products

and high charge density for polarisation of substrates and stabilisation of intermediates.[6] Binding sites for specific metals are provided by amino acids or special organic ligands within the protein. Ligands provide specificity for a certain metal, tune redox properties, influence lability and can structurally stabilise intermediate geometries in catalysis and electron transfer (entatic state).[6, 30, 31] A multitude of metal-ligand structures exist, tuned to their biological purpose.

Vanadium, the first biologically significant member of the first row of transition metals, is present as V(V) ligated by an axial histidine and three equatorial oxygen atoms in haloperoxidases, which utilise hydrogen peroxide and a halide to halogenate organic compounds.[32] Vanadium is also utilised by some bacteria under molybdenum limiting conditions, in V-Fe nitrogenases, to fix N_2 to ammonia.[33]

Manganese redox enzymes are involved in ribonucleotide reductase, catalase, peroxidase, superoxide dismutase and, arguably most impressively, water oxidation activity. The oxygen evolving complex of photosystem II contains an Mn_4CaO_5 cluster, stabilised by hard carboxylate ligands (Glu, Asp) and uses the high oxidising power of Mn(IV) to fully oxidise H_2O to O_2. This remarkable catalyst has provided essentially all the O_2 in our atmosphere.[6, 12, 34]

Iron is the most abundant transition metal in biological systems and is present in a great number of electron transfer proteins and redox enzymes.[2] Cytochromes are electron transfer proteins containing Fe in a porphyrin macrocycle (heme), further ligated axially by two amino acids that tune the redox properties.[35] Iron cycles between low spin Fe(III)/Fe(II) and an entering electron is delocalised across the highly conjugated porphyrin, minimising reorganisation energy and extending electron coupling for efficient electron transfer.[6] FeS cluster electron transfer centres typically contain a [2Fe2S], [4Fe4S] or [3Fe4S] core (Figure 1.3), further ligated by cysteine thiolate and occasionally non-thiolate amino acid ligands.[36, 37] They carry out single electron transfers in mixed valence systems of tertrahedrally coordinated high-spin Fe(III)/Fe(II) and an added electron is delocalised in the cluster, minimising bond length changes and reorganisation energy for electron transfer.[6, 38] They are present in essential electron shuttling proteins called ferredoxins and also arranged in relays like a "wire" in larger enzymes such as hydrogenases

(Chapters 6 and 7), to enable electrons to enter and exit remote redox centres.[39, 40] There is mounting evidence that relay FeS clusters do not simply act as a "wire" and their properties, controlled by immediate ligands and second coordination sphere effects, can affect important catalytic properties.[41, 42] This concept is thoroughly probed in Chapter 7.
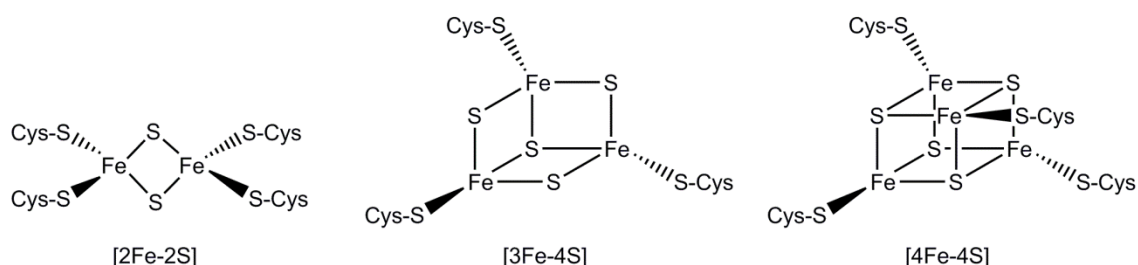
Figure 1.3 Common FeS cluster structures

Heme and non-heme iron enzymes are mostly involved in peroxidase (e.g. horseradish peroxidase), oxidase (e.g. cytochrome c oxidase) and oxygenase (e.g. cytochrome P450) activity, often using Fe(IV) as a highly oxidising intermediate.[3, 6] Fe can be present with other metal ions, such as in the FeMo cofactor of nitrogenases, as FeCu in cytochrome c oxidase, FeFe in methane monooxygenase and hydrogenases and NiFe in other hydrogenases (Chapter 6 and 7).[6] The [FeFe] and [NiFe] active sites of hydrogenases (Figure 1.4) contain the biologically unusual strong field ligands CO and CN^- which are thought to tune redox properties, impose the correct spin state and exert a strong trans influence, for H_2 binding and heterolytic cleavage.[40, 43]
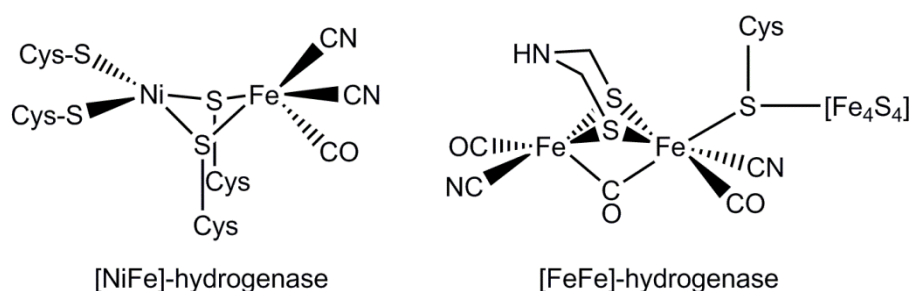
Figure 1.4 Hydrogenase active site structures

Cobalt is usually present as cobalamin in proteins, ligated by a corrin macrocycle and a further nitrogen base. Cobalt enzymes can utilise the stability of low spin square pyramidal Co(II) (d^7) to homolytically cleave a Co–C bond and catalyse radical rearrangements, in isomerisation, dehydration and deamination reactions. The high nucleophilicity of square planar Co(I) (d^8) is

utilised in methyl transfer reactions, such as methionine synthesis and reactions of the central metabolic pathway of methanogens.[6, 44, 45]

Ni redox enzymes are relatively rare but the few examples tend to deal with gases important in global carbon, oxygen and hydrogen cycles. Methyl-CoM reductase catalyses the release of methane at a Ni-corphin site, in the final step of methanogenesis and carbon monoxide dehydrogenase interconverts CO/CO_2 at a $NiFe_4S_4$ cluster. Superoxide dismutase converts harmful superoxide to O_2 and H_2O_2 at a 4-5 coordinate Ni-site, with the Ni(III)/Ni(II) couple tuned to an appropriate range to both oxidise and reduce superoxide.[46, 47] NiFe hydrogenases that catalyse the interconversion of protons and hydrogen are studied in Chapters 6 and 7.

The Cu(II)/Cu(I) redox couple plays an important role in both electron transfer proteins and redox enzymes.[48] The mononuclear 'blue' copper electron transfer centre is coordinated by at least two histidine and one cysteine ligands held rigidly in an almost trigonal planar manner by the protein structure. This rigid geometry, intermediate between the preferred planar and tetrahedral geometries of Cu(II) and Cu(I), minimises reorganisation energy and makes electron transfer fast.[3, 6] Two important examples are plastocyanin and azurin; electron transfer proteins in chloroplasts and bacteria, respectively. [6] The binuclear Cu electron transfer centre has a $Cu_2(S(Cys))_2$ core with a Cu–Cu bond, so upon one electron oxidation of Cu(I)Cu(I) the electron is delocalised between the two Cu atoms, minimising reorganisation energy and improving electron transfer.[48] This centre is used as the electron acceptor in cytochrome c oxidase of the respiratory electron transport chain.[49] Aside from electron transfer, many mono- and multi-nuclear Cu structures are used for oxidase, oxygenase, O_2 reduction and denitrification activity. One important example is the multicopper oxidases which contain a blue Cu centre that accepts electrons from a substrate and a tri-nuclear Cu centre which uses these electrons in the four electron reduction of O_2 to H_2O.[48, 50]

Molybdenum and tungsten are the only second and third row transition metals known to have specific roles in biology.[6] Molybdenum is used in the $[MoFe_7S_9]$ cluster of nitrogenases and as a mononuclear site in other molybdoenzymes.[22, 51] The mononuclear Mo centres utilise the series of stable oxidation states Mo(IV), Mo(V) and Mo(VI), afforded by the second row

transition metal, to perform two electron oxygen atom transfer reactions, such as sulfite oxidation and dimethyl sulfoxide reduction.[22] Tungsten is below Mo in Group 6, so the lower oxidation state W(IV) is more reducing and Mo is replaced by W when strong reducing power is needed.[6] The Mo-centre is always coordinated by oxygenic/sulphurous ligands and at least one organic pyranopterin dithiolene ligand (Figure 1.5).[22] The role of this elaborate organic cofactor is unclear and its potential non-innocence and redox activity in the Mo-enzyme YedY, a methionine sulfoxide reductase, is explored in Chapter 4.
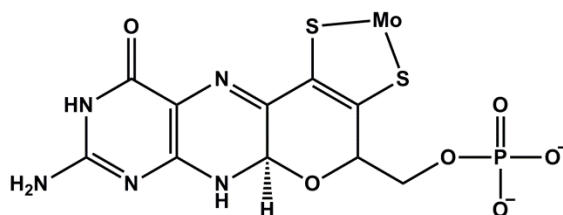
Figure 1.5 Pyranopterin ligand of mononuclear molybdoenzymes

1.1.3 Flavoproteins and quinoproteins

Redox proteins need not contain or solely contain a metal and flavo- and quinoproteins utilise delocalised organic cofactors, which can transfer electrons and perform catalysis through organic reactions with the cofactor.[3] Flavoproteins contain a flavin (Figure 1.6), typically a FMN or FAD cofactor non-covalently linked to the protein, with the protein environment diversifying the properties. Simple flavodoxins perform two or one (via radical semiquinone) electron transfer and flavoenzymes catalyse reactions including reductase, oxidase, dehydrogenase and disulphide oxidoreductase activity.[52] Quinoproteins contain a non-covalently bound pyrroloquinoline quinone (PQQ) (Figure 1.6) or a covalently bound modified amino acid quinone that can shuttle between quinone/semiquinone/quinol.

flavin   PQQ
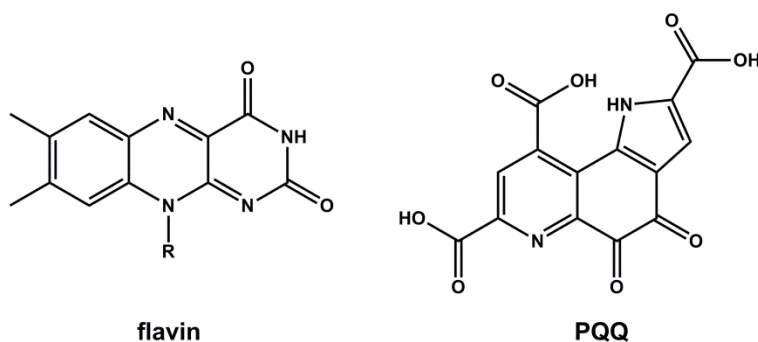
Figure 1.6 Flavin and PQQ cofactors

Quinoproteins are generally dehydrogenases of alcohol, sugar, aldehydes and amines.[53] Quinones can also act as electron transfer centres, notably Q_A and Q_B in photosystem II of the photosynthetic electron transport chain.[54]

1.1.4 Redox active amino acid residues

The amino acids tyrosine, tryptophan, cysteine, glycine and some post-translationallly modfied versions can form one electron oxidised radicals, to promote redox activity in non-metalloproteins, or function in concert with metal centres within the same protein. Redox active amino acid centres catalyse a wide range of radical reactions, including DNA synthesis (by ribonucleotide reductases) and energy transduction (in photosystem II).[55] Cysteine can also be redox active through the reversible formation of disulphide bonds, which regulates the structure and acitivity of a wide range of proteins. Thioredoxins perform this redox regulation via a CXXC amino acid motif that can reversibly catalyse the two electron reduction of disulphide bonds. The amino acid residues XX, hold the cysteines in a tight loop for fast electron transfer and tune the pKa and redox potential.[56] HypD, a biosynthetic protein which performs reductive insertion of cyanide ligands into the active site of NiFe-hydrogenases, contains a CXXC motif and its redox activity is explored in Chapter 5.

1.1.5 Technological applications

The biological function of redox proteins can be harnessed in a breadth of technological applications, including biosensors, energy conversion and pharmaceuticals.[3] Biosensors can use redox proteins as the biorecognition component that transduces the sensing event into a measurable electrochemical signal.[57] Arguably the most important and successful example is the glucose biosensor used by diabetics worldwide, which electrochemically measures blood glucose levels via glucose oxidation by the flavoenzyme glucose oxidase.[58]

Biofuel cells utilise enzymes or whole cell microbes to catalyse oxidation of fuel at the anode and reduction of an electron acceptor at the cathode, generating electrical power.[59] One example is a H_2/O_2 fuel cell using a hydrogenase to oxidise hydrogen and a multicopper oxidase to reduce O_2 (Figure 1.7 A).[60] An important advantage of enzymes over synthetic catalyst counterparts is minimisation of overpotential. This is an extra driving force required by the

catalyst above that dictated by the thermodynamics of the reaction, which reduces the voltage provided by the fuel cell.[61] The molecular control of overpotential in [NiFe]-hydrogenases is determined in Chapter 7.
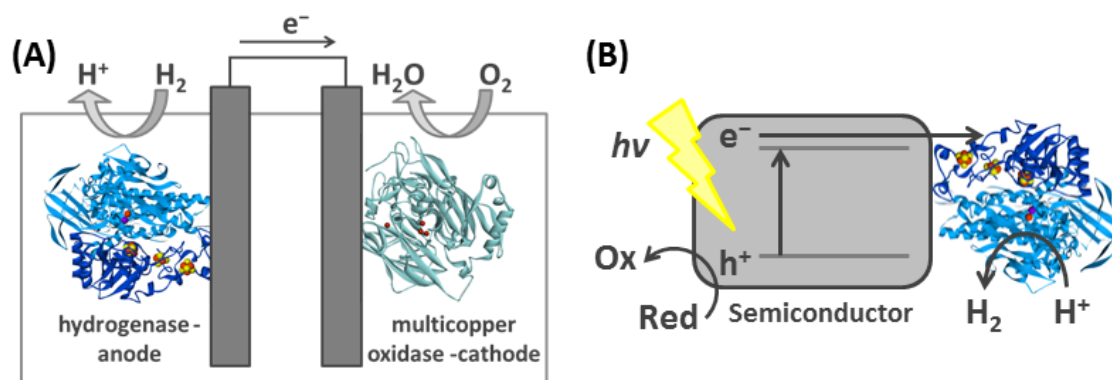
Figure 1.7 (A) Enzymatic H_2/O_2 fuel cell (B) Enzymatic solar fuel device

Solar fuel devices can use biological systems to achieve light-driven water oxidation and fuel production.[62, 63] For example, a hydrogenase coupled to a light sensitised semiconductor can utilise photo-generated electrons to reduce protons to hydrogen (Figure 1.7 B).[64] For this the hydrogenase must be catalytically biased towards hydrogen production rather than oxidation and a determinant of this catalytic bias is uncovered in Chapter 7. Industrialisation of hydrogenase fuel cell and solar fuel applications depends on large scale hydrogenase production, which is currently limited for [NiFe]-hydrogenases by limited understanding of the biosynthetic pathway.[65] HypD, a part of the biosynthetic machinery, is studied in Chapter 5.

Redox enzymes also have applications in the pharmaceutical and fine chemicals industries in biocatalytic small molecule synthesis.[3] For example, cytochrome P450s and engineered variants are used in drug synthesis.[66]

Due to the role of redox proteins in crucial biological processes, such as energy transduction, signalling, biosynthesis and repair it is certain that they will be important in health and medicine. Hydrogenases (Chapter 7) and by association their biosynthetic machinery (Chapter 5) may make good antibiotic targets, as respiratory use of H_2 for energy is required for virulence in *Salmonella enterica*.[67] The bacterial methionine sulfoxide reductase YedY (Chapter 4) repairs oxidatively damaged protein, so is important in repairing microbial proteins in response to oxidative stress.[28]

1.2 Techniques to study isolated redox proteins

1.2.1 Molecular biology and protein purification

Molecular biology techniques are often used to clone and overexpress the gene encoding the redox protein of interest, so that large amounts can be purified and studied. However, this approach is not always viable when working with complex metalloenzymes that require specialised biosynthetic machinery and so some, such as [NiFe]-hydrogenases (Chapters 6 and 7), may need to be expressed at native levels. Molecular biology is also used to introduce a tag to the protein, so that it can be easily purified using an affinity column. Site directed mutagenesis can be used to introduce amino acid point mutations to the protein, in order to assess the role in redox properties and catalytic function (as in Chapters 6 and 7) or to allow further modification by chemical biology methods to engineer the required properties for study by a certain technique.[68]

1.2.2 Structure determination

Since the seminal, Nobel prize winning work of Max Perutz and John Kendrew in solving the X-ray crystal structure of myoglobin, the structural determination of redox proteins (usually by X-ray crystallography and sometimes by NMR or electron microscopy) has been instrumental in elucidating the structural determinants of certain redox properties and catalytic activities.[69-71] A single high resolution structure provides a precise picture of the ligand field environment of redox active components, which is valuable in rationalising how amino acid sequence changes may relate to differences in reactivity. Comparative structures of oxidised and reduced states provide even more insight into the mechanism of electron transfer and substrate bound structures aid elucidation of catalytic mechanisms.[72]

1.2.3 Activity assays

General biochemical activity assays are used to study kinetics, substrate affinities, inhibitor effects and some mechanistic aspects of redox enzyme catalysis. This is often done by monitoring the colour change of a redox dye, as it receives or donates electrons to the enzyme performing oxidation or reduction catalysis. These assays have the advantage of simplicity but there is no precise

control of redox potential and the rates of fast enzymes cannot be measured accurately as diffusion limits the reaction.

1.2.4 Computational methods

Density functional theory (DFT) cluster and quantum mechanics / molecular mechanics (QM/MM) models, have been among the most important recent advances in understanding mechanistic aspects of redox proteins. Minima in the energy of the system define structures of reactants, intermediates and products and the saddle points are transition states that are not easily identified experimentally. In concert with experimental techniques quantum modelling can provide vital information to solve difficult mechanistic problems.[73] In particular, when studying extremely fast redox processes, the use of computational analysis enables the reaction timescale to be probed in a manner which can be otherwise experimentally inaccessible.

1.2.5 Spectroscopy

Beyond the rainbow of visible light, spectroscopic techniques use the broad range of the electromagnetic spectrum to access energetic transitions spanning across nuclear, electronic, vibration, rotation and spin (Figure 1.8).
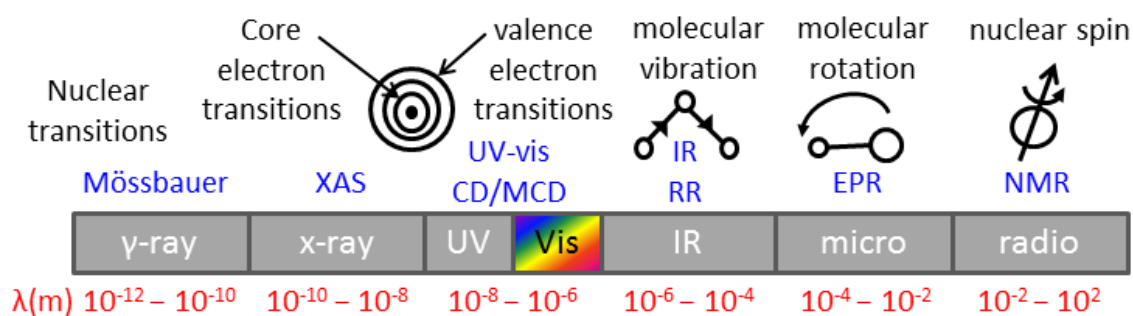
Figure 1.8 Electromagnetic spectrum in spectroscopy

Each provides access to different information about structures and mechanisms but may only be suitable if the correct spectroscopic handle is present within the protein. Redox proteins are particularly amenable as the metal or redox site of interest will often have a spectroscopic signature in a region which is distinct from the background protein "noise". In complement with techniques such as crystallography, which show the full structural detail but often lack kinetic resolution, spectroscopic time-course measurements can provide extremely valuable insight into redox mechanisms. Spectroscopic measurements are also

of great value to computational chemists, in providing experimental data that can be used to corroborate computational predictions.

Starting at the high energy end of the spectrum, Mössbauer spectroscopy measures absorption of γ-radiation by nuclei and utilises the Doppler effect to measure electronic environment perturbances on nuclear energies. It has been used to determine oxidation states, spin states and structural properties of Fe sites in proteins, as ^{57}Fe is particularly amenable to the technique.[74, 75]

X-ray absorption spectroscopy (XAS) measures the absorption of X-radiation by excitation of core electrons, yielding information about the electronic and physical structure of a metal site. The oxidation state, symmetry, geometry and metal ligand structures of many metalloproteins are studied and it is vitally useful in the research of otherwise spectroscopically silent metal ions, such as Cu(I) (d^{10}) with a filled valence band.[76]

UV-vis spectroscopy measures the absorbance of ultraviolet and visible light by valence electronic transitions.[6] The redox centres of many proteins have distinctive spectra, due to π-π transitions of conjugated organic cofactors or charge transfer at metal–ligand sites. The intensities and energies of transitions provide information on the electronic and chemical environment and usually changes in spectral properties of a distinct chromophore are used to monitor changes in oxidation state or addition of substrate or inhibitor.

Magnetic circular dichroism (MCD) measures the differential absorption of left and right circularly polarised light, induced by a parallel magnetic field. It measures the same transitions as UV-vis spectroscopy, but the more stringent selection rules and bisignate nature enhance the detail and resolution. This makes MCD a more powerful probe of structural and electronic properties of redox centres in proteins and can, for example, identify oxidation and spin states and distinguish iron-sulphur cluster structures.[77, 78]

Infrared (IR) spectroscopy measures the absorption of infrared light due to excitation of vibrational modes, with a changing electric dipole moment. Some metalloenzymes have native ligands that absorb intensively in the infrared region, such as the CN^- and CO ligands at a hydrogenase active site and others bind similar exogenous ligands. They can report on structure, induced changes to the coordination and electronic state of the metal and the kinetics

and mechanism of ligand or substrate binding and release.[79] Surface enhanced infrared absorption (SIERA) is often used to enhance signals.[80]

Raman spectroscopy indirectly measures vibrational energy level changes by inelastic scattering of higher energy incident light. Resonance Raman (RR) is usually performed, in which the laser frequency is tuned to an electronic transition of the chromophore of interest and the associated vibrational modes have greatly enhanced Raman scattering intensity. Tuning the incident frequency allows individual chromophores (e.g. organic redox cofactors or transition metal sites) to be independently studied, without interference from the rest of the protein or other chromophores, giving structural and electronic insights. Pump probe methods can be used to study kinetic aspects of mechanisms.[81, 82]

Electron paramagnetic resonance (EPR) spectroscopy measures the absorption of microwave radiation by unpaired electrons due to the non-degeneracy of electron spin energy levels in a magnetic field (Zeeman effect). This along with hyperfine coupling interactions to nuclear spins enables the structural and electronic characterisation of paramagnetic centres. Diamagnetic centres cannot be detected but many redox proteins have radical intermediates or paramagnetic transition metal centres. EPR is particularly useful as other parts of the protein and solvent are EPR silent, enabling examination of the site of interest alone. EPR of freeze quenched intermediate species aids understanding of catalytic mechanisms.[83]

At the low end of the spectrum, nuclear magnetic resonance (NMR) spectroscopy measures the absorption of radio frequencies by nuclei, due to the non-degeneracy of nuclear spin states in a magnetic field. Chemical shifts and J-couplings give information about structural environments and complex NMR experiments can be used to fully resolve metalloprotein structures. An advantage is that NMR can monitor dynamic motions and interactions.[84, 85]

The appearance or disappearance of a spectroscopic signature (e.g. UV-vis, MCD, IR, RR, EPR) with a change in oxidation state is routinely used in redox titrations of proteins, to determine the reduction potential of redox sites. This gives the thermodynamics of the electron transfer process, but no kinetic information.

1.2.6 Flash photolysis

Laser flash photolysis methodologies, pioneered by Harry Gray, have been instrumental experiments in understanding the kinetics and mechanism of electron transfer in proteins. A photosensitiser such as a Ru, Os or Re complex is conjugated to the protein a fixed distance from the natural redox site, excited by laser flash photolysis and the rate of electron transfer between it and the natural redox site measured by time-resolved spectroscopy.[4, 86] By using photosensitiser complexes with modified ligands and therefore reduction potentials, the contribution of thermodynamic driving force to the rate of electron transfer has been studied, in accordance with Marcus theory (Chapter 2.3.2). Changing the distance between the conjugated photosensitiser and protein redox site, shows an exponential dependence for driving force optimised electron transfer rates and proves an electron tunnelling mechanism.[4, 5] However, rates are strongly dependent on the intervening protein medium, which can improve donor and acceptor coupling and allow electron tunnelling through protein up to around 25 Å. Electron transfer over larger distances can be achieved by electron hopping via intermediates sites.[87] This was proven by flash photolysis experiments measuring the electron transfer rate between a Re sensitiser and Cu in azurin, via an engineered radical intermediate tryptophan site.[88]

1.3   Electrochemical techniques to study redox proteins

1.3.1   Protein electrochemistry

To fully understand a biological redox process it is important to measure the mechanism, thermodynamics and kinetics of the reaction. The thermodynamics are often measured by sample demanding spectroscopic titrations and kinetics have been measured by flash photolysis experiments on specifically engineered proteins. Electrochemical techniques have the power to study the mechanism, thermodynamics and kinetics of both electron transfer and catalysis on small samples of native protein and without the need for a spectroscopic handle.[89] An applied electrochemical potential controls the flow of electrons between an electrode and redox active protein, and the measured current describes the redox reaction. Historically, this bioelectrochemistry proved challenging, as there were problems with protein denaturation at electrode surfaces and slow

electron transfer.[90] Mediators were used to couple electron transfer between the electrode and protein, but reactions were then limited by the mediator and properties intrinsic to the protein could not be measured directly.[91] However, in 1977 Eddowes and Hill [92] and Yeh and Kuwana [93] separately demonstrated that reversible voltammetry of a solution of the heme protein cytochrome c was possible at appropriate electrodes of bis(4-pyridyl) modified gold and indium oxide, respectively. Further study showed that the reversible electrochemistry was due to transient absorption events at the electrode surface.[94, 95] This lead to the strategy, popularised as "protein-film electrochemistry" (PFE) by Armstrong and co-workers, of directly immobilising protein in an electroactive configuration at the surface of an electrode.[96] Immobilising the protein removes the limitations of slow protein diffusion in solution and enables the mechanism, thermodynamics and kinetics of electron transfer or redox catalysis intrinsic to the protein to be exquisitely resolved with sub-picomole samples. [90, 96] By 2012 around forty proteins had been studied in this manner and ever expanding mechanistic insight into biological electron transfer and redox catalysis continues to be gained with PFE.[89, 97]

1.3.2 Protein film electrochemistry

Protein film electrochemistry (PFE) requires that redox active protein is adsorbed onto the surface of a working electrode in an electroactive configuration such that it can efficiently exchange electrons with the electrode. This can be achieved by direct covalent attachment via linker chemistry or by non-covalent absorption. This is most commonly onto abraded pyrolytic graphite edge, on a self-assembled monolayer on gold, within a conducting polymer matrix or on nanostructured materials (Figure 1.9).[97]
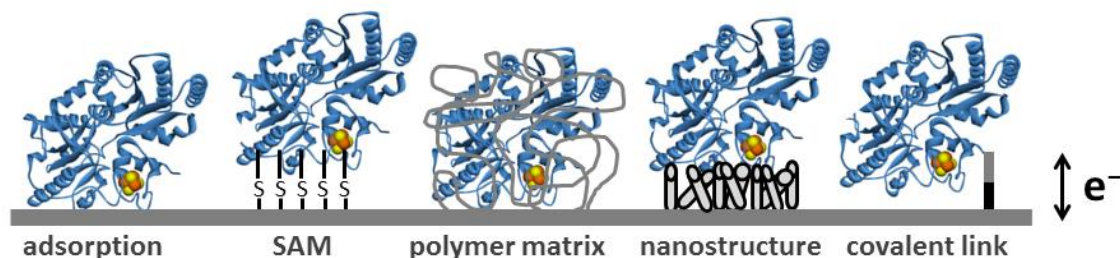
Figure 1.9 Protein-electrode attachment strategies

The working electrode is placed in a solution filled cell, in a standard three-electrode set-up alongside a reference and counter electrode (Figure 1.10).

Conditions such as temperature, gas atmosphere and pH are easily controlled inside the cell and a potentiostat imposes the potential and measures the resulting current.[97, 98] Potentials are applied between the working and reference electrodes and current flows through the counter electrode to minimise drops in potential due to solution resistance (ohmic drop) and prevent significant current flow through the reference electrode which would alter its potential.[98, 99]
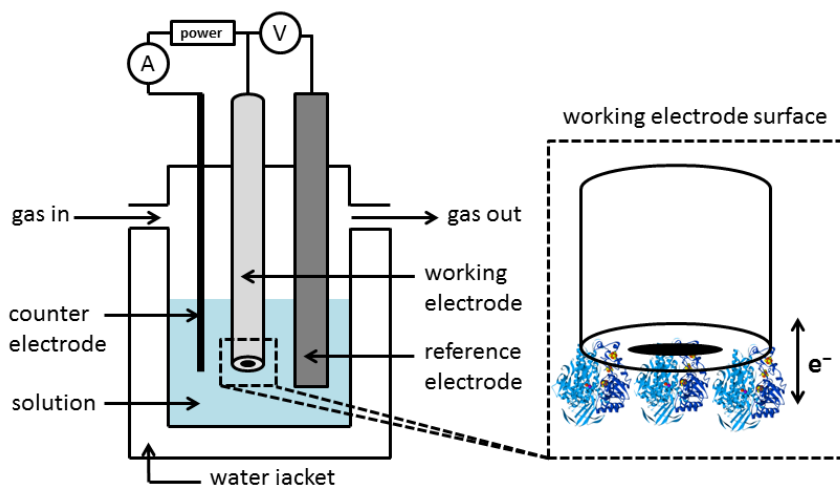
Fig 1.10 Protein film electrochemistry set-up. Adapted from references 98 and 103.

In cyclic voltammetry the potential is swept from one potential to another and then back at a defined scan rate and the measured current recorded as a function of applied potential. In chronoamperometry the potential is held constant as the current is measured.[99] There can be Faradaic and non-Faradaic components to the measured current. The non-Faradaic current is an ever-present background contribution due to the capacitance of the electrode, onto which any Faradaic current is superimposed. Figure 1.11 shows a typical non-Faradaic response from a cyclic voltammetry experiment.
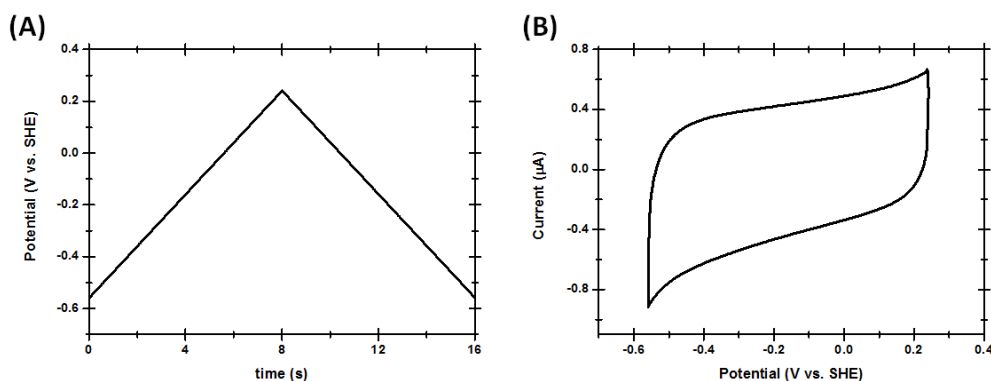
Figure 1.11 Cyclic voltammetry (A) Applied potential (B) Measured non-Faradaic current

Faradaic current arises from redox reactions at the electrode surface; net reduction or oxidation giving rise to negative or positive currents, respectively.[99, 100] In PFE Faradaic current can arise from electron transfer to or from redox active centres within the enzyme or from redox catalysis in which electrons flow to or from a substrate via the enzyme (Figure 1.12). These Faradaic responses reveal mechanistic, thermodynamic and kinetic details of the protein redox reactions.[89, 96, 97, 101-103] A full theoretical description is outlined in Chapter 2.6.
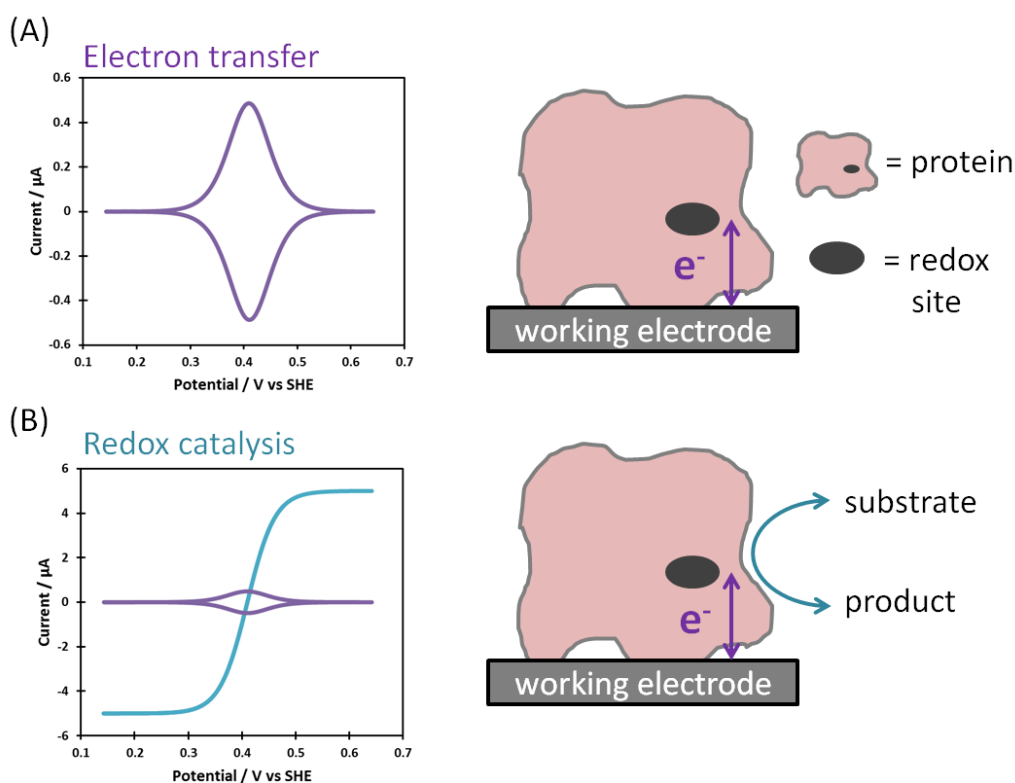
Figure 1.12 Faradaic responses for (A) Electron transfer and (B) Redox catalysis

1.3.3 Catalytic current

A redox enzyme adsorbed at an electrode will turn over substrate when the electrode potential provides sufficient driving force for catalysis. The net flow of electrons between the electrode and substrate gives the measured catalytic current and is proportional to the electroactive coverage of enzyme and the turnover rate.[89] If the turnover rate is high, as is often the case for enzymes, this leads to a greatly amplified catalytic current. Interfacial electron transfer can be rate limiting but this is generally avoided by ensuring good enzyme orientation on the electrode.[89, 101] Mass transport of substrate can also be rate limiting but this is prevented by using a rotating disk electrode, spun at a

sufficient rate to provide a constant supply of substrate.[89, 101] In the absence of these limitations the voltammetry then reports on the intrinsic catalytic properties of the enzyme. In the simplest case the catalytic current varies sigmoidally with electrochemical potential (Figure 1.12 B) due to the Nernstian shift of the active site between its oxidised and reduced states (Chapter 2.6.6). The catalytic current reaches a plateau limiting value when the all the active site is in its catalytically active state for reductive or oxidative catalysis. This simple sigmoidal current response can be complicated by a number of factors, [89, 102, 104] including intramolecular electron transfer (if there is a redox relay within the enzyme),[105, 106] substrate binding and release,[107] (in)activation processes [108, 109] and dispersion of enzyme orientations on the electrode.[110] The electrochemical response therefore reports on the thermodynamics and kinetics of many mechanistic aspects of electrocatalysis, which may be inaccessible by other techniques. A further advantage of electrochemistry is that the conditions in the cell, such as pH, temperature, solution composition, gas atmosphere etc. can be extremely rapidly titrated, so the enzymatic response under a range of conditions can be quickly investigated using one very small sample.[98]

Arguably the most important insight offered by catalytic voltammetry is the added dimension of potential in the assaying of enzyme kinetics, not afforded by the single potential of a redox dye in a solution assay.[102] Potential dependent turnover rates can be calculated from the current (if the electroactive coverage is known) and potential dependent substrate affinity (K_M) values can be calculated (if the substrate concentration is varied).[89] Rate and equilibrium constants for more complex kinetic schemes can also be investigated.[111] The potential domain also gives easy access to the catalytic bias and overpotential requirement of the enzyme. Catalytic bias is defined as the ratio of the maximum limiting oxidation and reduction currents, so is a measure of whether the enzyme is a faster catalyst of the reductive or oxidative reaction.[42, 112] Figure 1.13 A shows the voltammetric response from an enzyme biased towards oxidation (blue), reduction (red) and with no bias (black). An overpotential requirement is defined as extra potential (or driving force) required by the enzyme to drive net oxidation or reduction of substrate, further to the potential defined by the Nernstian equilibrium potential of the substrate / product couple (Figure 1.13 B).[113]
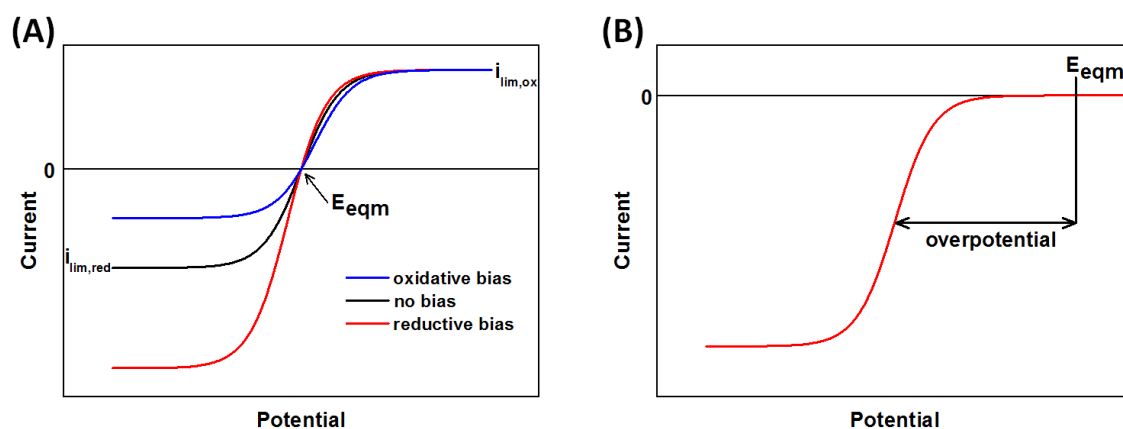
Fig 1.13 Voltammetric responses showing (A) Catalytic bias and (B) Overpotential

Catalytic bias and overpotential are extremely important parameters describing the efficiency of the enzyme catalyst and can be easily measured under an array of conditions using PFE. A full theoretical description is given in Chapter 2.6.6 and the role of an FeS cluster redox relay in determining the catalytic bias and overpotential requirement of a [NiFe]-hydrogenase is determined in Chapter 7.

1.3.4 Non-turnover current

PFE can be performed in the absence of catalysis and the "non-turnover" current measured results from reduction and oxidation of redox centres within the protein.[89] This can be for electron transfer proteins such as cytochromes and ferredoxins or for redox enzymes in the absence of catalysis.[112] For example, upon removal of substrate, addition of inhibitor or measured at high voltammetric scan rates that outpace catalysis but not electron transfer.[89, 112, 114, 115] A single redox site with a reversible redox couple gives a pair of well-defined positive and negative current peaks in cyclic voltammetry (Figure 1.12 A), due to oxidation and reduction of the site, respectively.[89, 96, 112] These so called "non-turnover" signals provide a thermodynamic description of the redox process. When the scan-rate is slow enough that the protein is under equilibrium conditions, the peak potentials equal the reduction potential, the peak width at half-height measures electron stoichiometry and integration of the peak area quantifies the amount of electroactive protein adsorbed.[89, 96, 112] Non-idealities in peak separation and width do arise and can be accounted for by a dispersion of protein orientations on the electrode giving dispersion in the thermodynamics and kinetics.[116] The situation is further complicated in multi-

centre proteins with numerous redox sites and a full theoretical account of non-turnover signals, appropriate to the work in this thesis, is detailed in Chapter 2.6.

Faster voltammetric scan rates are used to probe the kinetics of the electron transfer reaction. There are deviations from the Nernstian equilibrium peak shapes when the rate of electron transfer is too slow to maintain equilibrium between the electrode and redox site.[89, 112] The peaks broaden and the oxidative and reductive peaks separate.[89] The increase in peak separation with scan rate allows the standard heterogeneous rate constant of electron transfer to be approximated.[89, 112, 117] If the reductive and oxidative peak currents are of differing magnitude the voltammetric response can report on the rates of coupled chemical steps that are slow on the time-scale of the experiment, for example proton-coupled electron transfer.[89, 111, 112, 118] This access to kinetic and mechanistic information is a major advantage of dynamic electrochemical techniques over redox titrations. As with catalytic voltammetry the cell conditions can be rapidly titrated, so the kinetics, thermodynamics and mechanism of protein electron transfer can be investigated under a range of conditions using one very small sample.

However, it must be acknowledged that not all redox proteins can be adsorbed to electrodes in an electroactive configuration, so many are not amenable to electrochemical study. Further, for those that can be studied with electrochemical techniques there is a lack of associated structural information afforded by spectroscopy.[89] Electrochemistry is therefore best used in concert with other techniques. Recent developments in dynamic spectroelectrochemical techniques provide spectroscopic structural information in real-time concert with electrochemical data, affording a fuller description of redox changes within proteins.[119] A final issue with PFE is that "non-turnover" signals can be very small, as the electrode surface coverage of large proteins is low. These small signals are then superimposed on the vastly larger background capacitive current, so extraction of the signals by baseline subtraction can therefore be rather crude and inaccurate.[120] Quite often the very small signals are completely overwhelmed and invisible beneath the background capacitance current. In this case redox reactions within the protein cannot be probed and even if amplified catalytic currents can still be studied, the protein coverage is

unknown so absolute turnover rates cannot be calculated.[89] Modulated voltage sweeps in differential pulse[93], square-wave [121] and ac voltammetry [92] have been used to try and overcome this problem by giving better separation between the Faradaic and capacitive currents.

1.3.5 Differential pulse, square wave and ac voltammetry

There are numerous techniques in which the linear voltage sweep of dc voltammetry is periodically modulated, to enable Faradaic and non-Faradaic current to be separated and to provide a response that enhances discrimination of closely related mechanisms.[99] In fact, the first two papers describing reversible protein electron transfer by Eddowes and Hill [92] and Yeh and Kuwana [93], utilised ac and differential pulse voltammetry, respectively, for these purposes. A handful of further papers have utilised square wave voltammetry to enhance protein electron transfer signals.[121, 122]

In differential pulse voltammetry (DPV) a series of voltage pulses are superimposed on the linear potential sweep.[123, 124] Current is sampled immediately prior to each voltage change and the current differences plotted as a function of potential.[123, 124] Measuring current prior to the voltage steps minimises the involvement of the capacitive charging current, which is generated by changes in potential.[123, 124] Square-wave voltammetry (SWV) superimposes a regular square-wave over a staircase voltage sweep and can be considered as a special form of DPV in which equal time is spent at the ramped baseline potential and the pulse potential.[125] Both DPV and SWV use large-amplitude perturbations to enhance signals.

Traditionally, ac voltammetry employs a small amplitude sinusoidal perturbation to the linear voltage sweep and the ac component of the current is plotted against the mean (dc) potential of the sweep.[99] Historically, ac voltammetry has been used in mechanistic studies, as the dual time domain of dc scan and ac period, provide greater access to precise kinetic and mechanistic information.[126, 127] The ac method also allows discrimination against capacitive current but this advantage is limited compared to the DPV and SWV techniques due to the small amplitudes employed.[127] The historical reason for the application of small amplitudes in ac voltammetry is to simplify the theory so that the results can be interpreted with analytical solutions.[127] However,

modern computing and the ability to numerically model results means there is no longer a need to employ small amplitudes.[127-129] The large amplitudes classically used in DPV and SWV can be utilised in ac voltammetry to enhance signals and allow both capacitive current discrimination and mechanistic insight to be improved. It was noted by Bond and co-workers that in fact there is no real difference between these "different" forms of voltammetry, other than the exact form of the periodic perturbation to the linear potential sweep.[127] This lead to the consolidation and development of ac techniques and associated analysis into the form now known as Fourier Transformed ac Voltammetry (FTacV) (Chapter 1.3.6).[127] It would seem that the perceived complexity of ac techniques and their interpretation compared to dc voltammetry has prevented their widespread use in protein electrochemistry, since the seminal work of Eddowes and Hill [92] and Yeh and Kuwana [93]. FTacV could now open the door to improving protein electron transfer signals by discriminating against capacitive current and enhancing kinetic and mechanistic detail, as was promised in the earliest work of protein electrochemistry but not since capitalised on.

1.3.6 Fourier Transformed ac Voltammetry (FTacV)

The historic obsession with small amplitudes in ac voltammetry was overcome in 2000 by Gavaghan and Bond [128] and Engblom, Myland and Oldham [130], who presented numerical and analytical solutions for large amplitude ac voltammetry, the theory of which is reviewed in Chapter 2.7. It became clear that fast Fourier transform methods could be used to separate components of the current output and vastly improve the quality of data analysis and the kinetic, thermodynamic and mechanistic insight gained.[127, 128] The technique of FTacV was thus born and advanced extensively into its current form by Bond and co-workers [127, 131, 132], with the required instrumentation developed by Elton and co-workers.[127, 132, 133]

The electrochemical experimental set-up of FTacV is the same as for dc Voltammetry (dcV) but a bespoke potentiostat is used to apply a waveform of frequency (f) and amplitude (ΔE) onto the dc voltage sweep.[127, 131] A large amplitude sinusoid is most commonly used as a smooth sinusoid is easier to apply electronically and analyse theoretically than supposed step change perturbations. The total current output is measured as a function of time and

then Fourier transformed into the frequency domain to obtain a power spectrum
(Figure 1.14).[127, 131]
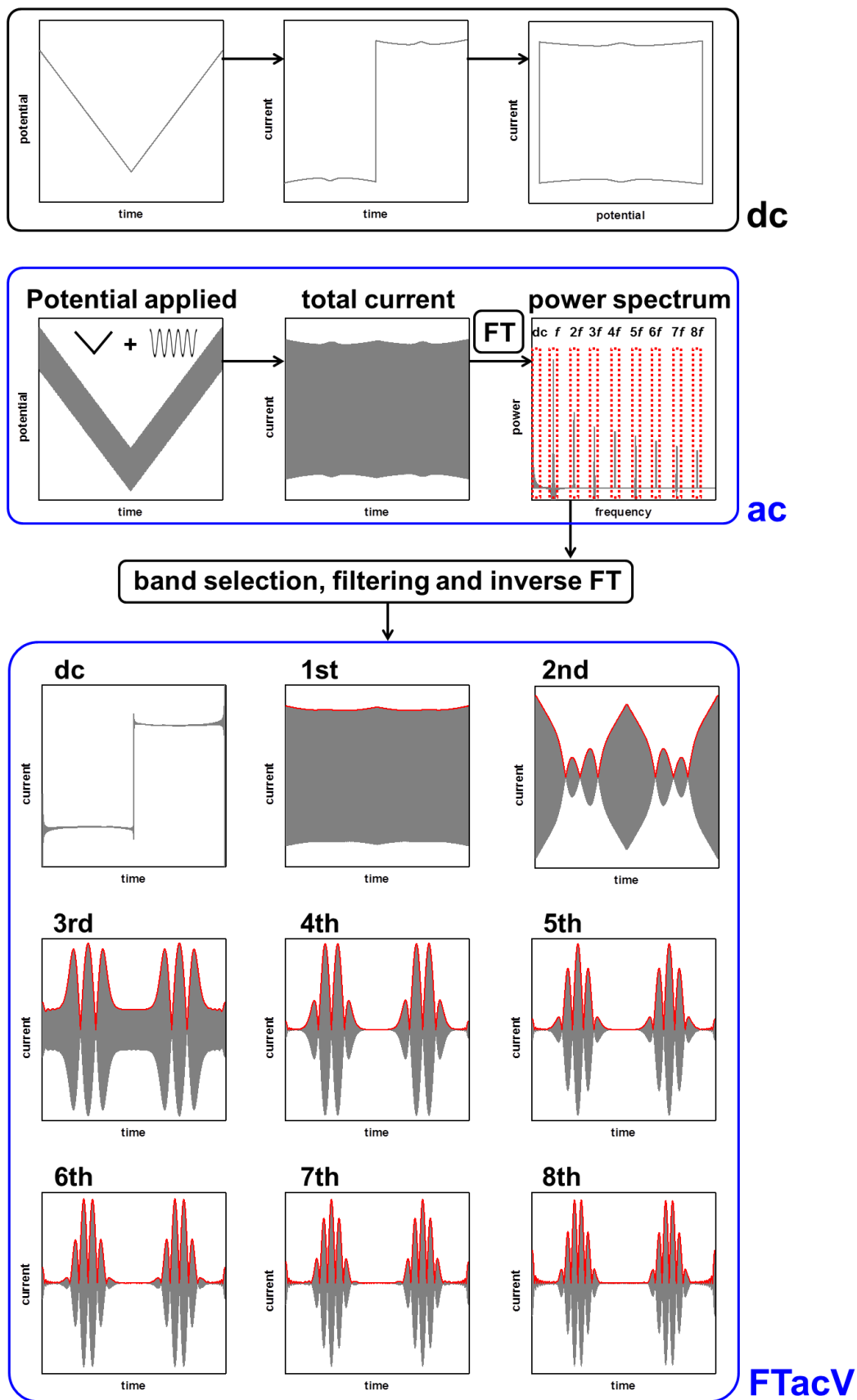
Figure 1.14 Comparison of FTacV and dc voltammetry techniques

The Faradaic component has a non-linear response to the oscillation and so the current output has harmonic contributions at multiples of the input frequency (f, $2f$, $3f$ etc) as well as an aperiodic dc component.[127] The capacitive component, if modelled by a potential–independent capacitor, has a linear response to the oscillation.[127, 134] Therefore, ideally, its response is simply at the input frequency (f) and there is no contribution to the second or higher harmonic components.[127, 134] In reality the double-layer capacitance at an electrode is potential dependent, which introduces non-linearity and the second, third and sometimes even fourth harmonics can contain a capacitive component.[134] However, the fifth and higher harmonics are usually completely devoid of a capacitive component and contain purely Faradaic current.[134] This enables efficient separation of the background capacitive current and the Faradaic current of interest.[131] Each harmonic component and the aperiodic dc component can be resolved by band selection and filtering, followed by inverse Fourier transform into the time domain (Figure 1.14).[127, 135] Each harmonic signal is represented as an envelope (red) of the total harmonic current response (grey) (Figure 1.14).[127, 131] The aperiodic dc component preserves the main attributes and information available from a dcV experiment but with some broadening or further distortion of the response due to Faradaic rectification enhanced by the large amplitude ac perturbation.[129, 136, 137] The higher harmonics give time-domain data with negligible background capacitive contribution compared to conventional dcV, so the often obscured Faradaic component of non-turnover protein film electrochemistry is vastly clearer.[120, 131] A direct comparison of an example response from dcV and equivalent 4th to 8th harmonic responses of FTacV shows the enormous improvement in clarity of the Faradaic signal, from small bumps on an large background to clear background-free signals (Figure 1.14).

Such enhancement in signal quality by FTacV enables much more reliable data analysis and greater information about the redox process to be extracted.[131, 132] Although pulse and square wave methods enhance Faradaic to capacitive current ratios, only the higher harmonic ac method gives theoretically zero capacitive contribution, so may be considered optimal in this respect.[120] The background-free high harmonic signals can be further amplified by using a larger amplitude waveform (ΔE), although a compromise needs to be reached due to concurrent broadening of the signals.[130] Changing the waveform

frequency (*f*) gives access to different kinetic regimes, to which electron transfer kinetics are highly sensitive and so easily measured.[131, 132]

FTacV also affords kinetic information much more efficiently than dcV.[131, 132] To study electron transfer kinetics with dcV the effect of increasing the scan-rate (so decreasing the time-scale of the experiment) is studied.[102, 131, 132] This is however time consuming and it cannot be guaranteed that the conditions are constant from experiment to experiment. With a single FTacV experiment, each higher order harmonic essentially represents a shorter time-scale that is more sensitive to kinetics, so vastly more kinetic data is obtained from a single experiment under one exact condition.[131, 132] Furthermore, the intricacies of the harmonic responses enable much clearer discrimination between different mechanisms of electron transfer.[127]

FTacV has further advantages over dcV in catalytic voltammetry, due to its ability to separate electron transfer from coupled electrocatalysis.[127, 131, 138, 139] The aperiodic dc component contains catalytic current, which is broadened by Faradaic rectification but the limiting current plateau is solely determined by the kinetics of catalysis and the usual advantages of catalytic PFE are maintained.[131, 136] The higher harmonics are rather insensitive to slower chemical catalysis and its contribution becomes insignificant when the frequency of the harmonic is sufficiently high.[131, 136] The higher harmonics are then solely influenced by the faster underlying electron transfer process.[131] FTacV can therefore simultaneously measure and deconvolute catalysis and the underlying electron transfer, into the aperiodic dc and higher harmonic components, respectively (Figure 1.15). As both can be measured at the same time under the same conditions it is possible to understand how electron transfer controls catalysis or how the presence of substrate influences the electron transfer centre. Furthermore, as *simultaneously* the surface coverage of electroactive protein can be calculated from the higher harmonic signals and the catalytic current is known from the aperiodic dc component, the exact turnover rate of the enzyme can be calculated. In dcV the surface coverage would have to be measured in a separate measurement, so it would not be known if the surface coverage was exactly the same during the catalytic measurement, introducing inaccuracies to the measured turnover rate. Furthermore, the non-turnover signals used to calculate the surface coverage

are often too small to be measurable with dcV and so the exact turnover rate cannot be measured at all.[89]
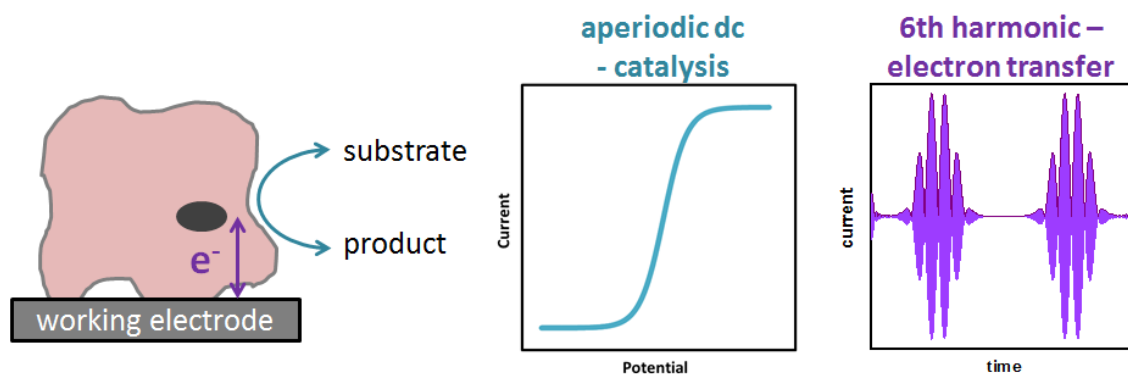
Fig 1.15 Deconvolution of catalytic and electron transfer current by FTacV

Numerical simulations of experimental electrochemical data are used to interrogate the thermodynamic, kinetic and mechanistic aspects of electron transfer reactions.[132, 140] Robust commercially available simulation packages (such as DigiSim, DigiElch and KISSA) can simulate the dc voltammetric response of a wide range of mechanisms.[140, 141] The same underlying methods and protocols are used to simulate FTacV data and the freely available MECSim software performs this function.[140] A full description of the underlying theory behind the simulations is given in Chapter 2.7. The simulated and experimental data are compared until satisfactory agreement establishes the mechanism and quantifies the kinetic, thermodynamic and other associated parameters.[127, 132] This can be achieved heuristically by manually adjusting the parameters in a time-consuming and potentially biased process.[132, 142] This approach is utilised in Chapter 4. Alternatively, automated multi-parameter data optimisation procedures can be used to find parameters that formally minimise an objective function to give the best fit between simulation and experiment.[143-145] When analysed in this way the more information rich FTacV experiment can provide much greater discernment between different mechanisms and the effects of different parameters than dcV, ultimately providing a more accurate description of the electron transfer process.[132] Automated data-optimisation procedures have been used to simulate simple solution phase redox reactions but only one part-heuristic part-automated approach has been described for FTacV protein study and this did not produce excellent theory-experiment comparisons.[146-148] FTacV of proteins presents a demanding situation due to the small Faradaic signals and

large background capacitive current, which cannot simply be ignored in simulations of high harmonics. This is because it contributes to the total current and therefore if the ohmic (iR) drop is significant it reduces the effective applied potential and can have some effect on all harmonics, although in many cases this is minimal.[140] It has been noted that the aperiodic dc and lower harmonic components are more sensitive to the capacitive current and the higher harmonics more sensitive to the Faradaic current. Parameter optimisation could therefore be improved by a two-step approach utilising this separation to first fit capacitive parameters and then Faradaic parameters. This new approach was developed and implemented by Martin Robinson (University of Oxford) to analyse data in Chapters 5 and 7.

1.3.7 Protein Film Fourier Transformed ac Voltammetry (PF-FTacV)

The advantages of FTacV have been well demonstrated for small redox molecules but the application of FTacV to PFE studies (which will be termed PF-FTacV) is somewhat in its infancy. Only a few redox active proteins that have been previously well characterised by dc voltammetry have been studied but these initial works have enhanced both the experimental and theoretical understanding of PF-FTacV and provided new insight into electron transfer processes, previously inaccessible by dcV. The first PF-FTacV study was on the blue copper protein azurin that has been extensively investigated with dcV and presents something of a model system for one electron transfer.[96, 117, 120, 149, 150] It was proven that PF-FTacV could successfully separate the Faradaic current from the large background capacitive current, with the 3rd harmonic being essentially background free.[120] The effect of scan rate, amplitude and frequency were explored and basic simulations, based on previous theoretical work [129], were used to estimate kinetics.[120] Further studies on azurin were undertaken using PF-FTacV in its square wave, as opposed to sine wave form. The harmonics separated quasireversible processes into the even harmonics and background and reversible processes into the odd harmonics, providing exquisite kinetic evaluation.[151, 152] Later sine wave FTacV studies on azurin showed that even higher harmonics (fourth and above) provided the best separation of background and Faradaic current and the differing kinetic sensitivity of each harmonic could be used to measure electron transfer rates.[153] Simulations showed non-idealities, most likely

arising from a dispersion of enzyme orientations on the electrode.[153] It was shown that FTacV could kinetically discriminate azurin on different length alkanethiols, in a model system of dispersion at a gold electrode.[154]

Cytochrome P450s have also been subject to a number of PF-FTacV studies. The first study experimentally proved that irreversible O_2 reduction catalysis and the underlying heme reversible electron transfer could be separated into the aperiodic dc and higher harmonic components respectively, allowing electron transfer processes to be probed under catalytic conditions.[139] This observation has since been proven theoretically.[136] In a second P450 study, PF-FTacV was simply used as a tool to measure the heme midpoint potential, using the background free 4th harmonic component.[155] The latest paper on a P450 utilised the kinetic sensitivity of PF-FTacV to show that electron transfer rates may be modified by protein-protein interactions.[156]

Recent PF-FTacV studies on different protein systems have been used to expand the theoretical framework of FTacV and to gain new insight into protein redox processes. A study into myoglobin utilised the information rich higher harmonics, which are sensitive to subtleties, to compare myoglobin and free heme.[157] Research into a ferredoxin showed that PF-FTacV could be used to resolve Faradaic processes from two centres with a small separation in their reversible potentials.[158] Theory was developed to simulate the PF-FTacV response of surface confined two-centre metalloproteins and heuristic simulations were used to calculate the kinetics and thermodynamics of electron transfer for each iron sulphur cluster within the ferredoxin.[158] Studies on a cytochrome c peroxidase led to the development of theory for simulation of the PF-FTacV response of two-electron transfers at a single surface confined centre.[159] The higher harmonic components were found to have enhanced sensitivity to the nuances of two-electron transfers and heuristic simulations were used to determine the level of cooperativity, as well as the kinetics and thermodynamics.[159] Again dispersion was deemed to be responsible for imperfection in theory-experiment comparisons.[159] Most recently the FAD centre of glucose oxidase was studied with PF-FTacV and the higher harmonics were again used to effectively discriminate between different mechanisms of two-electron transfers, with FAD showing consecutive one-electron transfers at approximately the same potential.[146] This study also introduced the use of

Marcus theory of electron transfer to simulations and the use of automated E-science approaches to find the best combinations of up to three parameters. However, many parameters were still found heuristically and experiment-theory comparisons were still not ideal.

1.4 This thesis

It has been well documented and experimentally proven that FTacV can bring great advantages to the study of redox proteins by PFE, particularly in terms of enhanced Faradaic and capacitive current separation, enhanced mechanistic, kinetic and thermodynamic insight and concurrent study of catalytic and underlying electron transfer processes. Chapter 2 of this thesis lays out the theoretical framework of PFE and FTacV and Chapter 3 outlines the experimental methods utilised. Prior to this thesis, PF-FTacV has largely been carried out on proteins previously well characterised by dcV, in order to gain further insight into the redox reaction or as experimental comparisons for advancements in the theory of FTacV. This thesis uses PF-FTacV to gain insight into the redox reactions of previously electrochemically uncharacterised redox proteins and finds optimal experimental parameters and conditions to push FTacV to make measurements impossible with standard electrochemistry. This is used in concert with spectroscopic, biochemical and molecular biology techniques to understand previously elusive or ambiguous aspects of important redox chemistry in proteins.

Chapter 4 utilises PF-FTacV to fully characterise the kinetics, thermodynamics and mechanism of a previously unknown two-electron two-proton redox reaction in the mononuclear molybdenum enzyme YedY, in addition to a one-electron reaction at the Mo site. This provides electrochemical evidence of redox activity of the pyranopterin ligand binding Mo, predicted by small molecule studies but not previously observed in biochemical measurements. The ability of FTacV to simultaneously measure catalysis and electron transfer is used to show that the proposed pyranopterin redox chemistry controls catalysis of a substrate mimic. This settles an ambiguity in how YedY, which displays only one-electron molybdenum chemistry, can catalyse two-electron reactions usually performed by Mo(IV)/Mo(VI) transitions in other molybdoenzymes. Since this work the biological function of YedY has been proven to be as a methionine sulfoxide

reductase, catalysing two-electron reduction of oxidatively damaged methionine in proteins.[28]

Chapter 5 uses PF-FTacV to quantify thermodynamic, kinetic and mechanistic aspects of a previously uncharacterised cysteine disulphide redox reaction in HypD. HypD is part of the biosynthetic machinery that builds [NiFe]-hydrogenases and the work aids understanding of how cyanide ligands may be reductively inserted into the hydrogenase active site. It is also shown for the first time that the signal enhancement and background current discrimination possible with FTacV is such that redox signals can be observed with FTacV even when no discernible signal can be measured with standard dcV.

Chapter 6 describes the design, construction and purification of variants of a [NiFe]-hydrogenase, used to enable study of how underlying electron transfer can control catalytic activity. Hydrogenases are particularly unamenable to the electrochemical study of redox centres within the enzyme, as the catalytic reduction of protons, which are always present in solution, masks the underlying electron transfers. An inactive variant is made to cut-out catalysis and enable electron transfer reactions of redox centres within the enzyme to be measured electrochemically. Further variants are made, with mutations close to the distal iron sulphur cluster relay where electrons enter and exit the enzyme, in order to ascertain how this electron transfer may control key catalytic properties.

Chapter 7 utilises high frequency PF-FTacV to separate the catalytic and electron transfer components of the Faradaic current from a [NiFe]-hydrogenase. True discrimination against catalytic current and pure measurement of electron transfer is confirmed by comparison with an inactive variant. PF-FTacV is used to characterise the measured one-electron transfer reaction and the signal is assigned to the distal cluster by comparison with a distal cluster mutant. It is shown that the potential of the distal cluster, far from the active site, influences the crucial catalytic properties of overpotential and catalytic bias, which had been proposed in a recent model but not yet experimentally proven.[41, 42] The simultaneous measure of catalytic current and enzyme coverage (from the high harmonic electron transfer signals) afforded by PF-FTacV also enables the absolute turnover rate of the hydrogenase to be calculated, which has not previously been able to be measured electrochemically.

The underlying theory of FTacV is now well developed and advances have been incorporated into the MECSim software package, such that most mechanisms can now be simulated. The MECSim software package was used to heuristically simulate results in Chapter 4. However, heuristic simulations are prohibitively time-consuming and inadequacies in experiment-theory comparisons remain, with dispersion of enzyme orientations on the electrode thought to be responsible. This thesis also seeks to improve the efficiency and accuracy of PF-FTacV simulations, which are so crucial in determining the kinetics, thermodynamics and mechanisms of redox reactions from the data collected. A collaboration was set-up with Martin Robinson and David Gavaghan of the Department of Computer Science at the University of Oxford to develop and implement appropriate computer automated multi-parameter optimisation procedures. Chapter 5 sees the implementation of a two-step optimisation procedure, in which capacitive parameters are fit using the lower harmonics and Faradaic parameters fit using the higher harmonics. This approach seems well suited to PF-FTacV studies and the same method is implemented in Chapter 7. The theory of the effect of dispersion on FTacV data has now been described [116] and Chapter 7 also sees the introduction of this into the data modelling.

It is hoped that the advances in experimental and analytical methods for PF-FTacV described can be implemented in the mechanistic understanding of a breadth of the important proteins that underpin the redox reactions of life, further to the three examples that will be detailed in this thesis. Full knowledge of the electron transfer and catalytic properties of redox proteins is key to understanding crucial life processes and for inspiration for chemical, biomedical and future energy technologies to be taken from Nature's fine example.

Chapter 2

Theory

2.1 Redox reactions

Redox reactions involve the transfer of electrons from one species to another (Equation 2.1).[6, 160]

$$x\ \mathbf{Ox_A} + y\ \mathbf{Red_B} \rightarrow x'\ \mathbf{Red_A} + y'\ \mathbf{Ox_B} \tag{2.1}$$
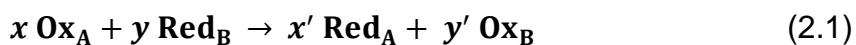
This can be expressed as two half-reactions (Equation 2.2 and 2.3).

$$x\ \mathrm{Ox}_a + n\ \mathrm{e}^- \rightarrow x'\ \mathrm{Red_A} \tag{2.2}$$

$$y\ \mathrm{Red_B} \rightarrow y'\ \mathrm{Ox_B} + n\ e^- \tag{2.3}$$

2.2 Thermodynamics of electron transfer

All reduction half reactions have a standard potential $E^{\ominus}$ (under standard conditions). This corresponds to the standard Gibbs energy of the reaction by Equation 2.4.[6, 160]

$$\Delta_r G^{\ominus} = -nFE^{\ominus} \tag{2.4}$$

The reduction of protons to hydrogen is specifically chosen to have $\Delta_r G^{\ominus} = 0$ and $E^{\ominus} = 0$ (Equation 2.5). All other values are reported relative to this.[6, 160]

$$\mathrm{H^+(aq)} + \mathrm{e}^- \rightarrow \tfrac{1}{2}\mathrm{H_2(g)} \qquad \Delta_r G^{\ominus} = 0 \quad E^{\ominus} = 0 \tag{2.5}$$
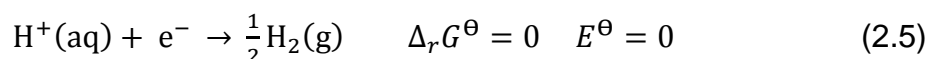
For a redox reaction $E^{\ominus}$ (the standard electromotive force) is the difference between the standard potentials of each half reaction.[6, 160]

2.2.1 Nernst equation

The potential, E, of a redox reaction at a particular composition and conditions is given by the Nernst equation (Equation 2.6).[6, 100, 160, 161]

$$E = E^{\ominus} - \frac{RT}{nF}\ln Q \tag{2.6}$$

Where Q is the reaction quotient, described by Equation 2.7 for a redox reaction of the type described in Equation 2.1.

$$Q = \frac{(a_{\mathrm{Red_A}})^{x'}(a_{\mathrm{Ox_B}})^{y'}}{(a_{\mathrm{Ox_A}})^{x}(a_{\mathrm{Red_B}})^{y}}$$

$$\tag{2.7}$$

The reaction quotient Q is described by Equation 2.8 for a reduction half reaction (Equation 2.2).

$$Q = (a_{Red_A})^{x'}/(a_{Ox_A})^{x} \tag{2.8}$$

The Nernst equation is directly derived from the relationship described in Equation 2.4 and the thermodynamic result describing the Gibbs free energy of a reaction (Equation 2.9).[6, 160]

$$\Delta_r G = \Delta_r G^{\ominus} + RT \ln Q \tag{2.9}$$

2.3 Kinetics of electron transfer

The kinetics of interfacial electron transfer at an electrode is most simply described by the phenomenological Butler-Volmer formalisms. Marcus theory is a microscopic and more general theory of electron transfer, with Marcus-Hush-Chidsey formalisms specifically describing the theory of electron transfer at electrodes.

2.3.1 Butler-Volmer theory

Butler-Volmer theory is empirical and justified by a phenomenological model. It assumes that the electrostatic energy of the transition state of an electron transfer reaction is an average of that in the oxidised and reduced states, weighted by the charge transfer coefficient.[99, 100, 161] Assuming Arrhenius-like behaviour the rate constants of reduction (k_{red}^{BV}) and oxidation (k_{ox}^{BV}) for a simple electron transfer (Equation 2.10) are described by Equation 2.11 and Equation 2.12.

$$Ox + n\,e^{-} \rightarrow Red \tag{2.10}$$

$$k_{red}^{BV} = k_0 \exp(-\alpha n F(E - E^{o'})/RT) \tag{2.11}$$

$$k_{ox}^{BV} = k_0 \exp((1-\alpha)n F(E - E^{o'})/RT) \tag{2.12}$$

where E is the electrode potential, $E^{o'}$ is the formal potential of the system, k_0 is the standard rate constant (when $E = E^{o'}$) and α is the charge transfer coefficient, which is usually found to be $\alpha = 0.5$.[99]

The kinetics of electron transfer are related to the net current (i) measured at the electrode by Equation 2.13.

$$i = nFA(k_{ox}[Red] - k_{red}[Ox])$$

(2.13)

where A is the area of the electrode. Substitution of Equation 2.11 and Equation 2.12 into Equation 2.13 gives the Butler-Volmer equation (Equation 2.14).

$$i = i_0 \left(\exp\left(\frac{(1-\alpha)nF(E - E^{o\prime})}{RT} \right) - \exp\left(\frac{-\alpha nF(E - E^{o\prime})}{RT} \right) \right)$$

(2.14)

where the standard exchange current (i_0) is given by Equation 2.15.

$$i_0 = nFAk_0[Red]^{\alpha}[Ox]^{1-\alpha}$$

(2.15)

At large oxidative overpotential Equation 2.14 simplifies to Equation 2.16.

$$\ln i = \ln i_0 + \frac{(1-\alpha)nF(E - E^{o\prime})}{RT}$$

(2.16)

At large reductive overpotential Equation 2.14 simplifies to Equation 2.17.

$$\ln(-i) = \ln i_0 - \frac{\alpha nF(E - E^{o\prime})}{RT}$$

(2.17)

The Butler-Volmer model therefore predicts exponential increases in current with increasing overpotential at large overpotentials. A Tafel analysis of $\ln|i|$ vs overpotential ($E - E^{o\prime}$) thus has a linear "Tafel region" at large overpotential.[99, 100, 161]

2.3.2 Marcus-Hush-Chidsey Theory

In Marcus theory electrons are transferred from donor to acceptor by tunnelling though a potential energy barrier.[100, 160, 162, 163] The height of this barrier is determined by the Gibbs free energy ($\Delta G^{\ominus}$) of the reaction and the reorganisation energy (λ), to bring the transition state to a geometry intermediate of the reduced and oxidised forms, such that the electron transfer follows the Franck-Condon Principle.[160, 162] The probability of electron

tunnelling is governed by the coupling between donor and acceptor (H_{AB}).[160] This leads to Equation 2.18, describing the rate constant for electron transfer.

$$k_{et}^{M} = \frac{2\pi}{\hbar}|H_{AB}|^2 \frac{1}{\sqrt{4\pi\lambda k_B T}} \exp\left(-\frac{(\Delta G^{\ominus} + \lambda)^2}{4\lambda k_B T}\right)$$

(2.18)

The electron transfer is activationless when $\Delta G^{\ominus} = -\lambda$ but the rate of electron transfer is slowed by an increasing activation barrier when the reaction becomes either more endergonic or exergonic. This gives the "inverted region", where the rate of electron transfer is slowed by more a negative $\Delta G^{\ominus}$.[160, 164]

If the electron transfer occurs at a metal electrode, electrons occupying a distribution of energy levels around the Fermi level may participate in the reaction.[165-168] Using Marcus theory and integrating across the Fermi-Dirac distribution, assuming a uniform density of states, gives the Marcus-Hush-Chidsey equation (Equation 2.19).[165]

$$k_{ox/red}^{MHC} = A \int_{-\infty}^{\infty} \exp\left(-\frac{(x - \lambda \pm n(E - E^{o\prime}))^2}{4\lambda k_B T}\right) \frac{dx}{1 + \exp(x/k_B T)}$$

(2.19)

where A is the pre-exponential factor that accounts for the electronic density of states and coupling strength and x is the energy of an electron relative to the Fermi level.[165] Marcus-Hush-Chidsey theory predicts that at a metal electrode there is no "inverted region" because at large overpotentials electrons below the Fermi level are capable of barrier-less transfer, which dominates the overall rate and gives a constant non-zero limiting rate.[165, 166, 168] The equations must be further modified for semimetals (such as graphite) and semiconductors (such as silicon), due to the distinct differences in the density of states.[169]

The Tafel analysis for Butler-Volmer, Marcus and Marcus-Hush-Chidsey theory is shown in Figure 2.1, adapted from reference [165]. Butler-Volmer theory predicts linear "Tafel regions" of increasing current at high overpotentials; Marcus theory predicts "inverted regions" of decreasing current at high overpotentials and Marcus-Hush-Chidsey theory predicts an approach to a constant current at high overpotentials.[165] When the overpotential is small compared to the reorganisation energy, Butler-Volmer theory is analogous to

Marcus-Hush-Chidsey theory.[165] This simple Butler-Volmer treatment is usually sufficient and is used in this thesis.
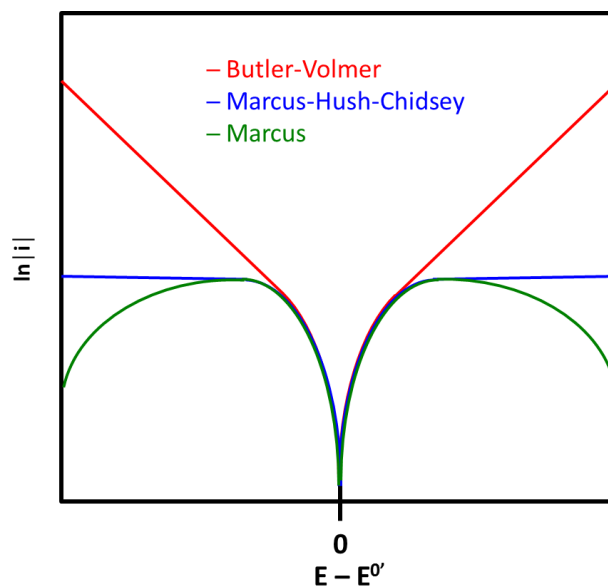
Figure 2.1 Tafel analysis of Butler-Volmer, Marcus and Marcus-Hush-Chidsey theory

2.4   Protein electron transfer theories

The semiclassical Marcus theory of electron transfer (Equation 2.18) has three crucial factors ($\Delta G^{\ominus}$, λ and H_{AB}) that control the rate of electron transfer between donor and acceptor. The Gibbs free energy ($\Delta G^{\ominus}$) and reorganisation energy (λ) are governed largely by the chemical composition and environment of the redox sites.[5, 87] The electronic coupling (H_{AB}) is a function of the donor-acceptor distance and the structure of the intervening medium.[5, 87] There are two major mechanisms of electron transfer between donor and acceptor in proteins; direct tunnelling or hopping via intermediate sites.[4, 5, 87, 170, 171]

2.4.1 Tunnelling

The simplest model of electron transfer in proteins is the "square barrier" model pioneered by Hopfield and developed by Dutton.[172-174] The protein tunnelling medium between donor and acceptor is modelled as a square barrier and solving the Schrödinger equation gives an electronic coupling (H_{AB}) and consequently rate of electron transfer (k_{et}) that decays exponentially with distance.[171, 174] Dutton and co-workers propose that proteins can be described as an average medium and the distance dependence has a decay constant β = 1.4 Å^{-1} weighted by a packing density ρ.[174] This simple

approximation provides a good description of experimentally measured biological electron transfer rates but it provides no insight into how the exact polypeptide bridging medium influences tunnelling rates.[171, 174]

The "pathway tunnelling" model proposed by Hopfield and co-workers accounts for the atomic structure of the protein bridging medium and tunnelling is mediated by consecutive electronic interactions between the atoms connecting donor and acceptor.[175, 176] This model accounts for the lower distance decay constant (β = 1.1 Å^{-1}) of beta-stand proteins and the large scatter about the exponential distance decay line, reported by Gray and co-workers in flash photolysis experiments (Chapter 1.2.6).[4, 177] This pathway model is an empirical version of the "superexchange" model, in which unoccupied atomic orbitals of the bridging medium enhance tunnelling but do not carry a significant excess electron population at any time.[170, 171] The modern "tunnelling currents" method uses explicit electronic structure calculations to find the atoms meditating tunnelling.[171] The most recent approach to modelling electron tunnelling in proteins is to use quantum mechanical electronic structure methods to access the wave functions of donor and acceptor, to directly calculate the electronic coupling element (H_{AB}).[171]

2.4.2 Hopping

The square barrier model developed by Dutton and co-workers predicts a maximum functional tunnelling distance of ~14 Å [174] and the pathway model developed by Gray and co-workers extends this to ~ 25 Å.[4] However, it is clear that charge transfer in proteins can extend over much larger distances than this single step limit, for example through respiratory chain complexes, photosynthetic machinery, multi-heme cytochromes used in extracellular respiration and multi-centre enzymes such as carbon monoxide dehydrogenases, nitrogenases and hydrogenases.[4] This long-range electron transfer is mediated by consecutive redox active cofactors or ionisable protein residues that are around 10 – 15 Å apart.[4, 5, 87] Gray and co-workers proved this experimentally by showing that 19 Å direct electron tunnelling between Cu and Re in a photosensitised azurin is accelerated by two orders of magnitude by an intermediate tryptophan residue.[88] There are three key models for this kind of mediated long range electron transfer; "hopping", "superexchange" and "flickering resonance".[171]

The charge hopping model describes a localised excess electron or charge hopping from donor to acceptor by consecutive tunnelling between intermediate sites.[87, 171] In the superexchange model electrons tunnel between donor and acceptor; the intermediate sites enhance the coupling and lower the barrier but the electron does not populate these bridging sites.[171] In the recently introduced flicking resonance model electron transfer from donor to acceptor takes place when thermal fluctuations simultaneously align the energy levels of donor, bridge and acceptor sites and the charge moves, with no nuclear relaxation, through the energy-aligned states onto the acceptor.[171, 177, 178] This contrasts with the superexchange model in which the bridging sites remain off-resonant during electron tunnelling and the hopping model in which the charge tunnels sequentially from one intermediate site to the next with nuclear relaxation in between.[171] These are all theoretical models derived for certain limits and the details of the actual electron transport process on the subfemtosecond scale are currently very difficult to observe experimentally.[171]

2.5 Enzyme catalysis

The chemical catalysis steps of a redox reaction by an oxidoreductase enzyme follow the same general models of enzyme kinetics as non-redox active enzymes, with Michaelis-Menten kinetics (Chapter 2.5.1) being a commonly used model.[89, 179, 180] The overall kinetics are however influenced by the overpotential (driving force) for the reaction and electron transfer rates, which dictate the electrochemical activity of the oxidoreductase (Chapter 2.6).[89]

2.5.1 Michaelis-Menten kinetics

The Michaelis-Menten model involves substrate (S) binding to enzyme (E) to form an enzyme substrate complex (ES), which then releases product (P) and regenerates enzyme (E), according to Equation 2.20. [160, 179, 180]

$$\text{E} + \text{S} \underset{k_r}{\overset{k_f}{\rightleftharpoons}} \text{ES} \xrightarrow{k_{cat}} E + P \tag{2.20}$$

Invoking the steady-state approximation for the enzyme-substrate complex and assuming a large excess of substrate, such that the free substrate concentration is approximately equal to the initial substrate concentration, leads

to the Michaelis-Menten equation (Equation 2.21) for the rate of product formation.[160, 179, 180]

$$v_{TO} = \frac{k_{cat}[E]_0}{1 + K_M/[S]_0} = k_{TO}[E]_0$$

(2.21)

where the Michaelis constant (K_M) is equivalent to the substrate concentration at which the rate is at half its maximum and so is characteristic of a certain enzyme's affinity for a specific substrate.[179] k_{TO} is the substrate concentration dependent turnover frequency and k_{cat} is the maximum turnover frequency when $[S]_0 \gg K_M$.

2.6 Protein film electrochemistry

The application of protein film electrochemistry (PFE) to the study of catalytic and non-catalytic reactions of redox active proteins is described in Chapter 1.3 and the underpinning theory is detailed herein.

2.6.1 Cyclic voltammetry

Cyclic voltammetry involves sweeping the potential of the working electrode from a certain potential E_1 to another E_2 and then back to E_1, at a certain scan rate v.[99, 100, 161] The applied potential is given by Equation 2.22.

$$E_{app}(t) = \begin{cases} E_1 + vt & \text{for } 0 \leq t < t_r \\ E_2 - v(t - t_r) & \text{for } t \geq t_r \end{cases} \qquad t_r = \frac{E_1 - E_2}{v}$$ (2.22)

The applied potential is attenuated by the Ohmic drop ($I_{tot}(t)\text{R}_\text{U}$) caused by uncompensated resistance (R_U) in the cell solution and the effective potential is given by Equation 2.23.[99, 140]

$$E_{eff}(t) = E_{app}(t) - I_{tot}(t)\text{R}_\text{U}$$ (2.23)

The resulting current is recorded as a function of applied potential. There are Faradaic (I_F) and non-Faradaic capacitive (I_C) components to the total current (I_{tot}), in accordance with Equation 2.24.[99, 161]

$$I_{tot} = I_F + I_C = I_F + \frac{dC_d(E)E_{eff}(t)}{dt}$$

(2.24)

Faradaic current arises from redox reactions at the electrode surface. Capacitive current arises from a redistribution of the electrical double-layer of ions in solution when a change in potential alters the electrode surface charge.[99, 100] There is therefore charging at the electrode surface analogous to a capacitor and $C_d(E)$ is the potential dependent double-layer capacitance.[134] This non-Faradaic current cannot be removed, so is a background upon which the Faradaic current is superimposed.

2.6.2 Equilibrium non-turnover voltammetry

When surface confined redox proteins or enzymes in the absence of catalysis are studied by cyclic voltammetry, signals arising from reduction and oxidation of redox sites within the protein can be observed.[89] For a single redox site, Equation 2.25 describes the case of n-electrons transferred simultaneously.

$$O + ne^- \rightleftharpoons R \tag{2.25}$$

A Langmuir isotherm is generally assumed, in which there are no interactions and all adsorptions sites are equivalent.[129, 181] The Faradaic current associated with the surface confined electron transfer is given by Equation 2.26.[129, 159, 181]

$$i = -nFA\frac{d\Gamma_R}{dt} = nFA\frac{d\Gamma_O}{dt}$$

$$\tag{2.26}$$

This can be rearranged to Equation 2.27.[129]

$$i = -nFA\frac{dE}{dt} \cdot \frac{d\Gamma_r}{dE}$$

$$\tag{2.27}$$

Where A is the electrode surface area and Γ_R and Γ_O are the surface concentrations of reduced and oxidised species, respectively. In the reversible limit these concentrations are described by the Nernst equation (Equation 2.6), which can be used with the fact that the total surface concentration $\Gamma = \Gamma_R + \Gamma_O$, to give Equation 2.28.[159]

$$\Gamma_R = \frac{\Gamma}{1 + \exp(nF(E - E^0)/RT)}$$

$$\tag{2.28}$$

Equation 2.28 can be substituted into Equation 2.27 to give Equation 2.29, describing the Faradaic current associated with the surface confined n-simultaneous electron transfer in the reversible limit.[89, 159]

$$i = \frac{n^2F^2A\Gamma}{RT} \cdot \frac{dE}{dt} \cdot \frac{\exp[nF(E - E^0)/RT]}{(1 + \exp[nF(E - E^0)/RT])^2}$$

(2.29)

where $dE/dt = v$ (the scan rate), E is the electrode potential and E^0 is the formal potential of the redox site. Equation 2.29 takes the form displayed in Figure 2.2, consisting of symmetrical oxidative (positive) and reductive (negative) peaks centred at E^0. Experimentally, this Faradaic current is superimposed on the capacitive background current and the Faradaic component is isolated by background subtraction.
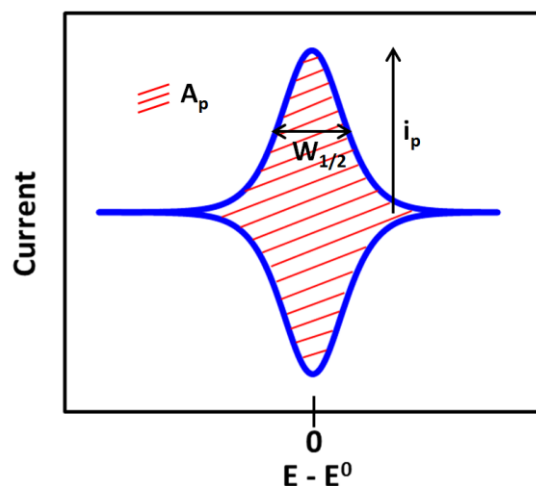
Figure 2.2 Faradaic response of a single surface confined redox site

The maximum peak height (i_p) is given by Equation 2.30.[89, 159]

$$i_p = \frac{n^2F^2vA\Gamma}{4RT}$$

(2.30)

The peak width at half the maximum height ($W_{1/2}$) is given by Equation 2.31 and is used to assess the number of electrons involved in the reaction.[89, 159]

$$W_{1/2} = 2\ln(3 + 2\sqrt{2})\,RT/nF = 90/n \text{ mV (at } 25°C)$$ (2.31)

The coverage of electroactive protein (Γ) can be calculated from the area under the peak (A_p), given by Equation 2.32.[89]

$$A_p = nFvA\Gamma \qquad\qquad (2.32)$$

The case of simultaneous transfer of n-electrons, so described, is the simplest case of surface confined electron transfer. The more complex case of co-operative two electron transfer, described by Equation 2.33 and Equation 2.34 is considered in Chapters 4 and 5.

$$A + e^- \overset{E_1^0}{\rightleftharpoons} B \qquad\qquad (2.33)$$

$$B + e^- \overset{E_2^0}{\rightleftharpoons} C \qquad\qquad (2.34)$$

The Faradaic current is now described by Equation 2.35.[159]

$$i = FA\left(\frac{d\Gamma_A}{dt} - \frac{d\Gamma_C}{dt}\right)$$

$$(2.35)$$

In the reversible limit, the Nernst Equation holds for Equations 2.33 and 2.34 and $\Gamma = \Gamma_A + \Gamma_B + \Gamma_C$. This is used to derive Equation 2.36, describing the Faradaic current associated with surface confined cooperative two electron transfer in the reversible limit.[159]

$$i = \frac{F^2vA\Gamma}{RT}\frac{y(1 + 4x + xy)}{(1 + y + xy)^2} \quad \begin{cases} x = \exp[F(E - E_1^0)/RT] \\ y = \exp[F(E - E_2^0)/RT] \end{cases}$$

$$(2.36)$$

When $E_1^0 \gg E_2^0$ there are two distinct sets of redox peaks centred at E_1^0 and E_2^0 (Figure 2.3), each described by Equations 2.29 – 2.32, with n = 1. The peak width at half maximum height ($W_{1/2}$) of each peak is therefore ~ 90 mV at 25°C. As E_1^0 and E_2^0 become closer in value the peaks merge (Figure 2.3) and when $E_1^0 - E_2^0 \leq (4RT/F)\ln 2$ only one peak is observed.[159] In the specific case that $E_1^0 = E_2^0$, $W_{1/2}$ is calculated to be ~ 65 mV at 25°C.[159] When $E_1^0 \ll E_2^0$ the two electron transfers are essentially simultaneous. The single redox peak is described by Equations 2.29 – 2.32, with n = 2, and $W_{1/2}$ is ~ 45 mV at 25°C. The value of $W_{1/2}$ is therefore used to determine the level of cooperativity of the

electron transfers; from consecutive, to cooperative, to essentially simultaneous.[89, 159]
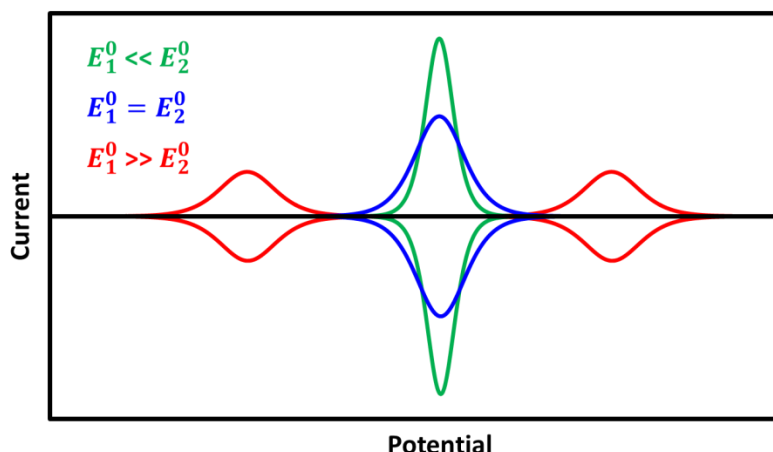
Figure 2.3 Faradaic response of two electron transfers with differing cooperativity

2.6.3 Kinetically controlled non-turnover voltammetry

The analytical solutions presented in Chapter 2.6.2 describe electron transfer in the reversible limit. However, at faster scan rates the rate of electron transfer may not be fast enough to maintain equilibrium between the redox site and the electrode potential, so full reversibility is not displayed and kinetic control is present.[89] Under this circumstance the models of electron transfer kinetics described in Chapter 2.3 must be taken into account. Laviron calculated the voltammetric peak shapes expected using Butler-Volmer kinetics for a simple one-electron reduction and oxidation.[181] The Nernstian reversible limit is achieved when $v < k_0 RT/F$ but at higher scan rates the reductive and oxidative peaks split apart and tend to the irreversible limit, in which the peak positions are described by Equation 2.37.[89, 181]

$$E_p = E^0 \pm \frac{RT}{F} \ln(Fv/2RTk_0) \qquad (2.37)$$

A useful analysis is a "trumpet plot" of peak positions *vs.* the logarithm of the scan rate (Figure 2.4), from which k_0 (the standard rate constant) can be estimated using Equation 2.37.[89, 181] However, as the peak positions are only sensitive to the logarithm of v/k_0, only the order of magnitude of k_0 can be determined.[89]
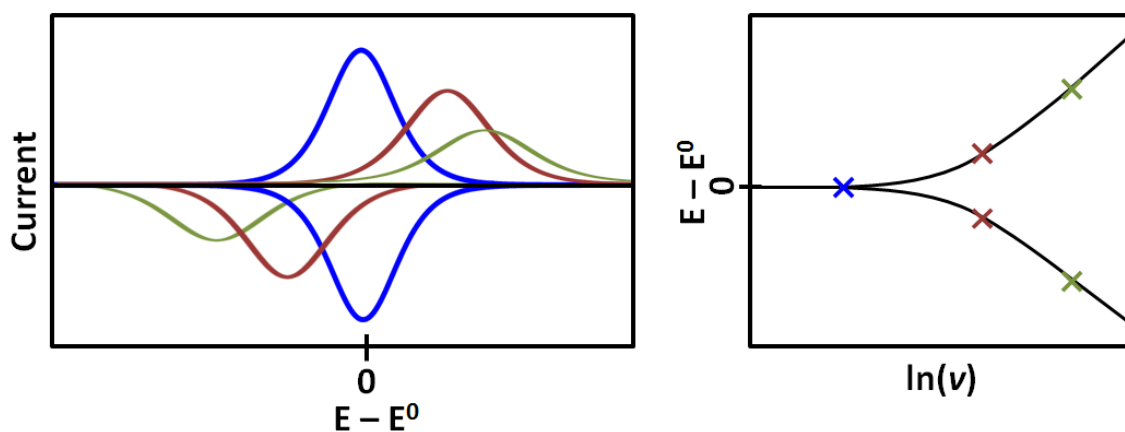
Figure 2.4 Faradaic responses at increasing scan rate and the associated trumpet plot

The complex analytical solutions describing the Faradaic response for surface confined non-Nernstian two-electron transfer reactions are given in reference [182]. An alternative to analysis based on analytical solutions is to directly use the Butler-Volmer or Marcus-Hush-Chidsey rate equations in numerical models of the process of interest. For the case of n-electrons transferred simultaneously (Equation 2.25) the Faradaic current is given by Equation 2.38.[129]

$$i = nFA(k_b \Gamma_R - k_f \Gamma_O) \tag{2.38}$$

where k_b is the rate constant for oxidation and k_f is the rate constant for reduction.

In the case of two electrons transferred cooperatively (Equation 2.33 and Equation 2.34) the Faradaic current is given by Equation 2.35, with $\frac{d\Gamma_A}{dt}$ and $\frac{d\Gamma_C}{dt}$ given by Equations 2.39 and 2.40.[159]

$$\frac{d\Gamma_A}{dt} = k_b^1(\Gamma - \Gamma_A - \Gamma_C) - k_f^1 \Gamma_A$$

$$\tag{2.39}$$

$$\frac{d\Gamma_C}{dt} = k_f^2(\Gamma - \Gamma_A - \Gamma_C) - k_b^1 \Gamma_C$$

$$\tag{2.40}$$

Numerical time-step simulations can be set-up using these equations, with k describing the potential dependent Butler-Volmer or Marcus rate constant and the potential described by Equation 2.23. Electron transfer rates can be calculated by experiment simulation comparison at high scan rates.[141]

2.6.4 Chemical processes coupled to electron transfer

Complexities in the non-turnover responses arise for chemically-coupled electron transfer reactions. An extremely common and biologically important coupled reaction is protonation. The simple case of an n-electron one-proton process can be represented as a square scheme (Figure 2.5).[89, 183]
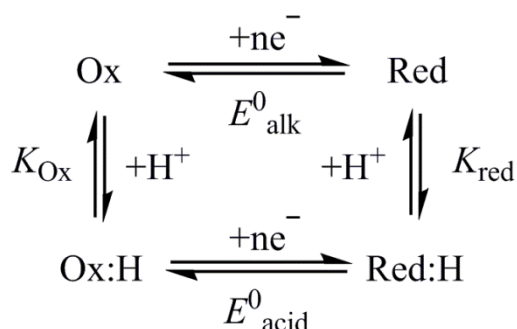
Figure 2.5 Square scheme for an n-electron one-proton reaction

In the Nernstian reversible limit, where both electron and proton transfer are fast on the voltammetric timescale, the redox couple behaves as a simple electron transfer reaction with a pH-dependent apparent reduction potential, $E^{app}(\text{pH})$. Using the Nernst equation and the fact that the sum of $\Delta_r G^0$ values around the square is zero, $E^{app}(\text{pH})$ is given by Equation 2.41.[89, 184]

$$E^{app}(\text{pH}) = E^0_{alk} + \frac{RT}{nF}\ln\left(\frac{K_{Ox}}{K_{Red}}\right) + \frac{RT}{nF}\ln\left(\frac{[\text{H}^+] + K_{Red}}{[\text{H}^+] + K_{Ox}}\right)$$

(2.41)

where $E^0_{acid} = E^0_{alk} + RT/nF \ln(K_{Ox}/K_{Red})$.

Usually $pK_{Ox} < pK_{Red}$ and the transformations can be schematically represented by the Pourbaix diagram shown in Figure 2.6.[183] For $pH < pK_{Ox}$ (equivalently $[\text{H}^+] > K_{Ox}$), $\frac{RT}{nF}\ln\left(\frac{[\text{H}^+]+K_{Red}}{[\text{H}^+]+K_{Ox}}\right)$ tends to zero and so $E^{app}(\text{pH})$ tends to E^0_{acid}.[89] In this acidic limit both Red and Ox are protonated and the reaction follows the bottom half of the square scheme (Figure 2.5). For $pH > pK_{red}$ (equivalently $[\text{H}^+] < K_{Red}$), $\frac{RT}{nF}\ln\left(\frac{[\text{H}^+]+K_{Red}}{[\text{H}^+]+K_{Ox}}\right)$ tends to $\frac{RT}{nF}\ln\left(\frac{K_{Red}}{K_{Ox}}\right)$ and so $E^{app}(\text{pH})$ tends to E^0_{alk}.[89] In this alkaline limit both Red and Ox are deprotonated and the reaction follows the top half of the square scheme (Figure 2.5). For $pK_{Ox} < pH < pK_{Red}$, $E^{app}(\text{pH})$ has the pH dependence outlined in Equation 2.41, which

at its maximum is $-2.3\frac{RT}{nF} = -0.059/n$ V per pH unit at 25°C.[89] In this limit Red is protonated but Ox is not and the reaction follows Equation 2.42.

$$Ox + ne^- + \text{H}^+ \rightleftharpoons \text{Red:H} \tag{2.42}$$
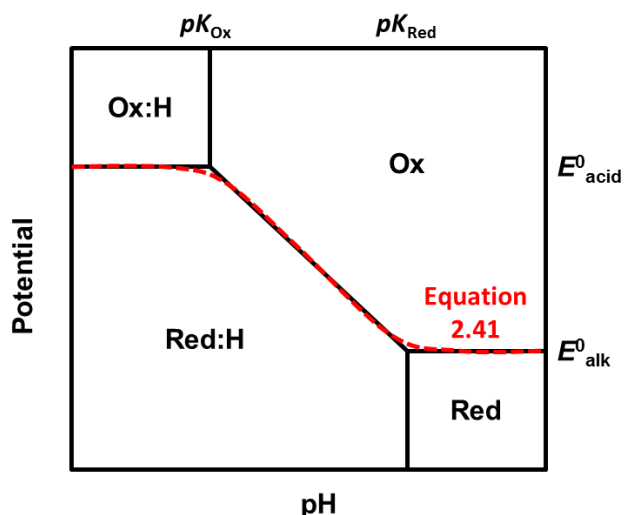
Figure 2.6 Pourbaix diagram for an n-electron one-proton reaction

In general, for a redox process with n electrons and m protons $E^{app}(\text{pH})$ has a maximum pH dependence of $-2.3\frac{RT}{F}\frac{m}{n} = -0.059m/n$ V per pH unit at 25°C.[89] In this limit the reaction follows Equation 2.43.

$$Ox + ne^- + m\text{H}^+ \rightleftharpoons \text{Red} \tag{2.43}$$

The Nernst equation for this process is given by Equation 2.44.

$$E = -\frac{2.3RT}{nF}\log_{10}\left(\frac{[Red]}{[Ox]}\right) - \frac{2.3RT}{F}\frac{m}{n}pH$$

$$\tag{2.44}$$

This explicitly shows the pH dependence and the relationship is often used to calculate the ratio of protons and electrons in a redox process.

Outside the Nernstian regime coupled protonations also influence the apparent kinetics of electron transfer reactions. When electron transfer is outside the reversible limit but coupled protonation is fast, this gives a pH-dependent apparent standard rate constant of electron transfer $k_0^{app}(pH)$. A full description for fast coupled protonation is given in references [89] and [183] but in this thesis the apparent kinetics are simply quoted. When protonation is slow on the

voltammetric timescale it can gate the redox process and the rate of de(protonation) can be measured from how the voltammetry depends on scan rate and pH.[89, 111]

2.6.5 Effect of dispersion on non-turnover voltammetry

A further key modification to the voltammetric behaviour of surface confined redox proteins is dispersion in the orientation of absorbed protein on the electrode surface.[116, 117] This leads to a distribution of distances and therefore rates of electron transfer between the redox site and electrode surface.[116, 117] This also gives a distribution in environments of the redox active site, which can result in variation in the reduction potential.[147, 185] This gives both kinetic dispersion in the distribution of k_0 and thermodynamic dispersion in the distribution of E^0.[147] These distributions have been recently proven and experimentally measured for fluorophore modified azurin on SAM modified gold electrodes.[186] This dispersion can be included when modelling the voltammetry by introducing a probability density function for molecules having given k_0 and E^0 values.[116] Dispersion in E^0 does not seem to impact the cyclic voltammetry response as much as kinetic dispersion.[116] The experimentally measured dispersion in k_0 predicts significant voltammetric peak broadening giving increased $W_{1/2}$, if k_0 and its distribution are lower than the reversible limit for a particular scan rate.[116] This peak broadening has been observed for a number of surface confined proteins. [116, 117, 186]

2.6.6 Catalytic voltammetry of single centre enzymes

The simplest case of surface confined catalytic reduction or oxidation is by a single redox site in an EC mechanism. The cases of irreversible reduction, irreversible oxidation and reversible reduction and oxidation of substrate (S) and product (P) are shown in Figure 2.7. Interfacial electron transfer between the electrode and enzyme redox site are assumed to be fully reversible.
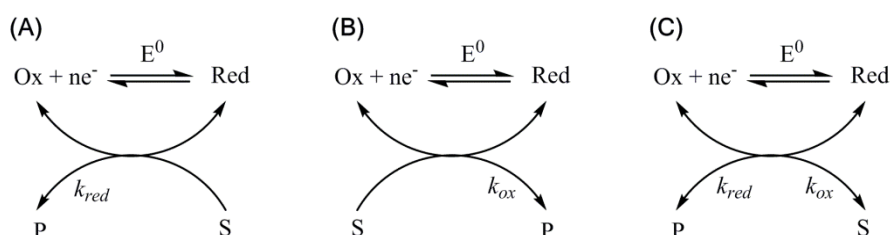
Figure 2.7 (A) Irreversible reduction (B) Irreversible oxidation (C) Reversible catalysis

E^0 is the enzyme redox site potential and k_{red} and k_{ox} are the turnover frequencies in the direction of reduction and oxidation, respectively. For irreversible reduction the catalytic reduction current is given by Equation 2.45.

$$i_{red} = -nFA\Gamma_R k_{red} \qquad (2.45)$$

The surface concentration of reduced enzyme (Γ_R) is governed by the Nernst equation in the reversible limit and is described by Equation 2.28. Substitution of Equation 2.28 into Equation 2.45 gives Equation 2.46, which describes the potential dependence of the catalytic current.[89, 187]

$$i_{red} = \frac{-nFA\Gamma k_{red}}{1 + \exp(nF(E - E^0)/RT)}$$

$$(2.46)$$

The potential dependence of the catalytic current for irreversible oxidative catalysis (Equation 2.47) is given by analogous analysis. [89, 187]

$$i_{ox} = \frac{nFA\Gamma k_{ox}}{1 + \exp(-nF(E - E^0)/RT)}$$

$$(2.47)$$

The catalytic current has a sigmoidal dependence on electrode potential (E) (Figure 2.8). At large overpotentials the current reaches limiting values of $i_{lim,red} = -nFA\Gamma k_{red}$ or $i_{lim,ox} = nFA\Gamma k_{ox}$, for reductive or oxidative catalysis, respectively. [89, 187] This is when the redox site of all adsorbed enzyme is in the catalytically active reduced or oxidised state. At $E = E^0$ the current is at half its limiting value and this "half-wave" potential ($E_{1/2}$) therefore indicates the potential of the catalytic centre.[89]
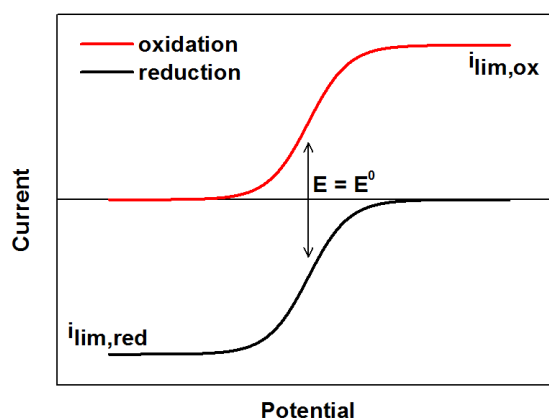
Figure 2.8 Potential dependence of catalytic current for irreversible catalysis

Many enzymes are reversible catalysts and in this case the catalytic current is described by Equation 2.48.

$$i = nFA(\Gamma_{ox}k_{ox} - \Gamma_{red}k_{red})$$ (2.48)

Substitution of the terms for Γ_{ox} and Γ_{red} in the Nernstian limit gives Equation 2.49, which rearranges to Equation 2.50 describing the potential dependence of the reversible catalytic current.

$$i = nFA\Gamma \left(\frac{k_{ox}}{1 + \exp(-nF(E - E^0)/RT)} - \frac{k_{red}}{1 + \exp(nF(E - E^0)/RT)} \right)$$ (2.49)

$$i = nFA\Gamma \left(\frac{k_{ox}\exp(nF(E - E^0)/RT) - k_{red}}{1 + \exp(nF(E - E^0)/RT)} \right)$$ (2.50)

Catalytic steps are governed by E^0 of the active site and the equilibrium potential of the substrate (E_{eqm}). Equilibrium thermodynamics dictate that $k_{red}/k_{ox} = [P]/[S]$ and substitution into the Nernst Equation gives Equation 2.51.

$$k_{red} = k_{ox} \exp\left[-nF(E^0 - E_{eqm})/RT\right]$$ (2.51)

Substitution of Equation 2.51 into Equation 2.50 gives Equation 2.52, describing the catalytic current.[188]

$$i = nFA\Gamma k_{ox} \left(\frac{\exp(nF(E - E^0)/RT) - \exp(nF(E_{eqm} - E^0)/RT)}{1 + \exp(nF(E - E^0)/RT)} \right)$$ (2.52)

The catalytic current has the sigmoidal dependence on electrode potential (E) displayed in Figure 2.9, passing through $i = 0$ when $E = E_{eqm}$, as dictated by thermodynamics. When the enzyme catalytic redox site potential $E^0 = E_{eqm}$ there is no catalytic bias and the reductive and oxidative currents reach the same absolute limiting value of $i_{lim} = nFA\Gamma k_{ox}$. If $E^0 < E_{eqm}$ then the enzyme is catalytically biased towards reduction and $|i_{lim,red}| > |i_{lim,ox}|$. If $E^0 > E_{eqm}$ then the enzyme is catalytically biased towards oxidation and $|i_{lim,ox}| > |i_{lim,red}|$. The "half-wave" potential ($E_{1/2}$) is now defined as the potential at which $i =$

$\left(i_{lim,red} + i_{lim,ox}\right)/2$ and equals the catalytic site potential (E^0).[188] The overpotential requirement can be defined as $\left|E_{1/2} - E_{eqm}\right|$, so is larger for a certain reaction direction when there is a greater difference between the catalytic site potential (E^0) and the equilibrium potential of the substrate product couple (E_{eqm}).[188]
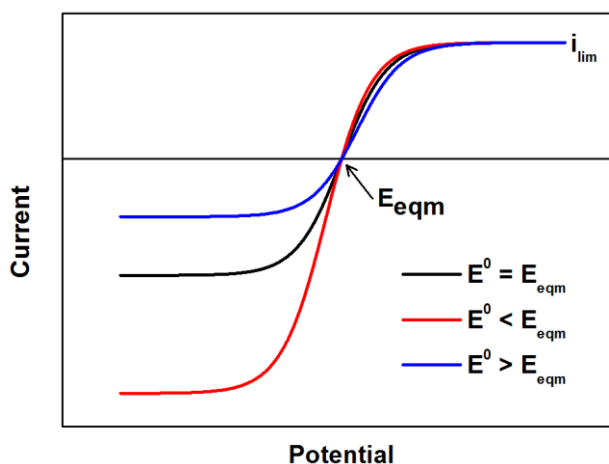
Figure 2.9 Potential dependence of catalytic current for reversible catalysis

This EC model of active site chemistry is the simplest case and more complex active site chemistry (such as the EEC mechanism) or further coupled chemical reactions (such as the ECEC mechanism) modify the kinetic schemes and rate equations accordingly. This alters the associated catalytic voltammogram waveshapes and the simple relations between the active site potential and the "half wave" potential, catalytic bias and overpotential no longer apply.[188] In these more complex cases the relationship between catalytic waveshapes and kinetic and thermodynamic parameters of the enzyme are modelled for the particular mechanism of action on a case by case basis.[188]

2.6.7 Catalytic voltammetry of multicentre enzymes

Multicentre enzymes that have relay centres acting as a "wire" for electron transport between the enzyme surface and active site present a further departure from the simple EC mechanism described. Interfacial electron transfer is at a site separate from the active site and intramolecular electron transfer steps between the relay sites are introduced to the kinetic schemes. These complex schemes can be used to fully model the catalytic waveforms [106, 188] but a simplified scheme which accurately models the catalytic waveforms of many multicentre enzymes has been recently introduced by

Armstrong and co-workers.[41, 42] This model separates interfacial electron transfer from all other catalytic events, including intramolecular electron transfer, which are described collectively (Figure 2.10).
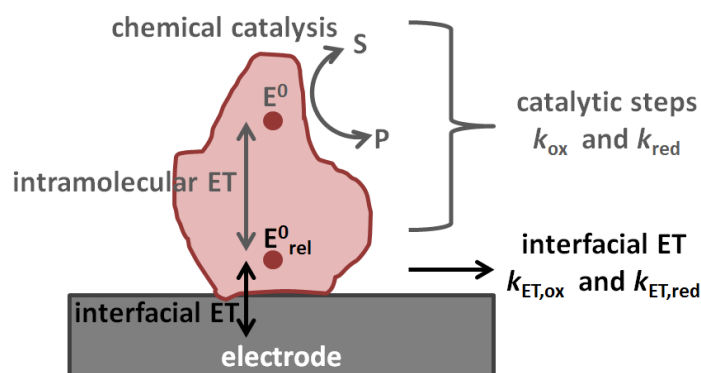
Figure 2.10 Armstrong [41, 42] model of electrocatalysis by multicentre enzymes

In this model [41, 42] it is assumed that electrons enter or exit the catalytic cycle via repetitive one-electron transfers by long-range tunnelling from the relay site at which electrons enter or exit the enzyme. The internal driving force for the reaction is now set up between the reduction potential of the relay centre (E_{rel}^0) and the equilibrium potential of the substrate product couple (E_{eqm}). In the Nernstian limit, the E^0 active site potential term in Equation 2.51 and therefore Equation 2.52 is replaced by E_{rel}^0. Electrocatalysis by a multicentre enzyme therefore follows the same general form as a single centre enzyme, but dependency on the active site potential E^0 is replaced by dependency on the relay site potential E_{rel}^0. In this simple model the rate in both directions is determined by the redox properties of the active site but the catalytic bias and overpotential are now determined by the potential (E_{rel}^0) of the relay centre at which electrons enter or exit. In this case, electron transfer onto the relay is the only potential dependent step and so the relay is the "electrochemical control centre" rather than the active site. This model is tested for a hydrogenase in Chapter 7 by using molecular biology approaches to alter the potential of the FeS cluster at which electrons enter and exit and observing changes in the catalytic bias and overpotential in cyclic voltammograms.

2.6.8 Effect of interfacial electron transfer on catalytic voltammetry

If interfacial electron transfer is slow enough then the catalytic waveform responses will deviate from the Nernstian limits described.[42, 89] The rates of

interfacial electron transfer, described by either Butler-Volmer or Marcus formalisms, will then need to be included in the kinetic scheme, as this will now govern the surface concentration of reduced or oxidised enzyme, rather than the equilibrium Nernst equation. Using Butler-Volmer formalisms gives Equation 2.53 describing the catalytic current, when interfacial electron transfer is not fully reversible. [41, 42]

$$i = nFAk_{ox}\left(\frac{e_1 - e_2}{1 + e_1 + pe_1{}^\alpha}\right)$$

(2.53)

where

$$e_1 = \exp\left(\frac{nF}{RT}(E - E^0)\right), e_2 = \exp\left(\frac{nF}{RT}(E_{eqm} - E^0)\right), p = \frac{k_{ox}+k_{red}}{k^0} = \frac{k_{ox}(1+e_2)}{k^0}$$

E^0 is the reduction potential of the "electrochemical control centre", which is the active site of a single centre enzyme or relay site of a multicentre enzyme. Figure 2.11 shows the effect of p (and therefore k^0) on a reversible catalytic waveform.
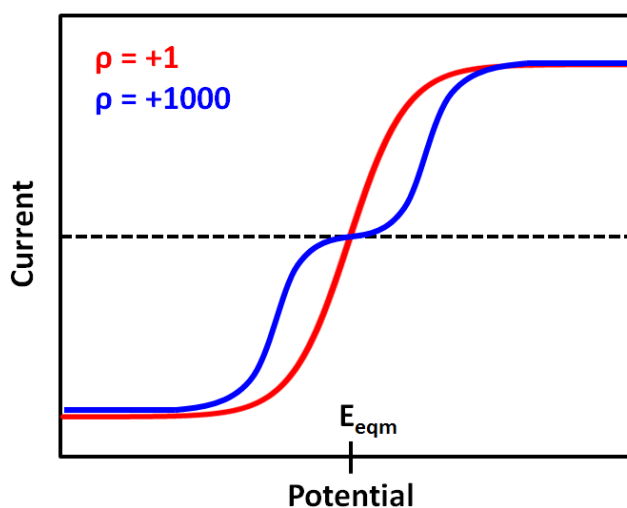
Figure 2.11 Effect of the rate of interfacial electron transfer on the catalytic waveform
Adapted from Reference [42]

When k^0, the standard rate constant of interfacial electron transfer, is large Equation 2.53 tends to the Nernstian limit described by Equation 2.52 and the current waveform passes sharply through zero at E_{eqm}. As k^0 decreases an inflection point appears about E_{eqm}, as larger overpotentials are required to drive the interfacial electron transfer, which is now limiting the current.[41, 42]

2.6.9 Effect of dispersion on catalytic voltammetry

Kinetic dispersion, as described in Chapter 2.6.5, can also influence catalytic waveforms. Leger and co-workers [110] showed that an even probability distribution of tunnelling distances within a certain range leads to a residual slope in the sigmoidal catalytic waveform, rather than a levelling off at i_{lim}. This is because more poorly oriented enzyme only becomes involved at higher driving forces, which compensate for the larger tunnelling distances. Dispersion is accounted for in a modified version of the Armstrong [41, 42] model of electrocatalysis (Equation 2.53), in which the catalytic current is described by Equation 2.54.

$$ i = \frac{nFAk_{ox}}{\beta d_0} \left(\frac{e_1 - e_2}{1 + e_1} \right) \ln \frac{pe_1{}^\alpha + (1 + e_1)}{pe_1{}^\alpha + (1 + e_1)\exp(-\beta d_0)} $$

$$ (2.54) $$

where βd_0 is an effective tunnelling factor that takes into account the dispersion in orientations and so dispersion in interfacial electron transfer rates. Larger βd_0 values decrease the apparent dependence of the catalytic current on increasing overpotential (Figure 2.12), as greater driving forces are needed to involve more poorly oriented enzymes. [41, 42]
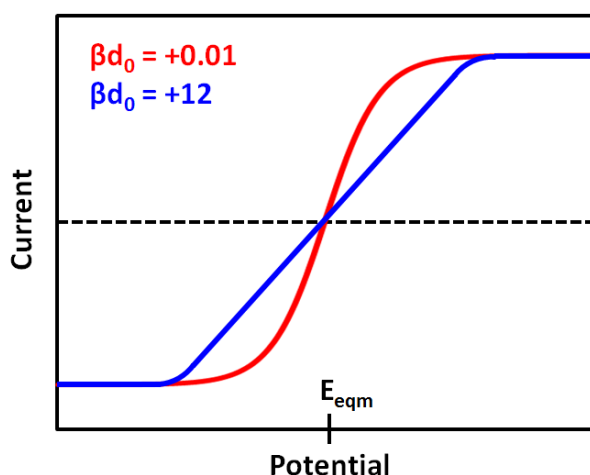
Figure 2.12 Effect of dispersion on the catalytic waveform Adapted from Reference [42]

2.6.10 Effect of (in)activation on catalytic voltammetry

There can be a potential dependence to the turnover frequency of the enzyme due to formation of a redox state with altered activity or different substrate or inhibitor affinity.[42] Transformation of enzyme to a more or less active state

beyond a certain potential leads to an increase or reduction in catalytic current in those regions and can lead to an array of unusual catalytic waveshapes.[89, 108, 109, 189] The waveshape can be fully related to the thermodynamics and kinetics of the (in)activation reaction, by incorporating the (in)activation step into the kinetic scheme and rate equations.[187, 190] (In)activation has been incorporated into the Armstrong model [42] in the limit of fully reversible (in)activation. However, most often the (in)activation is slow on the voltammetric timescale and there is significant hysteresis in the voltammetric response.[42] These complex responses have been modelled [187, 190] but in a commonly used and simple approach, the potential E_{sw} at which di/dE is greatest for the (in)activation process is used as a phenomenological descriptor of the thermodynamic and kinetic parameters of the (in)activation.[89]

2.6.11 Effect of substrate concentration on catalytic voltammetry

In the presented equations describing catalytic waveshapes the catalytic turnover frequencies (k_{ox} and k_{red}) can be described by the Michaelis-Menten equation (Equation 2.21). When the substrate concentration is in vast excess of K_M the turnover frequency is at its maximum (k_{cat}). When the substrate concentration does not greatly exceed K_M, the turnover frequency is attenuated from k_{cat} by a factor of $(1 + K_M/[S]_0)$.[89] This in turn attenuates the catalytic current that is proportional to turnover frequency and K_M can be calculated from measuring the current response at different substrate concentrations.

2.6.12 Effect of mass transport on catalytic voltammetry

The presented equations describing catalytic voltammetry have not taken account of mass transport of substrate to the electrode surface. In PFE enzyme is usually adsorbed onto a rotating disc electrode that is spun sufficiently fast to avoid mass transport limitations, such that the surface concentration of substrate available to the enzyme is equal to the bulk concentration. If the electrode is not spun quickly enough then mass transport can limit the current.[89] At a rotating disk electrode the limiting current is given by the Levich Equation 2.55.[99]

$$I_L = 0.62nFACD^{2/3}v^{-1/6}\omega^{1/2} \tag{2.55}$$

where C is the bulk concentration of substrate, D is its diffusion coefficient, v is the kinematic viscosity of the solvent and ω is the electrode rotation rate. The current will increase with the square root of the rotation rate, until mass transport is no longer limiting and the current is instead limited by the enzyme. In this thesis high enough rotation rates were used such that further increases in rotation rate did not increase the current and so mass transport was ensured not to be rate limiting.

2.6.13 Chronoamperometry

Chronoamperometry involves measuring current as a function of time, whilst the potential of the working electrode is held constant. This deconvolutes the time and potential dependences of a process, which are inherently linked in cyclic voltammetry. As catalytic current is proportional to the fraction of active enzyme, chronoamperometry enables direct measurement of the extent and rate of (in)activation after a potential step or introduction of inhibitor from the extent and rate of change of Faradaic current.[190]

2.7   Fourier Transformed ac Voltammetry

The application of Fourier Transformed ac Voltammetry (FTacV) to protein film electrochemistry (PFE) in the study of redox active proteins is described in Chapter 1.3.6 and the underpinning theory is detailed herein.

2.7.1 Measurement

In FTacV the applied potential is the sum of a dc component and an ac contribution. In the large amplitude sine wave version of FTacV utilised in this thesis the applied potential is given by Equation 2.56.[127, 129, 140]

$$E_{app}(t) = E_{dc}(t) + \Delta E \sin(\omega t)$$

$$E_{dc}(t) = \begin{cases} E_1 + vt & \text{for } 0 \le t < t_r \\ E_2 - v(t - t_r) & \text{for } t \ge t_r \end{cases} \qquad t_r = \frac{E_1 - E_2}{v}$$

(2.56)

where ΔE is the amplitude and $\omega = 2\pi f$ is the angular frequency of the sine wave.

As with dc voltammetry the applied potential $E_{app}(t)$ is attenuated by Ohmic drop and the effective applied potential $E_{eff}(t)$ is still given by Equation 2.23.[140] The total current I_{tot} is measured and as with dc voltammetry consists of capacitive and Faradaic components (Equation 2.24).[140] The total current output is Fourier transformed (Chapter 2.7.3) into the frequency domain to reveal harmonic components at $n \times f$ of the input frequency and an aperiodic dc component.[127, 131] Each component can be visualised in the time domain by band selection (Chapter 2.7.4), filtering and inverse Fourier transform (Chapter 2.7.3), as described in Chapter 1.3.6 and Figure 1.14.[127, 135]

2.7.2 Accessing high harmonics

There is a non-linear relationship between Faradaic current and potential.[127] In the Nernstian limit Equations 2.29 and 2.36 describe this $i - E$ relationship in specific cases of surface confined electron transfer relevant to PFE. Equations 2.46, 2.47 and 2.52 describe the $i - E$ relationship for specific cases of catalysis relevant to PFE. Outside the Nernstian limit the Faradaic current is influenced by electron transfer rates, with a potential dependence described by Marcus-Hush-Chidsey (Equation 2.19) or Butler-Volmer (Equation 2.14) theory, again giving non-linear $i - E$ relationships. Historically, ac voltammetry has employed small amplitudes, such that the dc and ac timescales are resolvable and so that the theoretical solution can be linearised.[99, 128, 130] When the current-potential relationship is linearised by using small amplitudes, a sinusoidally varying input potential (Equation 2.56) leads to a sinusoidal current response at the same frequency.[128, 130] Larger amplitudes expose the non-linearity in the Faradaic $i - E$ relationship, so the response is no longer simply at the input frequency but comprised of a series of sinusoidal signals at $n \times f$ of the input frequency plus an aperiodic dc component near 0 Hz.[127, 128] The current component at $n \times f$ is referred to as the nth harmonic response. Accessing these high harmonic signals with large amplitudes has a number of advantages, including separation of capacitive and Faradaic current, separation of catalytic and electron transfer current and enhanced kinetic and mechanistic analysis (Chapter 1.3.6).[127, 131] The perceived need to use small amplitudes was elegantly overcome by Engblom *et al* and Gavaghan *et al*, with the introduction of the necessary theoretical framework for interpretation of large amplitude ac voltammetry results.[128, 130] The apparent need to linearise the problem was

overcome by Engblom *et al* [130] in their presentation of analytical solutions for larger amplitudes and the need for resolvable time domains was overcome by Gavaghan *et al* [128] with the development of complete numerical simulations for large amplitude ac voltammetry; the results of which match the analytical results of Engblom *et al*. The analytical solutions and numerical simulations for surface confined electron transfer are described in Chapter 2.7.5 and Chapter 2.7.8, respectively.

2.7.3 Fourier transform and inverse Fourier transform

A discrete Fourier transform (dFT) converts a finite set of equally spaced samples of a function into the frequency domain representation of the original input sequence and is defined by Equations 2.57 and 2.58.[191, 192]

$$X_K = \sum_{n=0}^{N-1} x_n e^{-\frac{i2\pi kn}{N}}$$

(2.57)

$$x_n = \frac{1}{N}\sum_{k=0}^{N-1} X_K \cdot e^{\frac{2\pi ikn}{N}}$$

(2.58)

Equation 2.57 describes the Fourier transformation of the sequence of N complex numbers $x_0, x_1, \dots, x_{N-1}$ and Equation 2.58 is the inverse Fourier transform (iFT).

Direct evaluation of Equation 2.57 requires O(N^2) operations, as there are *N* outputs and each output is a sum of *N* terms. Fast Fourier transforms use an algorithm to compute the same result in just O(Nlog$N$) operations.[193] The Cooley-Tukey algorithm is the most commonly used and works by recursively re-expressing the DFT of a composite of size $N = N_1 N_2$ as smaller dFTs of sizes N_1 and N_2, for *N* a power of 2.[194] The FTacV potentiostat instrument automatically adjusts the dc scan rate and applied frequency so that 2^N data points are taken in a set. A fast Fourier transform can then be performed *via* the Cooley-Tukey algorithm, to give the frequency domain representation.[132] The frequency domain power spectrum reveals the harmonic and dc components. Each required harmonic or dc component can be individually selected by windowing (Chapter 2.7.4) and nulling the dataset before and after the

window.[127, 135] The selected and filtered harmonic or dc component can be resolved into the time domain by performing an iFT.[127]

2.7.4 Band selection (windowing)

A rectangular window that leaves the frequency content within the window unchanged and zero elsewhere is most commonly used in FTacV. A rectangular function centred at $f = 0$ is defined, in the frequency domain, by Equation 2.59.[135]

$$\text{rect}(f) = \begin{cases} 1, & -\dfrac{w}{2} \le f \le \dfrac{w}{2} \\ 0, & \text{otherwise} \end{cases}$$

(2.59)

where w is the width of the window.

The iFT of this rectangular function is $\text{R}(t) = w\text{sinc}(\pi t w)$ and the sinc function is defined by Equation 2.60.[135]

$$\text{sinc}(x) = \begin{cases} 1, & x = 0 \\ \dfrac{\sin x}{x}, & \text{otherwise} \end{cases}$$

(2.60)

Multiplying the frequency domain signal by a rectangular function convolutes the signal with the sinc function in the time domain, causing "ringing" artefacts.[135] The introduction of sharp discontinuities in the spectrum from the rectangular window generates these oscillatory artefacts in the filtered time domain signal.[135] Nevertheless, a rectangular window is often still adequate and the absence of ringing artefacts can be checked by visual inspection. Rectangular windows are used in Chapter 4. More sophisticated windows such as Kaiser or Hamming are bell-shaped, which removes the sharp discontinuities in the window function and reduces ringing artefacts.[135] These more sophisticated windows are used in Chapters 5 and 7.

2.7.5 Aperiodic dc and harmonic responses

Windowing and inverse Fourier transformation gives the time-domain current response of the aperiodic dc component and each individual harmonic. The form each harmonic takes can be understood and visualised with analytical

solutions. The simplest case of simultaneous transfer of n-electrons for a surface confined species, ignoring capacitive current and Ohmic drop contributions, was first solved by Honeychurch and Bond [129] and is presented here. The Faradaic current is described by Equation 2.29 and substitution of Equation 2.56 describing $E(t)$ for the forward ac voltammetric sweep gives Equation 2.61, describing the total Faradaic current.

$$i = \frac{n^2 F^2 A \Gamma}{RT} \cdot [v + \omega \Delta E \cos(\omega t)] \cdot \frac{\exp[nF(E - E^0)/RT]}{(1 + \exp[nF(E - E^0)/RT])^2}$$

(2.61)

Given that $E = E_{dc} + \Delta E \sin(\omega t)$, Equation 2.61 can be rearranged to give Equation 2.62.

$$i = \frac{n^2 F^2 A \Gamma}{RT} \cdot [v + \omega \Delta E \cos(\omega t)] \cdot f[a(t)]$$

(2.62)

where $[a(t)] = \frac{\xi \exp[a(t)]}{(1 + \xi[a(t)])^2}$, $\xi = \exp\left[\left(\frac{nF}{RT}\right)(E_{dc} - E^0)\right]$ and $a(t) = \left(\frac{nF}{RT}\right) \Delta E \sin(\omega t)$

It is assumed that the dc potential is constant $(\frac{dE_{dc}}{dt} \ll \frac{dE_{ac}}{dt})$ and $f[a(t)]$ is expanded, giving Equation 2.63 describing the total Faradaic current output of the ac voltammetric experiment. [129]

$$i = \frac{n^2 F^2 A \Gamma}{RT} \left[v \sum_{j=0}^{\infty} \frac{f^{(j)}(0)}{j!} \left(\frac{nF\Delta E}{RT}\right)^j \sin^j(\omega t) + \omega \Delta E \right.$$
$$\left. \cdot \sum_{j=0}^{\infty} \frac{f^{(j)}(0)}{j!} \left(\frac{nF\Delta E}{RT}\right)^j \sin^j(\omega t)\cos(\omega t) \right]$$

(2.63)

where $f^{(j)}$ is the jth derivative of $f(a)$.

Trigonometric identities are used to reduce $\sin^j(\omega t)$ and $\sin^j(\omega t)\cos(\omega t)$ to multiple harmonics and a dc term. Equation 2.64 describes the dimensionless dc current.[129]

$$\varphi_{dc} = \sum_{j=0}^{\infty} \frac{f^{(2j)}(0)}{2^{2j} j! j!} \left(\frac{nF\Delta E}{RT}\right)^{2j}$$

(2.64)

The dimensionless currents of the first three harmonics are described by Equations 2.65, 2.66 and 2.67.[129]

$$\varphi_\omega = \sum_{j=0}^{\infty} \frac{f^{(2j)}(0)}{2^{2j} j! \, (j+1)} \left(\frac{nF\Delta E}{RT} \right)^{2j} \cos(\omega t)$$

(2.65)

$$\varphi_{2\omega} = \sum_{j=2}^{\infty} \frac{f^{(2j-1)}(0)}{2^{2j-2}(j+1)! \, (j-2)!} \left(\frac{nF\Delta E}{RT} \right)^{2j-1} \sin(2\omega t)$$

(2.66)

$$\varphi_{3\omega} = -6 \sum_{j=1}^{\infty} \frac{f^{(2j)}(0)}{2^{2j+1}(j-1)! \, (j+2)!} \left(\frac{nF\Delta E}{RT} \right)^{2j} \cos(3\omega t)$$

(2.67)

These analytical solutions are only valid for $\Delta E < 65 \, \text{mV}$, as the series fails to converge for larger amplitudes.[129] A representative example of the form the dc and harmonic components take is shown in Figure 2.13.
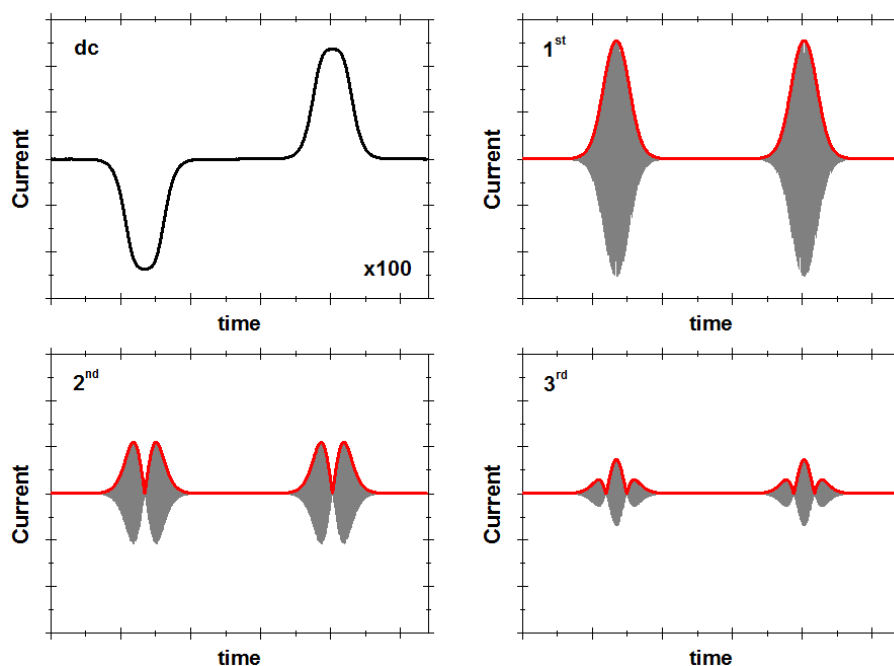
Fig 2.13 dc and 1$^{\text{st}}$ to 3$^{\text{rd}}$ harmonic components of a surface confined 1e$^-$ transfer

It must be noted that the aperiodic dc component (Equation 2.64) differs from what would be obtained from an equivalent dc voltammetry experiment with no ac perturbation. Whilst the main features of the dc experiment are preserved the ac perturbation causes peak broadening and, at larger amplitudes, peak

splitting of the recovered dc component.[129] The harmonic components, each centred at the reduction potential of the redox couple, continue to decrease in current magnitude and split into further lobes at higher harmonics.[129] The solutions presented in Figure 2.13 are for a surface confined reversible one-electron transfer reaction. The exact shape of each harmonic component is critically dependent on the mechanism and kinetics of the redox reaction and any coupled chemical processes.[131] Cumbersome analytical solutions that are often only valid in certain limits are useful for visualising and understanding the response but they are not used to analyse data. Instead, complete numerical simulations are used (Chapter 2.7.8) to model the data and determine the thermodynamics, kinetics and mechanism of the reaction.

2.7.6 Separation of capacitive and Faradaic current

If the double layer capacitance at the electrode surface behaves as a simple capacitor then the capacitance current-potential relationship is linear and given by Equation 2.68.

$$i_c = C_{dl}\frac{dE}{dt}$$

(2.68)

Substitution of Equation 2.56 (for the forward voltammetric sweep) into Equation 2.68 gives Equation 2.69.

$$i_c = C_{dl}[v + \omega\Delta E\cos(\omega t)] = C_{dl}\left[v + \omega\Delta E\sin\left(\omega t + \frac{\pi}{2}\right)\right] \qquad (2.69)$$

Therefore, for an ideal capacitor the sinusoidal current response is at the same frequency as the sinusoidally varying input potential but phase shifted by $\pi/2$.[99] The only harmonic response is at this fundamental (1st) harmonic and no higher harmonics are observed due to the linearity of the system.[127] Therefore, large amplitude ac voltammetry can be used to separate the background capacitive current confined to the fundamental harmonic, from the Faradaic current of interest found in the higher harmonics. Often, in reality, the double layer capacitance does not behave as a perfect capacitor and has a potential dependence, which introduces non-linearity to its current-potential relationship.[134] There is no physical model for this potential dependent capacitance but it can be modelled with a polynomial and a third order

polynomial is usually sufficient.[134] The capacitive current is then given by Equation 2.70.

$$i_c = c_{dl}\big(1 + c_{dl1}E(t) + c_{dl2}E^2(t) + c_{dl3}E^3(t)\big)\frac{dE(t)}{dt}$$

(2.70)

When the time–dependent potential described by Equation 2.56 is substituted into Equation 2.70, the total current can be separated into a dc and four harmonic components.[134] This is consistent with the experimental observation that the capacitive component is usually absent from the fifth and higher harmonics. The Faradaic current usually persists in higher harmonics so it is still possible to separate the capacitive background current confined to the lower harmonics and the Faradaic current of interest found in the higher harmonics.

2.7.7 Separation of catalytic and electron transfer current

It has been shown experimentally that for a catalytic process FTacV enables efficient separation of the catalytic and electron transfer components of the total current.[139] Catalysis dominates the aperiodic dc component and electron transfer dominates the higher harmonics. An analytical solution presented by Zhang and Bond [136] for the case of irreversible catalysis by a surface confined species showed that the catalytic reaction does not affect the magnitude of the nth harmonic if $k_{cat} \ll nf$ and so the influence of the catalytic component becomes less significant at higher harmonics. If the underlying electron transfer is sufficiently fast then using a high enough input frequency f will result in the highest harmonics being purely influenced by the faster electron transfer reaction and only the dc component and lowest harmonics being influenced by the slower catalytic reaction.[131, 136]

2.7.8 Numerical simulations

In order to determine the thermodynamics, kinetics and mechanism of a reaction from ac voltammetric data, comparison to a numerical simulation is made.[140] From the perspective of theory, ac voltammetry is closely related to dc voltammetry and where dc simulations of an electrode process exist, an analogous computational procedure can be used to simulate ac

voltammetry.[140] The same equations describe the current output but the appropriate equation describing the applied potential in ac voltammetry is used. Numerical simulations of ac voltammetric data exist for solution phase reactions [128], surface confined reactions [129], multi-electron processes [158, 159], chemically coupled reactions [140] and many other mechanisms and processes. [140] MECSim is a freely available software package [140] that enables most aspects of ac voltammetry to be simulated, including incorporation of uncompensated resistance, non-linear background capacitance and a choice of Butler-Volmer or Marcus-Hush-Chidsey electron transfer kinetics. The general approach used to simulate the large amplitude sine wave form of FTacV is described here.

The effective applied potential, accounting for uncompensated resistance (R_U), is described by Equation 2.71.[140]

$$E_{eff}(t) = E_{dc}(t) + \Delta E \sin(\omega t) - (i_c + i_f)R_U \qquad (2.71)$$

where $E_{dc}(t)$ is as described in Equation 2.56. i_c is given by Equation 2.70, with $E(t)$ given by $E_{eff}(t)$, or an equivalent equation using a higher order polynomial to more accurately fit the non-linear capacitance. i_f is given by the appropriate equation for the redox reaction studied. For example, surface confined simultaneous n-electron trasnfer is described by Equation 2.38. The associated electron transfer rate constants are described by Butler-Volmer (Equation 2.11 and Equation 2.12) or Marcus-Hush-Chidsey (Equation 2.19) formalisms. Modifications of the kinetic schemes due to coupled chemical processes or dispersion can be included.[116, 140] To increase the efficiency of the simulations the problems are recast as dimensionless equations using dimensionless variables.[128, 129] The equations are solved by discretising time-derivatives, so that the dimensionless current at each step $i + 1$ can be calculated using values from the previous step i. [128, 129] The software package MECSim was used to perform these simulations in Chapter 4. A full description of the comparable methods developed and used by Dr. Martin Robinson (University of Oxford) to simulate FTacV data in Chapters 5 and 7 are described in those chapters. Simulation experiment comparisons were optimised heuristically in Chapter 4, to find the thermodynamic and kinetic parameters associated with a reaction. New multi-parameter data-optimisation

procedures used to computationally find parameters by minimising an objective function, were fully developed and implemented by Dr. Martin Robinson (University of Oxford) and are introduced in Chapters 5 and 7.

2.7.9 Processing raw data to harmonic components

An example of how raw experimental data is processed to harmonic components is shown in Figure 2.14, for the data displayed in Chapter 5, Figure 5. The applied potential (Figure 2.14 A) with a scan rate of 22.35 mV s^{-1}, frequency of 9 Hz and amplitude of 150 mV results in the raw current measured over time (Figure 2.14 B). This time domain data is Fourier transformed into the frequency domain (Figure 2.14 C), giving a power spectrum containing harmonics at multiples of the input frequency and a dc component at 0 Hz. Each individual harmonic can then be inverse Fourier transformed to the time domain. In this example the 8th harmonic is selected with a rectangular window of 2 Hz width and inverse Fourier transformed to the time domain (Figure 2.14 D). The signal envelope (red line, Figure 2.14 D) is used to display harmonics in this thesis. The scan rate can be used to convert the time axis to an average potential axis, as in Chapter 5, Figure 5 and elsewhere in this thesis.
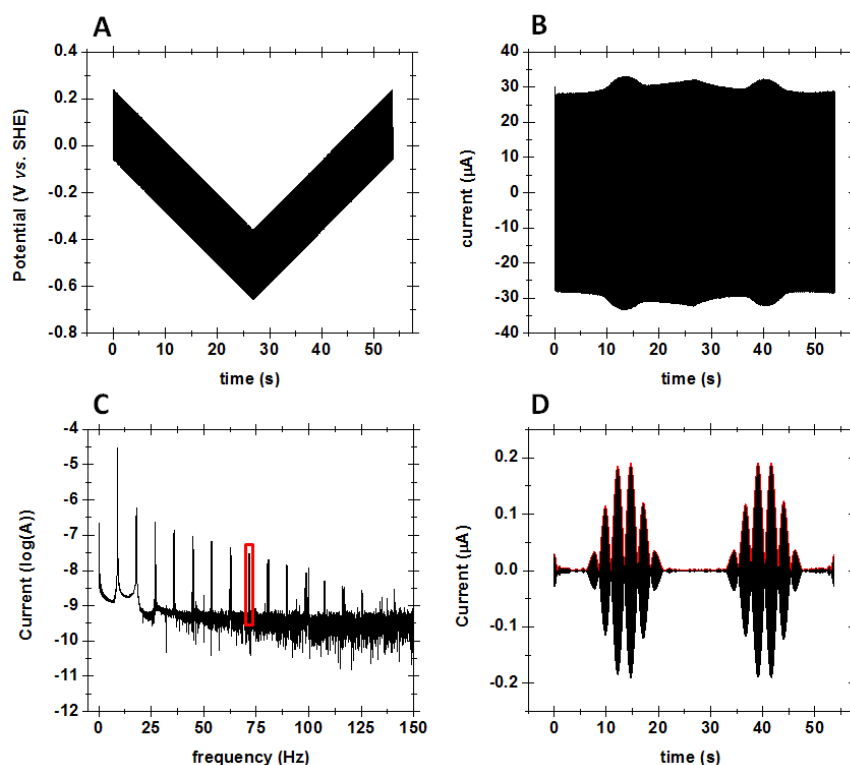
Figure 2.14 Conversion of raw data to harmonic components (A) Applied potential (B) Raw current (C) Frequency domain power spectrum (D) 8th harmonic component and envelope (red)

Chapter 3

Experimental Methods

3.1 Electrochemical methods

3.1.1 Electrochemistry experimental set-up

All electrochemical experiments were performed in an anaerobic glovebox with a bespoke electrical connection panel, manufactured by the University of York Department of Chemistry Mechanical Workshop. An all-glass water-jacketed and gas-tight electrochemical cell, custom manufactured by the University of York, Department of Chemistry Glassblowing Workshop, was used to house a conventional three-electrode set-up of platinum counter, saturated calomel reference and pyrolytic graphite edge (PGE) working electrodes (Figure 3.1).
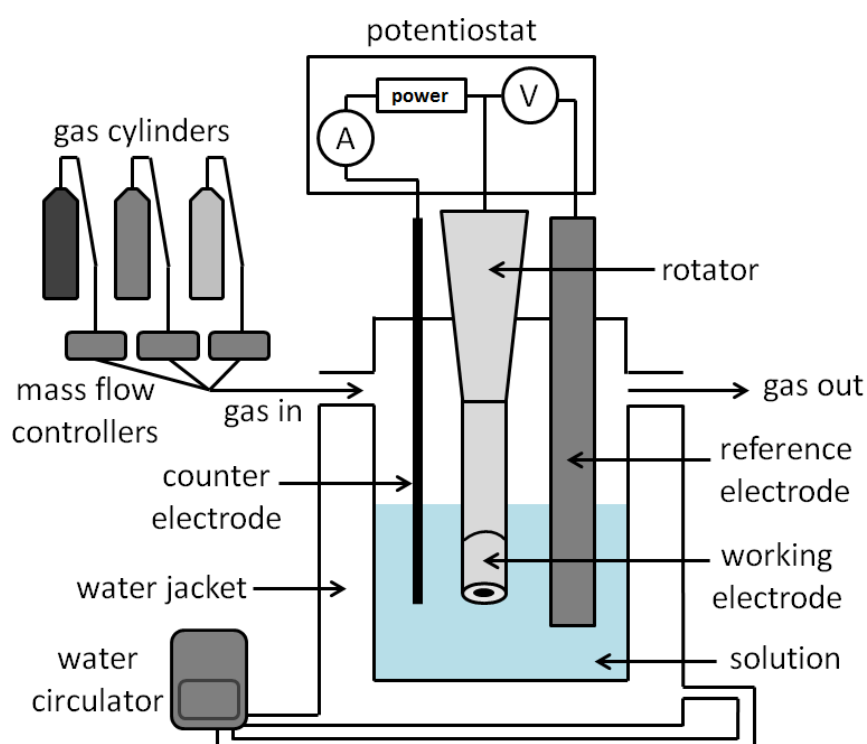
Figure 3.1 Electrochemistry set-up

Pyrolytic graphite edge working electrodes were custom manufactured by the University of York, Department of Chemistry Mechanical Workshop with a graphite geometric surface area of 0.03 cm^2. Connection to the working electrode was made via an OrigaTrod electrode rotator that was operated at sufficient rotational speed to prevent diffusion limitations in enzyme substrate experiments. The cell temperature was controlled with a water circulator (Grant TC120). The cell gas atmosphere was regulated by mass flow controllers (Sierra instruments) which controlled the flow of up to three experimental gasses (BOC) to a total flow rate of 100 scc min^{-1} and specific percentage mix.

Cell buffer solutions of specified composition and pH were made with deionised water (Pur1te, 7.4 MΩ·cm). All FTacV measurements were made in solutions containing 2 M NaCl, to minimise uncompensated solution resistance.

3.1.2 Protein film electrochemistry

The PGE working electrode surface was prepared by abrasion with P1200 sandpaper and then a "blank" control measurement performed under the experimental conditions, to assess the background capacitive current contribution (Chapter 1.3.2, Figure 1.11). A protein film was prepared on the surface by applying the specified amount (usually ~ 0.5 – 5 µl, 0.25 – 40 mg ml^{-1}) of protein sample to the surface for a short time (~ 1 to 10 minutes). The working electrode was then placed in the electrochemical cell and measurements made using a potentiostat. All potentials in this thesis have been converted to the standard hydrogen electrode (SHE) scale using the correction +241 mV *vs*. Hg|Hg$_2$Cl$_2$|KCl(sat.) at 25 °C.[99]

3.1.3 Potentiostats

An Ivium CompactStat potentiostat was used to make most dc cyclic voltammetry and all chronoamperometry measurements. Fourier Transformed ac Voltammetry (FTacV) measurements were performed using the custom-made instrumentation [127] built by Darrell Elton (La Trobe University, Australia) and loaned to the University of York by Prof. Alan Bond (Monash University, Australia). Some dc cyclic voltammetry measurements were also made using the instrumentation, by setting the ac oscillation amplitude to zero. Impedance measurements to determine uncompensated resistance were also performed with this instrumentation. Prior to use the instrument was fully calibrated with a series of resistors and capacitors, to the specifications made by the software.

3.1.4 Electrochemical simulations

Heuristic simulations of FTacV data (Chapter 4) were performed using the Monash Electrochemistry Simulator (MECSim) digital simulation software package [140] which models the response of a system to FTacV. The non-Faradaic (capacitive) component was modelled as a non-linear capacitor (Chapter 2.7.6) using a fifth order polynomial and the value of uncompensated resistance used was measured with a separate impedance measurement. The

Faradaic component was based on Butler−Volmer formalisms for heterogeneous electron transfer kinetics (Chapter 2.3.1) and the mechanisms detailed in Chapter 4. The charge transfer coefficient was assumed to be α = 0.5 in all simulations. All other simulation parameters were optimized to give a close fit between theoretical and experimental data using a heuristic approach.

Computer automated multi-parameter data optimisation procedures for simulation of FTacV data were fully developed and implemented by Dr. Martin Robinson and Prof. David Gavaghan (Department of Computer Science, University of Oxford). The methods and outcomes are detailed in Chapters 5 and 7.

3.2   Spectroelectrochemistry

The UV/Vis spectroelectrochemical measurements described in Chapter 4 were measured using a Hitachi U-1900 spectrophotometer in conjunction with a BASi quartz spectroelectrochemical cell of path length 1 mm (Figure 3.2).
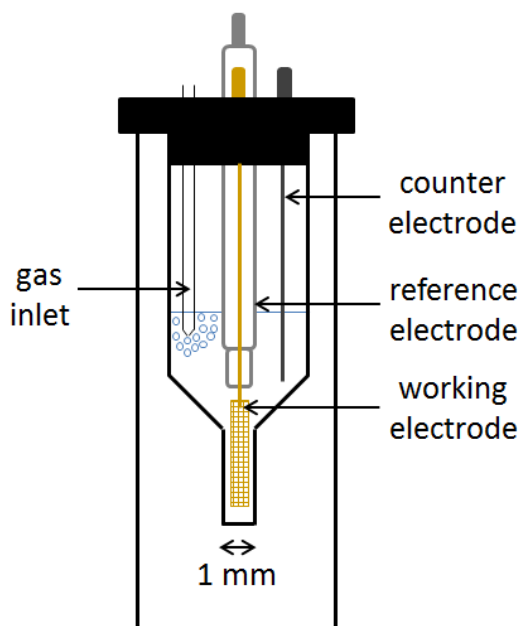
Figure 3.2 Spectroelectrochemical cell

This cell housed the gold mesh working, platinum wire counter and Ag/AgCl (3 M NaCl) reference electrodes in the sample solution, which was continuously purged with argon. The potential was controlled by an Ivium CompactStat potentiostat and all spectroelectrochemistry potentials were converted to the SHE scale using the correction +210 mV at 25°C.[99] Prior to measurement of

protein samples, correct calibration of the set-up was confirmed by UV/Vis spectroelectrochemical analysis of the redox dyes methylene blue and methyl viologen. Protein measurements were made on 300 µl samples of 5.3 mg ml^{-1} *E. coli* YedY in pH 7.0 20 mM MOPS.

3.3   Hydrogenase solution assays

All solution assays used to measure hydrogen oxidation kinetics (Chapter 7) were carried out in an anaerobic glovebox (Faircrest) at room temperature and performed by monitoring the concomitant reduction of methylene blue. The molar extinction coefficient of methylene blue at 626 nm was determined to be ε = 28 mM^{-1} cm^{-1} via measurement of the absorbance by 0 – 25 µM solutions. A solution of 25 µM methylene blue in pH 6 or pH 3 mixed buffer (15 mM each of MES, CHES, HEPES, TAPS and Na acetate, 0.1 M NaCl) was saturated with 100% H_2 and then 2 ml placed in a 3 ml cuvette. This was put in a LED spectrophotometer (Department of Chemistry Electronic Workshops, University of York) illuminated at 626 nm and covered with a light blocking lid. The solution was constantly stirred by a magnetic bead and stirrer plate. A baseline measure was taken for ~ 150 seconds before 10 – 50 µl of hydrogenase sample was injected to a final concentration of ~ 3 nM. The absorbance at 626 nM was then monitored until the methylene blue solution was completely reduced and decolourised. The fastest rate of absorbance change was converted to hydrogenase H_2 oxidation rates, using the molar extinction coefficient and the concentration of protein. Measurements were performed on "as-isolated" samples and "H_2-activated" samples, which had been activated overnight in a 100% H_2 atmosphere.

3.4   EPR measurements

All EPR measurements detailed in Chapter 7 were performed by John Wright in the lab of Dr. Maxie Roessler (Queen Mary University of London), using the methods described in reference [195], with any modifications detailed in Chapter 7. Each 25 – 40 µM hydrogenase sample sent for EPR analysis was dialysed into a buffer that is pH stable at cryogenic temperatures (50 mM HEPES, 50 mM dibasic sodium phosphate, 150 mM sodium chloride, 30% v/v glycerol, pH 7.0).

3.5 Molecular biology techniques

The methodology used to construct *E. coli* hydrogenase-1 variants using the Counter-Selection BAC Modification Kit (Cambio) is fully described in Chapter 6. It briefly comprises insertion of an *rpsL*-neo cassette carrying streptomycin sensitivity and kanamycin resistance into the desired locus of the *E. coli* chromosome, which is selected for by the introduced kanamycin resistance. The cassette is then swapped out by insertion of a linear piece of DNA carrying the desired mutation, which can be selected for by the removed streptomycin sensitivity. The technical protocols of the general methods described in Chapter 6 are detailed here.

3.5.1 PCR amplification

The T_m of all primers used in this study was such that the cycling parameters detailed in Table 3.1 were successful for all PCR reactions.

Table 3.1 Standard cycling parameters for all PCR reactions

Step	Temperature / °C	Time / s
1. Initiation	98	30
2. Denaturation	98	10
3. Anneal	65	30
4. Extension	72	90
5. Repeat 2-4	×35	
6. Elongation	72	600

PCR amplification was used to make the *rpsL*-neo cassette flanked by appropriate homology arms, for insertion at the desired locus of the *E. coli* chromosome. The *rpsL*-neo cassette template and appropriate primers were used in the reaction set-up detailed in Table 3.2.

Table 3.2 PCR amplification reaction to make *rpsL*-neo cassette with homology arms

Component	Amount
rpsL-neo template	0.5 µl (~ 1 µg µl^{-1})
neo_sense primer	0.25 µl (100 µM)
neo_antisense primer	0.25 µl (100 µM)
water (PCR grade)	24 µl
Q5 High-Fidelity 2X Master Mix (NEB)	25 µl

PCR amplification was also used to make linear non-selectable DNA that was used to swap out the cassette from the *E. coli* chromosome and introduce the

desired single-site mutation. The appropriate sense and antisense primers were used in the reaction set-up detailed in Table 3.3.

Table 3.3 PCR amplification reaction to make linear non-selectable DNA

Component	Amount
olap_sense primer	0.25 µl (100 µM)
olap_antisense primer	0.25 µl (100 µM)
water (PCR grade)	24.5 µl
Q5 High-Fidelity 2X Master Mix (NEB)	25 µl

Colony PCR was used to check for the presence or absence of the *rpsL*-neo cassette DNA at a certain point in the *E. coli* chromosome and to generate DNA for sequencing. Use of appropriate primers leads to amplification of DNA in the region of interest on the *E. coli* chromosome. A small number of cells from a single colony were picked with a sterile pipette tip and added to the PCR reaction mix detailed in Table 3.4.

Table 3.4 PCR amplification reaction for screening of bacterial colonies

Component	Amount
check_sense primer	0.625 µl (10 µM)
check_antisense primer	0.625 µl (10 µM)
water (PCR grade)	11.25 µl
Q5 High-Fidelity 2X Master Mix (NEB)	12.5 µl

3.5.2 Agarose DNA gel electrophoresis

DNA gels were used to check the length of DNA samples. Samples were prepared with 1 µl 6X Gel Loading Dye, Blue (NEB) and 5 µl sample. 0.7% agarose gels were used and made with 0.7 g of agarose (Melford) in 100 ml of pH 8.3 TAE buffer (40 mM Tris, 20 mM acetic acid, 1 mM EDTA, Fisher) with 5 µl of SYBR Safe (Invitrogen) added. Electrophoresis was run in pH 8.3 TAE buffer (40 mM Tris, 20 mM acetic acid and 1mM EDTA, Fisher) at 0.1 V for approximately 30 minutes. Either a 100 bp or 1 kb DNA Ladder (NEB) was used as a marker. DNA bands were visualised by the fluorescence of bound SYBR Safe upon illumination with blue light.

3.5.3 DNA extraction and purification

Amplified DNA for use in transformations was extracted from the PCR reaction mixture by ethanol precipitation. For 45 µl of PCR reaction mixture, 150 µl 100% ethanol (VWR) and 5 µl 3 M sodium acetate buffer, pH 7.0 (Fluka) were added

and the sample was then placed at −80°C for 10 minutes. DNA was extracted by centrifugation at 11,000 × g for 5 minutes. The ethanol was removed and DNA pellet washed with 500 µl 70% ethanol (VWR). The ethanol was then removed and the pellet dried at 37°C in a water bath, before resuspension in 10 µl of Elution Buffer 4 (10 mM Tris.HCl, pH 8, GE Healthcare).

Amplified DNA from colony PCR was extracted from agarose DNA gel bands for sequencing, using the illustra GFX PCR DNA and Gel Band Purification Kit (GE Healthcare) to the manufacturer's instructions.

DNA concentrations were determined by measuring the absorbance at 260 nm on a Denovix DS-11 small volume spectrophotometer. Samples were stored at −30°C.

3.5.4 DNA sequencing

Sequencing was used to determine if a desired mutation had been made whilst otherwise maintaining gene integrity. Samples containing 5 µl DNA (20 − 80 ng µl^{-1}) and 5 µl of the appropriate check_sense primer (5 µM) were submitted to the GATC Lightrun service for sequencing. Sequences were analysed using FinchTV software.

3.5.5 Routine growth of bacteria

E. coli strains were routinely grown in sterile (autoclaved) LB media, made of 10 g l^{-1} tryptone (Melford), 10 g l^{-1} NaCl and 5 g l^{-1} yeast extract (Melford). To prepare solid agar media, 1.5 % (w/v) agar was added to the LB media before autoclaving.

3.5.6 Preparation of competent *E. coli* cells

A single colony of the appropriate *E. coli* strain was used to inoculate 1 ml of LB media supplemented with 50 µg ml^{-1} ampicillin (Melford) and grown at 30°C overnight with 180 rpm shaking. This culture was used to inoculate 50 ml LB media supplemented with 50 µg ml^{-1} ampicillin and grown for 3 hours at 30°C with 180 rpm shaking. 1.8 ml of 10 % w/v l-arabinose (Sigma) was then added and the culture grown for 45 minutes at 37°C with 180 rpm shaking. Cells were harvested at 4000 × g for 20 minutes at 4°C and the pellet resuspended in 15 ml ice-cold buffer RF1 (Table 3.5). The suspension was incubated on ice for 15

minutes before centrifuging at 4000 × *g* for 10 minutes at 4°C. The pellet was then resuspended in 5 ml of ice-cold buffer RF2 (Table 3.5), incubated on ice for 15 minutes and then 400 µl aliquots stored at −80°C.

Table 3.5 Recipe for buffers RF1 and RF2 – made up to 200 ml with filter sterilised water

RF1		RF2	
Component	Amount	Component	Amount
KCl	2.4 g	KCl	0.3 g
$CaCl_2.2H_2O$	0.3 g	$CaCl_2.2H_2O$	2.2 g
glycerol	30 ml	glycerol	30 ml
Potassium acetate	0.6 g	0.5M MOPS pH 6.8	4 ml
$MgCl_2.4H_2O$	2 g	Adjusted to pH 6.8	

3.5.7 Transformation of competent *E. coli* cells with linear DNA

The stated amount of DNA was added to 100 µl of competent *E. coli* cells and then left on ice for 30 minutes. To introduce the *rpsL*-neo cassette flanked by homology arms, 30 µl of ~ 1 µg µl^{-1} DNA was added. To introduce the non-selectable DNA 5 – 10 µl of ~ 0.5 – 1.5 µg µl^{-1} DNA was added. The cells were then heat shocked at 42°C for 30 seconds, followed by incubation on ice for 2 minutes. 1 ml of LB media was added and the culture grown at 37°C with 180 rpm shaking for 1 hour. Cells were harvested at 6000 × *g* for 1 minute, 950 µl of supernatant removed and the pellet resuspended in the approximately 50 µl of remaining media. The suspension was plated onto an LB agar plate supplemented with 50 µg ml^{-1} each of ampicillin and the other appropriate antibiotic for counter selection (kanamycin for cassette insertion and streptomycin for non-selectable DNA insertion). Cells were grown for ~ 20 hours at 30°C and colonies that grew were restreaked on the same LB agar antibiotic media, before growth for another 20 hours at 30°C. Colonies that grew upon restreaking were picked and screened by colony PCR. Cells from the same colony were used to make a glycerol stock.

3.5.8 Glycerol stocks

For long term storage of *E. coli* strains, a glycerol stock was made. A colony of the strain was picked and inoculated in 1 ml LB media supplemented with 50 µg ml^{-1} each of ampicillin and the appropriate other antibiotic, then grown at 30°C with 180 rpm shaking overnight. Cells were harvested by centrifugation at 6000 × *g* for 1 minute. 500 µl of the supernatant was removed and the cells

resuspended in the remaining 500 µl of media and 500 µl of 50% glycerol. Samples were stored at −80°C.

3.6 Bacterial strains, plasmids, primers and linear DNA

3.6.1 Bacterial strains

Table 3.6 Strains of *E. coli* used in this thesis

Strain name	Strain Genotype and Description	Source
LAF003	F⁻ lambda⁻ *IN(rrnD-rrnE)1 rph-1 rpsL150 hyaA(histag) (StrepR)* "wild-type" strain encoding hydrogenase-1 with a polyhistidine tag at the C terminus of the small subunit	Lindsey Flanagan University of York[196]
HA001	F⁻ lambda⁻ *IN(rrnD-rrnE)1 rph-1 rpsL150 hyaA(histag) hyaB(E28Q):rpsL-neo (KanR StrepS)* Derived from LAF003, with *rpsL-neo* cassette inserted at position E28 of *hyaB*	This work
HA002	F⁻ lambda⁻ *IN(rrnD-rrnE)1 rph-1 rpsL150 hyaA(histag)(K189):rpsL-neo (KanR StrepS)* Derived from LAF003, with *rpsL-neo* cassette inserted at position K189 of *hyaA*	This work
HA003	F⁻ lambda⁻ *IN(rrnD-rrnE)1 rph-1 rpsL150 hyaA(histag) hyaBE28Q (StrepR)* Strain encoding hydrogenase-1 with a polyhistidine tag at the C terminus of the small subunit and an E28Q mutation in the large subunit (by a codon change in *hyaB* of the chromosome of LAF003)	This work
HA004	F⁻ lambda⁻ *IN(rrnD-rrnE)1 rph-1 rpsL150 hyaAR193L(histag) (StrepR)* Strain encoding hydrogenase-1 with a polyhistidine tag at the C terminus of the small subunit and a R193L mutation in the small subunit (by a codon change in *hyaA* of the chromosome of LAF003)	This work
HA005	F⁻ lambda⁻ *IN(rrnD-rrnE)1 rph-1 rpsL150 hyaAR193E(histag) (StrepR)* Strain encoding hydrogenase-1 with a polyhistidine tag at the C terminus of the small subunit and a R193E mutation in the small subunit (by a codon change in *hyaA* of the chromosome of LAF-003)	This work
HA006	F⁻ lambda⁻ *IN(rrnD-rrnE)1 rph-1 rpsL150 hyaAR185L(histag) (StrepR)* Strain encoding hydrogenase-1 with a polyhistidine tag at the C terminus of the small subunit and a R185L mutation in the small subunit (by a codon change in *hyaA* of the chromosome of LAF003)	This work
HA007	F⁻ lambda⁻ *IN(rrnD-rrnE)1 rph-1 rpsL150 hyaAH187C(histag) (StrepR)* Strain encoding hydrogenase-1 with a polyhistidine tag at the C terminus of the small subunit and a H187C mutation in the small subunit (by a codon change in *hyaA* of the chromosome of LAF003)	This work
HA008	F⁻ lambda⁻ *IN(rrnD-rrnE)1 rph-1 rpsL150 hyaAH187G(histag) (StrepR)* Strain encoding hydrogenase-1 with a polyhistidine tag at the C terminus of the small subunit and a H187G mutation in the small subunit (by a codon change in *hyaA* of the chromosome of LAF003)	This work
HA009	F⁻ lambda⁻ *IN(rrnD-rrnE)1 rph-1 rpsL150 hyaAH187S(histag) (StrepR)* Strain encoding hydrogenase-1 with a polyhistidine tag at the C terminus of the small subunit and a H187S mutation in the small subunit (by a codon change in *hyaA* of the chromosome of LAF003)	This work
HA010	F⁻ lambda⁻ *IN(rrnD-rrnE)1 rph-1 rpsL150 hyaAK189H (histag) (StrepR)* Strain encoding hydrogenase-1 with a polyhistidine tag at the C terminus of the small subunit and a K189H mutation in the small subunit (by a codon change in *hyaA* of the chromosome of LAF003)	This work
HA011	F⁻ lambda⁻ *IN(rrnD-rrnE)1 rph-1 rpsL150 hyaAK189N (histag) (StrepR)* Strain encoding hydrogenase-1 with a polyhistidine tag at the C terminus	This work

	of the small subunit and a K189N mutation in the small subunit (by a codon change in *hyaA* of the chromosome of LAF003)	
HA012	F⁻ lambda⁻ *IN(rrnD-rrnE)1 rph-1 rpsL150 hyaAC190G (histag) (StrepR)* Strain encoding hydrogenase-1 with a polyhistidine tag at the C terminus of the small subunit and a C190G mutation in the small subunit (by a codon change in *hyaA* of the chromosome of LAF003)	This work
HA013	F⁻ lambda⁻ *IN(rrnD-rrnE)1 rph-1 rpsL150 hyaAC190H (histag) (StrepR)* Strain encoding hydrogenase-1 with a polyhistidine tag at the C terminus of the small subunit and a C190H mutation in the small subunit (by a codon change in *hyaA* of the chromosome of LAF003)	This work
HA014	F⁻ lambda⁻ *IN(rrnD-rrnE)1 rph-1 rpsL150 hyaAY191E (histag) (StrepR)* Strain encoding hydrogenase-1 with a polyhistidine tag at the C terminus of the small subunit and a Y191E mutation in the small subunit (by a codon change in *hyaA* of the chromosome of LAF003)	This work

3.6.2 Plasmids

Table 3.7 Plasmids used in this thesis

Plasmid Name	Plasmid Function	Source
pRed/ET	Red/ET expression plasmid, which confers ampicillin resistance and encodes the proteins for homologous recombination	Gene Bridges – Counter selection BAC modification kit

3.6.3 Oligonucleotide primers

Table 3.8 Oligonucleotide primers used in this thesis

Primer Name	Primer Function	Primer sequence (5'-3')	Source
hyaB_E28Q_neo_sense	cassette homology arm for HyaB_E28Q_neo	CCATCAATAATGCCGGACGCCGCCT GGTGGTCGACCCGATTACGCGCATC GGCCTGGTGATGATGGCGGGATCG	Sigma
hyaB_E28Q_neo_antisense	cassette homology arm for HyaB_E28Q_neo	TTGGTGATCACATTCTGATCGTTAAT ATTCACTTCGCAGCGCATGTGGCCTT GTCAGAAGAACTCGTCAAGAAGGCG	Sigma
hyaA_K189_neo_sense	cassette homology arm for HyaA_K189_neo	TCGACAGAATGGGCCGTCCGCTGAT GTTCTATGGTCAGCGAATCCACGAT GGCCTGGTGATGATGGCGGGATCG	IDT
hyaA_K189_neo_antisense	cassette homology arm for HyaA_K189_neo	TCCCAACTCTGGACGAACTCTCCGG CGTCGAAGTGGGCGCGGCGATAGC ATTTTCAGAAGAACTCGTCAAGAAGG CG	IDT
hyaB_E28Q_olap_sense	To make HyaB_E28Q_dsfrag	CCATCAATAATGCCGGACGCCGCCT GGTGGTCGACCCGATTACGCGCATC CAAGGCCAC	Sigma
hyaB_E28Q_olap_antisense	To make HyaB_E28Q_dsfrag	TTGGTGATCACATTCTGATCGTTAAT ATTCACTTCGCAGCGCATGTGGCCTT GGATGCG	Sigma
hyaA_R193L_olap_sense	To make HyaA_R193L_dsfrag	GCCGTCCGCTGATGTTCTATGGTCA GCGAATCCACGATAAATGCTATCGC CTCGCCCAC	IDT
hyaA_R193L_olap_antisense	To make HyaA_R193L_dsfrag	GCAGCGTCATCATCCCAACTCTGGA CGAACTCTCCGGCGTCGAAGTGGGC GAGGCGATA	IDT
hyaA_R193E_olap_sense	To make HyaA_R193E_dsfrag	GCCGTCCGCTGATGTTCTATGGTCA GCGAATCCACGATAAATGCTATCGC GAGGCCCAC	IDT
hyaA_R193E_olap_antisense	To make HyaA_R193E_dsfrag	GCAGCGTCATCATCCCAACTCTGGA CGAACTCTCCGGCGTCGAAGTGGGC	IDT

		CTCGCGATA	
hyaA_R185L_ol ap_sense	To make HyaA_R185L_dsfrag	GCTTGCCAGATGTCGACAGAATGGG CCGTCCGCTGATGTTCTATGGTCAG CTAATCCAC	IDT
hyaA_R185L_ol ap_antisense	To make HyaA_R185L_dsfrag	ACGAACTCTCCGGCGTCGAAGTGGG CGCGGCGATAGCATTTATCGTGGAT TAGCTGACC	IDT
hyaA_H187C_ol ap_sense	To make HyaA_H187C_dsfrag	CAGATGTCGACAGAATGGGCCGTCC GCTGATGTTCTATGGTCAGCGAATCT GCGATAAA	IDT
hyaA_H187C_ol ap_antisense	To make HyaA_H187C_dsfrag	CTCTGGACGAACTCTCCGGCGTCGA AGTGGGCGCGGCGATAGCATTTATC GCAGATTCG	IDT
hyaA_H187G_ol ap_sense	To make HyaA_H187G_dsfrag	CAGATGTCGACAGAATGGGCCGTCC GCTGATGTTCTATGGTCAGCGAATC GGCGATAAA	IDT
hyaA_H187G_ol ap_antisense	To make HyaA_H187G_dsfrag	CTCTGGACGAACTCTCCGGCGTCGA AGTGGGCGCGGCGATAGCATTTATC GCCGATTCG	IDT
hyaA_H187S_ol ap_sense	To make HyaA_H187S_dsfrag	CAGATGTCGACAGAATGGGCCGTCC GCTGATGTTCTATGGTCAGCGAATCA GCGATAAA	IDT
hyaA_H187S_ol ap_antisense	To make HyaA_H187S_dsfrag	CTCTGGACGAACTCTCCGGCGTCGA AGTGGGCGCGGCGATAGCATTTATC GCTGATTCG	IDT
hyaA_K189H_ol ap_sense	To make HyaA_K189H_dsfrag	TCGACAGAATGGGCCGTCCGCTGAT GTTCTATGGTCAGCGAATCCACGATC ACTGCTAT	IDT
hyaA_K189H_ol ap_antisense	To make HyaA_K189H_dsfrag	TCCCAACTCTGGACGAACTCTCCGG CGTCGAAGTGGGCGCGGCGATAGC AGTGATCGTG	IDT
hyaA_K189N_ol ap_sense	To make HyaA_K189N_dsfrag	TCGACAGAATGGGCCGTCCGCTGAT GTTCTATGGTCAGCGAATCCACGATA ATTGCTAT	IDT
hyaA_K189N_ol ap_antisense	To make HyaA_K189N_dsfrag	TCCCAACTCTGGACGAACTCTCCGG CGTCGAAGTGGGCGCGGCGATAGC AATTATCGTG	IDT
hyaA_C190G_ol ap_sense	To make HyaA_C190G_dsfrag	ACAGAATGGGCCGTCCGCTGATGTT CTATGGTCAGCGAATCCACGATAAA GGCTATCGC	IDT
hyaA_C190G_ol ap_antisense	To make HyaA_C190G_dsfrag	TCATCCCAACTCTGGACGAACTCTCC GGCGTCGAAGTGGGCGCGGCGATA GCCTTTATC	IDT
hyaA_C190H_ol ap_sense	To make HyaA_C190H_dsfrag	ACAGAATGGGCCGTCCGCTGATGTT CTATGGTCAGCGAATCCACGATAAAC ACTATCGC	IDT
hyaA_C190H_ol ap_antisense	To make HyaA_C190H_dsfrag	TCATCCCAACTCTGGACGAACTCTCC GGCGTCGAAGTGGGCGCGGCGATA GTGTTTATC	IDT
hyaA_Y191E_ol ap_sense	To make HyaA_Y191E_dsfrag	GAATGGGCCGTCCGCTGATGTTCTA TGGTCAGCGAATCCACGATAAATGC GAGCGCCGC	IDT
hyaA_Y191E_ol ap_antisense	To make HyaA_Y191E_dsfrag	TCATCATCCCAACTCTGGACGAACTC TCCGGCGTCGAAGTGGGCGCGGCG CTCGCATTT	IDT
hyaA_check_se nse	Primer for colony PCR of *hyaA* variant	CGCTGCCGGAGCCAGCGCGAT	Sigma
hyaB_check_se nse	Primer for colony PCR of *hyaB* variant	TCGTTCTACAGCCGCGTGGTC	Sigma
hyaB_check_ant isense	Primer for colony PCR of *hyaA and hyaB* variants	AGGCGTTCCATATTGACTGCC	Sigma

3.6.4 Linear DNA

Table 3.9 Linear DNA used and made in this thesis

Linear DNA name	DNA Description and Function	Source
rpsL-neo template	PCR template for generating a *rpsL*-neomycin (kanamycin) counter-selection/selection cassette.	Gene Bridges – Counter selection BAC modification kit
HyaB_E28Q_neo	*rpsL-neo* cassette flanked by homology arms, used to introduce the cassette at the E28 position of *hyaB*	This work
HyaA_K189_neo	rpsL-neo cassette flanked by homology arms, used to introduce the cassette at the K189 position of *hyaA*	This work
HyaB_E28Q_dsfrag	Non-selectable DNA used to swap out the cassette and introduce the E28Q mutation to *hyaB*	This work
HyaA_R193L_dsfrag	Non-selectable DNA used to swap out the cassette and introduce the R193L mutation to *hyaA*	This work
HyaA_R193E_dsfrag	Non-selectable DNA used to swap out the cassette and introduce the R193E mutation to *hyaA*	This work
HyaA_R185L_dsfrag	Non-selectable DNA used to swap out the cassette and introduce the R185L mutation to *hyaA*	This work
HyaA_H187C_dsfrag	Non-selectable DNA used to swap out the cassette and introduce the H187C mutation to *hyaA*	This work
HyaA_H187G_dsfrag	Non-selectable DNA used to swap out the cassette and introduce the H187G mutation to *hyaA*	This work
HyaA_H187S_dsfrag	Non-selectable DNA used to swap out the cassette and introduce the H187S mutation to *hyaA*	This work
HyaA_K189H_dsfrag	Non-selectable DNA used to swap out the cassette and introduce the K189H mutation to *hyaA*	This work
HyaA_K189N_dsfrag	Non-selectable DNA used to swap out the cassette and introduce the K189N mutation to *hyaA*	This work
HyaA_C190G_dsfrag	Non-selectable DNA used to swap out the cassette and introduce the C190G mutation to *hyaA*	This work
HyaA_C190H_dsfrag	Non-selectable DNA used to swap out the cassette and introduce the C190H mutation to *hyaA*	This work
HyaA_Y191E_dsfrag	Non-selectable DNA used to swap out the cassette and introduce the Y191E mutation to *hyaA*	This work

3.7 Protein production and purification

The *E.coli* YedY protein studied in Chapter 4 was purified by Shannon Murphy in the lab of Prof. Joel Weiner (University of Alberta, Canada), according to published protocols.[197, 198] The *E.coli* HypD protein studied in Chapter 5 was purified by Dr. Basem Soboh in the lab of Prof. Gary Sawers (Martin Luther University, Germany), using established methods.[26] A modified version of the protocol detailed by Flanagan *et al* [103] was used to purify the *E.coli* hydrogenase-1 studied in Chapter 7 and the methods are detail here.

3.7.1 Growth

The appropriate *E. coli* strain was streaked onto an LB agar plate supplemented with 50 µg ml^{-1} ampicillin and 50 µg ml^{-1} streptomycin then grown at 30°C overnight. A single colony was used to inoculate 10 ml of LB media supplemented with 50 µg ml^{-1} ampicillin and 50 µg ml^{-1} streptomycin and then grown at 30°C with 180 rpm shaking for 7 hours. 3 ml of this starter culture was used to inoculate a full 6 litre bottle of sterile LB supplemented with 0.5% (v/v) glycerol, 0.5% (w/v) sodium fumarate and 50 µg ml^{-1} streptomycin. Bottles were grown anaerobically with no shaking at 37°C overnight, to an OD$_{600}$ > 1.5. Typically, to screen variant strains, 2 or 3 × 6 litre cultures were grown per purification and for large scale protein production for electrochemistry, assay and EPR studies, 6 × 6 litre cultures were grown.

3.7.2 Isolation

Isolation of solubilised proteins is described for a typical 18 litre preparation. Cells were harvested by centrifugation at 6000 × *g* for 20 minutes at 4°C. Cell pellets were resuspended in approximately 125 ml ice cold pH 7.5 resuspension buffer (0.1 M Tris, 0.3 M NaCl, 20% w/v sucrose) and stirred at 4°C for ~ 40 minutes. Cells were then harvested at 6000 × *g* for 20 minutes at 4°C. Pellets were resuspended in approximately 300 ml of ice cold water (Pur1te) and stirred at 4°C for ~ 40 minutes to promote osmotic lysis. The solution was adjusted to pH 7.5, 0.1 M Tris, 0.15 M NaCl, 3% Triton X-100, 2 × Pierce™ protease inhibitor tablets, EDTA-free (Fisher), 10 µg ml^{-1} DNAse (Sigma) and 50 µg ml^{-1} lysozyme (Sigma) then stirred at 4°C overnight. The solution was split into 2 × 150 ml samples and each sonicated on ice for 25 × 30 seconds, as a final cell lysis step. Cell debris was removed by centrifugation at 20000 × *g* for 30 minutes at 4°C. Imidazole (50 mM) was added to the supernatant.

3.7.3 Purification

An ÄKTA start (GE Life Sciences) was used to load the sample onto a 5 ml HiTrap Ni affinity column (GE Healthcare) that had been equilibrated with buffer A (pH 7.3, 20 mM Tris, 150 mM NaCl, 50 mM imidazole). Non-specifically bound protein was washed off the column with ten column volumes of buffer A. In early purifications used to screen variants, protein was eluted using an

imidazole gradient of 0 – 100 % buffer B (pH 7.3, 20 mM Tris, 150 mM NaCl, 1 M imidazole) over ten column volumes. In later large-scale protein purifications, protein was eluted with stepped imidazole concentrations between 5 % and 100 % buffer B, to improve sample purity. Protein elution was monitored by the UV/vis absorbance at 280 nm and 3 ml fractions were collected. Fractions containing hydrogenase were confirmed by SDS-PAGE, pooled and dialysed at 4°C overnight into buffer C (pH 7.3, 20 mM Tris, 150 mM NaCl) using 6 – 8 kDa MWCO dialysis tubing (Fisher). Protein was concentrated using a 50 kDa MWCO Vivaspin centrifugal concentrator (GE Healthcare) and purity confirmed by SDS-PAGE. The sample was then stored at −80°C. For EPR samples the protein was then dialysed in a 3.5 kDa MWCO Slide-A-Lyzer cassette (ThermoFisher) into buffer D (pH 7.0, 50 mM HEPES, 50 mM dibasic sodium phosphate, 150 mM NaCl, 30% v/v glycerol). For all assay and electrochemical experiments the protein was further purified by size exclusion chromatography (gel filtration).

3.7.4 Gel filtration

For most samples an ÄKTA purifier was used to load a ~ 250 µl sample onto a Superdex 200 10/30 column (GE Healthcare) equilibrated in buffer C. For large samples, an ÄKTA start was used to load a ~ 2 ml sample onto a Superdex 200 16/600 column (GE Healthcare). Protein was eluted from the column with buffer C at a flow rate of 0.5 – 0.75 ml min^{-1}. The presence of protein and iron sulphur clusters were monitored through the absorbance at 280 nm and 420 nm, respectively, as 0.5 ml fractions were collected. Fractions containing completely pure hydrogenase were confirmed by SDS-PAGE, pooled and concentrated using a 50 kDa MWCO Vivaspin centrifugal concentrator (GE Healthcare). Final sample purity was confirmed by SDS-PAGE.

3.7.5 SDS-PAGE

Samples were prepared in an appropriate volume of 5× SDS gel loading buffer (Sigma) and denatured prior to loading. SDS-PAGE low range standards (Bio-Rad) or PageRuler™ Prestained Protein Ladder 10 to 180 kDa (Thermo Scientific) were used as standard markers. SDS-PAGE was carried out on 12 % acrylamide gels with Tris-glycine running buffer at 200 V for ~ 45 minutes. Bands were visualised by staining with Coomassie Brilliant Blue.

3.7.6 Bradford Assay

All protein concentrations were determined using the Coomassie (Bradford) Protein Assay (Thermo Scientific) with bovine serum albumin (BSA) calibration standards, to the manufacturer's instructions.

3.8 Chemicals and reagents

All chemicals and reagents were obtained at high purity from the named supplier, or if no supplier is named they were obtained at high purity from multiple reputable suppliers.

Chapter 4

Electrochemical evidence that pyranopterin redox chemistry controls the catalysis of YedY, a mononuclear Mo enzyme

Declaration
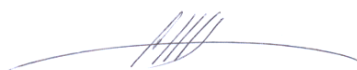
I designed the research with Dr. Alison Parkin (University of York) and performed all the research, data analysis and simulations described in the paper. Dr. Alexandr N. Simonov (Monash University) provided extensive advice regarding the simulations and performed some checks on them. Prof. Alan Bond (Monash University) provided the FTacV instrumentation and along with Dr. Alexandr N. Simonov advised on electrochemical experiments and data analysis. Michelina Kierzek and Shannon Murphy purified the YedY protein in the lab of Dr. Richard Rothery and Prof. Joel Weiner (University of Alberta). I wrote the complete first draft of the paper and with Dr. Alison Parkin revised this into its final form to include contributions and suggestions from Dr. Alexendr N. Simonov, Dr. Richard Rothery, Prof. Joel Weiner and Prof. Alan Bond.

Signed   Dr. Alison Parkin

Signed   Dr. Alexandr Simonov

Reference:

Adamson, H., et al., *Electrochemical evidence that pyranopterin redox chemistry controls the catalysis of YedY, a mononuclear Mo enzyme.* Proceedings of the National Academy of Sciences, 2015. **112**(47): p. 14506-14511

Biological Sciences, Biochemistry

Electrochemical Evidence that Pyranopterin Redox Chemistry Controls the Catalysis of YedY, a Mononuclear Mo Enzyme

FTacV of YedY: Pyranopterin Redox Chemistry

Hope Adamson[a], Alexandr N. Simonov[b], Michelina Kierzek[c], Richard Rothery[c], Joel H. Weiner[c], Alan M. Bond[b], and Alison Parkin[a,1]

[a]Department of Chemistry, University of York, Heslington, York YO10 5DD, United Kingdom; [b]School of Chemistry, Monash University, Clayton, Victoria 3800, Australia; and [c]Department of Biochemistry, 474 Medical Science Building, University of Alberta, Edmonton, Alberta T6G 2H7, Canada

Dr Alison Parkin, Department of Chemistry, University of York, Heslington, York YO10 5DD, United Kingdom; Telephone: 00441904322561; Email: alison.parkin@york.ac.uk.

Abstract

A longstanding contradiction in the field of mononuclear Mo enzyme research is that small-molecule chemistry on active site mimic compounds predicts ligand participation in the electron-transfer reactions, but biochemical measurements only suggest metal-centred catalytic electron transfer. With the simultaneous measurement of substrate turnover and reversible electron-transfer which is provided by Fourier transformed alternating current voltammetry we show that *Escherichia coli* YedY is a mononuclear Mo enzyme which reconciles this conflict. In YedY, addition of three-protons and three-electrons to the well-characterised "as-isolated" Mo(V) oxidation state is needed to initiate the catalytic reduction of either dimethyl sulfoxide or trimethylamine N-oxide. Based on comparison with earlier studies and our UV-vis redox titration data, we assign the reversible one-proton and one-electron reduction process centred around +174 mV *vs* SHE at pH 7 to a Mo(V) to Mo(IV) conversion but ascribe the two-proton and two-electron transition occurring at negative potential to the organic pyranopterin ligand system. We predict that a dihydro to tetrahydro transition is needed to generate the catalytically active state of the enzyme. This is a novel mechanism, suggested by the structural simplicity of YedY, a protein in which Mo is the only metal site.

Significance Statement

The mononuclear Mo enzymes are ubiquitous throughout life and the notion that their activity arises from Mo(VI/V/IV) redox cycling is a central dogma of bioinorganic chemistry. We prove that YedY, a structurally simple mononuclear Mo enzyme, operates via a strikingly different mechanism: the catalytically active state is generated from addition of three-electrons and three-protons to the Mo(V) form of the enzyme, suggesting for the first time that organic-ligand based electron-transfer reactions at the pyranopterin play a role in catalysis. We showcase Fourier transformed alternating current voltammetry as a technique with powerful utility in metalloenzyme studies, allowing the simultaneous measurement of redox catalysis *and* the underlying electron-transfer reactions.

Introduction

Most living species require a Mo enzyme (1) and apart from nitrogenase all of these Mo-containing proteins are part of the large family of "mononuclear Mo" enzymes. The general ability of mononuclear Mo enzymes to catalyse two-electron oxygen atom transfer reactions has been attributed to the Mo(IV)/Mo(V)/Mo(VI) oxidation-state cycling of the active site, and this mechanism is a common part of Undergraduate syllabuses (1, 2). *Escherichia coli* YedY is a mononuclear Mo enzyme (3) and, based on sequence homology, the majority of sequenced Gram-negative bacterial genomes encode a YedY-like protein (3-5). Uniquely for a mononuclear Mo enzyme, it has not been possible to form the YedY Mo(VI) state in experiments using ferricyanide as an oxidising agent, and an unusually positive reduction potential for the Mo(V/IV) transition (+132 mV *vs.* SHE at pH 7) was determined from EPR experiments (6). Although the physiological substrate of YedY is unknown, a possible role in the reduction of reactive nitrogen species is suggested by experiments on the pathogen *Campylobacter jejuni*, where deletion of the Cj0379 YedY-homologue generated a mutant which is deficient in chicken colonization and has a nitrosative stress phenotype (4). YedY catalysis can be assayed by measuring the two-electron reduction of either dimethyl sulfoxide (DMSO) or trimethylamine N-oxide (TMAO) (3) but the inaccessibility of the YedY Mo(VI) means the enzyme mechanism does not proceed via the common two-electron Mo-redox cycle. In small molecule analogues of mononuclear Mo enzymes the pterin ligands are described as "non-innocent" meaning that the redox processes could be ligand or metal based (7). This study explores the possibility that ligand-based redox chemistry plays a role in YedY catalysis.

YedY has been structurally characterised via both X-ray crystallography and X-ray absorption spectroscopy (XAS) (3, 8, 9). In most mononuclear Mo enzymes, heme groups and iron sulphur clusters are found within the same protein as the Mo centre, but the only metal site in YedY is Mo, making this enzyme a helpfully simple system for studying redox chemistry (Fig. 1) (1, 3). Within the active site the X-ray structure was interpreted to show Mo(V) in a square pyramidal environment (3), identical to other members of the "sulfite oxidase" family of mononuclear Mo enzymes. In contrast, XAS has suggested a pseudooctahedral Mo center (8, 9) with an additional O (from Glu104) or N (from Asn45) axial

ligand coordinating *trans* to the apical oxo group (Fig. 1) (8). The equatorial ligation is provided by one oxygen-containing ligand and three sulphur donor atoms, one provided by cysteine (Cys102) and two from the pyranopterin cofactor which binds to the Mo in a bidentate fashion via the enedithiolate side chain (3).
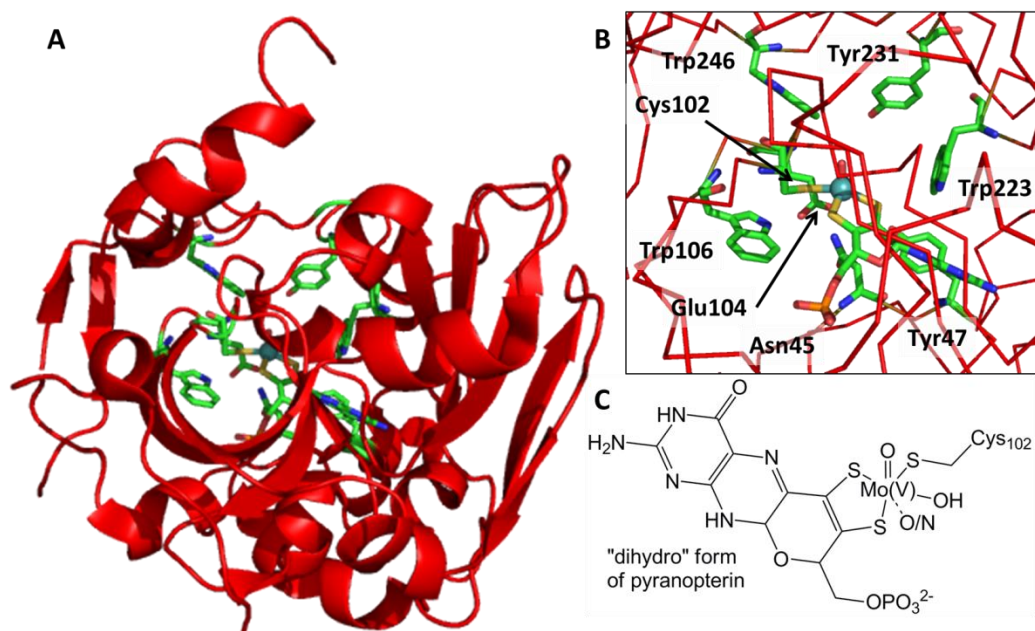
Figure 1. Structure of *Escherichia coli* YedY. (A & B) The protein structure, PDB 1XDQ (3). **(C)** The active site in the as-isolated Mo(V) state containing the "dihydro" form of pyranopterin.

A 2012 computational study provided evidence that two different oxidation states can be accessed by protein-bound pyranopterin ligands (10). Conformational analysis and electronic structure calculations were used to assign redox states to the pyranopterin ligands in all known mononuclear Mo enzyme structures (10). It was concluded that while enzymes from the sulfite oxidase family (such as YedY) contain pyranopterin ligands in the "dihydro" form, the xanthine dehydrogenase family of enzymes contain the two proton, two electron more reduced "tetrahydro" form of the pyranopterin (10).

Traditionally, redox-potential measurements of enzymes have required substrate-free conditions to either permit a solution equilibrium to be established (spectroscopic redox titrations) or to prevent catalytic signals from masking the non-catalytic response (film electrochemistry). Fourier transformed alternating current voltammetry (FTacV) is a technique which offers the ability to measure catalytic chemical redox reactions and reversible electron transfer processes in a single experiment (11, 12). In the FTacV measurement, a large amplitude sine

wave of frequency f is superimposed on a linear voltage-time sweep (11, 13-15) and the resulting current-time response is measured and then Fourier transformed (FT) into the frequency domain to give a power spectrum of harmonic contributions at frequencies f, $2f$, $3f$ etc. Band selection of the individual harmonics followed by inverse FT resolves the data back into the time domain. The higher harmonic components only arise from fast, reversible redox reactions, devoid of catalysis and baseline contributions, but the aperiodic (dc) component ($f = 0$) gives the same catalytic information as a traditional direct current cyclic voltammetry (dcV) experiment, and can therefore show catalytic turnover (13, 14, 16).

In this study we both discover novel mononuclear Mo enzyme redox chemistry as well as demonstrate the significant advantages of using FTacV to probe the mechanism of a redox active enzyme.

Results

Electrochemical Observation of Two Redox Transitions by YedY. We prove that YedY can reversibly form three different oxidation states, i.e. the enzyme can undergo two different redox transitions. This is shown in Fig. 2A which contains dcV YedY electrochemistry data measured under conditions of pH 7, 25°C. The enzyme has been adsorbed onto the surface of the electrode and the signals which are observed are typical for non-catalytic redox-enzyme "film" electrochemistry (SI Appendix (Fig. S1)) (17). In Fig. 2A, both enzyme-redox transitions are visible as "peak" Faradaic signals at around +170 mV and -250 mV (control experiments confirm that these signals are not present with a YedY-free electrode). The YedY signals were stable over at least 20 continuous 100 mVs^{-1} cyclic voltammograms but only one scan is shown for clarity.

A significant limitation of the protein film dcV technique is that the Faradaic non-catalytic enzyme signals are very small in relation to the "background" signal from the non-Faradaic (double layer charging) electrode process. To permit analysis of the YedY-only redox chemistry we have computed the non-Faradaic response using a polynomial function and then subtracted this from the experimental data to give pure Faradaic data. The baseline-subtracted signals thus obtained are scaled by a 20-fold multiplication factor in Fig. 2A. From Fig. 2A the integrated area of the baseline subtracted negative potential process,

centred around -250 mV, is approximately 1.8 times larger than the integrated area of the baseline subtracted positive potential process centred around +170 mV. We therefore conclude that almost twice as many electrons are passed in the negative potential redox transition relative to the positive potential redox transition.
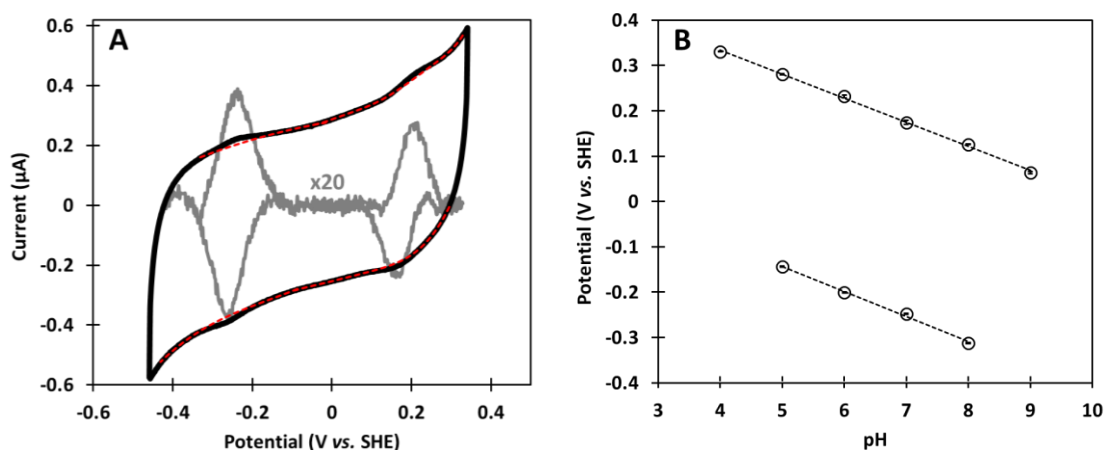
Figure 2. Redox transitions of YedY measured by dcV at a scan rate of 100 mV s^{-1}. (A) A cyclic voltammetry measurement of YedY in 50 mM MES buffer, pH 7 is shown by the black solid line. The baseline is shown by the red dashed line, the baseline subtracted signal (scaled by a multiplication factor of 20) is depicted by the gray solid lines. **(B)** pH dependence of peak midpoint potentials derived from voltammetry experiments conducted in 50 mM buffer solution of either acetate (pH 4 and 5), MES (pH 6 and 7) or Tris (pH 8 and 9). Error bars shown within data point circles reflect the standard error calculated from at least 3 repeat experiments. Other conditions: stationary electrode, and temperature 25°C.

As shown in the SI Appendix (Fig. S2B), the redox transition measured for YedY at positive potential is well modelled by a Nernstian one-electron process (equivalent to a peak width at half height, δ, of 90 mV) with a pH 7 mid-point potential $E_{m, 7}$ = +174 ± 4 mV. We attribute this process to the Mo(V/IV) redox transition. Our assignment of the positive potential redox process as a metal-based transition is supported by UV-vis solution spectroelectrochemistry measurements made from 750 to 320 nm under an atmosphere of Ar and shown in the SI Appendix (Fig. S3). As-purified YedY, known to be in the Mo(V) state, exhibits two peaks in the optical spectrum (6, 18): a broad absorbance centred at 503 nm and another at approximately 360 nm. Upon lowering the solution potential from +0.21 V to −0.09 V, i.e. passing through the positive potential redox transition, both spectral signals are bleached, indicating a metal-based reduction. These spectral changes can be reversed by raising the potential back to +0.21 V. No spectral changes accompany the negative

potential redox reaction, i.e. no UV-vis changes are measured when the solution potential is stepped between -0.44 and -0.09 V.

Using film electrochemistry, there is no evidence of any further redox transitions at more positive potentials, even when the potential range is extended to the solvent/electrode limit (SI Appendix (Fig. S4)), so in agreement with other techniques, we also cannot observe a Mo(VI/V) redox transition.

Analysis of the negative potential baseline-subtracted dcV waveshape shown in the SI Appendix (Fig. S2C) suggests a cooperative, non-simultaneous two electron charge transfer process, i.e. one electron is transferred and then a second electron follows onto the same centre (19-22). We measure $E_{m, 7} = -248 \pm 1$ mV but using dcV it is very difficult to derive more precise mechanistic information regarding the separate one-electron processes which combine to give the "envelope" signal.

Experiments at different pH reveal that the E_m values for the Mo(V/IV)-assigned reaction and the negative potential redox processes change by -53 and -55 mV per pH unit, respectively (Fig. 2B), close to the -59 mV per pH unit expected for a one-proton per electron process at 25°C (23). "Trumpet plots" of the reductive and oxidative peak potentials *vs.* scan rate show greater peak separation at lower scan rates for the Mo(V/IV) signals compared to the negative potential transition, suggesting that the Mo-based redox process has a slower electron transfer rate (SI Appendix (Fig. S5)) (24). Combining all the dcV information, we suggest a $1H^+ + 1e^-$ process for the Mo(V/IV) transition and a faster $2H^+ + 2e^-$ process for the negative potential transition, over the pH range measured.

Fourier Transformed ac Voltammetry (FTacV) of YedY. Analogous to the dcV experiment shown in Fig. 2, FTacV was used to interrogate YedY redox chemistry over a wide potential range and this is shown in the SI Appendix (Fig. S6). There are two significant differences between the two results; firstly, relative to dcV, the signal-to-background response of YedY at around -250 mV is much larger in the higher harmonic components of the FTacV measurements; secondly, whereas in dcV the peak area for the negative potential YedY signal is approximately double the peak area of the Mo(V/IV) signal, in FTacV the Mo(V/IV)-assigned signal is not visible above the noise. The fact that very little

Mo(V/IV) signal is observed means that the 9 Hz frequency applied in the FTacV outpaces Mo-based electron transfer processes and we can therefore state that YedY's negative potential electron transfer processes is much faster than the Mo(V/IV) redox transition. Based on analysis of the FTacV signals we define the Mo(V/IV) process as a quasi-reversible electron transfer reaction with an apparent heterogeneous charge transfer rate k_{app}^0 of less than 10 s^{-1}, consistent with analysis of dcV trumpet plot data which suggests $k_{app}^0 = 3 - 6$ s^{-1}.
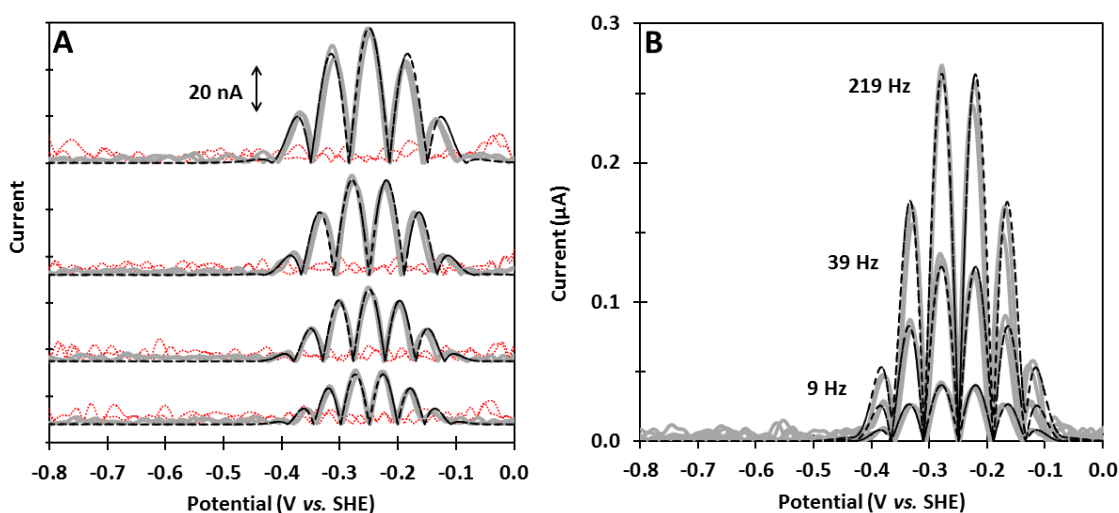
Figure 3. FTacV measurements of the YedY two-electron redox transition. (A) Gray solid lines show, in descending order, the 7th, 8th, 9th and 10th ac harmonic signals measured for YedY using FTacV with a frequency of 9 Hz. The response from a bare (YedY-free) graphite electrode under the same conditions is shown by light red dotted line. **(B)** Gray solid lines compare the 8th ac harmonic from YedY FTacV experiments at different frequencies, as denoted in the graph. **(A & B)** Black dashed lines depict simulated data for a 1e$^-$ + 1e$^-$ mechanism with parameters $E^0_{app(1)}$ = −239 mV $E^0_{app(2)}$ = −261 mV, $(k^0_1)_{app}$ = $(k^0_2)_{app}$ = 2·10^4 s^{-1}, R_u = 50 Ω, polynomial capacitance, Γ = 1.15 pmol cm^{-2} (9 Hz), Γ_{app} = 0.86 pmol cm^{-2} (39 Hz), Γ_{app} = 0.66 pmol cm^{-2} (219 Hz). Other experimental conditions: scan rate 15.83 mVs^{-1}, amplitude 150 mV, buffer solution of 50 mM MES and 2 M NaCl, pH 7, 25°C.

In order to learn more about the negative potential process, Fig. 3A shows 9 Hz FTacV measurements focussed on the YedY reversible redox transition centred at around -250 mV. At least 12 harmonic components are detected and, in stark contrast to dcV, no baseline subtraction is required prior to analysis of the higher harmonic signals because YedY-free controls confirm there is negligible baseline contribution from a bare electrode. The potentials of the central maxima of the odd harmonics and the central minima of the even harmonics provide a direct measure of the midpoint potential and these values agree with the baseline subtracted dcV E_m data. Similar to changing the scan rate in dcV,

changing the frequency in FTacV provides a qualitative means of assessing the electron transfer rate. As shown in Fig. 3B, when the same negative potential range is interrogated using a range of frequencies, well defined ac harmonics are observed up to 219 Hz, indicating that the low potential YedY redox reaction involves extremely fast electron transfer.

Electrocatalytic Activity of YedY. The ability of FTacV to separately resolve catalytic and electron transfer steps in a single experiment is shown in Fig. 4. Solution assays have shown that YedY catalyses the reduction of N- or S-oxides with concomitant oxidation of reduced benzyl viologen (3). The enzyme has the largest specificity constant, k_{cat}/K_M, for the substrates DMSO and TMAO, where k_{cat} refers to the catalytic turnover rate and K_M denotes the Michaelis constant (3). When YedY is adsorbed onto a graphite electrode and then placed in a solution of DMSO, the negative catalytic reduction current, revealed by the dc component of the data (Fig. 4B), steadily increases as the electrode potential is lowered below approximately −0.3 V at pH 7 ("control" enzyme-free electrode experiments in the presence of DMSO show no reductive current, see SI Appendix). In contrast, the aperiodic component resembles a "blank" electrode in the presence of YedY but absence of substrate (Fig. 4B). The reduction potential for DMSO is +160 mV at pH 7 and work by Heffron et al. shows that the enzyme *E. coli* DMSO reductase is capable of reducing DMSO at more positive voltages than YedY (25). In Fig. 4B the "onset potential", i.e. the electrochemical voltage required to initiate YedY-catalysed DMSO reduction, is therefore an enzyme-specific property and not a substrate related behaviour.

The 6th harmonic signal for YedY, shown in Fig. 4A, is unchanged in the presence or absence of 200 mM DMSO, showing that substrate has not affected the electron transfer properties of the negative potential redox process: it remains very clearly distinguishable, revealing the redox potential without any need for background subtraction. Comparison between the high harmonic data in the presence and absence of substrate therefore suggests that the negative potential two-electron, two-proton reduction process generates the catalytically active state of YedY, since catalysis does not commence until the potential is sufficiently negative for this reaction to have occurred. Experiments at different pH further support the hypothesis that the most reduced state of the enzyme

reacts with substrate because the onset potential of YedY-catalysed DMSO-reduction changes between pH 5 and 8 in exactly the same way as the potential of the two-electron non-catalytic redox signal (SI Appendix (Fig. S7)). Data extracted from experiments at pH 7 and different DMSO concentrations also corroborate published solution assay measurements with K_M = 35 ± 5 mM at pH 7, 25 °C and k_{cat} = 4.2 ± 0.9 s^{-1} at −359 mV, pH 7, 25 °C (SI Appendix (Fig. S8)) (3, 8, 26). Electrocatalytic experiments have also been conducted using TMAO as a substrate; these are shown in the SI Appendix (Fig. S9). With TMAO as a substrate we again observe that the onset potential of YedY catalysis is approximately -0.3 V at pH 7, far more negative than the equilibrium redox potential for the substrate (TMAO has reduction potential +130 mV at pH 7 (27)).
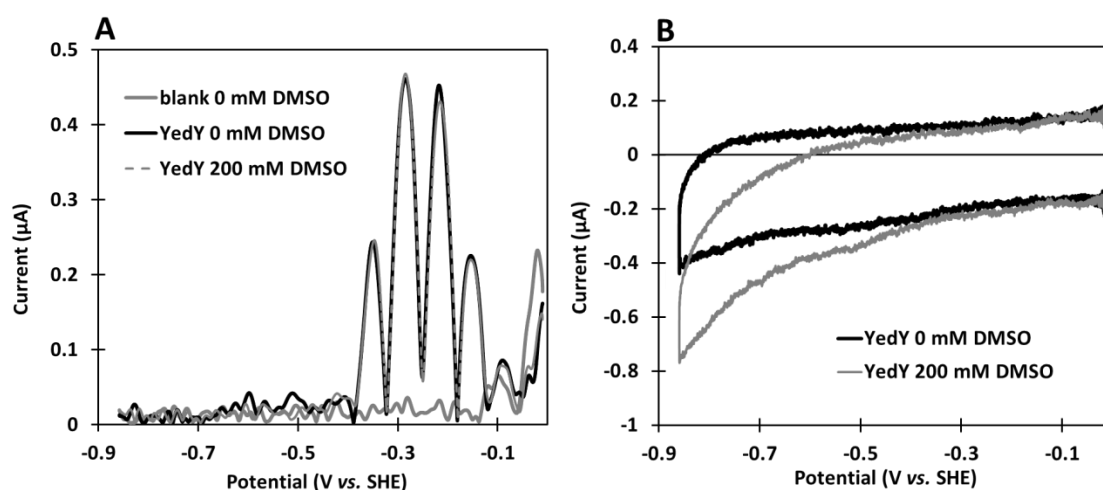
Figure 4. FTacV of YedY in the presence and absence of DMSO substrate. (A) 6th harmonic component of a 219 Hz FTacV experiment on YedY in the absence (black solid line) and presence (gray dashed line) of 200 mM DMSO. The response of a blank or bare (YedY-free) graphite electrode in the absence of DMSO, measured using the same FTacV parameters, is shown by the gray solid line. **(B)** The aperiodic dc component of the same FTacV experiment on YedY in the absence (black solid line) and presence (gray solid line) of DMSO. Other conditions: scan rate 15.83 mVs^{-1}, amplitude 150 mV, buffer solution of 50 mM MES and 2 M NaCl, pH 7, 25°C and stationary electrode.

Simulation of the FTacV data. Simulation of the FTacV data makes it possible to harness the technique's ability to provide a quantitative measure of electron transfer rates and deconvolution of separate redox potentials in a single experiment, insight that we cannot access with dcV (22). Fig. 3A shows simulations of the FTacV data using the 1e$^-$ + 1e$^-$ mechanism described in the SI Appendix. The same parameters were used to simulate all the harmonic signals. To minimise the parameter space used in simulations the value for

uncompensated resistance, R_u, was derived from a separate impedance spectroscopy measurement and Γ_{app}, the apparent coverage of enzyme on the electrode, was estimated from dcV measurements. Both electron transfer steps exhibit fast kinetics as reflected by $(k_1^0)_{app}$, $(k_2^0)_{app}$= 2.0·10^4 s^{-1} used in simulations. To achieve a close agreement to experimental data the apparent reversible potentials of the two sequential one-electron transfers must be similar and $(E_1^0)_{app}$= −239 mV and $(E_2^0)_{app}$ = −261 mV are used to produce data in Fig. 3. The charge transfer coefficient α was always assumed to be 0.5 and its exact value could not be determined as the simulations are insensitive to α at these very high electron transfer rates. As expected, simulations using Marcus theory rather than Butler Volmer theory made no difference under these reversible conditions. As shown in the SI Appendix we confirmed that different redox reaction models will not simulate the data, confirming that the low potential YedY redox reaction is neither a 1e$^-$ reaction (Fig. S10) or a simultaneous 2e$^-$ transfer mechanism (as opposed to a stepwise 1e$^-$ + 1e$^-$ reaction, Fig. S11).

When simulating the FTacV data obtained from experiments at different frequency (Fig. 3B), all the same parameters were used except for the enzyme-electrode coverage value, Γ_{app}, which was lowered with increasing frequency from 1.15 pmol cm^{-2} in the first 9 Hz measurement, to 0.615 pmol cm^{-2} for 519 Hz (Fig. 3B and SI Appendix (Fig. S12)). This trend did not reflect true enzyme desorption because a final measurement at 9 Hz yielded data that was best simulated using Γ_{app} of 0.9 pmol cm^{-2}. As described in a recent theoretical study (28), kinetic dispersion, meaning that different enzyme orientations on the electrode surface have different electron transfer rates (k^0_{app}), is believed to be the major reason that Γ_{app} decreases as the frequency increases. Dispersion is a common observation in protein film electrochemistry measurements (29).

Discussion

We present dcV and FTacV data that prove that *E. coli* YedY forms three stable oxidation states. Relative to the well-characterised Mo(V) form of the enzyme, formation of the catalytically active state requires addition of three electrons and three protons and we summarise our proposed mechanism in Fig. 5. We assign the YedY redox transition which has $E_{m,7}$ = +174 ± 4 mV to the Mo(V/IV)

process and ascribe the redox transition with $(E_1^0)_{app}$= −239 mV and $(E_2^0)_{app}$ = −261 mV to a pyranopterin dihydro-tetrahydro interconversion.
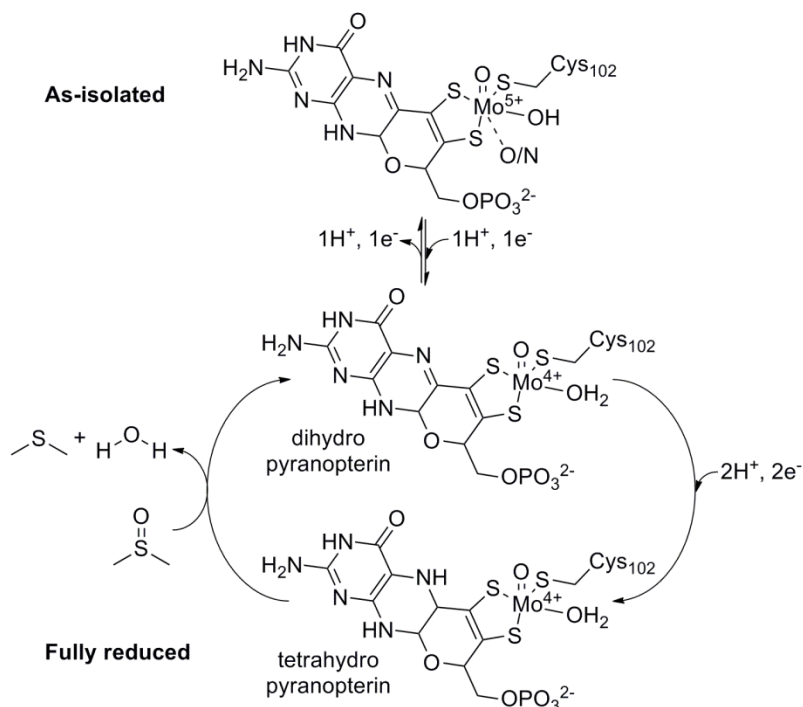
Figure 5. Proposed redox state cycling of YedY.

Using spectroelectrochemistry it has been demonstrated that application of -0.09 V is sufficient to bleach the absorbance peaks observed in UV-vis spectra of the as-isolated, Mo(V), enzyme. The disappearance of the absorbance centred at 503 nm is consistent with our assignment of the positive potential redox process being Mo-based; dithiolene-S ligand to metal charge transfer processes give rise to this spectral feature so it should be a reporter signal for changes to the metal redox state (18). Both dcV trumpet plot data and low intensity FTacV harmonic currents indicate that the Mo(V/IV) redox reaction has a slow electron transfer rate, from 3 – 6 s^{-1}, which suggests structural reorganisation. This correlates with the XAS mechanism that six coordinate Mo(V) is reduced to a five coordinate Mo(IV) species (9).

Varying the pH from 4 to 9 causes the electrochemically-determined E_m(Mo(V/IV)) value to decrease by 53 mV per pH unit which indicates a one-electron, one-proton transition in agreement with the proposed XAS mechanism: Mo(V)−OH + 1H$^+$ + 1e$^-$ → Mo(IV)−OH$_2$ (9). There is a discrepancy between the midpoint potentials we measure using electrochemistry and those reported from an EPR redox titration, with respective $E_{m, 7}$ values of +174 mV

and +132 mV (6). The EPR data is also pH-independent over a range of pH 6-8 (6). Whereas the dcV electrochemical data could be accurately simulated as a one-electron Nernstian process, the EPR Nernst plots were fit as physically impossible 1.3 and 1.63 electron processes for the oxidative and reductive titrations, respectively. As noted in the EPR study (6), the complex spectroscopic data is difficult to interpret and we suggest that the disparity in midpoint potential values may reflect this challenge. We also note that the electrochemical and EPR redox potential measurements are made on very different timescales as protein film electrochemistry affords the advantage of "wiring" the enzyme to the electrode, permitting rapid potential control, whereas achieving solution redox potential equilibration for EPR requires many minutes.

Our experiments at highly oxidising potentials confirm the unusual stability of the YedY Mo(V) state with respect to oxidation, setting a limiting value of $E_{\mathrm{m,7}}$(Mo(IV/V)) > +600 mV. The Mo(VI) oxidation state is therefore defined as physiologically irrelevant and thus plays no direct role in a catalytic reaction mechanism.

FTacV permitted simultaneous measurement of the putative pyranopterin redox transition *and* catalysis. The onset potential for enzymatic reduction of either DMSO or TMAO is more negative than the redox potential of either substrate (27) and instead correlates with the pyranopterin-assigned two-electron, two-proton reversible redox transition across the pH range 5 to 8. We assign this process to the pyranopterin cofactor because the structural simplicity of YedY is such that there are no other putative redox active centres apart from the Mo (3). In sulfite oxidase fold enzymes such as YedY, which is crystallised in the Mo(V) oxidation state, the geometry of the pyranopterin is consistent with a 10,10a-dihydro form (10); in Fig. 5 we show the three-electron, three-proton reduced catalytically active Mo(IV) form of the enzyme with a tetrahydro pyranopterin ligand. We have chosen to display the two-electron reduced pyranopterin ligand in a ring-closed tetrahydro state because this is consistent with the structure found most frequently at the active site of Mo-containing enzymes (10). However it should be noted that an alternative, ring-opened confirmation exists at the same oxidation state level (7). For simple pterins, reversible two-electron and two-proton transitions between tetrahydro and dihydro forms are well known, as is further oxidation of the dihydro state, so pyranopterin redox

reactions would be expected on the basis of chemical analogues (7, 30). It has been proposed that a nitrate reductase undergoes reversible enzymatic inactivation under oxidising conditions because the pyranopterin converts from the tetrahydro to the dihydro state, however all the substrate reactions were still thought to be solely metal based (31). Our experiments therefore provide the first evidence of catalytically relevant pyranopterin redox chemistry (Fig. 5).

It is not possible to conclude if the two electrons for substrate reduction are supplied directly by the pyranopterin or if reduction of the pyranopterin ligand activates the Mo in such a way as to promote changes to the metal redox state catalysis. In the reduced tetrahydro state, the dithiolene chelate of a pyranopterin has increased electron donating ability to Mo, which will decrease the Mo reduction potentials, because relative to the oxidised dihydro form π-delocalisation is lost between the dithiolene chelate and the pterin ring (10). This could make the Mo(VI) state indirectly accessible. There is no conclusive structural information about how the substrate coordinates to YedY, XAS experiments on the Mo(V) state at pH 8 showed a possible long-range coordination of TMAO to Mo, but DMSO coordination was undetectable (8). To probe substrate binding, future experiments would need to be conducted under reducing conditions.

Comparison of Fig. 2 and Fig. 3 demonstrates how the complete absence of background current in the higher harmonic FTacV YedY signals results in much better defined non-catalytic redox peaks, overcoming the need for the significant baseline subtraction which is required in analysis of dcV data. Simulation of the higher harmonic YedY FTacV responses has also provided detailed information on the thermodynamics (apparent E^0), kinetics (apparent k^0 at E^0_{app}) and mechanism of the pyranopterin-assigned electron transfer. Simulation of the FTacV data suggests that the pyranopterin redox reaction proceeds via a sequential $1e^-$ + $1e^-$ process and is extremely fast $((k^0_1)_{app}, (k^0_2)_{app} \geq 2.0 \ 10^4 \ s^{-1})$. Previous measurements of biological electron transfer rates using FTacV have been predominantly on metal centres and much slower electron transfer rates have been calculated (13, 16, 22, 32-34), supporting our conclusion that the delocalised organic ligand is the site for oxidation state changes.

Materials and Methods

Samples and Solutions. *Escherichia coli* YedY was prepared as described previously (3, 6) and stored in a buffer solution of 20mM 3-(N-morpholino)propanesulfonic acid (MOPS), pH 7 which was also used for the UV-vis spectroelectrochemical experiments. For film-electrochemistry experiments, a protein concentration of approximately 10 mg mL^{-1} was used, for spectroelectrochemistry the protein concentration was 5.3 mg mL^{-1}.

All film electrochemistry experiment solutions were prepared using deionised water from a Pur1te Select water purification system (7.4 MΩ cm). The buffer salts were either: pH 4 to 5, 50 mM acetate; pH 6 to 7, 50 mM 2-(N-morpholino)ethanesulfonic acid (MES); pH 8 to 9, 50 mM tris(hydroxymethyl)aminomethane (Tris). The pH was adjusted by addition of NaOH or HCl for MES and Tris buffers and acetic acid for acetate buffer. Additional supporting electrolyte of NaCl was used where stated. Dimethyl sulfoxide (DMSO, Fisher) or trimethylamine N-oxide (TMAO, Sigma) were used as enzyme substrates. All solids were of at least 99% purity.

Protein Film Electrochemistry Apparatus and Methods. Direct current voltammograms were measured with an Ivium CompactStat potentiostat and FTacV measurements were performed using custom made instrumentation described elsewhere (11, 14). All electrochemical experiments were performed under a N$_2$ atmosphere in a glove box (manufactured by University of York Chemistry Mechanical and Electronic Workshops). A conventional three-electrode setup was used with the pyrolytic graphite edge working electrode (0.03 cm^2 geometric area, made in-house), Pt wire counter electrode (Advent research materials) and saturated calomel reference electrode (Scientific laboratory supplies) all located in an all-glass, water-jacketed electrochemical cell (manufactured by University of York Chemistry Glassblower). The connection to the working electrode was made via an OrigaTrod electrode rotator and the electrode was rotated during dcV catalysis experiments to ensure that substrate and product mass transport did not limit the enzyme activity. The electrode was not rotated for FTacV catalysis experiments. All experiments were performed at 25 °C and all potentials have been converted to the standard hydrogen electrode (SHE) scale using the correction +241 mV at 25°C (23). A clean working electrode surface was obtained by abrading the

pyrolytic graphite edge surface with P1200 sandpaper and then rinsing with deionised water. Enzyme was adsorbed onto the electrode surface by pipetting on 4 µL of YedY solution and allowing this to dry for approximately 10 min. All values quoted are the average of at least three experiments and the error bars are the standard errors calculated from all repeat data.

Electrochemical Simulations. Simulations of FTacV data were based on a Butler−Volmer formalism for heterogeneous electron transfer kinetics (22) and the mechanism described in the SI Appendix and were performed using the Monash Electrochemistry Simulator (MECSim) digital simulation software package (35). The charge transfer coefficient was assumed to be $\alpha = 0.5$ in all simulations and all other simulation parameters were optimised to give a close fit between theoretical and experimental data using a heuristic approach.

Author contributions. H.A. and A.P. designed research; H.A. performed research; M.K., R.A.R., J.H.W., and A.M.B. contributed new reagents/analytic tools; H.A. and A.N.S. analyzed data; and H.A., A.N.S., R.A.R., J.H.W., A.M.B., and A.P. wrote the paper.

References

1. Hille R, Hall J, & Basu P (2014) The Mononuclear Molybdenum Enzymes. *Chem Rev* 114(7):3963-4038.
2. Hille R (2013) The molybdenum oxotransferases and related enzymes. *Dalton Trans* 42(9):3029-3042.
3. Loschi L*, et al.* (2004) Structural and Biochemical Identification of a Novel Bacterial Oxidoreductase. *J Biol Chem* 279(48):50391-50400.
4. Hitchcock A*, et al.* (2010) Roles of the twin-arginine translocase and associated chaperones in the biogenesis of the electron transport chains

of the human pathogen *Campylobacter jejuni*. *Microbiology* 156(10):2994-3010.

5. Rothery R & Weiner J (2015) Shifting the metallocentric molybdoenzyme paradigm: the importance of pyranopterin coordination. *J Biol Inorg Chem* 20(2):349-372.

6. Brokx SJ, Rothery RA, Zhang G, Ng DP, & Weiner JH (2005) Characterization of an *Escherichia coli* Sulfite Oxidase Homologue Reveals the Role of a Conserved Active Site Cysteine in Assembly and Function. *Biochemistry* 44(30):10339-10348.

7. Basu P & Burgmayer SJN (2011) Pterin chemistry and its relationship to the molybdenum cofactor. *Coord Chem Rev* 255(9–10):1016-1038.

8. Havelius KGV*, et al.* (2010) Structure of the Molybdenum Site in YedY, a Sulfite Oxidase Homologue from *Escherichia coli*. *Inorg Chem* 50(3):741-748.

9. Pushie MJ*, et al.* (2010) Molybdenum Site Structure of *Escherichia coli* YedY, a Novel Bacterial Oxidoreductase. *Inorg Chem* 50(3):732-740.

10. Rothery RA, Stein B, Solomonson M, Kirk ML, & Weiner JH (2012) Pyranopterin conformation defines the function of molybdenum and tungsten enzymes. *Proc Natl Acad Sci USA* 109(37):14773-14778.

11. Bond AM*, et al.* (2015) An integrated instrumental and theoretical approach to quantitative electrode kinetic studies based on large amplitude Fourier transformed a.c. voltammetry: A mini review. *Electrochem commun* 57:78-83.

12. Bond AM, Mashkina EA, & Simonov AN (2014) A Critical Review of the Methods Available for Quantitative Evaluation of Electrode Kinetics at Stationary Macrodisk Electrodes. *Developments in Electrochemistry*, (John Wiley & Sons, Ltd), pp 21-47.

13. Guo S, Zhang J, Elton DM, & Bond AM (2003) Fourier Transform Large-Amplitude Alternating Current Cyclic Voltammetry of Surface-Bound Azurin. *Anal Chem* 76(1):166-177.

14. Bond AM, Duffy NW, Guo S-X, Zhang J, & Elton D (2005) Changing the Look of Voltammetry. *Anal Chem* 77(9):186 A-195 A.

15. Simonov AN*, et al.* (2014) New Insights into the Analysis of the Electrode Kinetics of Flavin Adenine Dinucleotide Redox Center of Glucose

Oxidase Immobilized on Carbon Electrodes. *Langmuir* 30(11):3264-3273.

16. Fleming BD, Zhang J, Bond AM, Bell SG, & Wong L-L (2005) Separation of Electron-Transfer and Coupled Chemical Reaction Components of Biocatalytic Processes Using Fourier Transform ac Voltammetry. *Anal Chem* 77(11):3502-3510.

17. Léger C & Bertrand P (2008) Direct Electrochemistry of Redox Enzymes as a Tool for Mechanistic Studies. *Chem Rev* 108(7):2379-2438.

18. Yang J, Rothery R, Sempombe J, Weiner JH, & Kirk ML (2009) Spectroscopic Characterization of YedY: The Role of Sulfur Coordination in a Mo(V) Sulfite Oxidase Family Enzyme Form. *J Am Chem Soc* 131(43):15612-15614.

19. Hudson JM*, et al.* (2005) Electron Transfer and Catalytic Control by the Iron−Sulfur Clusters in a Respiratory Enzyme, *E. coli* Fumarate Reductase. *J Am Chem Soc* 127(19):6977-6989.

20. Heering HA, Weiner JH, & Armstrong FA (1997) Direct Detection and Measurement of Electron Relays in a Multicentered Enzyme: Voltammetry of Electrode-Surface Films of *E. coli* Fumarate Reductase, an Iron−Sulfur Flavoprotein. *J Am Chem Soc* 119(48):11628-11638.

21. Hirst J (2006) Elucidating the mechanisms of coupled electron transfer and catalytic reactions by protein film voltammetry. *Biochim Biophys Acta* 1757(4):225-239.

22. Stevenson GP*, et al.* (2012) Theoretical Analysis of the Two-Electron Transfer Reaction and Experimental Studies with Surface-Confined Cytochrome c Peroxidase Using Large-Amplitude Fourier Transformed AC Voltammetry. *Langmuir* 28(25):9864-9877.

23. Bard AJ & Faulkner LR (2010) *Electrochemical Methods: Fundamentals and Applications, 2nd Edition* (Wiley).

24. Armstrong FA*, et al.* (2000) Fast voltammetric studies of the kinetics and energetics of coupled electron-transfer reactions in proteins. *Faraday Discuss* 116(0):191-203.

25. Heffron K, Léger C, Rothery RA, Weiner JH, & Armstrong FA (2001) Determination of an Optimal Potential Window for Catalysis by *E. coli* Dimethyl Sulfoxide Reductase and Hypothesis on the Role of Mo(V) in the Reaction Pathway. *Biochemistry* 40(10):3117-3126.

26. Sabaty M, *et al.* (2013) Detrimental effect of the 6 His C-terminal tag on YedY enzymatic activity and influence of the TAT signal sequence on YedY synthesis. *BMC Biochem* 14(1):1-12.

27. Buc J, *et al.* (1999) Enzymatic and physiological properties of the tungsten-substituted molybdenum TMAO reductase from *Escherichia coli*. *Mol Microbiol* 32(1):159-168.

28. Morris GP, *et al.* (2015) Theoretical Analysis of the Relative Significance of Thermodynamic and Kinetic Dispersion in the dc and ac Voltammetry of Surface-Confined Molecules. *Langmuir* 31(17):4996-5004.

29. Léger C, Jones AK, Albracht SPJ, & Armstrong FA (2002) Effect of a Dispersion of Interfacial Electron Transfer Rates on Steady State Catalytic Electron Transport in [NiFe]-hydrogenase and Other Enzymes. *The Journal of Physical Chemistry B* 106(50):13058-13063.

30. Raghavan R & Dryhurst G (1981) Redox chemistry of reduced pterin species. *J Electroanal Chem Interfacial Electrochem* 129(1–2):189-212.

31. Jacques JGJ, *et al.* (2014) Reductive activation in periplasmic nitrate reductase involves chemical modifications of the Mo-cofactor beyond the first coordination sphere of the metal ion. *Biochim Biophys Acta* 1837(2):277-286.

32. Fleming BD, Barlow NL, Zhang J, Bond AM, & Armstrong FA (2006) Application of Power Spectra Patterns in Fourier Transform Square Wave Voltammetry To Evaluate Electrode Kinetics of Surface-Confined Proteins. *Anal Chem* 78(9):2948-2956.

33. Fleming BD, Zhang J, Elton D, & Bond AM (2007) Detailed Analysis of the Electron-Transfer Properties of Azurin Adsorbed on Graphite Electrodes Using dc and Large-Amplitude Fourier Transformed ac Voltammetry. *Anal Chem* 79(17):6515-6526.

34. Lee C-Y, *et al.* (2011) Theoretical and experimental investigation of surface-confined two-center metalloproteins by large-amplitude Fourier transformed ac voltammetry. *J Electroanal Chem* 656(1–2):293-303.

35. Kennedy G (2012) Monash Electrochemistry Simulator (MECSim). Available at www.garethkennedy.net/MECSim.html. Accessed January 29, 2015.

Supporting Information for "Electrochemical Evidence that Pyranopterin Redox Chemistry Controls the Catalysis of YedY, a Mononuclear Mo Enzyme"

Short title: FTacV of YedY: Pyranopterin Redox Chemistry

Hope Adamson[a], Alexandr N. Simonov[b], Michelina Kierzek[c], Richard Rothery[c], Joel H. Weiner[c], Alan M. Bond[b], and Alison Parkin[a,1]

[a]Department of Chemistry, University of York, Heslington, York YO10 5DD, United Kingdom; [b]School of Chemistry, Monash University, Clayton, Victoria 3800, Australia; and [c]Department of Biochemistry, 474 Medical Science Building, University of Alberta, Edmonton, Alberta T6G 2H7, Canada

1. YedY is confined to the surface of the graphite electrode

Figure S1 depicts the linear relationship between dcV baseline-corrected peak current, I_P, and scan rate for the YedY-redox signals centred at approximately +170 mV (Figure A) and -250 mV (Figure B). This linear correlation proves that the electrochemical signals arise from surface-confined enzyme rather than solution electrochemistry (1, 2).
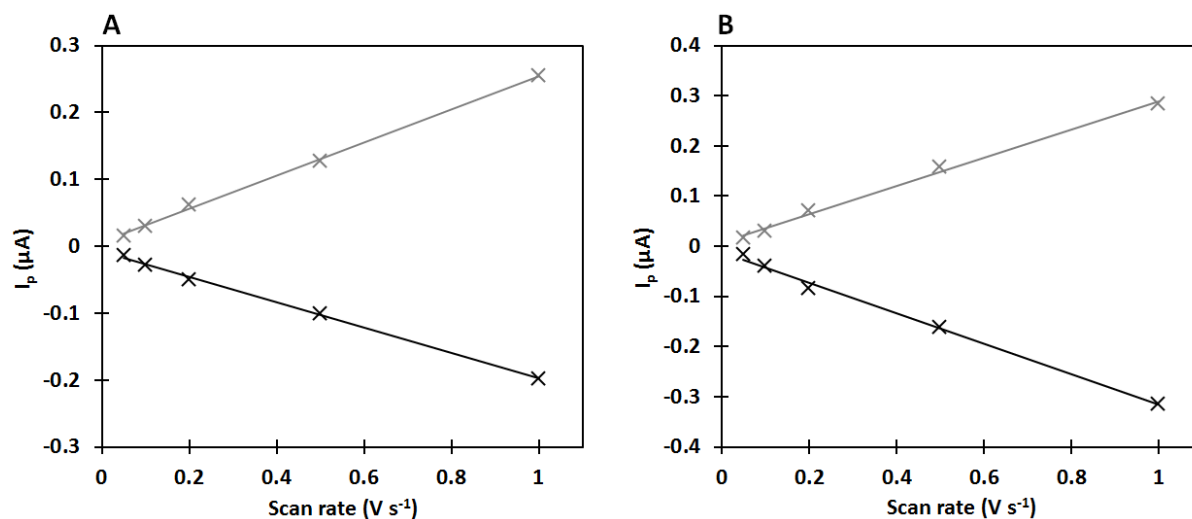
Figure S1: Dependence of YedY oxidative (gray) and reductive (black) baseline subtracted dcV peak currents with scan rate for (A) Faradaic peak current at approximately +170 mV and (B) Faradaic peak current at approximately -250 mV. Data from experiments measured at 25°C in a pH 7 buffer solution of 50 mM MES and 2 M NaCl.

2. Direct current voltammetry measurements over narrower ranges and at different pH values

The background subtraction of direct current voltammetry (dcV) measurements is more accurate over smaller potential ranges so as well as analysing YedY over a wide potential range (Fig. 2A and Fig. S1A), each redox transition was studied separately, as shown in Fig. S2B and S2C.

Over all the voltage ranges studied, "blank" (enzyme-free) control experiments confirmed the absence of Faradaic redox processes arising from the bare electrode. However, a simple subtraction of this "blank" data from the enzyme-electrode voltammetry could not be carried out because adsorbing enzyme caused a slight change in capacitive response as well as giving rise to substantial Faradaic signals. Instead, background subtraction was achieved by fitting a polynomial function to the current either side of the Faradaic response in order to extrapolate the baseline. In Fig. 2A, Fig. S2 and Fig. S4 dashed lines are used to show polynomial "baselines".

The baseline subtracted signals were simulated using Equation S1 which describes a positive (oxidative sweep) or negative (reductive sweep) peak-shaped current, symmetrical around E^0 (3). An empirical measure of electron-transfer cooperativity is given by the value of n_{app}, the apparent number of electrons, while n_s represents the stoichiometric number of electrons. The other equation parameters are: v, the scan rate; Γ, the surface concentration; A, the electrode area; E, the applied potential; all other symbols have their usual meaning (3).

$$i = \pm \frac{n_s n_{app} F^2 v A \Gamma}{RT} \frac{exp\{n_{app}F(E - E_p)/RT\}}{\left(1 + exp\{n_{app}F(E - E_p)/RT\}\right)^2} \qquad S1$$

Midpoint potentials, denoted E_m, are calculated by averaging the E_p (peak potential) value used to fit the peak in the oxidative sweep and the E_p value used to fit the peak in the reductive sweep of the voltammogram. As shown by the black dashed line in Fig. S2B the redox transition measured for YedY at positive potential is well modelled by a Nernstian $n_{app} = 1.01 \pm 0.05$, $n_s = 1$ process (equivalent to a peak width at half height, δ, of 90 mV) with a pH 7 mid-point potential $E_{m, 7} = +174 \pm 4$ mV. We attribute this process to the Mo(V/IV) redox transition.

Figure S2C shows that YedY's negative potential redox process is best fit to Equation S1 with phenomenological values of n_{app} = 1.35 ± 0.06, n_s = 2 (equivalent to δ = 67 mV) and $E_{m, 7}$ = −248 ± 1 mV. This suggests a cooperative, non-simultaneous two electron charge transfer process, i.e. one electron is transferred and then a second electron follows onto the same centre (3-6). This is the first observation of such a transition in YedY.

Figure S2D summarises the results obtained from analysing experiments conducted at different pH and is a duplication of Fig 2B.
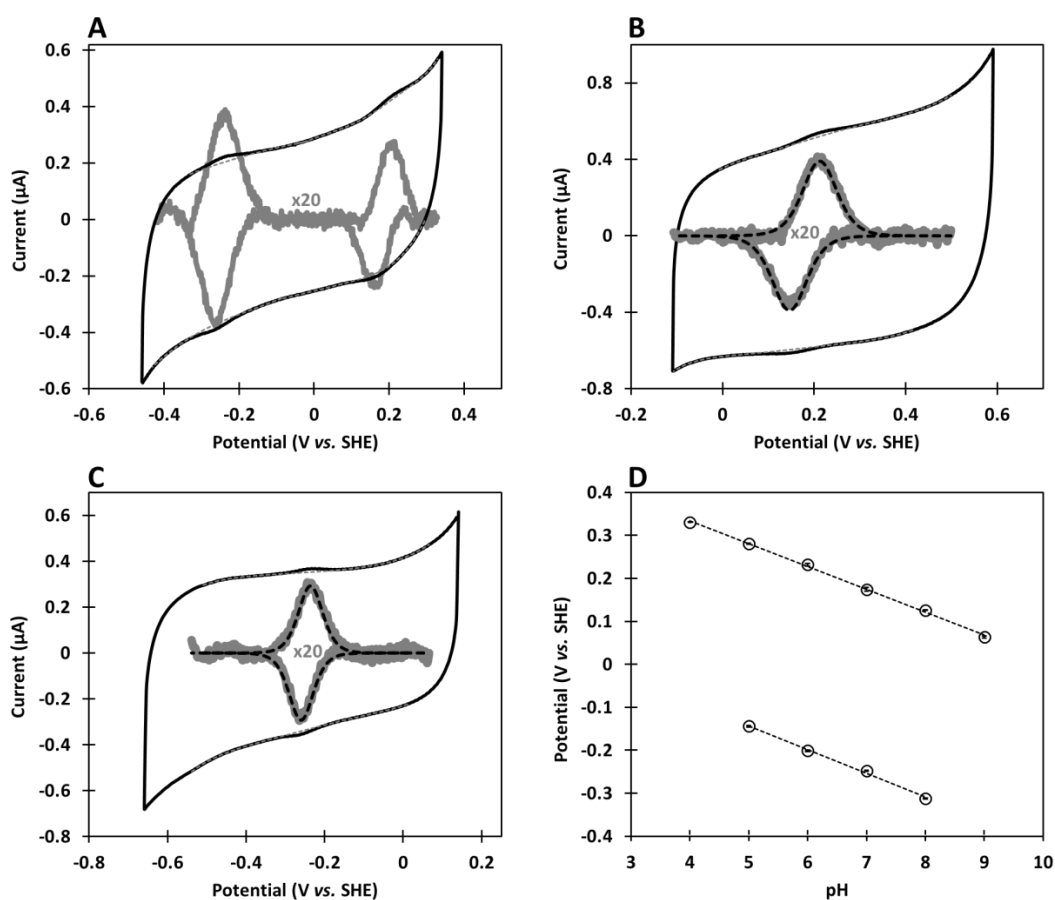
Figure S2: Redox transitions of YedY measured by dcV at a scan rate of 100 mV s^{-1}. (A-C) Cyclic voltammograms of YedY measured over different potential ranges are shown by black solid lines. The baselines are shown by the gray dashed lines, the baseline subtracted signals (scaled by a multiplication factor of 20) are depicted by the gray solid lines and the fit to Equation S1 (also x20) is overlaid as a black dashed line. Other conditions: stationary electrode, buffer solution of 50 mM MES, pH 7 and temperature 25°C. **(D)** pH dependence of E_m potentials derived from using Equation S1 to fit to experimental data as for A-C, except buffer solution is changed according to pH: 50 mM acetate (pH 4 and 5), 50 mM MES (pH 6 and 7) and 50 mM Tris (pH 8 and 9). Error bars shown within data point circles reflect the standard error calculated from at least 3 repeat experiments.

3. Spectroelectrochemistry of YedY

UV-vis spectra (Fig. S3) were measured using a Hitachi U-1900 spectrophotometer in conjunction with a BASi quartz spectroelectrochemical cell of path length 1 mm containing 300 μL of YedY solution and gold mesh working, platinum wire counter and Ag/AgCl (3 M NaCl) reference electrodes. The potential was controlled by an Ivium CompactStat potentiostat and all spectroelectrochemistry potentials have been converted to the SHE scale using the correction +210 mV at 25°C (2). The cell atmosphere was continuously purged with Ar.
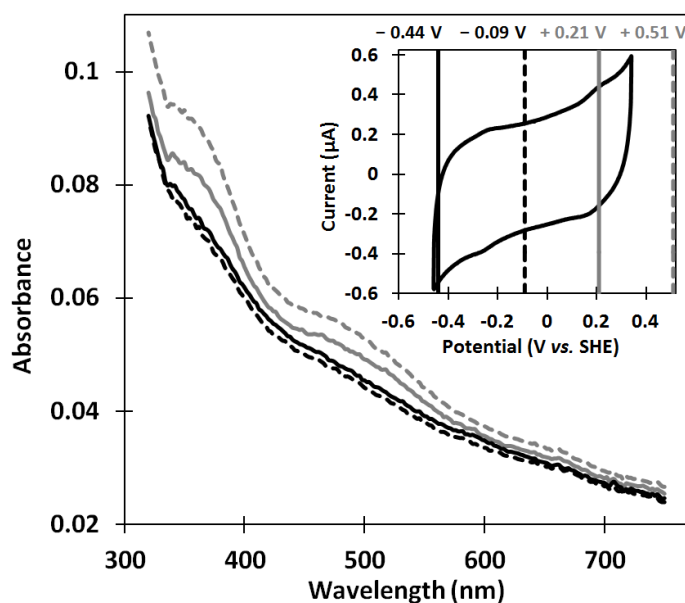
Figure S3: UV-vis spectroelectrochemistry of 5.3 mg mL^{-1} YedY. The UV-vis spectrum of enzyme solution poised at potentials of +0.51 V (gray dashed line), +0.21 V (gray solid line), −0.09 V (black dashed line) and −0.44 V (black solid line). Other conditions: buffer solution of 20 mM MOPS buffer, pH 7, room temperature, Ar atmosphere. **(Inset)** A dcV of YedY at a scan rate of 100 mVs^{-1} in buffer solution of 50mM MES, pH 7, 25°C, N$_2$ atmosphere. The voltammogram is annotated with vertical lines to indicate the potentials used for spectroelectrochemistry.

4. YedY Mo(VI) state is inaccessible in protein film electrochemistry experiments

Figure S4 shows that when the electrode potential was swept between +0.11 and +0.74 V at 100 mVs^{-1} in pH 7 experiments it was not possible to observe any Faradaic signals which would indicate oxidation of the YedY Mo(V) state to generate Mo(VI). Solution breakdown at more positive potentials makes it impossible to probe more positive voltages. The only observable redox process was the one-electron signal centred at around +174 mV which we have assigned to the Mo(V/IV)-transition based on comparison with YedY EPR data (7) and our own UV-vis measurements.
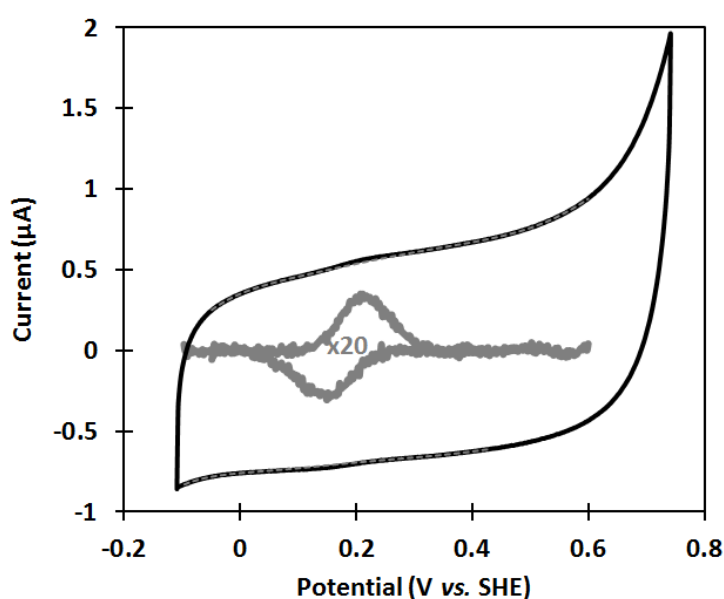
Figure S4: Cyclic voltammogram measured for YedY adsorbed onto a graphite electrode at positive potentials. The potential is swept from +109 to +741 mV and back at a scan rate of 100 mVs^{-1} (solid black line). The simulated enzyme-free baseline is depicted by a gray dashed line; the solid gray lines show the result of subtracting the baseline and multiplying the resultant current by 20. Other conditions: buffer solution of 50 mM MES, pH 7; 25°C.

5. YedY dcV peak potential versus scan rate "trumpet plot"

Figure S5 shows how the potential of the baseline-corrected peak current changes as a function of scan rate for both the high potential (centred at +174 mV) and low potential (centred at -248 mV) YedY redox transitions. The data are extracted from dcVs and for each redox transition there are two data points at each scan rate because the potential of the peak current is more positive during the oxidative "sweep" of the voltammogram (gray data points) compared to the reductive potential sweep (black data points). The name "trumpet plots" is used to describe such graphs because at higher scan rates there is an increasing divergence between the potentials measured in the oxidising and reducing scan sweeps. For YedY this divergence is much more pronounced for the positive potential process, ascribed to a $1e^-/1H^+$ Mo(V/IV) redox transition, compared to the $2e^-/2H^{+-}$ transition at negative potential and we can therefore conclude that the rate of electron transfer is faster for the redox reaction which occurs at negative potential (8).
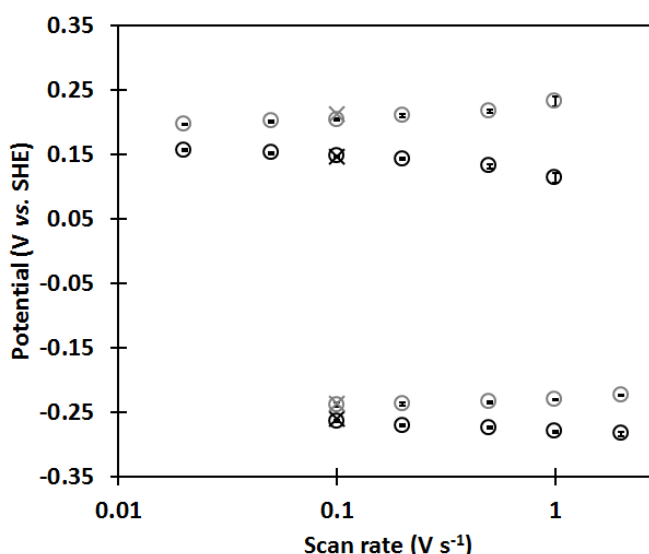
Figure S5: YedY trumpet plot of peak potentials *vs.* scan rate. High salt (2 M NaCl) measurements of oxidative and reductive baseline subtracted peak potentials are depicted by gray and black circles, respectively, and error bars quantifying the standard error from at least 3 repeat experiments are shown within data point circles. NaCl-free measurements of oxidative and reductive baseline subtracted peak potentials at 100 mVs^{-1} are depicted by gray and black crosses. Other conditions: 50 mM MES, pH 7, 25°C.

When measuring trumpet plot data it is essential to use high concentrations of electrolyte to ensure that the measurements at fast scan rates are not significantly perturbed by uncompensated resistance. To confirm that the redox chemistry of the enzyme was unaffected by the addition of large amounts of

NaCl, control data were measured at slow scan rate (100 mVs^{-1}) in both 2 M NaCl (circle data points) and NaCl-free conditions (cross data points). Within the circle data points the vertical bar represents standard error calculated from at least three repeat experiments.

6. FTacV measurement of YedY over a wide potential range

Figure S6 shows an FTacV measurement of YedY analogous to the dcV experiment showed in Fig. 2.
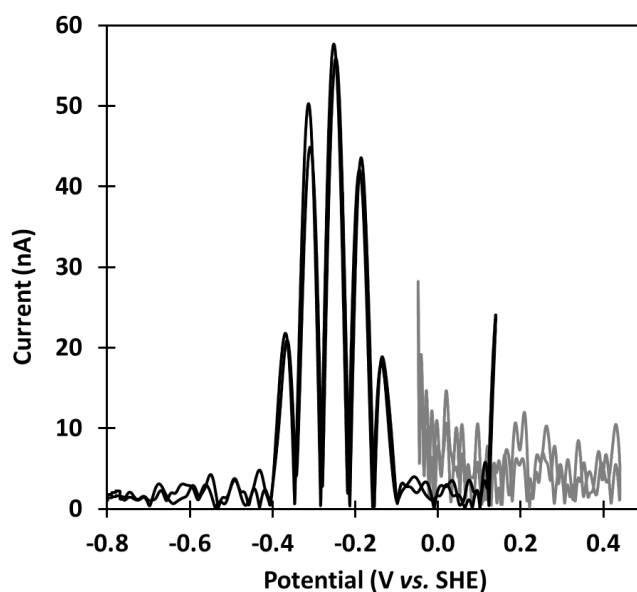
Figure S6: FTacV measurement of all the non-catalytic redox transitions of YedY. 7th ac harmonic response measured for YedY using FTacV with a frequency of 9 Hz, over a positive (gray) and negative (black) potential range. Other experimental conditions: scan rate 15.83 mVs^{-1}, amplitude 150 mV, buffer solution of 50 mM MES and 2 M NaCl, pH 7, 25°C.

7. dcV measurements of YedY-catalysed reduction of dimethyl sulfoxide

Figure S7 shows dcV measurements of YedY-catalysed dimethyl sulfoxide (DMSO) reduction at pH 8 and pH 5, with a DMSO substrate concentration of 200 mM. Vertical lines show the midpoint redox potentials, E_m, measured for the negative potential YedY redox transition in non-catalytic dcV experiments at these pH values (data taken from Fig. 2B/Fig S2D).
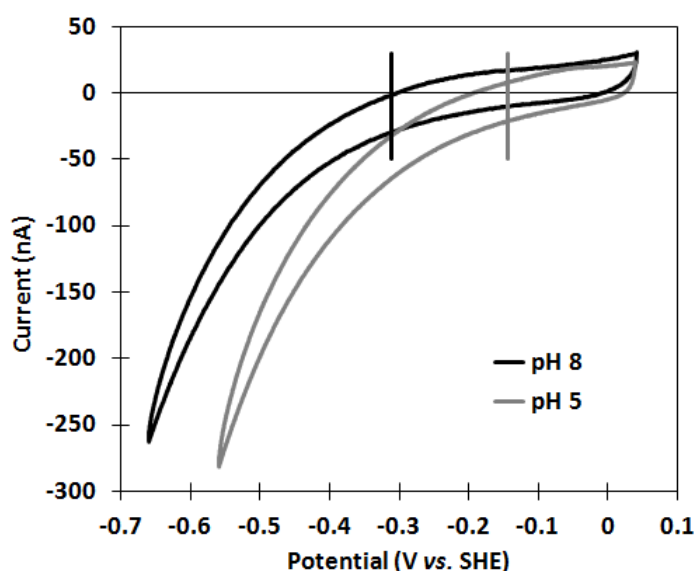
Figure S7: pH dependence of YedY-catalysed DMSO reduction measured using dcV. In the presence of 200 mM DMSO, the electrode potential was decreased from +41 mV to −659 mV (pH 8, black line) or −559 mV (pH 5, gray line) and then swept back at a scan rate of 5 mV s^{-1} and with electrode rotation of 500 rpm. Vertical lines show midpoint redox potential data taken from Figure 2D. Other conditions: buffer solution of 50 mM Tris (pH 8) or 50 mM acetate (pH 5) and temperature 25°C.

Figure S8 shows dcV measurements made at different concentrations of DMSO; both YedY measurements and bare-electrode control data is shown, confirming that no DMSO reduction is observed in the absence of YedY. The electrochemical catalysis measurements can be validated by comparison to published solution assay data; this confirms the structural and catalytic integrity of YedY adsorbed on the electrode surface. First, the K_M for DMSO reduction was determined by analysing the catalytic current as a function of substrate concentration at -359 mV, the reduction potential of benzyl viologen. As shown in the inset to Fig. S8, such analysis yielded $K_M = 35 \pm 5$ mM at pH 7, 25 °C and this compares well to the published range of K_M values, 12 mM to 261 mM at pH 6-7 (9-11). Secondly, the k_{cat} value for YedY catalysed DMSO reduction was calculated using Equation S2 where i_{cat} is the catalytic current, n is the number of electrons involved in catalysis (two for DMSO reduction), F is the Faraday

constant, A is the electrode surface area and Γ denotes the electroactive surface concentration of the enzyme on the electrode.

$$i_{cat} = k_{cat}nFA\Gamma \qquad\qquad Equation\ S2$$

Fitting the data shown in Fig. S2C to Equation S1 gave Γ values of 2 pmol cm^{-2}, assuming a geometric electrode surface area of 0.03 cm^2. This is a submonolayer of enzyme, assuming an enzyme footprint of approximately 12.5 nm^2 (12). In conjunction with the catalytic current in 200 mM DMSO this gives k_{cat} = 4.2 ± 0.9 s^{-1} at −359 mV, pH 7, 25 °C which is close to the published value of k_{cat} = 4.83 s^{-1} at pH 7 (9). Finally, in accordance with solution assays (10), the electrochemical activity of YedY at −359 mV also increases at lower pH (Fig. S5).
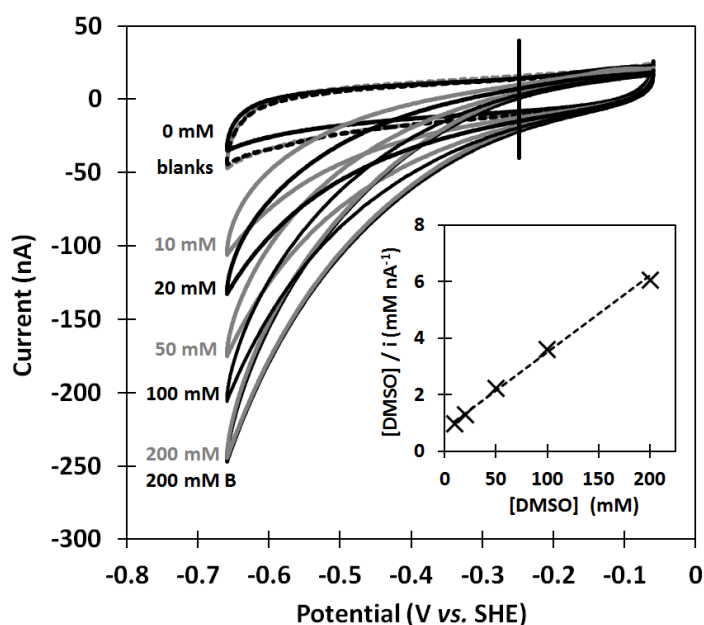
Figure S8: dcV measurement of YedY-catalysed DMSO reduction at pH 7. The electrode potential was swept from −59 mV to −659 mV and back at a rate of 5 mV s^{-1} with an electrode rotation rate of 500 rpm. The "bare" / "blank" (YedY-free) graphite electrode response under two different DMSO concentrations is shown by dashed lines: black, DMSO-free; gray, 200 mM. Cyclic voltammograms of YedY in the presence of various DMSO concentrations are depicted by solid black and gray lines and substrate concentration is stated in the Figure. The vertical line at -248 mV highlights how the onset potential for catalytic activity correlates with the negative potential redox transition measured in Fig. 2. Other conditions: buffer solution of 50 mM MES, pH 7 and temperature 25°C. **(Inset)** Hanes Woolf plot analysis of K_M at -359 mV. The catalytic current (*i*) was calculated by averaging the current from the forward and back potential sweep in the presence of DMSO and then subtracting the average current from the DMSO-free control. Dashed line shows linear regression fit of data to Michaelis-Menten equation.

8. dcV measurements of YedY-catalysed reduction of trimethylamine N-oxide

YedY-catalysed trimethylamine N-oxide (TMAO) reduction at pH 7 is depicted in Figure S9 which compares the dcV response of a "blank" graphite electrode in the presence and absence of TMAO (solid lines) to the response of a graphite electrode with YedY adsorbed (dashed lines).
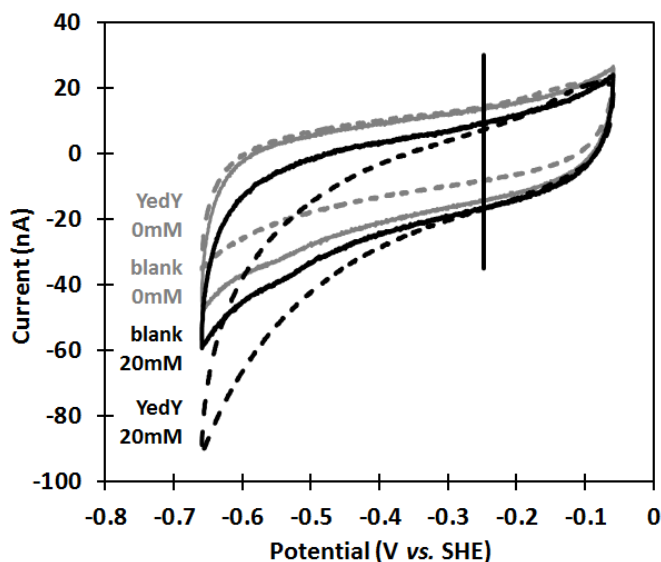
Figure S9: YedY-catalysed TMAO reduction at pH 7 measured using dcV. The electrode potential was swept from −59 mV to −659 mV and back at a scan rate of 5 mV s^{-1} and with an electrode rotation rate of 500 rpm. Dashed lines show activity from a YedY-modified electrode while solid lines show the response for a "bare"/"blank" (YedY-free) graphite electrode; line colour indicates the different TMAO concentrations: gray, TMAO-free; black, 20 mM. The vertical line at -248 mV highlights how the onset potential for catalytic activity correlates with the negative potential redox transition measured in Figure 2. Other conditions: buffer solution of 50 mM MES, pH 7 and temperature 25°C.

9. Simulation mechanism

The negative potential electron transfer process for the enzyme (now designated Enz) corresponds to an overall two-electron two-proton reaction as in Equation S3.

$$Enz + 2H^+ + 2e^- \rightleftharpoons [Enz - 2H] \tag{S3}$$

This overall reaction can be rewritten in terms of two single one-electron one-proton reactions.

$$Enz + H^+ + e^- \rightleftharpoons [Enz - H] \tag{S4}$$

$$[Enz - H] + H^+ + e^- \rightleftharpoons [Enz - 2H] \tag{S5}$$
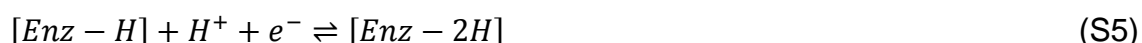
In turn, each of these reactions can be written in terms of separate electron transfer and proton transfer steps, with reversible potential E_n^0 and acidity constants pK_n, respectively.

$$Enz + e^- \rightleftharpoons Enz^- \qquad\qquad Reversible\ potential\ E_1^0 \tag{S6a}$$

$$Enz^- + H^+ \rightleftharpoons [Enz - H] \qquad\qquad Acidity\ constant\ pK_1 \tag{S6b}$$

$$[Enz - H] + e^- \rightleftharpoons [Enz - H]^- \qquad Reversible\ potential\ E_2^0 \tag{S7a}$$

$$[Enz - H]^- + H^+ \rightleftharpoons [Enz - 2H] \qquad Acidity\ constant\ pK_2 \tag{S7b}$$
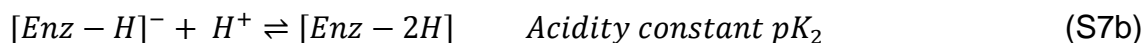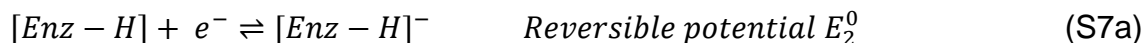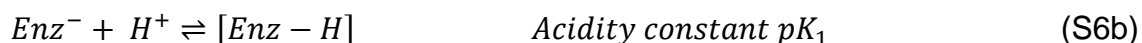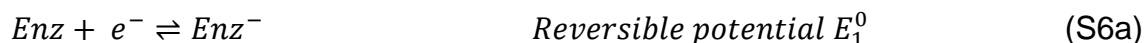
Assuming that the acid-base equilibria are diffusion controlled processes and are chemically reversible under the relevant voltammetric conditions, the electron transfer processes can be treated as the simple reactions S8-S9 with apparent reversible potentials $(E_n^0)_{app}$ defined by the E_n^0 and pK_n terms for reactions S6-S7.

$$Enz + e^- \rightleftharpoons Enz^- \qquad\qquad (E_1^0)_{app} \tag{S8}$$

$$Enz^- + e^- \rightleftharpoons Enz^{2-} \qquad\qquad (E_2^0)_{app} \tag{S9}$$
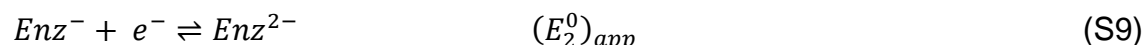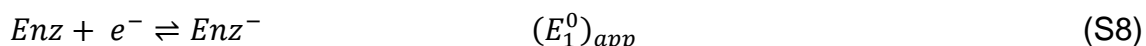
In terms of electrode kinetics, and assuming the Butler-Volmer theory applies with $(k_n^0)_{app}$ being the apparent values of the heterogeneous charge transfer rate constant and $(E_n^0)_{app}$ and $(\alpha_n^0)_{app}$ being the apparent charge transfer coefficient, allows the theory for dc and FTacV to be solved as detailed previously (6). Apart from the effects of $(k_n^0)_{app}$, $(\alpha_n)_{app}$ and R_u, the ac signal

shape and other characteristics are to a great extent governed by the relative values of $(E_1^0)_{app}$ and $(E_2^0)_{app}$ (13, 14). There are 3 limiting cases: (a) if $(E_2^0)_{app}$ is considerably more negative than $(E_1^0)_{app}$ then two well-resolved sequential one-electron reduction processes may be observed; (b) If $(E_1^0)_{app} = (E_2^0)_{app}$ then a single broad process will be detected; (c) if $(E_2^0)_{app}$ is considerably more positive than $(E_1^0)_{app}$, then a single process with the characteristics of a simultaneous two electron reaction will be observed. The $(E^0)_{app}$ values are not likely to cross over from normal order (case (a)) to give case (c) if the pK_2 is greater than pK_1.

The details of the various possible scenarios and how they gave rise to the signals described are explained in reference (6) and the interested reader can refer to this paper and references contained therein for more information. The assumption is made at this time that all enzymes have the same $(E_n^0)_{app}$, $(k_n^0)_{app}$ and $(\alpha_n)_{app}$ values, they do not interact with each other and that Butler-Volmer kinetic model applies.

10. FTacV data cannot be simulated using a 1e⁻transfer mechanism

Figure 3 of the paper demonstrates that the higher harmonic FTacV signals recorded for the $E_{m,\,7}$ = -248 mV YedY redox transition can be well simulated using a 1e⁻ + 1e⁻ mechanism. Using the same model parameters for each harmonic, including dcV measured values for enzyme surface concentration (Γ) and heuristically determined heterogeneous electron transfer rate constants (k^0_{app}), the simulation data accurately fits the 7th to 10th ac harmonic experimental data, matching both the current amplitude and the signal width. In contrast, Figure S10 shows that a simpler 1e⁻ transfer mechanism fails to simulate (black dashed lines) the 7th to 10th harmonic experimental data (gray solid lines) when (A) the Γ and k^0_{app} values are the same as for the 1e⁻ + 1e⁻ simulation, or (B) Γ values are nearly doubled. In Figure S10A the magnitude of the simulated current is too small across all harmonic components whereas in Figure S10B (using a physically unrealistic Γ value), the simulated current amplitudes are too low in higher (9th and above) harmonics. It is therefore concluded that, as suggested by dcV measurements, the negative potential redox transition of YedY involves transfer of 2e⁻, not 1e⁻.
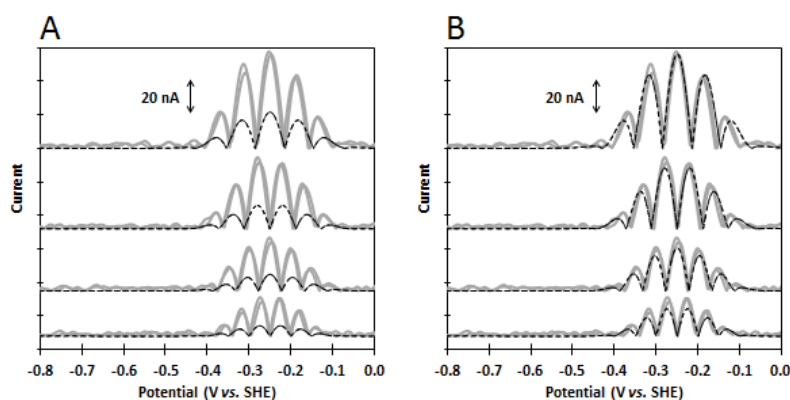
Figure S10: Simulations of a 1e⁻ redox reaction do not provide a good fit to the 7th, 8th, 9th and 10th harmonics of an experimental 9 Hz YedY FTacV signal (gray solid lines with harmonics in descending order, 7th top and 10th bottom). Black dashed lines depict simulated data for a 1e⁻ mechanism with parameters E^0_{app} = -250 mV, k^0_{app} = 2.0·10⁴ s⁻¹, R_u = 50 Ω, polynomial capacitance and **(A)** Γ = 1.15 pmol cm⁻² or **(B)** Γ = 3 pmol cm⁻². Other experimental conditions: scan rate 15.83 mV s⁻¹, amplitude 150 mV, buffer solution of 50 mM MES and 2 M NaCl, pH 7, 25°C.

11. FTacV data cannot be simulated using a simultaneous 2e⁻ transfer mechanism

In addition to the stepwise 1e⁻ + 1e⁻ mechanism used to simulate the FTacV data in Figure 3, the possibility that two electrons are transferred in a simultaneous fashion was also explored. Figure S11 shows that a 2e⁻ transfer mechanism fails to simulate (black dashed lines) the 7th to 10th harmonic experimental data (gray solid lines) when (A) the Γ and k^0_{app} values are the same as for the 1e⁻ + 1e⁻ simulation, or (B) Γ values are decreased by almost a third, or (C) k^0_{app} is decreased 1000-fold. Decreasing the electron transfer rate is particularly unrealistic because signals are observed in very high frequency (519 Hz) experiments, and it is notable that when k^0_{app} is lowered to try and make simulated data fit experimental measurements Γ must also be lowered by 40% (Figure S11C). In Figure S11A the simulated ac current magnitude is too large across all harmonic components whereas in Figure S11B (using a physically unrealistic Γ value), the simulated current amplitudes are too large in higher ac harmonics, and in Figure S11C (using a very low k^0_{app} and a significantly decreased Γ), the signal shapes are completely wrong. It is therefore concluded that the negative potential redox transition of YedY involves stepwise, not simultaneous, 2e⁻ transfer.
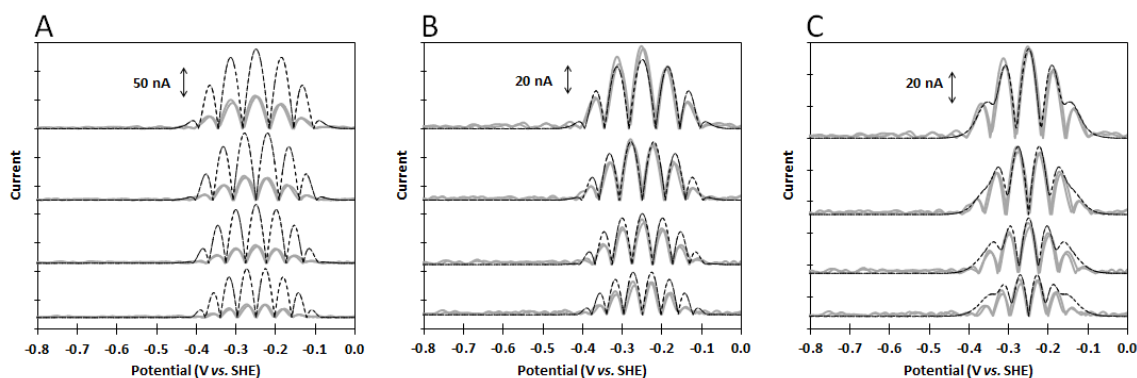
Figure S11: Simulations of a simultaneous 2e⁻ redox reaction do not provide a good fit to the 7th, 8th, 9th and 10th ac harmonics of an experimental 9 Hz YedY FTacV signal (gray solid lines with harmonics in descending order, 7th top and 10th bottom). Black dashed lines depict simulated data for a 2e⁻ mechanism with parameters E^0_{app} = −250 mV, R_u = 50 Ω, polynomial capacitance and **(A)** k^0_{app} = 2.0·10^4 s^{-1}, Γ = 1.15 pmol cm^{-2}; **(B)** k^0_{app} = 2·10^4 s^{-1}, Γ = 0.4 pmol cm^{-2}; **(C)** k^0_{app} = 20 s^{-1}, Γ = 0.7 pmol cm^{-2}. Other experimental conditions: scan rate 15.83 mV s^{-1}, amplitude 150 mV, buffer solution of 50 mM MES and 2 M NaCl, pH 7, 25°C.

12. Simulations of FTacV experiments at different frequencies suggests dispersion

Figures S12A-H depict experimental (gray solid lines) and simulated (black dashed lines) data for YedY FTacV experiments conducted at different frequencies. In Figures S12A to H, the only simulation parameter varied is the apparent surface coverage of the enzyme, Γ_{app}, with Figure S12I summarising these changes. Kinetic dispersion, meaning that different enzyme orientations on the electrode surface have different electron transfer rates ($(k^0_1)_{app}$ and $(k^0_2)_{app}$), is believed to be the major reason that Γ_{app} decreases as the frequency increases (15).
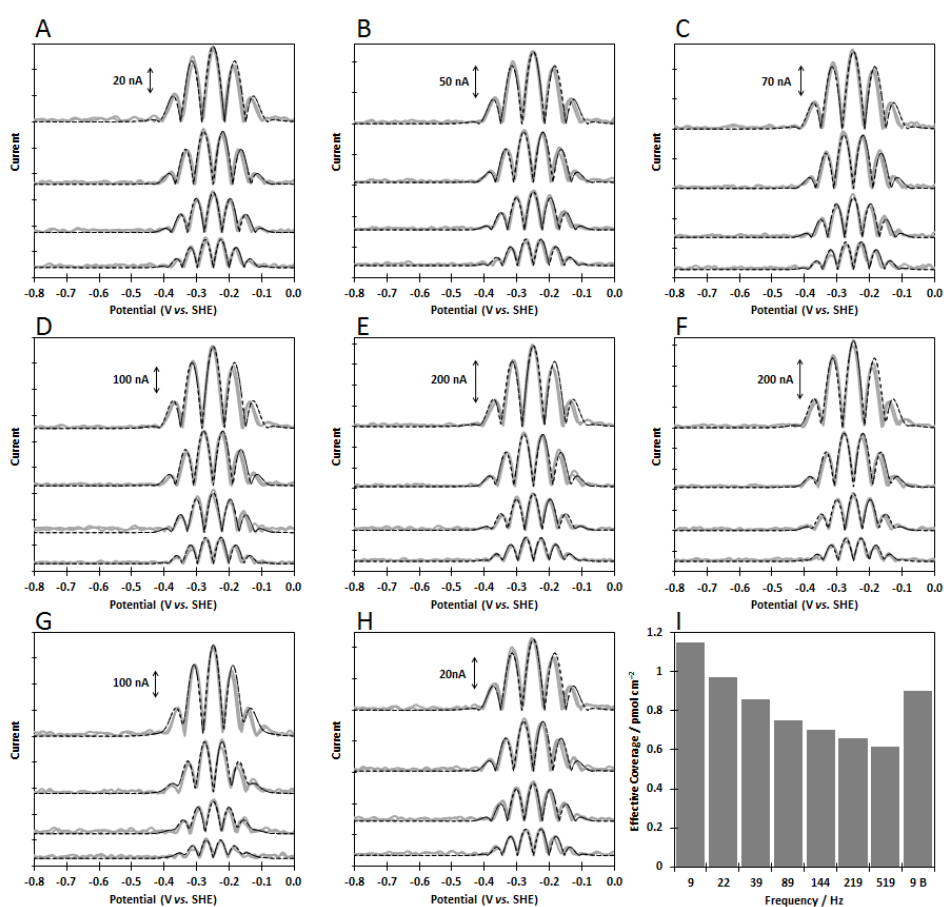
Figure S12: Simulations of YedY FTacV experiments at different frequencies. (A-H) Dark gray lines show, in descending order, the 7th, 8th, 9th and 10th harmonic components of FTacVs measured for YedY with a frequency of **(A)** 9 Hz, first run; **(B)** 22 Hz; **(C)** 39 Hz; **(D)** 89 Hz; **(E)** 144 Hz; **(F)** 219 Hz; **(G)** 519 Hz; **(H)** 9 Hz, second run (to assess if enzyme desorption occurs). Black dashed lines depict simulated data for a 1e⁻ + 1e⁻ mechanism with parameters $(E^0_1)_{app}$ = -239 mV, $(E^0_2)_{app}$ = -261 mV, $(k^0_1)_{app}$ = $(k^0_2)_{app}$ = 2·10⁴ s⁻¹, R_u = 50 Ω, polynomial capacitance and (A, 9 Hz run 1) Γ_{app} = 1.15 pmol cm⁻²; (B, 22Hz) Γ_{app} = 0.97 pmol cm⁻²; (C, 39 Hz) Γ_{app} = 0.86 pmol cm⁻²; (D, 89 Hz) Γ_{app} = 0.75 pmol cm⁻²; (E, 144 Hz) Γ_{app} = 0.7 pmol cm⁻²; (F, 219 Hz) Γ_{app} = 0.66 pmol cm⁻²; (G, 519 Hz) Γ_{app} = 0.615 pmol cm⁻²; (H, 9 Hz run 2) Γ_{app} = 0.9 pmol cm⁻². **(I)** Summary of changes in the Γ_{app} values used for simulations. Other experimental conditions: scan rate 15.83 mV s⁻¹, amplitude 150 mV, buffer solution of 50 mM MES and 2 M NaCl, pH 7, 25°C.

References

1.   Léger C & Bertrand P (2008) Direct Electrochemistry of Redox Enzymes as a Tool for Mechanistic Studies. *Chem Rev* 108(7):2379-2438.

2.   Bard AJ & Faulkner LR (2010) *Electrochemical Methods: Fundamentals and Applications, 2nd Edition* (Wiley).

3.   Heering HA, Weiner JH, & Armstrong FA (1997) Direct Detection and Measurement of Electron Relays in a Multicentered Enzyme: Voltammetry of Electrode-Surface Films of *E. coli* Fumarate Reductase, an Iron−Sulfur Flavoprotein. *J Am Chem Soc* 119(48):11628-11638.

4.   Hudson JM*, et al.* (2005) Electron Transfer and Catalytic Control by the Iron−Sulfur Clusters in a Respiratory Enzyme, *E. coli* Fumarate Reductase. *J Am Chem Soc* 127(19):6977-6989.

5.   Hirst J (2006) Elucidating the mechanisms of coupled electron transfer and catalytic reactions by protein film voltammetry. *Biochim Biophys Acta* 1757(4):225-239.

6.   Stevenson GP*, et al.* (2012) Theoretical Analysis of the Two-Electron Transfer Reaction and Experimental Studies with Surface-Confined Cytochrome c Peroxidase Using Large-Amplitude Fourier Transformed AC Voltammetry. *Langmuir* 28(25):9864-9877.

7.   Brokx SJ, Rothery RA, Zhang G, Ng DP, & Weiner JH (2005) Characterization of an *Escherichia coli* Sulfite Oxidase Homologue Reveals the Role of a Conserved Active Site Cysteine in Assembly and Function. *Biochemistry* 44(30):10339-10348.

8.   Armstrong FA*, et al.* (2000) Fast voltammetric studies of the kinetics and energetics of coupled electron-transfer reactions in proteins. *Faraday Discuss* 116(0):191-203.

9.   Loschi L*, et al.* (2004) Structural and Biochemical Identification of a Novel Bacterial Oxidoreductase. *J Biol Chem* 279(48):50391-50400.

10.   Havelius KGV*, et al.* (2010) Structure of the Molybdenum Site in YedY, a Sulfite Oxidase Homologue from *Escherichia coli*. *Inorg Chem* 50(3):741-748.

11.   Sabaty M*, et al.* (2013) Detrimental effect of the 6 His C-terminal tag on YedY enzymatic activity and influence of the TAT signal sequence on YedY synthesis. *BMC Biochem* 14(1):1-12.

12. YedY radius is approximately 2 nm based on pdb file 1XDQ. Assuming a circular footprint, the enzyme area is therefore 1.25×10^{-13} cm^2 so a monolayer would have coverage 13 pmol cm^{-2}.

13. Lee C-Y*, et al.* (2011) Theoretical and experimental investigation of surface-confined two-center metalloproteins by large-amplitude Fourier transformed ac voltammetry. *J Electroanal Chem* 656(1–2):293-303.

14. Simonov AN*, et al.* (2014) New Insights into the Analysis of the Electrode Kinetics of Flavin Adenine Dinucleotide Redox Center of Glucose Oxidase Immobilized on Carbon Electrodes. *Langmuir* 30(11):3264-3273.

15. Morris GP*, et al.* (2015) Theoretical Analysis of the Relative Significance of Thermodynamic and Kinetic Dispersion in the dc and ac Voltammetry of Surface-Confined Molecules. *Langmuir* 31(17):4996-5004.

Chapter 5

Analysis of HypD Disulfide Redox Chemistry via Optimization of Fourier Transformed ac Voltammetric Data

Declaration

I designed the research with Dr Alison Parkin (University of York) and performed all electrochemical experiments. Dr Basem Soboh purified the HypD protein in the lab of Prof. Gary Sawers (Martin Luther University Halle-Wittenberg) and Paul Bond (University of York) performed protein structure simulations, in collaborations which I coordinated. Darrell Elton (La Trobe University) and Prof. Alan Bond (Monash University) provided the FTacV instrumentation. I performed initial heuristic simulations, with the advice of Dr Alexandr N. Simonov (Monash University), which informed and guided the data optimisation process. Dr Martin Robinson, alongside Dr Kathryn Gillow and Prof. David Gavaghan (University of Oxford), fully developed and implemented the data optimisation procedures, with some general suggestions from myself, Dr Alison Parkin and Prof. Alan Bond. Prof. Alan Bond also advised on data analysis. All authors contributed to the writing of the paper, which was developed from a complete first draft which I produced, and alongside Dr Alison Parkin, I was the main author of the final version of the introduction, electrochemical and conclusion sections, with Dr Martin Robinson acting as lead author of the data optimisation section.

Signed   Dr. Alison Parkin

Signed   Dr. Martin Robinson

Reference:

Adamson, H., et al., *Analysis of HypD Disulfide Redox Chemistry via Optimization of Fourier Transformed ac Voltammetric Data*. Analytical Chemistry, 2017. **89**(3): p. 1565–1573

Analysis of HypD Disulfide Redox Chemistry via Optimization of Fourier Transformed ac Voltammetric Data

Hope Adamson,[‡,1] Martin Robinson,[‡,2] Paul S. Bond,[1] Basem Soboh,[3] Kathryn Gillow,[4] Alexandr N. Simonov,[5] Darrell M. Elton,[6] Alan M. Bond,[5] R. Gary Sawers,[7] David J. Gavaghan,*[,2] Alison Parkin*[,1]

[1]Department of Chemistry, University of York, Heslington, York, YO10 5DD, United Kingdom

[2]Department of Computer Science, University of Oxford, Wolfson Building, Parks Road, Oxford, OX1 3QD, United Kingdom

[3]Experimental Molecular Biophysics, Freie Universität Berlin, Arnimalle 14, 14195 Berlin, Germany

[4]Mathematical Institute, Andrew Wiles Building, University of Oxford, Radcliffe Observatory Quarter, Woodstock Road, Oxford, OX2 6GG, United Kingdom

[5]School of Chemistry and the ARC Centre of Excellence for Electromaterials Science, Monash University, Clayton, Victoria 3800, Australia

[6]School of Engineering and Mathematical Sciences, La Trobe University, Bundoora, Victoria 3086, Australia

[7]Institute for Biology/Microbiology, Martin Luther University Halle-Wittenberg, Halle (Saale), Germany

*E-mail: david.gavaghan@cs.ox.ac.uk, fax: +44 1865 283532; e-mail: alison.parkin@york.ac.uk, fax +44 1904 322516

†Author Contributions
These authors contributed equally to the experimental work

Abstract

Rapid disulfide bond formation and cleavage is an essential mechanism of life. Using large amplitude Fourier transformed alternating current voltammetry (FTacV) we have measured previously uncharacterized disulfide bond redox chemistry in *Escherichia coli* HypD. This protein is representative of a class of assembly proteins that play an essential role in the biosynthesis of the active site of [NiFe]-hydrogenases, a family of H_2-activating enzymes. Compared to conventional electrochemical methods, the advantages of the FTacV technique are the high resolution of the Faradaic signal in the higher order harmonics and the fact that a single electrochemical experiment contains all the data needed to estimate the (very fast) electron transfer rates (both rate constants ≥ 4000 s^{-1}) and quantify the energetics of the cysteine disulfide redox-reaction (reversible potentials for both processes approximately -0.21 ± 0.01 V vs SHE at pH 6). Previously, deriving such data depended on an inefficient manual trial-and-error approach to simulation. As a highly advantageous alternative, we describe herein an automated multiparameter data optimization analysis strategy where the simulated and experimental Faradaic current data are compared for both the real and imaginary components in each of the 4th to 12th harmonics after quantifying the charging current data using the time-domain response

Introduction

[NiFe]-hydrogenases are highly efficient and active Pt-free microbial H_2-catalysts that have been used for cofactor regeneration,(1) mixed-feed fuel cells,(2) and solar water splitting.(3) However, commercialization of such technology requires large scale hydrogenase production, a feat which is currently limited by a lack of understanding of how [NiFe]-hydrogenases are constructed in vivo.(4-6) Previous studies of *E. coli* HypD have shown that it is a 42 kDa protein that acts in concert with HypC to provide a scaffold for building the $Fe(CN)_2CO$ component of a [NiFe]-hydrogenase active site.(7-9) While the CN is known to originate from carbamoyl phosphate, identifying the source of the CO ligand is far more complex.(4) Based on sequence alignment and comparison with a known crystal structure for *Thermococcus kodakarensis* (*T. kodakarensis*) HypD,(10) all HypD proteins contain a Fe_4S_4 cluster and at least one disulfide bond. HypD plays an essential role in reductive CN insertion,(7-9) and it has been postulated(11) that redox activity by HypD may also enable the two-electron reduction of CO_2 to CO. This reactivity cannot be simply attributed to the Fe_4S_4 center because EPR and Mössbauer experiments show that this cluster remains in the oxidized $Fe_4S_4^{2+}$ state even upon reaction of the protein with dithionite, indicating that there is no readily accessible $Fe_4S_4^{1+}$ reduced-cluster state.(12) However, disulfide bonds can also be centers for reversible redox reactions in biology (Figure 1). Moreover, deletion of the cysteine (Cys) residues that should form a disulfide bond in *E. coli* HypD (Cys-69 and Cys-72) renders the protein inactive in terms of hydrogenase assembly, suggesting that these residues play an important role.(7, 13) We now probe the redox chemistry of HypD using protein film large amplitude Fourier transformed alternating current voltammetry (PF-FTacV) to analyze previously uncharacterized disulfide redox chemistry.

$$\begin{array}{c} \text{protein} \\ | \quad | \\ \text{S—S} \end{array} + 2e^- + 2H^+ \rightleftharpoons \begin{array}{c} \text{protein} \\ | \quad | \\ \text{SH SH} \end{array}$$
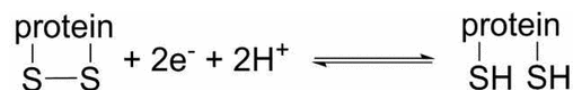
Figure 1. Redox reaction for disulfide bond cleavage/formation within a protein.

Protein film electrochemistry has previously been used to measure the midpoint potential of disulfide bond redox chemistry in thioredoxins.(14-17) Because direct-current voltammetric (dcV) measurements were used, a background subtraction method was required to separate the Faradaic (protein) signal from

the dominant capacitive-charging background.(14-17) Such analysis concludes that these protein disulfide redox reactions proceed via two consecutive one-electron steps but extracting the separate redox potentials for each electron transfer is not directly possible using such protein film dcV (PF-dcV) experiments.(14-16) Another limitation of this technique is that a "trumpet plot" kinetic analysis to measure the electron transfer rate cannot be carried out unless large amounts of protein are adsorbed onto the electrode surface, because otherwise, the significant levels of background electrode charging current at fast scan rates effectively mask the Faradaic signals.(18)

In contrast to PF-dcV, PF-FTacV is a technique that provides an essentially background-free measurement of the Faradaic current derived from fast protein redox processes by providing access to fourth and higher order harmonic signals that have negligible capacitive current.(19-23) The detection sensitivity for PF-FTacV is therefore much higher than that available in dc experiments. From a single PF-FTacV experiment, the position of the higher order harmonic signals gives an estimate of the midpoint potential, while a full evaluation of the kinetics (rate of redox reaction) and thermodynamics (reversible potentials) is provided from simulation versus experiment comparisons.(24) Previously, a limitation in the PF-FTacV technique has been the data analysis methodology, which has relied on the experimentalist carrying out a "heuristic" optimization of each model parameter. This represents a time-consuming process that counteracts the very high efficiency of the experimental procedure.(19-21) Automated multiparameter optimization approaches have been developed(25-29) to analyze the electrode kinetics associated with FTacV measurements of solution phase redox reactions such as $[Fe(CN)_6]^{3-} + e^- \leftrightarrows$ $[Fe(CN)_6]^{4-}$. However, these are not suitable for PF-FTacV data due to the substantial background current contributions encountered in the voltammetry of surface-confined redox active species, especially at carbon-based electrodes like pyrolytic graphite edge (PGE). Instead, we have developed a computationally efficient two-step procedure to (1) assign capacitive background parameters to the time (total current) signal and then (2) determine the parameters that define the protein Faradaic redox process by modeling the real and imaginary components of the 4th to 12th order harmonic ac data using data optimization methods.

Experimental Section

The proteins *E. coli* HypC, HypD, and HypCD were purified anaerobically as described previously.(7) For electrochemical experiments, 0.5 µL of either 23 mg mL^{-1} HypCD, 37 mg mL^{-1} HypD, or 15 mg mL^{-1} HypC was adsorbed onto a PGE "working" electrode of geometric surface area 0.03 cm^2. Electrochemical experiments were performed using a standard three-electrode setup comprising a saturated calomel "reference" (a correction factor of +0.241 V is used to convert all potentials to the standard hydrogen electrode, SHE, scale)(30) and a platinum wire "counter" electrode in addition to the PGE working electrode. The all-glass electrochemical cell (built by University of York Department of Chemistry Glass Workshop) was water-jacketed and connected to a thermostated water-circulation unit to provide temperature control. Experiments were conducted at 25 °C in a mixed buffer solution of 15 mM each of MES, CHES, HEPES, TAPS, and Na acetate with 2 M NaCl supporting electrolyte. *N*-Ethylmaleimide (NEM) was used to alkylate the two free sulfhydryl groups formed by reducing the disulfide bond.(31) All experiments were performed inside an anaerobic nitrogen-filled glovebox, which was built by University of York Department of Chemistry Mechanical Workshop.

All dcV experiments were conducted using an Ivium potentiostat and software, and the FTacV instrumentation is as described previously.(24, 32) Background correction of the dcV data was carried out by fitting a polynomial function to the potential region of the voltammogram where there was no Faradaic current and then using this to extrapolate the background signal, which was then subtracted. The uncompensated resistance value used in FTacV-simulations was determined from the electrochemical impedance spectra measured at potentials devoid of Faradaic current and use of a simple RC circuit model.

The structural model of *E. coli* HypD was produced using the crystal structure of *T. kodakarensis* HypD (PDB 2Z1D) as a template.(10) A sequence alignment was first produced between the *E. coli* sequence (Uniprot P24192) and the *T. kodakaraensis* sequence (Uniprot Q5JII1) using the Align123 program within Accelrys Discovery Studio 3.5.(33) The Build Homology Models protocol within Discovery Studio was then used to build an initial model. It was specified that there should be a disulfide bond between Cys69 and Cys72 and that the Fe$_4$S$_4$ cluster should be copied to the resulting model. This initial model was

further processed using a restrained molecular dynamics simulation to account for the differences in bonding. The Cys323 residue was rotated so that it could coordinate the Fe_4S_4 cluster. VMD 1.9.2(34) was then used to patch the S–S and Fe–S bonds and to solvate and neutralize the system with 150 mM NaCl. The simulation was performed in NAMD 2.9(35) using an NPT ensemble with periodic boundary conditions and 5 kcal mol^{-1} restraints on the protein backbone atoms. After 100 steps of minimization the simulation ran for 5000 steps using a 2 fs time step. Parameterization was carried out using the CHARMM22(36) all-atom force field with CMAP(37) correction and an FeS cluster force field developed by Chang and Kim.(38)

Mathematical Model: In the simulations of the voltammetry of *E. coli* HypD we assume a model having three species, A, B and C that are surface confined, with the proposed reactions

$$A + e^- \leftrightarrows B \tag{1}$$

$$B + e^- \leftrightarrows C \tag{2}$$

In the particular problem we are addressing, B and C are involved in very rapid (assumed to be reversible) protonation and bond breaking/forming reactions (also assumed reversible), to give the net two-electron two-proton reaction shown in Figure 1. This implies that, from a thermodynamic perspective, the standard reversible potentials (E^o) and equilibrium constants associated with acid-base reactions and bond making/breaking are coupled into a term that we denote as E_{rev} when referring to parameters derived from HypD experimental data.

On the basis of Butler–Volmer theory,(30) the forward $k_i^{red}(t)$ and backward $k_i^{ox}(t)$ reaction rates for the electron transfer steps are given by eqs 3 and 4, respectively, with k_i^0 and α_i being the electron transfer rate constants at E_i^0, and charge transfer coefficients, respectively.

$$k_i^{red}(t) = k_i^0 exp\left(-\frac{\alpha_i F}{RT}\left[E_r(t) - E_i^0\right]\right) \tag{3}$$

$$k_i^{ox}(t) = k_i^0 \exp\left((1 - \alpha_i)\frac{F}{RT}\left[E_r(t) - E_i^0\right]\right) \tag{4}$$

The real or effective potential $E_r(t)$ is the input applied potential $E(t)$ minus the potential due to uncompensated resistance R_u as reflected in the Ohmic (IR_u) drop.

$$E_r(t) = E(t) - R_u I_{tot}(t)$$

and the input potential is the sum of dc (E_{dc}) and ac contributions

$$E(t) = E_{dc}(t) + \Delta E \sin(\omega t + \eta) \tag{5}$$

where ΔE is the amplitude of the sine wave of frequency ω ($\omega = 2\pi f$, where f is frequency in Hz) and phase η. Furthermore,

$$E_{dc}(t) = \begin{cases} E_{start} + vt, & \text{for } 0 \leq t < t_r \\ E_{reverse} - v(t - t_r), & \text{for } t_r \leq t \end{cases}$$

$$t_r = \frac{E_{reverse} - E_{start}}{v}$$

where v is the dc scan rate, E_{start} is the initial potential and $E_{reverse}$ is the reverse potential.

Now, let θ_1 be the proportion of A on the electrode surface and θ_2 be the proportion of C, then the ordinary differential equations (ODEs) governing their behavior are given by

$$\frac{d\theta_1}{dt} = k_1^{ox}(1 - \theta_1 - \theta_2) - k_1^{red}\theta_1$$

$$\frac{d\theta_2}{dt} = k_2^{red}(1 - \theta_1 - \theta_2) - k_2^{ox}\theta_2$$

with initial conditions $\theta_1(0) = 1$ and $\theta_2(0) = 0$.

These equations assume noninteracting redox active centers (Langmuir isotherm) which requires that all surface-confined species exhibit identical electrode kinetics and thermodynamics (kinetic and thermodynamic dispersion absent).(30, 39)

The total current measured (I_{tot}) is the sum of the capacitive (I_c) and Faradaic (I_f) components

$$I_{tot} = I_c + I_f$$

where

$$I_f = FS\Gamma\left(\frac{d\theta_1}{dt} - \frac{d\theta_2}{dt}\right)$$

with S being the electrode area (assumed equal to the geometric area) and Γ the surface coverage per unit area.

We do not have a reliable model for the capacitive current of PGE electrodes so we instead account for this using a third order polynomial in E_r,

$$I_c = C_{dl}(1 + C_{dl1}E_r(t) + C_{dl2}E_r^2(t) + C_{dl3}E_r^3(t))\frac{dE_r}{dt}$$

Dimensionless Equations and Numerical Solution: The model equations can be represented using dimensionless variables $i = I/I_0$, $\epsilon = E/E_0$ and $\tau = t/T_0$. Substituting these into the model and setting

$$E_0 = \frac{RT}{F}, \quad T_0 = \frac{E_0}{v}, \quad I_0 = \frac{Fa\Gamma}{T_0},$$

gives the dimensionless equations

$$\frac{d\theta_1}{d\tau} = \kappa_1^0\left((1 - \theta_1 - \theta_2)e^{(1-\alpha_1)(\epsilon_r - \epsilon_1^0)} - \theta_1 e^{-\alpha_1(\epsilon_r - \epsilon_1^0)}\right),$$

$$\frac{d\theta_2}{d\tau} = \kappa_2^0\left((1 - \theta_1 - \theta_2)e^{-\alpha_2(\epsilon_r - \epsilon_2^0)} - \theta_2 e^{(1-\alpha_2)(\epsilon_r - \epsilon_2^0)}\right),$$

$$i = \gamma(1 + \gamma_1\epsilon_r + \gamma_2\epsilon_r^2 + \gamma_3\epsilon_r^3)\frac{d\epsilon_r}{d\tau} + \zeta\left(\frac{d\theta_1}{d\tau} - \frac{d\theta_1}{d\tau}\right),$$

where

$$\epsilon_r = \epsilon - \rho i,$$

$$\epsilon = \epsilon_{start} + \tau + \Delta\epsilon\sin(\omega\tau + \eta)$$

The parameters γ, ρ, κ_i^0, ϵ_i^0 and ζ are the dimensionless double layer capacitance, uncompensated resistance, reaction kinetics parameter, reversible potential and electrode coverage, respectively. The unknown time dependent variables $\theta_1(t)$, $\theta_2(t)$, $i(t)$, are the dimensionless proportions of A, C (see eqs (1) and (2)), and total current respectively. The input ac signal is parameterized by its dimensionless amplitude $\Delta\epsilon$, angular frequency ω and phase η.

To solve these equations, we discretize the time derivatives $d\theta_i/d\tau$ and $di/d\tau$ using the implicit Euler method. Substituting this back into the equation for i gives an implicit equation in terms of θ_i^{n+1}, θ_i^n, i^{n+1} and i^n, which was solved using the Newton-Raphson method implemented in the Boost C++ library (https://www.boost.org).

The difficulty in a data fitting exercise with a complex model like the one described in the theory above, is that six parameters are needed to define the electrode kinetics (k_1^0, k_2^0, α_1, α_2) and thermodynamics (E_1^0, E_2^0). Multiparameter fitting with this model therefore has the possibility of producing different combinations of the six parameters with equally good fits to the experimental data, implying there is no unique solution available. In addition there will be uncertainty in estimates of parameters such as R_u, C_{dl} and Γ, and in the validity of the model itself (in the present case questions arise such as how valid are the Langmuir *versus* Frumkin isotherm; the Butler-Volmer *versus* Marcus relationship; and whether thermodynamic and kinetic dispersion is significant (40)). These additional factors can also contribute to uncertainties in the final report of kinetic and thermodynamic parameters of interest derived from the data optimization exercise. Finally, it should also be noted that since data optimization software by definition will typically generate values of each parameter requested, checks that reported values are chemically sensible also need to be included as part of the data analysis strategy. Searches for ambiguities derived from the above considerations are undertaken in the present example.

Results and Discussion

Structural Model: There is a crystal structure for HypD from *T. kodakarensis*,(10) but this protein contains two disulfide bonds, one between residues Cys-66 and Cys-69, equivalent to residues Cys-69 and Cys-72 in *E. coli* HypD, and a second disulfide closer to the Fe_4S_4 cluster and not conserved in *E. coli* (Figure 2a). To account for this crucial difference, we have used the crystal structure of *T. kodakarensis*(10) HypD (PDB 2Z1D) to create the model structure of *E. coli* HypD shown in Figure 2b. Based on this model, we estimate a 10.6 Å distance between Cys-69 of the disulfide bond and Cys-41, a residue

predicted to ligate the Fe(CN)$_2$CO complex, which is assembled on a HypCD complex.(7)
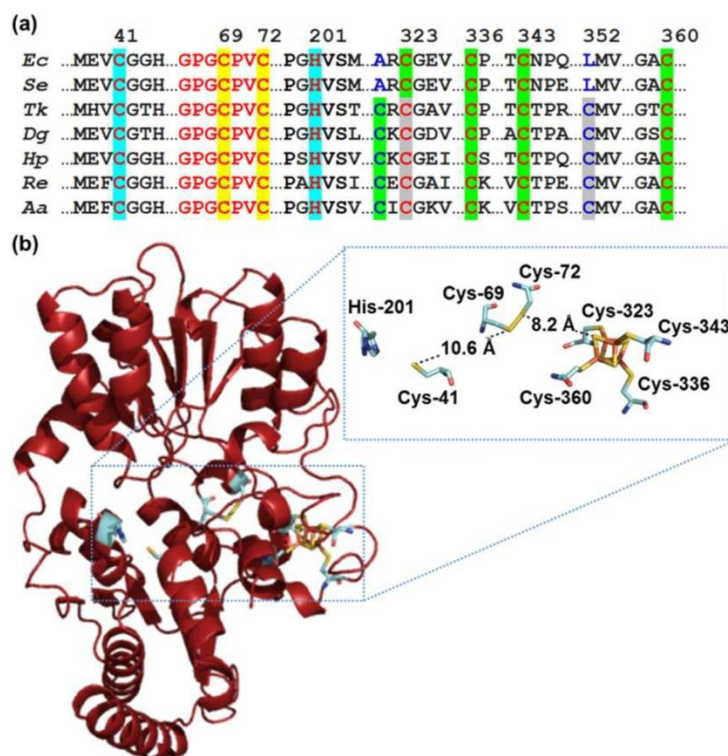
Figure 2. (a) Alignment of various HypD protein sequences with *E. coli* numbering (*Ec, E. coli; Tk, Thermococcus kodakaraensis; Re, Ralstonia eutropha; Hp, Helicobacter pylori; Se, Salmonella enterica; Aa, Aquifex aeolicus; Dg, Desulfovibrio gigas*). Red text indicates conserved residues and blue text indicates key regions where *Ec* and *Se* proteins differ from the others. Highlights: cyan indicates the putative Fe(CN)$_2$CO binding residues, yellow indicates the conserved disulfide bond residues, green indicates the Fe$_4$S$_4$ ligands, and gray indicates the residues which form an "extra" disulfide bond in some HypD proteins. **(b) Model structure for E. coli HypD**, including detail of the relative positioning of the conserved elements highlighted in (a).

HypD PF-dcV: To provide an initial picture of the redox properties of *E. coli* HypD, the protein was adsorbed onto a PGE electrode that was placed in pH 7 buffer. The potential was swept from +0.04 to −0.56 V versus SHE (all potentials are subsequently reported vs this scale) and back at 100 mV s^{-1}. This PF-dcV experiment (Figure 3, black line) reveals a single Faradaic process centered at approximately −0.26 V. No additional protein-related redox processes are observed in experiments that explore wider potential ranges (Figure S1). Analysis of the HypCD complex reveals the same Faradaic process (Figure S2), while no redox activity was observed for HypC alone. Background subtraction of the HypD data gives a pair of reduction and oxidation peaks (Figure 3, black dashed line, note × 10 scaling) with a midpoint potential of E_m = −0.26 V and peak-width at half height of δ = 59 mV. Such a signal is indicative

of a two-electron reaction that comprises two consecutive one-electron transfers, since an ideal reversible one-electron redox reaction has $\delta = 90$ mV and for a simultaneous two-electron transfer $\delta = 45$ mV.(41)
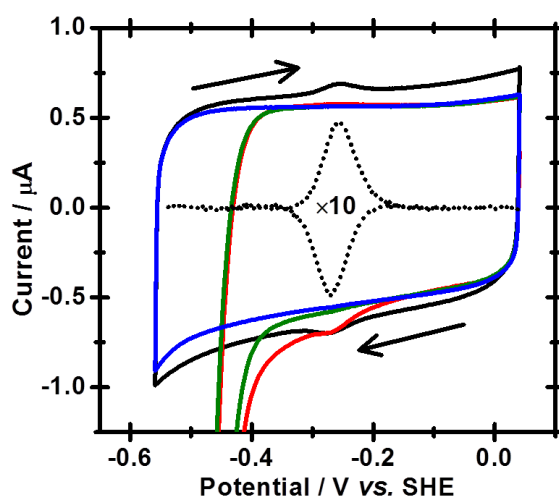
Figure 3. PF-dcV at *v* = 100 mV s^{-1} of HypD on PGE at pH 7 in "pre-NEM" buffer-only conditions (all data, black line; background subtracted signals ×10, black dashed line), in the presence of 1 mM NEM (scan 1, red line; scan 2, green line), and under "post-NEM" buffer-only conditions (blue line). Arrows indicate sweep direction, starting from +0.04 V. Other conditions: N_2 atmosphere, 25 °C.

When the cysteine cross-linking reagent NEM(31) is added to the electrochemical cell buffer solution and the potential of a HypD-coated electrode is scanned from +0.04 to −0.56 V, a peak-like signal is visible at approximately −0.26 V, corresponding to reduction of the enzyme (Figure 3, red line). When the scan direction is reversed, no corresponding oxidation peak is observed and both the reductive and oxidative redox signals are absent in the subsequent scan [Figure 3, green line; NB: The negative Faradaic current at potentials more negative than approximately −0.4 V is ascribed to NEM-reduction. HypD redox activity is not recovered upon returning to NEM-free solutions (Figure 3, blue line)]. This is consistent with NEM binding covalently and irreversibly to the free sulfhydryl groups formed by the reduction of a disulfide bond.(31) We therefore assign the HypD redox activity to the reversible (two one-electron) oxidation and reduction of the disulfide bond formed between Cys-69 and Cys-72.(13)

HypD PF-FTacV: More detailed analysis of the redox chemistry of HypD is facilitated by PF-FTacV. Figure 4 illustrates the higher sensitivity measurements that are accessible by comparing experiments conducted using both PF-FTacV and PF-dcV to interrogate the same low coverage protein-electrode film.
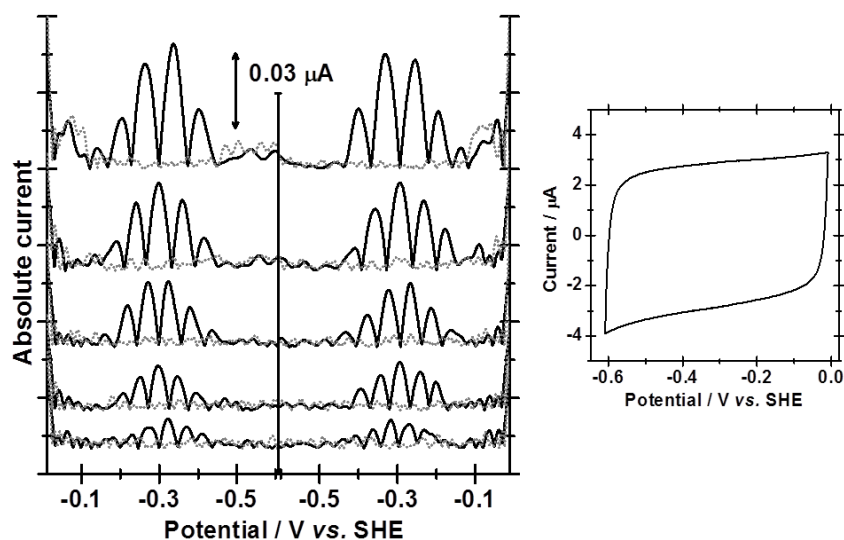
Figure 4. Comparison between (left, top to bottom) 6th to 10th harmonics of PF-FTacV measurement (black lines) and (right) 500 mV·s⁻¹ PF-dcV measurement of low surface coverage HypCD film at pH 8, 25 °C, N₂ atmosphere. Protein-free control FTacV data also shown by gray dashed lines. Other FTacV conditions: v = 22.35 mV s⁻¹, f = 8.9593 Hz, ΔE = 150 mV.

The PF-dcV measurement is dominated by capacitance, and the Faradaic response is invisible against the large background. In PF-FTacV, background-free, clear Faradaic signals are derived by applying a discrete Fourier transform to the total dc plus ac current, to convert the data from the time domain into the frequency domain. The frequency responses (harmonics) are then isolated and transformed back to the time domain via inverse Fourier transformation.(42) While nonprotein capacitive current provides the majority of the fundamental harmonic signal and progressively weaker signals up to about the third harmonic, the fourth and higher order harmonics consist of solely Faradaic current. These can be visualized in the absolute current magnitude envelope format used in Figure 4, or alternatively the real and imaginary components of the harmonics can be displayed, as shown later. The x-axis can be time or converted into a potential scale using the scan rate. Because of the zero-background, conversion to a potential scale has enabled us to simply extract "midpoint potential" values by measuring the position of the center of the signals in the forward and back scan sweeps of FTacV experiments conducted on high protein coverage films (Figure 5). We find that this HypD midpoint potential has a pH dependence of approximately −60 mV per pH unit between pH 4 and 6, reducing to approximately −38 mV per pH unit above pH 7 (Figure 5). Based on the simplistic reaction for disulfide bond making/breaking shown in Figure 1, we expect coupling between proton and electron transfer.

155

However, relative to well-characterized proton-coupled protein electron transfers in iron sulfur clusters,(43) interpretation of the pH dependence of disulfide redox chemistry is more complex because of the bond making/breaking steps. Ideally, one would wish to know the dependence of the reversible potential of each electron transfer step on pH rather than that of the midpoint potential, and this requires simulation.
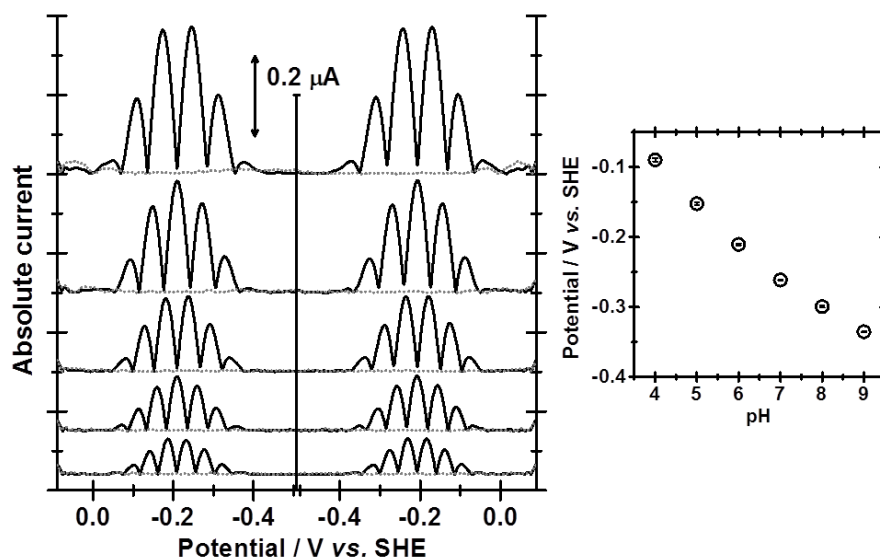
Figure 5. (left) The 6th to 10th harmonics of the PF-FTacV data for a high surface-coverage HypD electrode-film measured at pH 6, 25 °C, N_2 atmosphere, v = 22.35 mV s^{-1}, f = 8.9593 Hz, ΔE = 150 mV. **(right) pH dependence of midpoint potentials** as determined from experiments such as that shown, conducted in different buffer solutions. Error bars indicate the standard error of at least 3 repeat experiments.

PF-FTacV Parameter Optimization: In the case of the *E. coli* HypD surface confined process studied here, the model introduced to describe the assumed 1e$^-$ + 1e$^-$ protein-film redox transition on a high capacitance electrode (see Theory), gives rise to simulated responses that can be visually compared to the experimental data in both the absolute current magnitude form used in Figures 4 and 5 and earlier publications(19-23) and in the more sophisticated real and imaginary component form, as commonly used in impedance spectroscopy (Figure 6). A caveat to using the latter display style is that the phase angle information must be calibrated carefully, as described here.
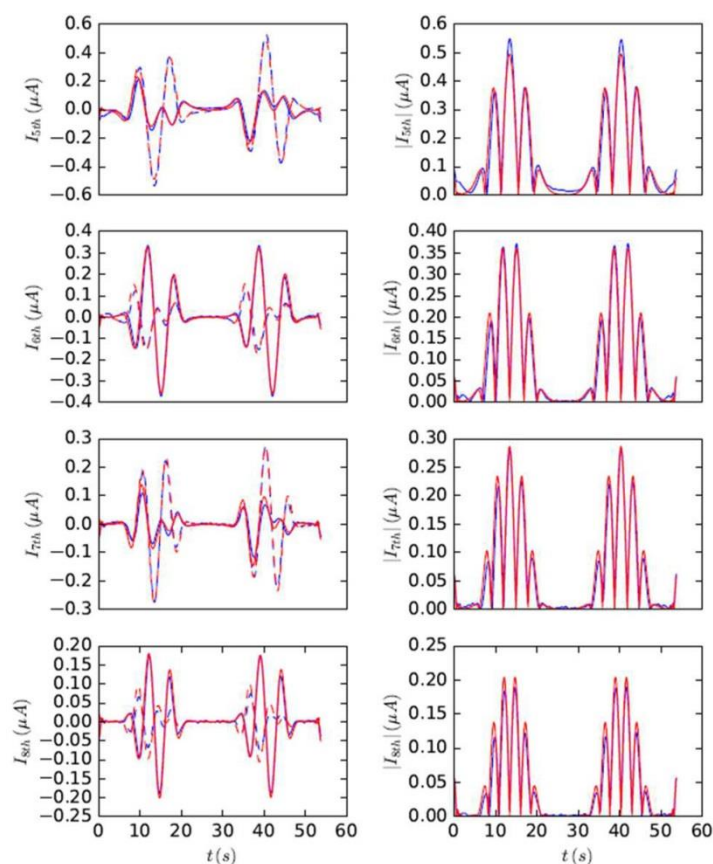
Figure 6. Comparison of the 5th–8th (I_fifth − I_eighth) harmonics of the FTac voltammograms simulated using a reversible model (red lines) and experimental data against which the parameter optimization process was applied (blue lines, same data as shown in left panel of Figure 5). (left) Plots show the real (solid lines) and imaginary (dashed lines) components, and (right) the plots show the absolute current magnitudes. The filtered harmonics have been frequency shifted to a center frequency of zero for display purposes.

Unlike most PF-FTacV studies, a new automated (rather than manual) process for finding the parameter values that give the best match between simulated (numerical) and experimental data has been developed. In order to do this parameter-optimization, it is necessary to have an objective function to determine the "distance" between the simulated i_n and experimental i_e data. A commonly used distance function in the time domain is the least-squares function, or Euclidean distance, $\mathcal{L}_t$, which has been used to compare the total dc + ac current in previous FTacV studies where the reactants are in the solution phase rather than being surface-confined.(25, 27, 44)

$$\mathcal{L}_t = \sqrt{\sum_{j=1}^{N} [i_n(\tau_j) - i_e(\tau_j)]^2}$$

Since the higher order harmonic signals (4th and above) are background-free, but the lower harmonics are not, it becomes useful to define an objective

function $\mathcal{L}_f$ based on the distance between harmonics $n = n_0 \ldots n_M$ of the simulated and experimental data ($f_n(\omega)$ and $f_e(\omega)$, respectively).

$$\mathcal{L}_f = \sqrt{\sum_k^N |w(\omega_k)(f_n(\omega_k) - f_e(\omega_k))|^2}, \tag{6}$$

$$w(\omega_k) = \sum_{n=n_0}^{n_M} w_n(\omega_k). \tag{7}$$

where w_n is the Kaiser window(45) centered on the nth harmonic. This enables separation between the capacitive and Faradaic contributions so that parameter fitting can be achieved via a two-stage process.

Stage 1 - Fitting Capacitive Parameters: The first stage of the fitting process aims to determine the capacitive parameters (C_{dl}, C_{dl1}, C_{dl2}, C_{dl3}), matched to the ac signal frequency ω and the phase η. Although ω and η are known parameters in principle, they are rarely available at sufficient accuracy for reliable fitting between the numerical model and the experimental data, with significant phase differences being encountered by the end of the simulation. There is also a significant phase-shift due to the IR drop that must also be determined through the fitting process.

We first define an objective function $\mathcal{L}_c$ based on the time domain data that is devoid of any significant influence of the Faradaic current.

$$\mathcal{L}_c^2 = \sum_{j=1}^N \begin{cases} 0 & \text{for } \tau_l \leq \tau_j - n\tau_p < \tau_h, \\ [i_n(\tau_j) - i_e(\tau_j)]^2 & \text{otherwise}, \end{cases}$$

where $\boldsymbol{n}$ is any integer and

$$\tau_l = \frac{1}{5}(\epsilon_{\text{reverse}} - \epsilon_{\text{start}}),$$

$$\tau_h = \frac{4}{5}(\epsilon_{\text{reverse}} - \epsilon_{\text{start}}),$$

$$\tau_p = \epsilon_{\text{reverse}} - \epsilon_{\text{start}}.$$

Here we have chosen the time samples that contribute to $\mathcal{L}_c$ so that they are unaffected by the Faradaic current, which is isolated to times within the middle three fifths of the sweep range.

Minimization of the objective function in this study is done using the CMA-ES method, which is a stochastic, derivative-free global minimization algorithm. Defining a parameter vector for this stage of

$$v_c = [C_{\mathrm{dl}}, C_{\mathrm{dl1}}, C_{\mathrm{dl2}}, C_{\mathrm{dl3}}, \omega, \eta]$$

we apply box bounds on the parameters using

$$0 \leq C_{\mathrm{dl}} \leq 10, \qquad -0.1 \leq C_{\mathrm{dl3}} \leq 0.1,$$
$$-1 \leq C_{\mathrm{dl1}} \leq 1, \qquad 0.99\omega_0 \leq \omega \leq 1.01\omega_0,$$
$$-0.1 \leq C_{\mathrm{dl2}} \leq 0.1, \qquad -0.9\pi \leq \eta \leq 1.1\pi$$

(where ω_0 is the estimated frequency) and then find v_c which minimises our objective function $\mathcal{L}_c$.

Stage 2 - Fitting Faradaic Parameters: We now use the capacitive parameters obtained in stage 1 and a new objective function based on the higher harmonics of the signal, $\mathcal{L}_f$, in order to fit for the Faradaic parameters, assuming α_1 and α_2 are 0.5, R_u is known (pre-determined) and Γ can be adjusted as a scaling factor, ζ, starting from a value of 6.5 pmol cm^{-1} based on the integration of the current-time data in background subtracted voltammograms of the kind displayed in Figure 3. Since the influence of the capacitive current is restricted to frequencies below the fourth harmonic, using an objective function based on the harmonics above this mitigates any inaccuracies in our capacitive model. Due to the level of noise in the experimental data, we have determined that the highest harmonic that is above the noise threshold is the 12th, so $\mathcal{L}_f$ is based on the $n = 4..12$ harmonics. That is, $\mathcal{L}_f$ is calculated using equations (6) and (7) with $n_0 = 4$ and $n_M = 12$.

We then find the parameters $v_f = [k_1^{\mathrm{rev}}, E_1^{\mathrm{rev}}, k_2^{\mathrm{rev}}, E_2^{\mathrm{rev}}, \eta, \zeta]$ that minimize $\mathcal{L}_f$, using box bounds

$$0 \leq k_1^{\mathrm{rev}} \leq 4000, \qquad 0 \leq k_2^{\mathrm{rev}} \leq 4000,$$
$$\epsilon_{\min} \leq E_1^{\mathrm{rev}} \leq \epsilon_{\max}, \qquad \epsilon_{\min} \leq E_2^{\mathrm{rev}} \leq \epsilon_{\max},$$
$$-0.9\pi \leq \eta \leq 1.1\pi, \qquad 0.1 \leq \zeta \leq 10,$$

with $\epsilon_{\min} = \epsilon_{\text{start}} + 0.2(\epsilon_{\text{reverse}} - \epsilon_{\text{start}})$ and $\epsilon_{\max} = \epsilon_{\text{start}} + 0.8(\epsilon_{\text{reverse}} - \epsilon_{\text{start}})$. The kinetic rate constant upper bound of 4000 was determined as the rate above which the simulation results did not change significantly.

Modeling HypD PF-FTacV as 1e⁻ + 1e⁻ Process: Using the two-stage fitting method to find the parameter values that give the best fit between the pH 6 HypD PF-FTacV measurements and our 1e⁻ + 1e⁻ model generates simulations that closely resemble our experimental data sets (Table 1). We only simulate low frequency experiments (8.9593 Hz) in order to ensure both that the experimental conditions match the assumptions of equilibrium conditions, that is, no chemical gating applies, and to reduce the computer time required by the parameter optimization exercises.

Table 1. Fitted Faradaic Parameter Values from Simulation of Different Experiments
Conducted at pH 6, 25 °C, N_2 Atmosphere, v = 22.35 mV s−1 , f = 8.9593 Hz, ΔE = 150 mV[a]

Data set	Model	k_1^{rev} (s⁻¹)	E_1^{rev} (V)	k_2^{rev} (s⁻¹)	E_2^{rev} (V)	ζ	η (rad)	$10^{-2}\mathcal{L}_f$
1	quasi-reversible	>4000	-0.216	1280	-0.200	0.813	3.16	265
		>4000	-0.201	202	-0.212	0.799	3.27	259
	reversible	n.a.	-0.217	n.a.	-0.200	0.813	3.15	267
2	quasi-reversible	>4000	-0.203	342	-0.211	0.984	3.24	356
		>4000	-0.210	1070	-0.207	0.995	3.18	357
	reversible	n.a.	-0.211	n.a.	-0.207	0.996	3.16	358
3	quasi-reversible	359	-0.195	>4000	-0.221	0.556	3.24	196
		>4000	-0.207	>4000	-0.207	0.581	3.16	193
	reversible	n.a.	-0.207	n.a.	-0.207	0.582	3.16	192
4	quasi-reversible	>4000	-0.206	>4000	-0.215	0.538	3.19	225
	reversible	n.a.	-0.206	n.a.	-0.214	0.538	3.19	225
5	quasi-reversible	>4000	-0.198	201	-0.215	1.06	3.15	460
		>4000	-0.214	>4000	-0.203	1.05	3.02	478
		194	-0.200	>4000	-0.222	1.06	3.15	456
	reversible	n.a.	-0.214	n.a.	-0.203	1.05	3.02	478

[a] The stopping tolerance for the CMA-ES algorithm (i.e. maximum deviation of $\mathcal{L}_f$ from the true local minimum) was set to 10^{-11}.

In order to assist understanding of the significance of parameter values deduced from the data analysis process we undertake 30 different fitting runs on each experimental data set before identifying the best fit, and then we repeat this process at least twice per experimental data set to determine how consistent such "best fit" values are. Table 1 and Supporting Information, Table S1 summarize the results from applying this data optimization strategy to the analysis of five different PF-FTacV data sets, all derived from different electrode films of HypD. Clearly, on the basis of the model used for simulations, there are

a range of combinations of parameters that generate almost the same objective function, and local minima are frequently detected when all values from the 30 data optimization runs are interrogated. However, although Table 1 shows that the best fit k^{rev} values vary considerably from experiment to experiment, these rate constants are always large. This feature is expected for electron transfer reactions close to the reversible limit and is consistent with the observation that in control experiments the objective function $\mathcal{L}_f$ was found to be independent of α_i. So, while we set $\alpha_i = 0.50$ in all simulations, this assumption is not expected to have any impact on the results.

The most consistently defined parameters are the E^{rev} values, which are almost always in the range of −0.20 to −0.22 V. However, even in the estimation of these redox-potential parameters there was an interesting outlier (shown in Supporting Information, section 5) that had a minimum objective function with well separated E^{rev} values that gave an excellent fit of simulated and experiential 4th to 12th harmonic data. This case is discussed in the Supporting Information to emphasize the care needed in drawing conclusions on the significance of parameters deduced from data optimization exercises requiring multiparameter estimation using a complex model.

Consideration of the variability in the parameter estimates obtained using a model with quasi-reversible electron transfer suggests that a preferable model to employ would be one derived for reversible electron transfer, achieved by making both k^{rev} values 4000 s^{-1}. Now the only parameters to be fitted are E_1^{rev} and E_2^{rev}, and the resultant best-fit data is summarized in Table 1 and shown in Figure 6. The close equivalence of the E^{rev} values is maintained, with an average value of −0.21 V, and this biochemically sensible model allows us to state that electron transfer is reversible on the time scale of the experiment, suggesting k^{rev} variables are greater than 4000 s^{-1}.

To further illustrate the advantage of our new data analysis approach, we first use the frequency based objective function $\mathcal{L}_f$, as described above, and compare this with 30 different fitting runs using instead the traditional least-squares objective function $\mathcal{L}_f$, which uses the entire time-domain (total current) signal (see Supporting Information). The $\mathcal{L}_f$ objective function results in a clearly

worse fit, particularly in the phase of the filtered harmonics, and an example of this is displayed in Figure 7.
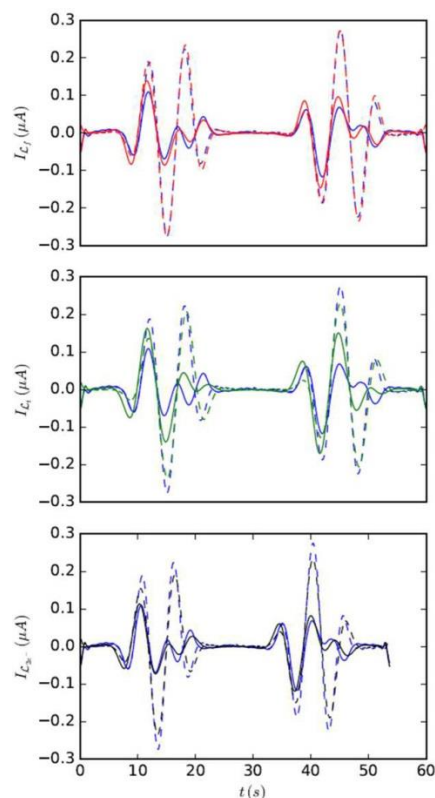
Figure 7. Comparison of the 7th harmonic of the best fit for the Faradaic parameters using (top) the frequency objective function $\mathcal{L}_f$, (middle) the time-based objective function $\mathcal{L}_t$, and (bottom) the simultaneous 2e⁻ model. The fit for the 2e⁻ model uses the $\mathcal{L}_f$ objective function. Experimental data as in Figure 5 and simulation details are as given in Figure 6 and in text.

We also fit the data to a single 2e⁻ redox reaction, that is, $A + 2e^- \leftrightarrows C$. We use the frequency based objective function $\mathcal{L}_f$ to fit the new model to the data, and obtain best fit Faradaic parameters of E^{rev} = -0.208 V and $k^{rev} \geq 4{,}000$ s⁻¹ giving an objective function $\mathcal{L}_f$ a factor of 1.25 times that from the original model. This relatively poor fit is also illustrated in Figure 7.

Conclusion

At pH 6, *E. coli* HypD displays reversible redox activity, participating in an overall two-electron process via one electron intermediates, with both reversible potentials being very similar. We attribute this reactivity to the disulfide bond formation and excision. We cannot measure any Fe_4S_4 redox transitions, even over a very wide potential window. The FTacV technique is a powerful tool with

which to study these processes, yielding clear protein redox signals even when nothing can be seen in dcV.

Comparison between the midpoint redox potential we measure for HypD at pH 7 (−0.26 V) and the standard redox potential for the cytoplasmic reducing agent of *E. coli*, Trx1 ($E^{o'}$ = −0.27 V), suggests that in vivo reduction of HypD should be possible.(46) The conversion of CO_2 to CO would be thermodynamically unfavorable, but oxidation of the Cys residues should be capable of activating the reductive transfer of CN^- from the C-terminal cysteine residue of protein HypE to the HypCD complex, therefore, initiating assembly of the $Fe(CN)_2CO$ active site fragment, as suggested in the first stages of the HypD mechanism by Watanabe and co-workers.(9) This hypothesis is supported by Böck's work, which showed that purified HypCD was oxidatively inactivated by $K_3[Fe(CN)_6]$ to a state that could not accept CN.(12)

The oxidative formation of a disulfide bond between two cysteine residues (Figure 1) is an essential biological redox reaction, which is important in far more processes than just hydrogenase biosynthesis. Errors in the regulation of disulfide bond formation in human cells have been linked to the neurodegenerative diseases of Alzheimer, Parkinson, and amyotrophic lateral sclerosis (ALS).(47) We have demonstrated that PF-FTacV is a powerful methodology with which to probe such redox bioelectrochemistry and the technique has been significantly improved by the development of a two-step protocol for automated parameter estimation. This enables us to derive the fundamentally important Faradaic parameters and allows the identification of a very fast $1e^-$ + $1e^-$ transfer over the alternative $2e^-$ transfer. We do not extract information on the chemical steps that accompany electron transfer; this may emerge with more broadly based studies at higher frequency over a wide pH range but considerably more complexity, and an associated increase in the number of parameters, will need to be introduced into the simulations.

Acknowledgement

References

(1) Reeve, H. A.; Lauterbach, L.; Lenz, O.; Vincent, K. A. *ChemCatChem* **2015**, *7*, 3480-3487.

(2) Xu, L.; Armstrong, F. A. *RSC Adv.* **2015**, *5*, 3649-3656.

(3) Mersch, D.; Lee, C.-Y.; Zhang, J. Z.; Brinkert, K.; Fontecilla-Camps, J. C.; Rutherford, A. W.; Reisner, E. *J. Am. Chem. Soc.* **2015**, *137*, 8541-8549.

(4) Lacasse, M. J.; Zamble, D. B. *Biochemistry* **2016**, *55*, 1689-1701.

(5) Beimgraben, C.; Gutekunst, K.; Opitz, F.; Appel, J. *Appl. Environ. Microbiol.* **2014**, *80*, 3776-3782.

(6) Bürstel, I.; Siebert, E.; Winter, G.; Hummel, P.; Zebger, I.; Friedrich, B.; Lenz, O. *J. Biol. Chem.* **2012**, *287*, 38845-38853.

(7) Stripp, S. T.; Soboh, B.; Lindenstrauss, U.; Braussemann, M.; Herzberg, M.; Nies, D. H.; Sawers, R. G.; Heberle, J. *Biochemistry* **2013**, *52*, 3289-3296.

(8) Soboh, B.; Lindenstrauss, U.; Granich, C.; Javed, M.; Herzberg, M.; Thomas, C.; Stripp, Sven T. *Biochem. J.* **2014**, *464*, 169-177.

(9) Watanabe, S.; Matsumi, R.; Atomi, H.; Imanaka, T.; Miki, K. *Structure* **2012**, *20*, 2124-2137.

(10) Watanabe, S.; Matsumi, R.; Arai, T.; Atomi, H.; Imanaka, T.; Miki, K. *Mol. Cell* **2007**, *27*, 29-40.

(11) Stripp, S. T.; Lindenstrauss, U.; Granich, C.; Sawers, R. G.; Soboh, B. *PLoS One* **2014**, *9*, e107488.

(12) Blokesch, M.; Albracht, S. P. J.; Matzanke, B. F.; Drapal, N. M.; Jacobi, A.; Böck, A. *J. Mol. Biol.* **2004**, *344*, 155-167.

(13) Blokesch, M.; Böck, A. *FEBS Lett.* **2006**, *580*, 4065-4068.

(14) Hamill, M. J.; Chobot, S. E.; Hernandez, H. H.; Drennan, C. L.; Elliott, S. J. *Biochemistry* **2008**, *47*, 9738-9746.

(15) Chobot, S. E.; Hernandez, H. H.; Drennan, C. L.; Elliott, S. J. *Angew. Chem., Int. Ed.* **2007**, *46*, 4145-4147.

(16) Bewley, K. D.; Dey, M.; Bjork, R. E.; Mitra, S.; Chobot, S. E.; Drennan, C. L.; Elliott, S. J. *PLoS One* **2015**, *10*, e0122466.

(17) Johnson, D. L.; Martin, L. L. *J. Am. Chem. Soc.* **2005**, *127*, 2018-2019.

(18) Hirst, J.; Armstrong, F. A. *Anal. Chem.* **1998**, *70*, 5062-5071.

(19) Lee, C.-Y.; Stevenson, G. P.; Parkin, A.; Roessler, M. M.; Baker, R. E.; Gillow, K.; Gavaghan, D. J.; Armstrong, F. A.; Bond, A. M. *J. Electroanal. Chem.* **2011**, *656*, 293-303.

(20) Stevenson, G. P.; Lee, C.-Y.; Kennedy, G. F.; Parkin, A.; Baker, R. E.; Gillow, K.; Armstrong, F. A.; Gavaghan, D. J.; Bond, A. M. *Langmuir* **2012**, *28*, 9864-9877.

(21) Adamson, H.; Simonov, A. N.; Kierzek, M.; Rothery, R. A.; Weiner, J. H.; Bond, A. M.; Parkin, A. *Proc. Natl. Acad. Sci. U.S.A.* **2015**, *112*, 14506-14511.

(22) Simonov, A. N.; Grosse, W.; Mashkina, E. A.; Bethwaite, B.; Tan, J.; Abramson, D.; Wallace, G. G.; Moulton, S. E.; Bond, A. M. *Langmuir* **2014**, *30*, 3264-3273.

(23) Simonov, A. N.; Holien, J. K.; Yeung, J. C. I.; Nguyen, A. D.; Corbin, C. J.; Zheng, J.; Kuznetsov, V. L.; Auchus, R. J.; Conley, A. J.; Bond, A. M.; Parker, M. W.; Rodgers, R. J.; Martin, L. L. *PLoS One* **2015**, *10*, e0141252.

(24) Bond, A. M.; Elton, D.; Guo, S.-X.; Kennedy, G. F.; Mashkina, E.; Simonov, A. N.; Zhang, J. *Electrochem. Commun.* **2015**, *57*, 78-83.

(25) Morris, G. P.; Simonov, A. N.; Mashkina, E. A.; Bordas, R.; Gillow, K.; Baker, R. E.; Gavaghan, D. J.; Bond, A. M. *Anal. Chem.* **2013**, *85*, 11780-11787.

(26) Bentley, C. L.; Bond, A. M.; Hollenkamp, A. F.; Mahon, P. J.; Zhang, J. *Anal. Chem.* **2014**, *86*, 2073-2081.

(27) Simonov, A. N.; Morris, G. P.; Mashkina, E. A.; Bethwaite, B.; Gillow, K.; Baker, R. E.; Gavaghan, D. J.; Bond, A. M. *Anal. Chem.* **2014**, *86*, 8408-8417.

(28) Bond, A. M.; Mashkina, E. A.; Simonov, A. N. In *Developments in Electrochemistry*; John Wiley & Sons, Ltd, 2014, pp 21-47.

(29) Tan, S.-y.; Zhang, J.; Bond, A. M.; Macpherson, J. V.; Unwin, P. R. *Anal. Chem.* **2016**, *88*, 3272-3280.

(30) Bard, A. J.; Faulkner, L. R. *Electrochemical Methods: Fundamentals and Applications*; Wiley, 2000.

(31) Zu, Y.; Fee, J. A.; Hirst, J. *Biochemistry* **2002**, *41*, 14054-14065.

(32) Bond, A. M.; Duffy, N. W.; Guo, S.-X.; Zhang, J.; Elton, D. *Anal. Chem.* **2005**, *77*, 186 A-195 A.

(33) Accelrys Inc., San Diego, CA, USA, 2012.

(34) Humphrey, W.; Dalke, A.; Schulten, K. *J. Mol. Graphics* **1996**, *14*, 33-38.

(35) Phillips, J. C.; Braun, R.; Wang, W.; Gumbart, J.; Tajkhorshid, E.; Villa, E.; Chipot, C.; Skeel, R. D.; Kalé, L.; Schulten, K. *J. Comput. Chem.* **2005**, *26*, 1781-1802.

(36) MacKerell, A. D.; Bashford, D.; Bellott, M.; Dunbrack, R. L.; Evanseck, J. D.; Field, M. J.; Fischer, S.; Gao, J.; Guo, H.; Ha, S.; Joseph-McCarthy, D.; Kuchnir, L.; Kuczera, K.; Lau, F. T. K.; Mattos, C.; Michnick, S.; Ngo, T.; Nguyen, D. T.; Prodhom, B.; Reiher, W. E.; Roux, B.; Schlenkrich, M.; Smith, J. C.; Stote, R.; Straub, J.; Watanabe, M.; Wiórkiewicz-Kuczera, J.; Yin, D.; Karplus, M. *J. Phys. Chem. B* **1998**, *102*, 3586-3616.

(37) Mackerell, A. D.; Feig, M.; Brooks, C. L. *J. Comput. Chem.* **2004**, *25*, 1400-1415.

(38) Chang, C. H.; Kim, K. *J. Chem. Theory Comput.* **2009**, *5*, 1137-1145.

(39) Bond, A. M. *Broadening Electrochemical Horizons: Principles and Illustration of Voltammetric and Related Techniques*; Oxford University Press, 2002.

(40) Morris, G. P.; Baker, R. E.; Gillow, K.; Davis, J. J.; Gavaghan, D. J.; Bond, A. M. *Langmuir* **2015**, *31*, 4996-5004.

(41) Heering, H. A.; Weiner, J. H.; Armstrong, F. A. *J. Am. Chem. Soc.* **1997**, *119*, 11628-11638.

(42) For the band-pass filters for harmonic *n* we use smooth Kaiser windows centred around *nω* and with a bandwidth of 1.5 (in dimensionless units). For the dc harmonic we use a low-pass Hamming window with a cutoff at *ω* = 1.5.

(43) Hirst, J.; Duff, J. L. C.; Jameson, G. N. L.; Kemper, M. A.; Burgess, B. K.; Armstrong, F. A. *J. Am. Chem. Soc.* **1998**, *120*, 7085-7094.

(44) Simonov, A. N.; Morris, G. P.; Mashkina, E.; Bethwaite, B.; Gillow, K.; Baker, R. E.; Gavaghan, D. J.; Bond, A. M. *Anal. Chem.* **2016**, *88*, 4724-4732.

(45) Kaiser, J. F. *Proc. 1974 IEEE International Symposium on Circuits & Systems, San Francisco DA, April* **1974**, 20-23.

(46) Åslund, F.; Berndt, K. D.; Holmgren, A. *J. Biol. Chem.* **1997**, *272*, 30780-30786.

(47) Andreu, C. I.; Woehlbier, U.; Torres, M.; Hetz, C. *FEBS Lett.* **2012**, *586*, 2826-2834.

Supplementary Information for "Analysis of HypD Disulfide Redox Chemistry via Optimization of Fourier Transformed ac Voltammetric Data"

Hope Adamson,[‡,1] Martin Robinson,[‡,2] Paul S. Bond,[1] Basem Soboh,[3] Kathryn Gillow,[4] Alexandr N. Simonov,[5] Darrell M. Elton,[6] Alan M. Bond,[5] R. Gary Sawers,[7] David J. Gavaghan,[*,2] Alison Parkin[*,1]

[1]Department of Chemistry, University of York, Heslington, York, YO10 5DD, United Kingdom

[2]Department of Computer Science, University of Oxford, Wolfson Building, Parks Road, Oxford, OX1 3QD, United Kingdom

[3]Experimental Molecular Biophysics, Freie Universität Berlin, Arnimalle 14, 14195 Berlin, Germany

[4]Mathematical Institute, Andrew Wiles Building, University of Oxford, Radcliffe Observatory Quarter, Woodstock Road, Oxford, OX2 6GG, United Kingdom

[5]School of Chemistry and the ARC Centre of Excellence for Electromaterials Science, Monash University, Clayton, Victoria 3800, Australia

[6]School of Engineering and Mathematical Sciences, La Trobe University, Bundoora, Victoria 3086, Australia

[7]Institute for Biology/Microbiology, Martin Luther University Halle-Wittenberg, Halle (Saale), Germany

*E-mail: david.gavaghan@cs.ox.ac.uk, fax: +44 1865 283532; e-mail: alison.parkin@york.ac.uk, fax +44 1904 322516;

1.   Wide potential-range cyclic voltammetry of HypD

In order to establish that only one redox reaction could be detected for *Escherichia coli* HypD the wide potential range experiments shown in Figure S1 were conducted. Two separate "negative potential" (black line) and "positive potential" (grey line) measurements were made to avoid overlap from solvent redox reactions. As shown, only the redox process at approximately −0.26 V *vs.* SHE, which is ascribed to the disulfide bond chemistry, was seen over the total potential range of -0.96 to +0.44 V *vs.* SHE.
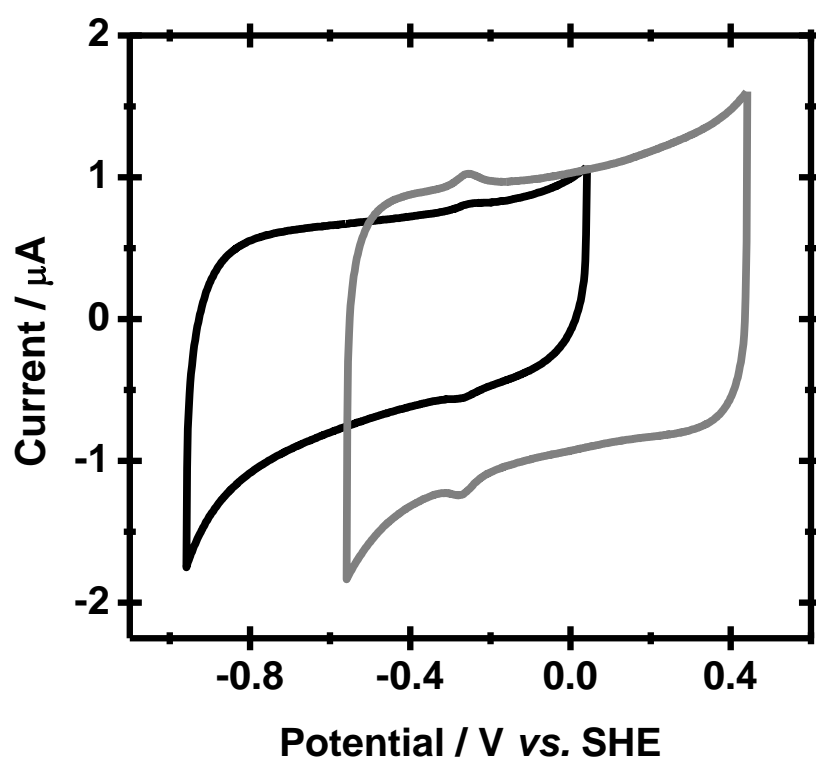
Figure S1. PF-dcV of HypD at 100 mV s^{-1} between +0.44 and −0.56 V *vs.* SHE (grey) and +0.04 and −0.96 V *vs.* SHE (black). Other conditions: pH 7, 25°C, N_2 atmosphere.

2.   dc cyclic voltammetry of HypCD

HypCD exhibits the same redox transformation as HypD.
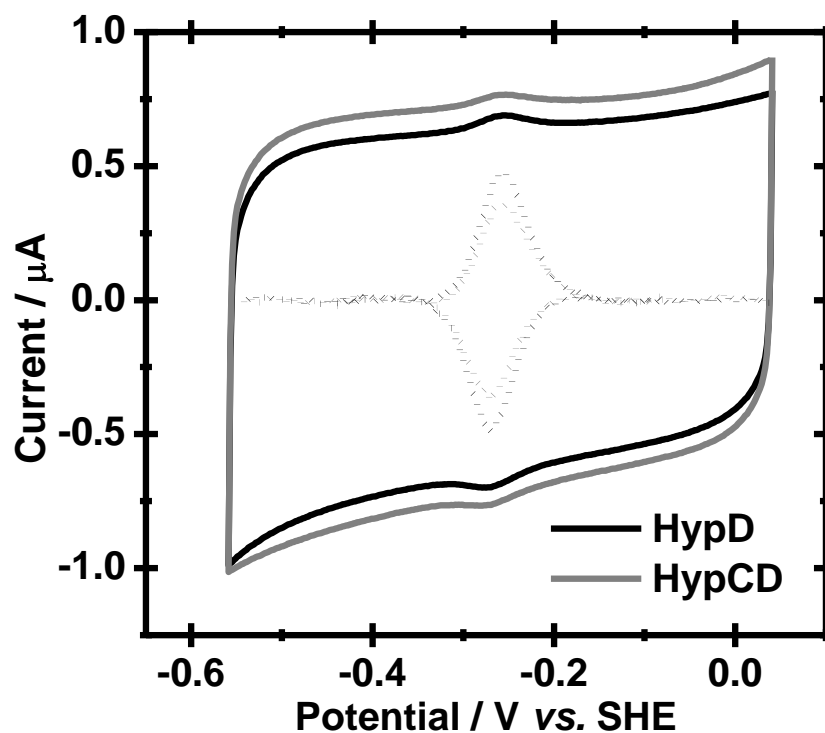
Figure S2. PFdcV of adsorbed HypD (black) and HypCD (grey) at 100 mV s^{-1}. Background corrected data are shown by a dashed lines and the current has been scaled by a multiplication factor of x 10. Other conditions: pH 7, 25°C, N$_2$ atmosphere.

3. FTacV of protein free blank PGE electrode

The 1st to 3rd harmonic components of an FTac voltammogram of a protein free blank PGE electrode exhibit a significant current due to the non-linear potential dependent capacitance. The current is small in harmonic 4 and negligible in harmonic 5.
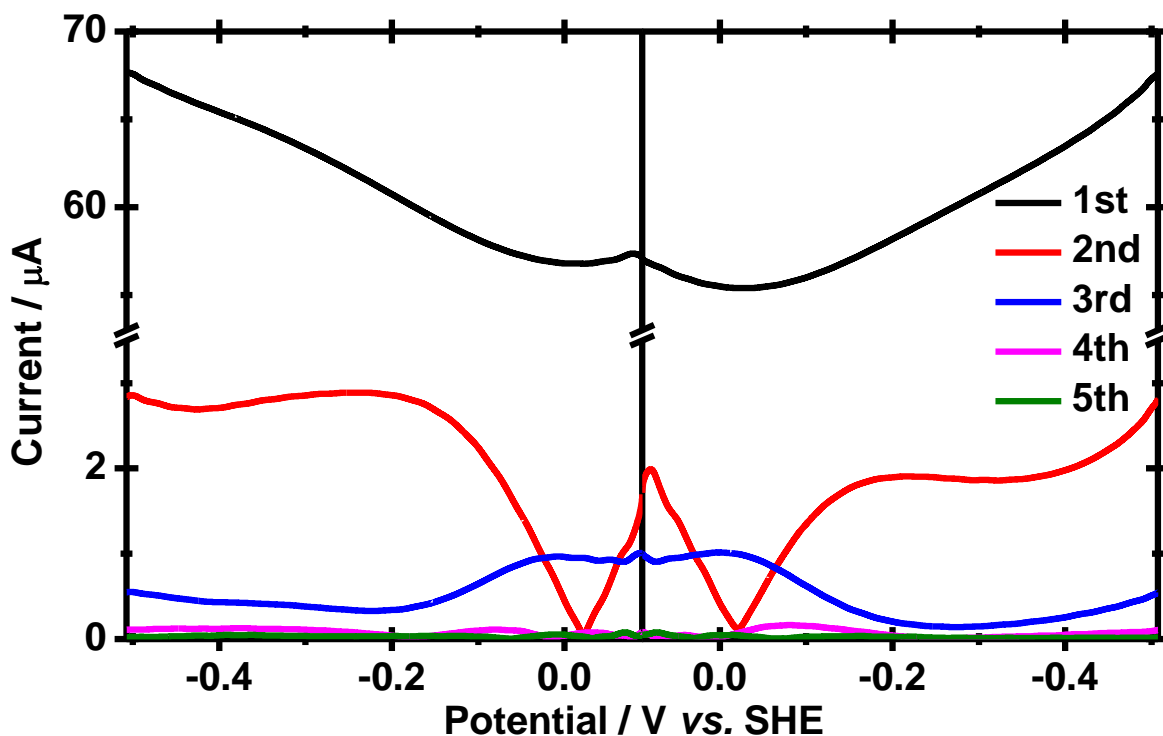
Figure S3. 1st to 5th harmonic components of FTac voltammogram for a protein free PGE electrode. Other conditions: scan rate = 22.35 mV s^{-1}, frequency = 9 Hz, amplitude = 150 mV, 25°C, N$_2$ atmosphere, pH 6.

4. Best fit parameters for capacitive background

Table S1. Fitted Capacitance Parameter Values (see Stage 1 - Fitting Capacitive Parameters, in main text)

Dataset	C_{dl} / Farad cm^{-2}	C_{dl1}	C_{dl2}	C_{dl3}
1	141e^{-6}	0.0196	6.40e^{-4}	6.95e^{-6}
2	287e^{-6}	0.0162	2.82e^{-4}	-1.63e^{-6}
3	a	a	a	a
4	253e^{-6}	0.0128	1.45e^{-5}	-6.81e^{-6}
5	a	a	a	a

[a] *No reasonable capacitance fit could be obtained for these datasets. Instead the parameters in the first row of the table were used for the Faradaic fitting stage. Since this stage uses only harmonics 4-12, the capacitance parameters have little effect on these results.*

5. Example outlier fit for two-electron transfer mode

Figure S4 shows an example of an outlier "best" fit for the PF-FTacV parameter estimation algorithm detailed in the main paper. While the objective function (equations (6) and (7) in the main paper) calculates a good fit comparable with the other parameter sets in Table 1, a quick look at the time domain data shows that this fit is erroneous, illustrating the care needed when drawing conclusions from complex multi-parameter data fitting problems.
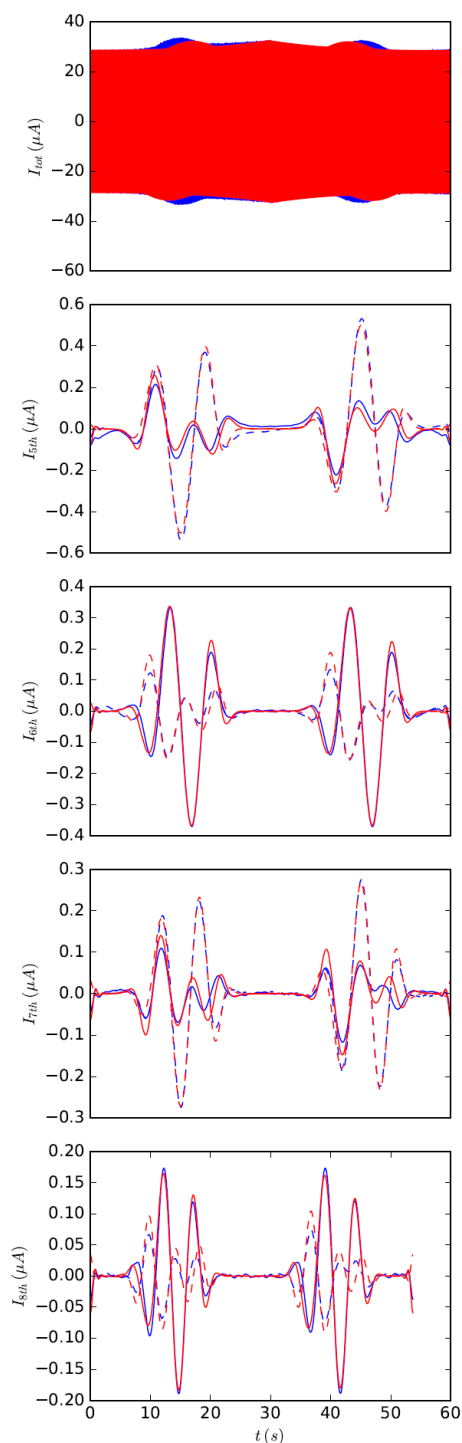
Figure S4. Comparison of the outlier parameter fit (red lines) and experimental data using the quasi-reversible model.

The top plot shows the total time domain current, and the remainder show different harmonics from the 5th-8th. The harmonic plots show the real (solid lines) and imaginary (dashed lines) components, and the filtered harmonics have been frequency shifted to a center frequency of zero.

The fitted parameters in this case were set to $k_1^{rev} = 3103.6$ s^{-1}, $k_2^{rev} > 4000$ s^{-1}, $E_1^{rev} = -0.0373$ V *vs* SHE, $E_2^{rev} = -0.38$ V *vs* SHE, $\zeta = 0.718$, and $\eta = 3.413$ rad. The objective function is $\mathcal{L}_f = 25821$, very similar to the other best fits obtained from the algorithm (see Table 1 in the main paper).

As can be seen from the figure, the simulated and experimental (total) time domain current are clearly different from each other, due to poor placements of the reversible potentials. However, the widely spaced reversible potentials combine to form harmonics that are indistinguishable from the experimental harmonics. Since the automated fitting process uses only the information provided from the 4th-12th harmonics, care must be taken to remove these obviously erroneous fits from the fitting process.

Additional Material

Introduction

Further work carried out on *E. coli* HypD is presented here, which was not included in the paper and will be the subject of future studies. The paper utilised data optimisation of low frequency (9 Hz) FTacV measurements because the optimisation of high frequency measurements was prohibitively slow. Low frequency measurements hindered the amount of kinetic information that could be extracted and the electron transfer and associated chemical steps had to be simply modelled as reversible. It is hoped that the data-optimisation process can be improved to handle high frequency measurements and permit full kinetic analysis, for both HypD and other proteins exhibiting fast electron transfer. A series of fast scan rate dcV and high frequency FTacV experiments were performed, to permit greater kinetic and mechanistic information to be extracted about the HypD disulphide redox reaction and with the aim of using such results in the advancement of FTacV data optimisation to high frequency. All experimental methods are as described in the paper. Additional work also probed the postulated ability of HypD to reduce CO_2 to CO, for insertion into the hydrogenase active site.(1,2)

Results and Discussion

The kinetics of the HypD disulphide redox process were first probed by repeating dcV measurements (Figure A1 A) at a range of scan rates between 0.01 and 100 Vs^{-1} and between pH 4 and pH 9. Trumpet plots (Chapter 2.6.3) of the baseline subtracted oxidative and reductive peak potentials versus scan rate at each pH are shown (Figure A1 B). At low scan rates that are slow compared to the electron transfer and coupled chemical reaction kinetics the peak separation should theoretically approach zero. However, this is not the case and a constant gap of ~10 mV remains. This non-ideality has been observed previously for surface confined proteins and other redox species and does not indicate slow kinetics, due to the constant separation with scan rate. (3-5) Above scan rates of ~10 V s^{-1} the oxidative and reductive peaks begin to separate significantly at each pH, suggesting that the scan rate is now fast compared to the electron transfer kinetics. However, at ~20 V s^{-1} the background capacitance current is very large (~200 µA) and so the influence of

the ~20 Ω uncompensated resistance and associated IR drop is now significant. Simulations of the voltammetric response in MECSim suggest that this uncompensated resistance will lead to ~20 mV peak separation at ~20 V s^{-1}, which is close to the actual peak separation of ~35 mV and so it is hard to unravel the influences of kinetics and uncompensated resistance.

(A)

(B)
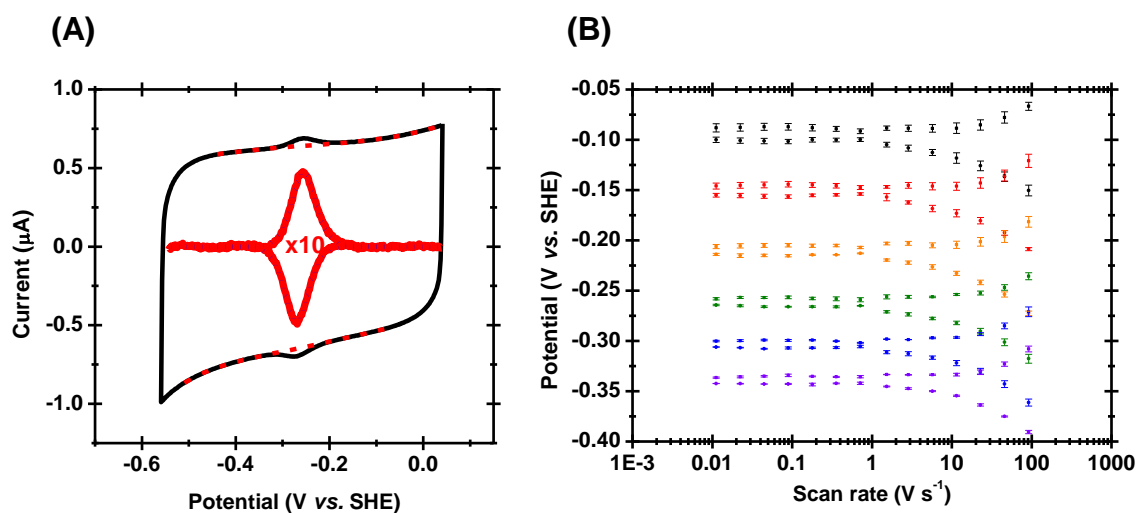
Figure A1 (A) Cyclic voltammetry of adsorbed HypD Experimental current shown in black, baseline in red dash, baseline subtracted current (x10) in red and fit to Equation A1 in blue dash. Other conditions: 100 mV s^{-1}, 100% N_2, pH 7 and 25°C. **(B) Trumpet plot of HypD oxidative and reductive peak potentials versus scan rate** Data shown for pH 4 (black), pH 5 (red), pH 6 (orange), pH 7 (green), pH 8 (blue) and pH 9 (purple). Error bars show standard error of three repeats.

The reductive peak potentials shift slightly more with increasing scan rate than the oxidative peak potentials. This can be due to a relatively slow chemical step associated with reduction or, as observed previously, could possibly be an artefact of chemical changes to the PGE surface.(4) Furthermore, the background capacitance current tends to be slightly larger for the reductive sweep and so the greater IR drop may also cause artefacts. Due to the inaccuracies in the large baseline subtractions employed at very fast scan rates and the potential artefacts described, little weight can be placed on the small asymmetry observed here.

Baseline subtracted peak currents show a linear dependence on scan rate up to ~ 1 V s^{-1} (Figure A2 A), which confirms a surface absorbed species. However, at higher scan rates there is an attenuation in the peak current away from this linear relationship (Figure A2 B). This is accompanied by broadening in the width of the peak. At low scan rate the peak width at half height ($W_{1/2}$) is ~ 60

mV and fitting to equation A1 (introduced in Chapter 4, Supplementary Information) gives $n_{app} \sim 1.5$.

$$i = \pm \frac{n_s n_{app} F^2 v A \Gamma}{RT} \frac{exp\{n_{app}F(E - E_p)/RT\}}{\left(1 + exp\{n_{app}F(E - E_p)/RT\}\right)^2} \qquad A1$$

This indicates a two-electron reaction comprising two consecutive one electron transfers of similar reduction potential, fully consistent with the results of FTacV data optimisation. However, at higher scan rates the n_{app} value decreases significantly (Figure A3 A), reflecting the broadening of peak width. The decrease in peak height is not simply due to the peak broadening, as there is also a decrease in the area of the peak with increasing scan rate. This is reflected in a decrease in the fitted surface coverage (Figure A3 B). The scans were performed from high scan rate to low scan rate and so the change in apparent surface coverage is not due to film loss.

(A)

(B)
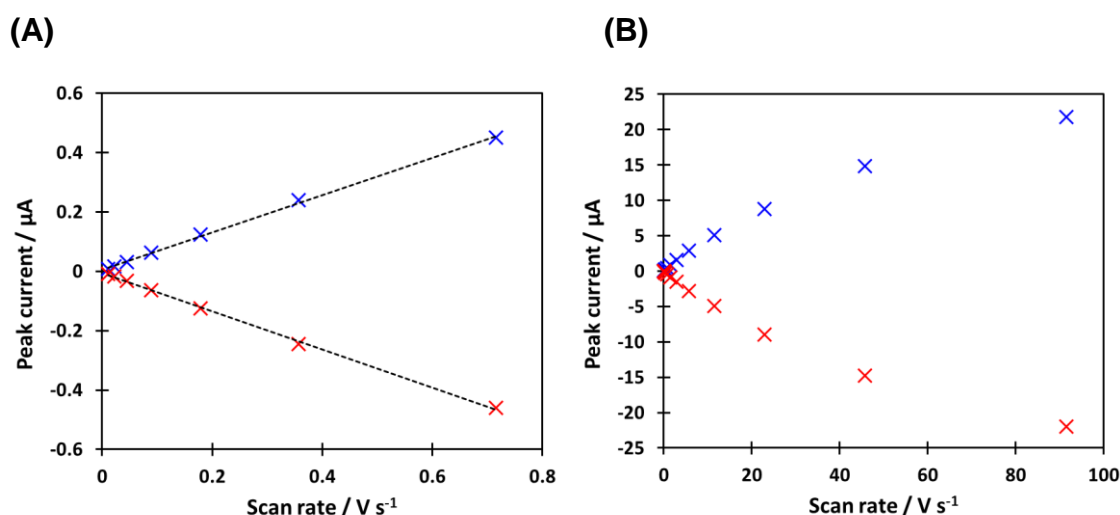
Figure A2 Peak current *vs*. scan rate plots for HypD redox process over A) low and B) high scan rate range Conditions: pH 7, 25°C, N_2 atmosphere.

It is tempting to relate the drop in n_{app} towards 1 and approximate halving in apparent surface coverage at fast scan rates to a shift from a two to one-electron reaction, by outpacing one of the electron transfers. However, these effects of peak broadening, decrease in peak height and decrease in peak area with scan rate have been observed previously and could occur for a number of reasons.(4,5) Peak broadening and decrease in peak height can be accounted for by Butler-Volmer or Marcus theories of electron transfer kinetics (5) but the significant uncompensated resistance could also be responsible. Thermodynamic and kinetic dispersion of protein on the electrode has been

theorised and shown to cause peak broadening (4-6) and poorly orientated enzyme could be outpaced at faster scan rates leading to decreased apparent surface coverage.(5) It must be acknowledged that inaccuracies in baseline subtraction, particularly of the extremely large capacitance currents at high scan rate, could also cause artefacts. Therefore, detailed mechanistic information cannot be extracted from these observations.

(A)   **(B)**
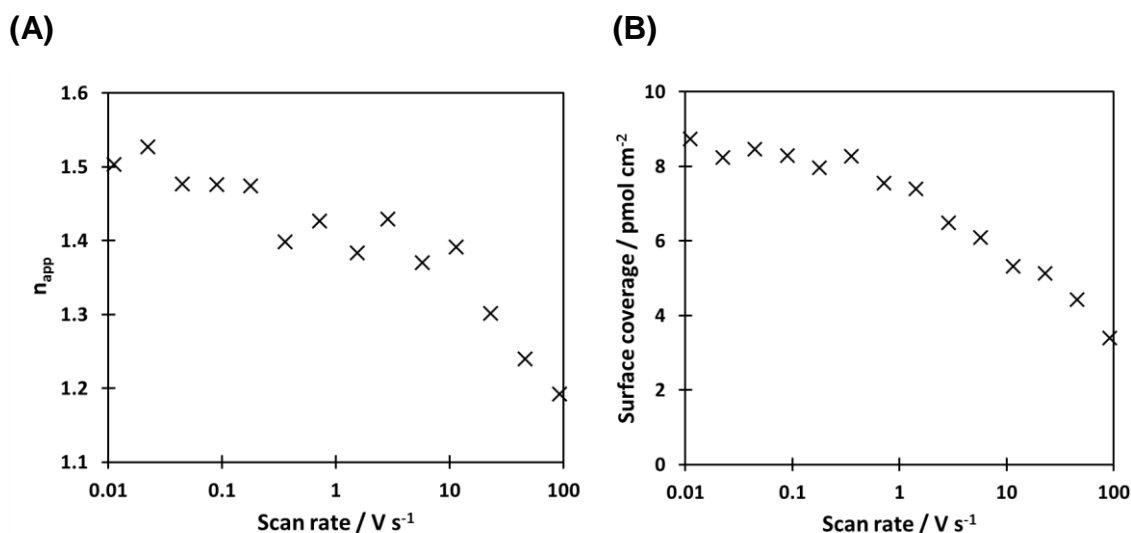
Figure A3 A) n_{app} electrons transferred and B) surface coverage of enzyme *vs.* scan rate for HypD Conditions: pH 7, 25°C, N_2 atmosphere.

The baseline-free high harmonic signals of FTacV should give results less prone to artefacts than the conventional dcV methodology. Furthermore, a single FTacV experiment contains a plethora of kinetic information because each harmonic essentially represents a different time scale. Therefore, kinetics can be studied in a single experiment, as compared with measurements at multiple scan rates with dcV, which introduces measurement to measurement inaccuracies. Higher frequency FTacV measurements access faster kinetic regimes. FTacV was performed on HypD at 22.35 mV s^{-1} and ΔE = 150 mV at frequencies of 9 to 144 Hz and between pH 4 and 9. At frequencies higher than 144 Hz the uncompensated resistance becomes significant. At each pH the harmonic responses remain well defined and consistent with reversible electron transfer, even up to the high tenth harmonic of a 144 Hz measurement. Figure A4 shows the 10th harmonic for f = 9 to 144 Hz at pH 7, as an example. This suggests it is hard to probe the kinetics of both electron transfer and coupled chemical steps, as they are both still reversible even in 144 Hz measurements. This could be due to the cysteines of the disulphide bond being held rigidly

close together by the protein structure to enable fast bond breaking / making and by proton transfer pathways making (de)protonation rapid. The electron transfer rates must be much faster than the >4000 s^{-1} predicted by data optimisation of 9 Hz measurements shown in the paper and so the peak splitting effects observed beyond ~10 V s^{-1} in dcV measurements must be largely due to artefacts, as discussed. This shows the importance of the more sensitive and accurate FTacV technique in determining kinetics. Advances in low uncompensated resistance electrochemical cells, FTacV instrumentation that can perform higher frequency measurements and efficient-data optimisation analysis procedures will be needed to probe beyond reversibility and measure the extremely fast kinetics of electron transfer and associated chemical steps observed here. Advances in FTacV data optimisation analysis to high frequency and incorporation of kinetic and thermodynamic models of dispersion [6] would also discern if this is responsible for the peak broadening and diminishing peak area with scan rate observed in dcV analysis.
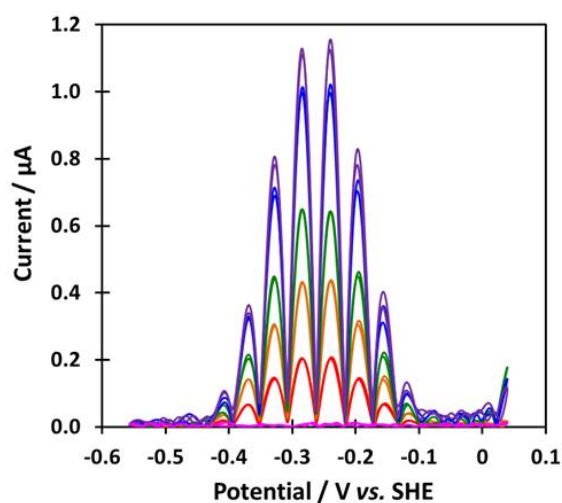
Figure A4 10th harmonic FTacV response of HypD Conditions: v = 22.35 mV s^{-1}, ΔE = 150 mV, pH 7, 25°C and N$_2$ atmosphere. Data shown is for f = 9 (red), 22 (orange), 39 (green), 89 (blue), 144 (purple) Hz. A blank is shown for 9 Hz (pink).

In the paper the HypD midpoint potential was observed to have a pH dependence of approximately −60 mV per pH unit between pH 4 and 6, reducing to approximately −38 mV per pH unit between pH 7 and 9. This is suggestive of a shift from a 2e$^-$ + 2H$^+$ towards a 2e$^-$ + 1H$^+$ reaction, implying that the pK$_a$ of one cysteine is ~7 and the other is above 9. However, the pH dependence of disulfide redox chemistry is more complex because of the bond making/breaking steps in the reaction scheme. Greater mechanistic understanding would be provided by data-optimisation of FTacV responses at

each pH, so that the pH dependence of the potential of each of the two electron transfers is known rather than just that of the midpoint potential.

Further to the study of HypD electron transfer reactions, experiments to test if CO_2 reduction catalysis could be observed were also performed, according to the recently postulated role of HypD in CO_2 reduction for CO insertion into the hydrogenase active site. (1, 2) No evidence of CO_2 reduction by HypD was observed in catalytic cyclic voltammetry experiments. Chronoamperometry experiments were then performed, as this allows much smaller catalytic currents to be measured than in cyclic voltammetry experiments because the background electrode capacitance processes only dominate in the first ~60s of the experiment. The potential was held at -0.608 V *vs.* SHE and the current measured in gas atmospheres of 100% CO_2 and 100% N_2 (Figure A5). There is sufficient thermodynamic driving force for CO_2 reduction at pH 6,(7) but no current corresponding to CO_2 reduction by HypD or HypCD was observed. The residual current under all conditions is due to graphite electrode processes. In comparable experiments conducted at 45°C and at pH 7 there was again no detectable CO_2 reduction current. This is unsurprising if the disulphide bond is responsible for catalysis because the measured midpoint potential is −0.21 V *vs.* SHE at pH 6, so CO_2 reduction would be thermodynamically unfavourable.
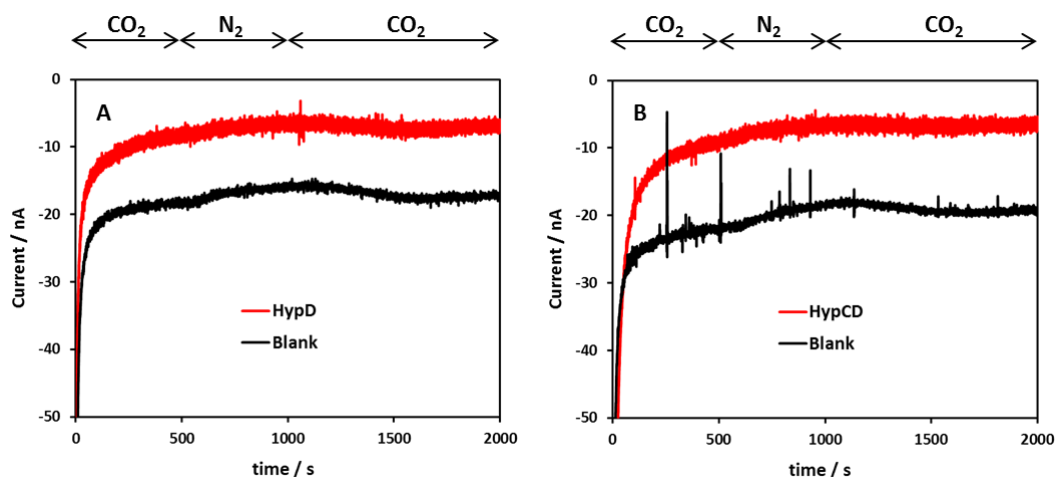
Figure A5 Chronoamperometry at −0.608 V *vs.* SHE of (A) HypD and (B) HypCD in the presence and absence of CO_2. Other conditions: 3000 rpm, 25°C, 0.2 M MES, pH 6.

Despite no CO_2 reduction activity being observed, the reverse reaction of CO oxidation has been observed at pH 7 in solution assays using methyl viologen as an electron acceptor (Gary Sawers, personal communication). Attempts were made to observe this CO oxidation by HypCD electrochemically. The

potential was held at -0.408 V *vs.* SHE, a potential with a comparable driving force for CO oxidation as methyl viologen, and the current measured in gas atmospheres of 100% CO and 100% N_2 (Figure A6). No CO oxidation current was observed. In comparable experiments conducted at −0.208 V *vs.* SHE, a potential greater than the disulphide midpoint potential of −0.26 V *vs.* SHE at pH 7, no CO oxidation was observed either.
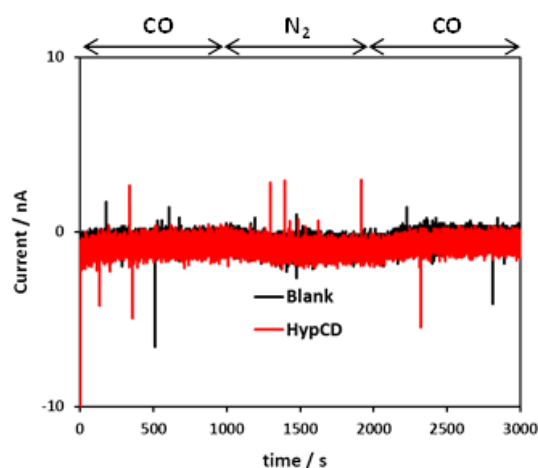
Figure A6 Chronoamperometry of HypCD at −0.408 V vs SHE in the presence and absence of CO Other conditions: 3000 rpm, 25°C, 0.2 M MES, pH 7.

It is most likely that the turnover rate of HypCD is too low to be detectable in electrochemical measurements. The assay measured turnover rate for CO oxidation by HypCD was 0.017 s^{-1} and from "non-turnover" experiments the electrochemical surface coverage of enzyme is known to be up to 8 pmol $cm^{−2}$. This would give an expected catalytic current of approximately 0.8 nA and so would be extremely difficult to measure above noise.

Conclusion

FTacV measurements provide a more sensitive and accurate measure of electron transfer kinetics than conventional dcV methods. However, advances in low uncompensated resistance cells and FTacV instrumentation that can perform higher frequency measurements are needed to probe the extremely fast kinetics of electron transfer and associated chemical steps observed in HypD. Furthermore, efficient-data optimisation procedures are required to analyse such high frequency measurements. Despite the extremely fast electron transfer kinetics, no evidence of the postulated catalytic CO_2 reduction or CO oxidation could be observed electrochemically; the former appearing thermodynamically unfavourable and the latter seemingly to slow for detection.

References

(1) Stripp, S.T., et al., HypD is the scaffold protein for Fe-(CN) 2CO cofactor assembly in [NiFe]-hydrogenase maturation. Biochemistry, 2013. **52**(19): p. 3289-3296.

(2) Stripp, S.T., et al., The Influence of Oxygen on [NiFe]–Hydrogenase Cofactor Biosynthesis and How Ligation of Carbon Monoxide Precedes Cyanation. PloS one, 2014. **9**(9): p. e107488.

(3) Feldberg, S.W. and I. Rubinstein, Unusual quasi-reversibility (UQR) or apparent non-kinetic hysteresis in cyclic voltammetry: an elaboration upon the implications of N-shaped free energy relationships as explanation. Journal of electroanalytical chemistry and interfacial electrochemistry, 1988. **240**(1-2): p. 1-15.

(4) Armstrong, F.A., et al., Fast voltammetric studies of the kinetics and energetics of coupled electron-transfer reactions in proteins. Faraday discussions, 2000. **116**: p. 191-203.

(5) Hirst, J. and F.A. Armstrong, Fast-scan cyclic voltammetry of protein films on pyrolytic graphite edge electrodes: characteristics of electron exchange. Analytical chemistry, 1998. **70**(23): p. 5062-5071.

(6) Morris, G.P., et al., Theoretical analysis of the relative significance of thermodynamic and kinetic dispersion in the dc and ac voltammetry of surface-confined molecules. Langmuir, 2015. **31**(17): p. 4996-5004.

(7) Parkin, A., et al., Rapid and efficient electrocatalytic CO2/CO interconversions by Carboxydothermus hydrogenoformans CO dehydrogenase I on an electrode. Journal of the American Chemical Society, 2007. **129**(34): p. 10328-10329.

Chapter 6

Site-directed mutagenesis and purification of *Escherichia coli* hydrogenase-1

6.1   Introduction

In Nature hydrogenases provide energy for organisms through H_2 oxidation and balance cell redox potentials by removing reducing equivalents through H_2 production or providing electrons by hydrogen oxidation.[1, 2] They are remarkable metalloenzymes that perform this efficient interconversion of protons and hydrogen at abundant metal active sites of [Fe], [FeFe] or [NiFe].[1-3] *E. coli* hydrogenase-1 is a membrane-bound [NiFe]-hydrogenase, comprising a large subunit housing the active site and a small subunit containing three iron-sulphur clusters that act as a relay to transfer electrons to and from the active site (Figure 6.1).[4, 5]
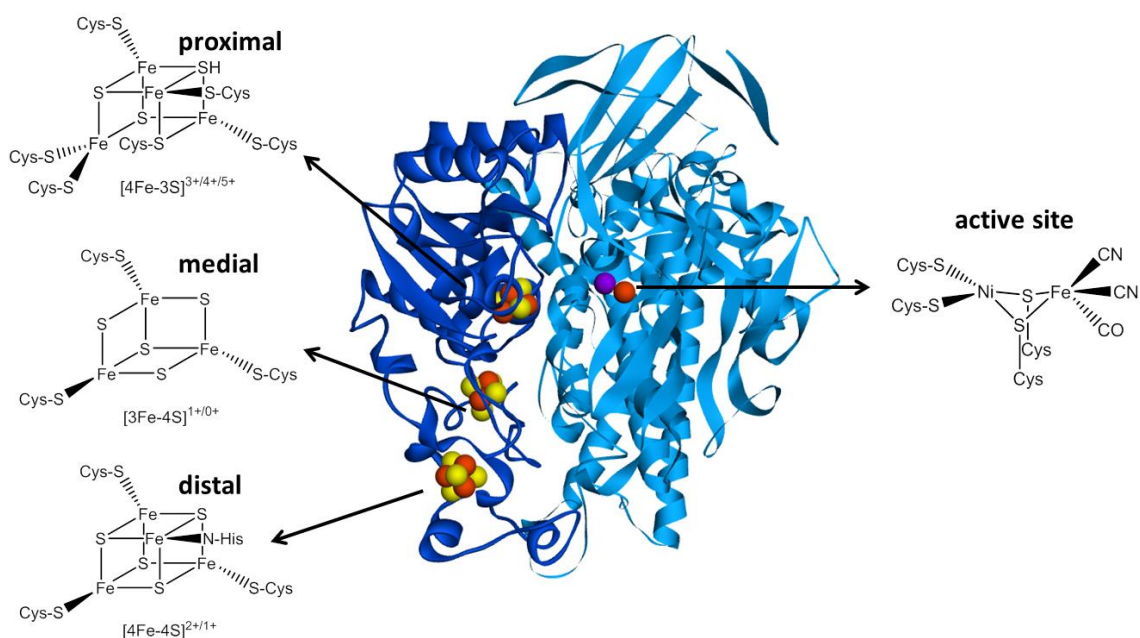
Figure 6.1 Structure of *E. coli* hydrogenase-1. The large subunit (cyan) houses the [NiFe] active site and small subunit (blue) contains the proximal [4Fe3S], medial [3Fe4S] and distal [4Fe4S] clusters. Pdb code: 4C3O

E. coli hydrogenase-1 belongs to the specific subclass of O_2-tolerant [NiFe]-hydrogenases that are able to maintain catalysis in oxygen and have garnered significant interest for use in technological applications.[5-8] The O_2-tolerance enables use in H_2/O_2 mixed feed fuel cells (Chapter 1.1.5) [9-11] and hydrogen producing solar fuel devices with concomitant water splitting to O_2 (Chapter 1.1.5).[12-14] However, the O_2-tolerant hydrogenases have increased overpotential (Chapter 1.3.3) for hydrogen oxidation and greater catalytic bias (Chapter 1.3.3) towards hydrogen oxidation, compared to their O_2-sensitive counterparts (Figure 6.2).[6, 15, 16]
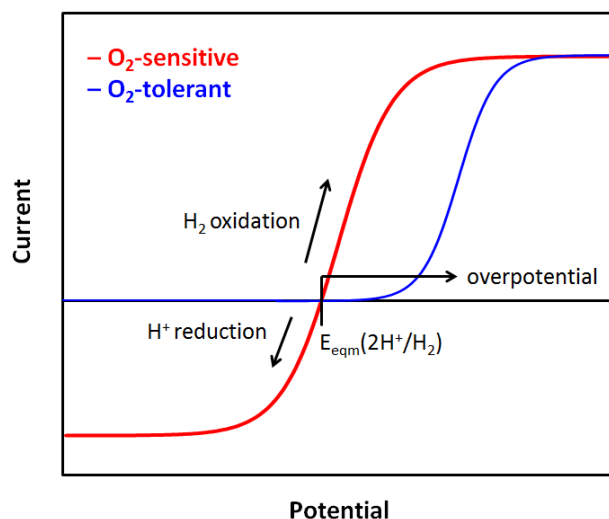
Figure 6.2 Typical voltammetric responses of O$_2$-sensitive and O$_2$-tolerant [NiFe]-hydrogenases in a hydrogen atmosphere.

The overpotential represents an energy loss in fuel cells [9] and the catalytic bias precludes significant hydrogen production in solar fuel devices.[17] [NiFeSe]-hydrogenases, in which selenocysteine replaces a cysteine at the active site, have some O$_2$-tolerance and enhanced bias towards H$_2$-production, so are often used in solar fuel devices.[17-19]

The molecular control of overpotential and catalytic bias in *E. coli* hydrogenase-1 is studied electrochemically in Chapter 7. This is done in accordance with the model outlined in Chapter 2.6.7, in which the potential of the distal iron sulphur cluster where electrons enter and exit the enzyme controls these key catalytic properties.[20, 21] A catalytically inactive but otherwise structurally and electronically sound variant needed to be generated, to remove catalytic current from the reduction of protons ubiquitously present in solution and unmask the underlying non-turnover electron transfer current. A distal cluster variant with altered reduction potential also needed to be produced, to fingerprint the source of the electron transfer signal and to assess the effect of the distal cluster on overpotential and bias. This chapter describes the design and generation of the inactive and distal cluster variants.

E. coli hydrogenase-1 is encoded by the *hyaABCDEF* operon; *hyaA* encodes the small subunit, *hyaB* the large subunit, *hyaC* a membrane associated cytochrome and *hyaD, hyaE* and *hyaF* encode maturase and chaperone proteins.[1, 22] Further complex maturation machinery encoded by the *hypABCDEF* operon is required to assemble the iron-sulphur clusters and

[NiFe] active site containing biologically unusual CO and CN ligands.[1, 23, 24] Additional proteins may be required for complete successful construction of the enzyme.[23, 25] As the multistage process of assembly is not yet fully understood, it is hard to construct a plasmid containing the full complement of necessary genes for successful overexpression of *E. coli* hydrogenase-1.[24, 26] As such, all variants of hydrogenase-1 produced in this study were generated by making chromosomal mutations and natively expressing the protein, as is the standard literature approach.[7, 26-28]

6.2 Design of variants

6.2.1 *hyaB* variant

An E28Q mutation in *hyaB* (Figure 6.3) was chosen to generate the inactive variant. This was based on previous studies on the equivalent E25Q variant of the *Desulfovibrio fructosovorans* [NiFe]-hydrogenase, in which exchange of this conserved glutamic acid close to the active site for a glutamine residue resulted in total loss of activity.[29, 30] The spectroscopic properties and para-H_2/ortho-H_2 conversion were not affected and so the enzyme, along with its iron-sulphur clusters and active site, was otherwise correctly assembled and structurally sound. There has since been a further example in which the equivalent E17Q variant of the *Pyrococcus furiosus* soluble [NiFe]-hydrogenase had significantly diminished activity.[31] E28 is proposed to be an essential proton transfer residue, so its exchange for a non-ionisable residue results in catalytic inactivity.
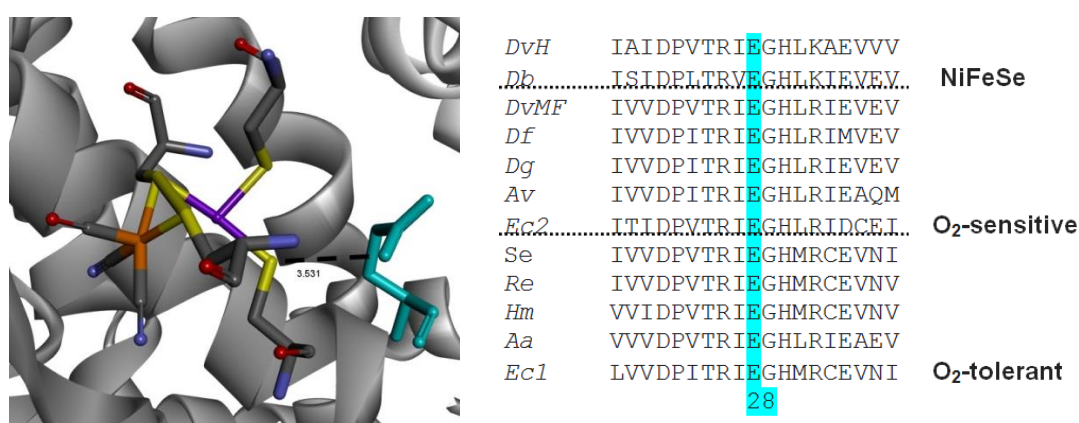
Figure 6.3 Structure and sequence alignment of HyaB. *E.coli* hydrogenase-1 structure (PDB 43CO), with the distance between the active site and residue E28 (cyan) shown in Å. *Dv*H = *D. vulgaris* Hildenborough, *Db* = *Dm. baculatum*, *Dv*MF = *D. vulgaris* Miyazaki F, *Df* = *D. fructosovorans*, *Dg* = *D. gigas*, *Av* = *A. vinosum*, *Ec*2 = *E. coli* Hyd-2, *Se* = *S. enterica* Hyd-5, *Re* = *R. eutropha* MBH, *Hm* = *H. marinus*, *Aa* = *A. aeolicus*, *Ec*1 = *E. coli* Hyd-1. Numbering used is for *E. coli* Hyd-1 and residue 28 is highlighted in cyan.

6.2.2 *hyaA* variants

In the only previous mutagenesis study focused on the distal iron-sulphur cluster of a [NiFe]-hydrogenase the conserved histidine ligand of the distal cluster was exchanged for cysteine and glycine residues, in *Desulfovibrio fructosovorans* [NiFe]-hydrogenase.[32] This resulted in severely impaired rates of interfacial and intramolecular electron transfer, such that this was rate limiting and fine tuning of catalytic bias and overpotential could not be studied.[32] As a starting point in the design of a distal cluster variant with altered reduction potential, the equivalent mutations were made in *E. coli* Hyd-1 (H187C and H187G) along with H187S. The objective was to remove the histidine ligation (H187G) or alter the hard / soft nature of the ligand (H187C/S), in the aim of changing the reduction potential of the cluster. A similar strategy was employed in exchanging a conserved cysteine ligand for glycine and histidine (C190G and C190H).

As well as exchanging direct ligands of the distal cluster, a more subtle approach exchanging residues close to the cluster was also employed. A number of residues around the distal cluster seem to be generally different between O_2-tolerant and the O_2-sensitive [NiFe]-hydrogenases (Figure 6.4), which are thought to have a lower distal cluster potential, resulting in greater bias towards H_2 production and a lower overpotential for H_2 oxidation. Quite often a positive or neutral residue in an O_2-tolerant hydrogenase is exchanged for a neutral or negative residue in an O_2-sensitive or NiFeSe hydrogenase (Figure 6.4). It is well known that second coordination sphere effects can alter the reduction potentials of redox centres [33-35] and there have been numerous examples for FeS clusters.[36-41] A number of residues close to the distal cluster in *E. coli* Hyd-1 were therefore exchanged for the equivalent residue found in an O_2-sensitive [NiFe]-hydrogenase, with the aim of lowering the cluster potential. An R185L variant was generated, with the positively charged arginine exchanged to the neutral leucine residue found in *E. coli* Hyd-2 O_2-sensitive [NiFe]-hydrogenase. K189H and K189N variants were generated with the positively charged lysine residue exchanged for the ionisable histidine residue found in *E. coli* Hyd-2 and the neutral asparagine residue found in *D. fructosovorans and D. gigas* O_2-sensitive [NiFe]-hydrogenases. A Y191E variant was generated with the neutral aromatic tyrosine residue exchanged for

the negatively charged glutamic acid residue found in *E. coli* Hyd-2. An R193L variant was generated with the positively charged arginine exchanged for the neutral leucine residue found in many O_2-sensitive [NiFe]-hydrogenases. Based on the *E. coli* Hyd-1 structure, R193L was considered to be a particularly promising variant, as the 3.6 Å distance between the arginine residue and the conserved histidine ligand of the distal cluster suggests a pi-cation interaction is present between the two residues (Figure 6.4). Introducing a neutral leucine residue would remove this pi-cation interaction; the interaction should stabilise the reduced cluster and so its removal may be expected to result in a reduction in the cluster potential.
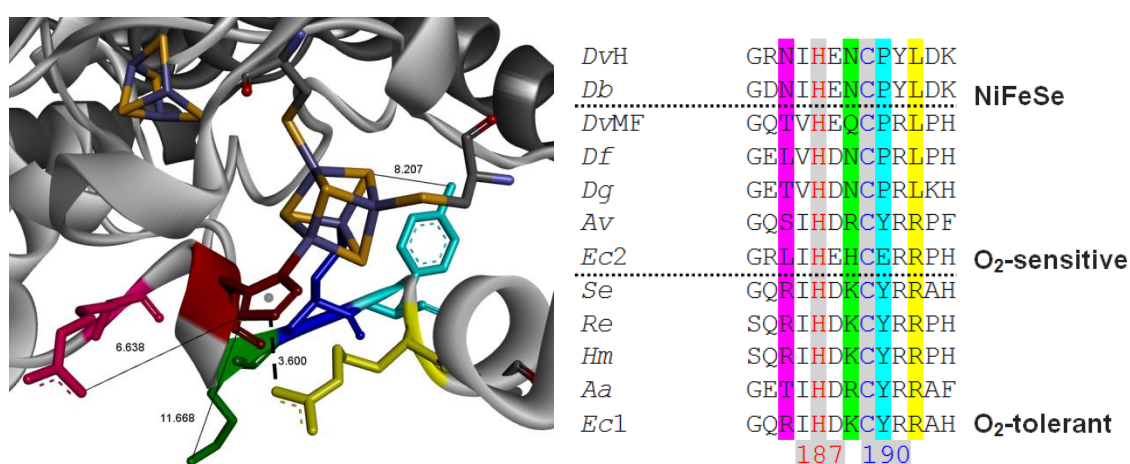
Figure 6.4 Structure and sequence alignment of HyaA. Structure of *E.coli* hydrogenase-1 (PDB 43CO) with residues around the distal iron-sulphur cluster highlighted; R185 (pink), H187 (red), K189 (green), C190 (blue), Y191 (cyan) and R193 (yellow). Distances are in shown in Å. *Dv*H = *D. vulgaris* Hildenborough, *Db* = *Dm. baculatum*, *Dv*MF = *D. vulgaris* Miyazaki F, *Df* = *D. fructosovorans*, *Dg* = *D. gigas*, *Av* = *A. vinosum, Ec*2 = *E. coli* Hyd-2, *Se* = *S. enterica* Hyd-5, *Re* = *R. eutropha* MBH, *Hm* = *H. marinus, Aa* = *A. aeolicus, Ec*1 = *E. coli* Hyd-1. Conserved residues that ligate the distal iron-sulphur cluster are highlighted in grey, with residues 187 and 190 written in red and blue, respectively. Highlighted residues are 185 (pink), 189 (green), 191 (cyan) and 193 (yellow). Numbering used is for *E. coli* Hyd-1.

6.3   Construction of variants

6.3.1   Red/ET recombination methodology

All variant strains were generated by making chromosomal mutations with the Counter-Selection BAC Modification Kit (Cambio), using the modified streptomycin counter selection protocol of Heermann *et al*,[42] as previously described by Flanagan *et al*.[26] The general methodology for insertion of a point mutation into the chromosome by Red/ET homologous recombination and streptomycin counter selection is outlined here. The technical protocols and

tables of strains, plasmids, primers and linear DNA used, are described in Chapters 3.5 and 3.6.

The Counter-Selection BAC Modification Kit (Cambio) provides the pRedET expression plasmid. This carries the *red*γβα operon expressed under the control of the pBAD promoter, so expression of the Redα/Redβ recombinase protein pair that performs the double-stranded break repair of homologous recombination is arabinose inducible. The plasmid also carries the *tetR* gene, conferring ampicillin resistance and the *repA* gene, which makes replication temperature sensitive. The kit also contains *rpsL*-neo template DNA, which is a PCR-template for generating an *rpsL*-neomycin (kanamycin) counter-selection/selection cassette. It contains genes conferring kanamycin resistance and streptomycin sensitivity to enable counter selection, upon insertion and removal from the chromosome. Counter selection is possible for strains originally carrying a streptomycin resistance mutation in the *rpsL* gene because the resistance is recessive when the wild-type allele conferring streptomycin sensitivity is also present, upon introduction of the cassette.

The "native" strain from which all variant strains described in this thesis were derived is the W3110-derived *E. coli* K-12 strain LAF003.[26] This was kindly donated by Lindsey Flanagan (Department of Biology, University of York) and has an engineered *hyaA*(*his₇*)*BCDEF* operon that produces "wild-type" *E. coli* hydrogenase-1 with a polyhistidine tag at the C terminus of the small subunit.[26] The strain has the *rpsL*150 allele (strepR) to enable streptomycin counter selection and contains the pRedET expression plasmid. General growth was at 30°C with ampicillin, to maintain the temperature sensitive plasmid. In the first step of the recombination methodology, an increase in temperature from 30°C to 37°C and addition of L-arabinose induces expression of the genes mediating Red/ET recombination and the cells are then made chemically competent (Chapter 3.5.6). A linear *rpsL*-neo cassette flanked by appropriate homology arms for insertion at the desired locus is generated by PCR amplification (Chapter 3.5.1), checked by DNA gel (Chapter 3.5.2), purified (Chapter 3.5.3) and then transformed into the competent cells via heat shock (Chapter 3.5.7) (Figure 6.5 A). The cassette is inserted into the target locus by Red/ET recombination and colonies with the modified chromosome are selected for by growth on kanamycin and checked by colony PCR (Chapter 3.5.1). This

generates a strain carrying the cassette at the desired locus. In the next step, expression of the recombinase proteins is induced in this strain and the cells are made chemically competent (Chapter 3.5.6). Non-selectable linear DNA carrying the desired point mutation and at least 50 base pairs of homology on either side is produced by PCR amplification (Chapter 3.5.1), checked by DNA gel (Chapter 3.5.2), purified (Chapter 3.5.3) and then transformed into the competent cells by heat shock (Chapter 3.5.7) (Figure 6.5 B). Red/ET recombination replaces the *rpsL*-neo cassette with the non-selectable DNA and modified colonies lacking the cassette (and so wild type *rpsL* gene) are selected for by growth on streptomycin. Removal of the cassette is checked by colony PCR and sequencing confirms if the desired mutation has been introduced (Chapter 3.5.4). The variant strains derived from LAF003 are detailed here and tabulated in Chapter 3.6.1.
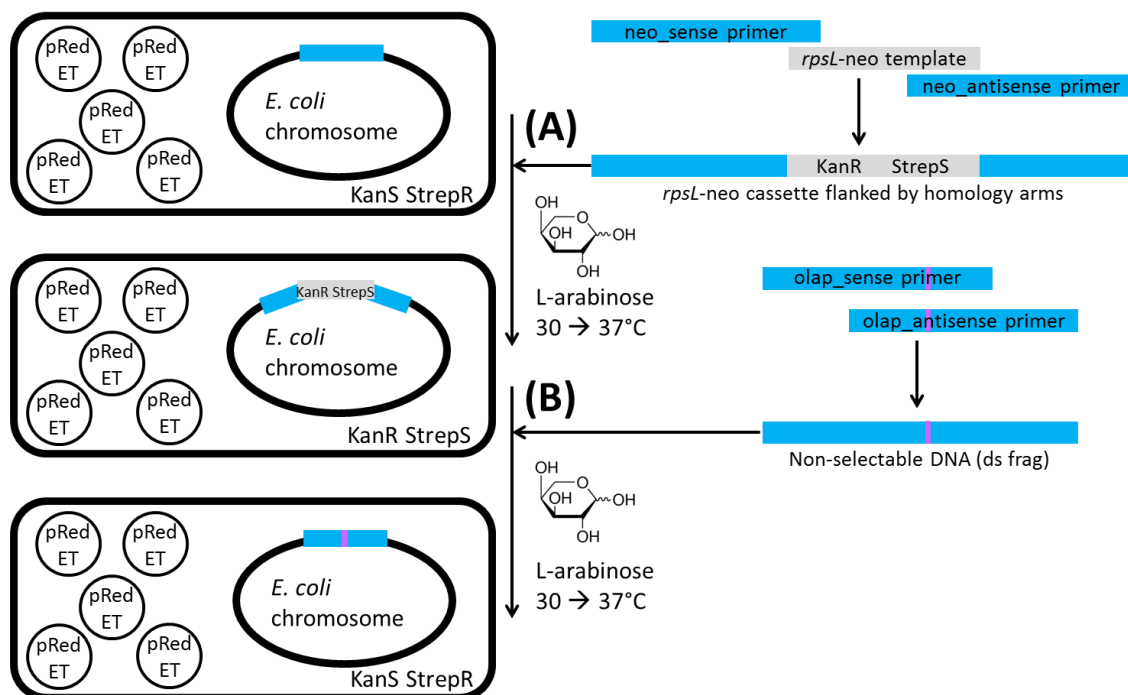
Figure 6.5. Red/ET recombination methodology

6.3.2 Generation of *hyaB* variant

Using the methodology described (Chapter 6.3.1) an E28Q mutation was introduced to *hyaB* to generate strain HA003, which produces hydrogenase-1 with a polyhistidine tag at the C terminus of the small subunit (HyaA) and an E28Q mutation in the large subunit (HyaB) (Figure 6.6).
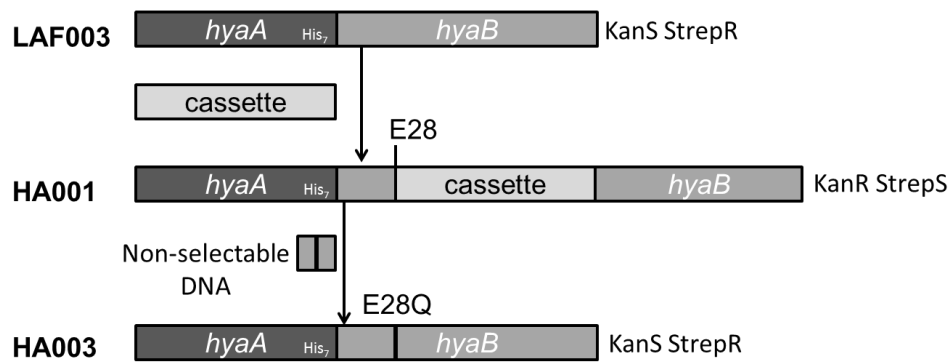
Figure 6.6 Generation of the *hyaB* variant

Generation of the ~1.4 kb *rpsL*-neo cassette flanked by appropriate homology arms (HyaB_E28Q_neo, Chapter 3.6.4, Table 3.9) from PCR amplification of the *rpsL*-neo template and homology arm primers (hyaB_E28Q_neo_sense, hyaB_E28Q_neo_antisense, Chapter 3.6.3, Table 3.8) was confirmed by agarose DNA gel (Figure 6.7 A).
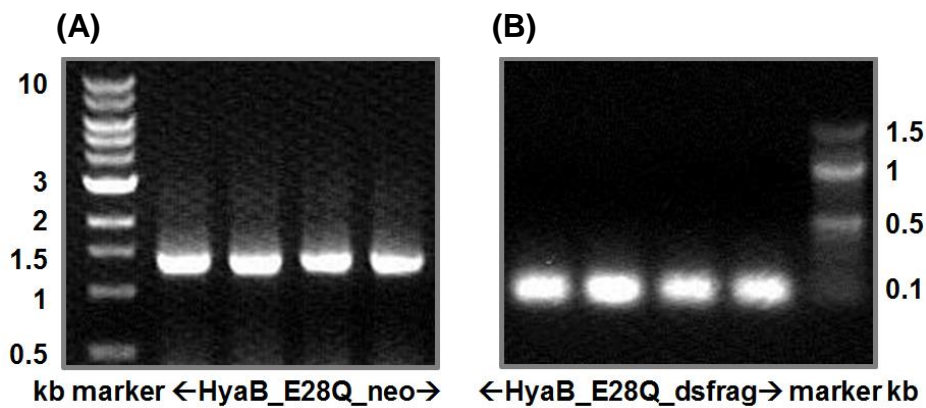
Figure 6.7 Agarose DNA gel of (A) ~1.4 kb HyaB_E28Q_neo cassette linear DNA (B) ~0.1 kb HyaB_E28Q_dsfrag non-selectable linear DNA.

Successful transformation of HyaB_E28Q_neo DNA into competent LAF003 cells was confirmed by colony PCR using primers hyaB_check_sense and hyaB_check_antisense (Chapter 3.6.3, Table 3.8). An agarose DNA gel on the PCR products confirmed the increase in length of DNA between the primers, from ~1 kb to ~2.3 kb (Figure 6.8), indicating successful insertion of the cassette into the chromosome and generation of strain HA001. This was confirmed by sequencing (Figure 6.9 A).
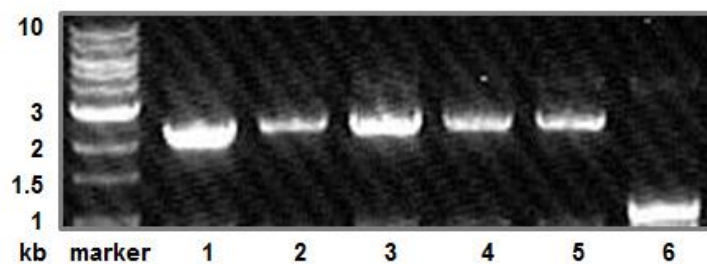
Figure 6.8 Agarose DNA gel of HA001 (lane 2-5) and HA003 (lane 6) colony PCR products

Generation of the ~0.1 kb non-selectable linear DNA carrying the E28Q mutation (HyaB_E28Q_dsfrag, Chapter 3.6.4, Table 3.9) from PCR amplification of primers HyaB_E28Q_olap_sense and HyaB_E28Q_olap_antisense (Chapter 3.6.3, Table 3.8) was confirmed by agarose DNA gel (Figure 6.7 B). Successful transformation of HyaB_E28Q_dsfrag DNA into competent HA001 cells was confirmed by colony PCR using primers hyaB_check_sense and hyaB_check_antisense (Chapter 3.6.3, Table 3.8). An agarose DNA gel on the PCR products confirmed the decrease in length of DNA between the primers, from ~2.3 kb to ~1 kb (Figure 6.8), indicating successful removal of the cassette from the chromosome and generation of strain HA003. Introduction of the E28Q mutation was confirmed by sequencing (Figure 6.9 B).

 (A)   (B)
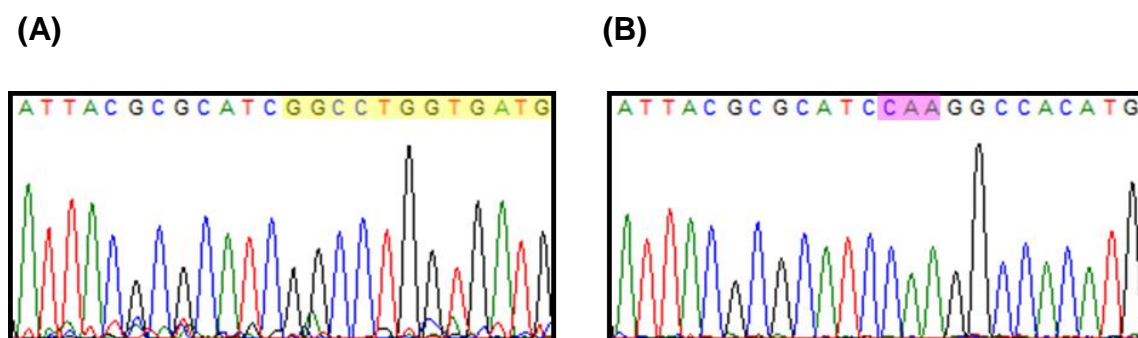
Figure 6.9. Sequencing of *hyaB* near position E28 for (A) HA001 and (B) HA003. Cassette DNA is highlighted in yellow and the E28Q mutation (gaa to caa) is highlighted in pink.

6.3.3 Generation of *hyaA* variants

Using the methodology described (Chapter 6.3.1) a number of single-site mutations were introduced to *hyaA* to generate strains HA004 to HA014, which produce hydrogenase-1 variants with a polyhistidine tag at the C terminus of the small subunit (HyaA) and a single-site mutation in the small subunit (HyaA) (Figure 6.10). All strains were made via a single intermediate strain HA002, with

the cassette inserted at position K189 of *hyaA*. This was possible because all mutations were made within 4 amino acids of K189, so there was sufficient homology for successful recombination to occur when swapping out the cassette for non-selectable DNA. This greatly increased the efficiency of variant generation.
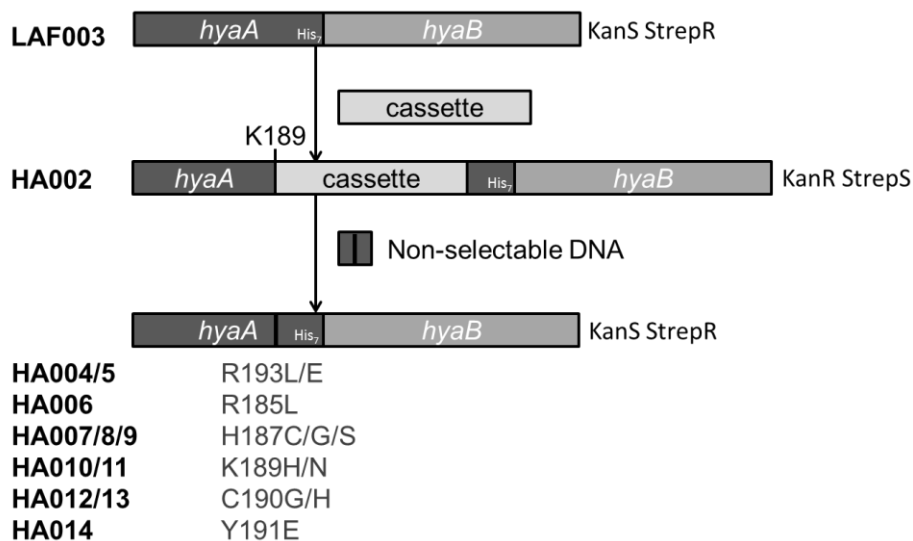
Figure 6.10 Generation of the *hyaA* variants

Generation of the ~1.4 kb *rpsL*-neo cassette flanked by appropriate homology arms (HyaA_K189_neo, Chapter 3.6.4, Table 3.9) from PCR amplification of the *rpsL*-neo template and homology arm primers (hyaA_K189_neo_sense, hyaA_K189_neo_antisense, Chapter 3.6.3, Table 3.8) was confirmed by agarose DNA gel (Figure 6.11 A).
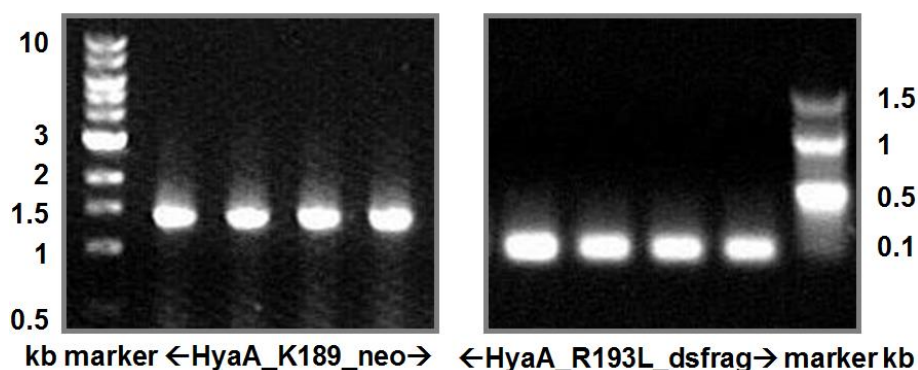
Figure 6.11 Agarose DNA gel of (A) ~1.4 kb HyaA_K189_neo cassette linear DNA (B) ~0.1 kb HyaA_R193L_dsfrag non-selectable linear DNA.

Successful transformation of HyaA_K189_neo DNA into competent LAF003 cells was confirmed by colony PCR using primers hyaA_check_sense and hyaB_check_antisense (Chapter 3.6.3, Table 3.8). An agarose DNA gel on the

PCR products confirmed the increase in length of DNA between the primers, from ~1.4 kb to ~2.7 kb (Figure 6.12 A), indicating successful insertion of the cassette into the chromosome and generation of strain HA002. This was confirmed by sequencing (Figure 6.13 A).
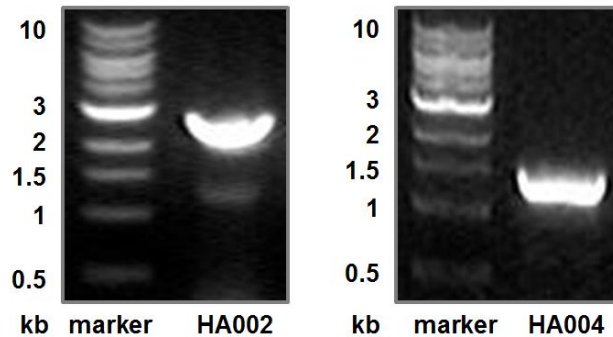
Figure 6.12. Agarose DNA gel of colony PCR products of (A) HA002 and (B) HA004

Generation of the ~0.1 kb non-selectable linear DNA carrying the R193L mutation (HyaA_R193L_dsfrag, Chapter 3.6.4, Table 3.9) from PCR amplification of primers HyaA_R193L_olap_sense and HyaA_R193L_olap_antisense (Chapter 3.6.3, Table 3.8) was confirmed by agarose DNA gel (Figure 6.11 B). Successful transformation of HyaA_R193L_dsfrag DNA into competent HA002 cells was confirmed by colony PCR using primers hyaA_check_sense and hyaB_check_antisense (Chapter 3.6.3, Table 3.8). An agarose DNA gel on the PCR products confirmed the decrease in length of DNA between the primers, from ~2.7 kb to ~1.4 kb (Figure 6.12 B), indicating successful removal of the cassette from the chromosome and generation of strain HA004. Introduction of the R193L mutation was confirmed by sequencing (Figure 6.13 B).
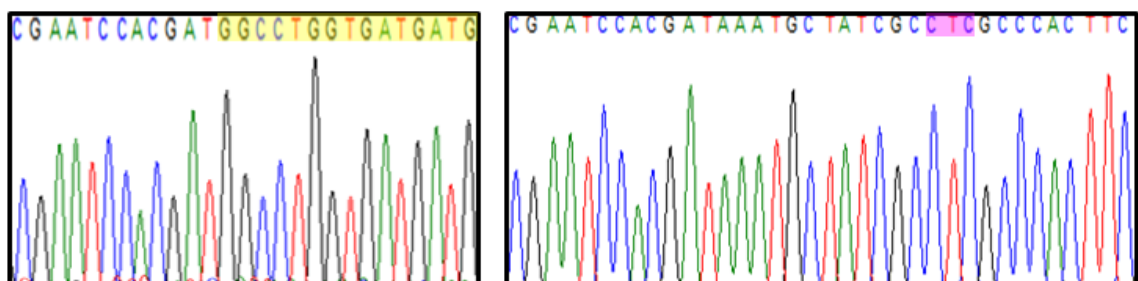
Fig 6.13. Sequencing of *hyaA* near position K189 for (A) HA002 and (B) HA004. Cassette DNA is highlighted in yellow and the R193L mutation (cgc to ctc) is highlighted in pink.

All other *hyaA* variant strains (HA005-HA014) were derived from HA002 in the same way as HA004; swapping out the cassette with non-selectable linear DNA carrying the desired mutation (Chapter 3.6.4, Table 3.9). Table 6.1 shows the sequencing of strains HA005 – HA014, used to confirm the correct single-site mutations to *hyaA*.

Table 6.1 Sequencing of strains HA005 – HA014

Strain	Mutation to *hyaA*	Sequencing
HA005	R193E	
HA006	R185L	
HA007	H187C	
HA008	H187G	
HA009	H187S	
HA010	K189H	

HA011	K189N	
HA012	C190G	
HA013	C190H	
HA014	Y191E	

6.4   Purification of variants

The results of protein purifications are described here and full details of purification protocols are provided in Chapter 3.7. A modified version of the methods described by Flanagan *et al* was used.[26] To initially screen the expression, purification and activity of hydrogenase-1 from strains LAF003 and HA003 – HA014, 12 – 18 L growths of each strain were cultured anaerobically and harvested at stationary phase, to maximise natural expression. Cell pellet yields were ~ 3.3 g L^{-1} for all strains. Following lysis and solubilisation, protein was purified on a HiTrap Ni affinity column with a gradient imidazole elution (0.05 M to 1 M). A typical elution profile and the associated SDS-PAGE analysis is shown for strain LAF003 (Figure 6.14).
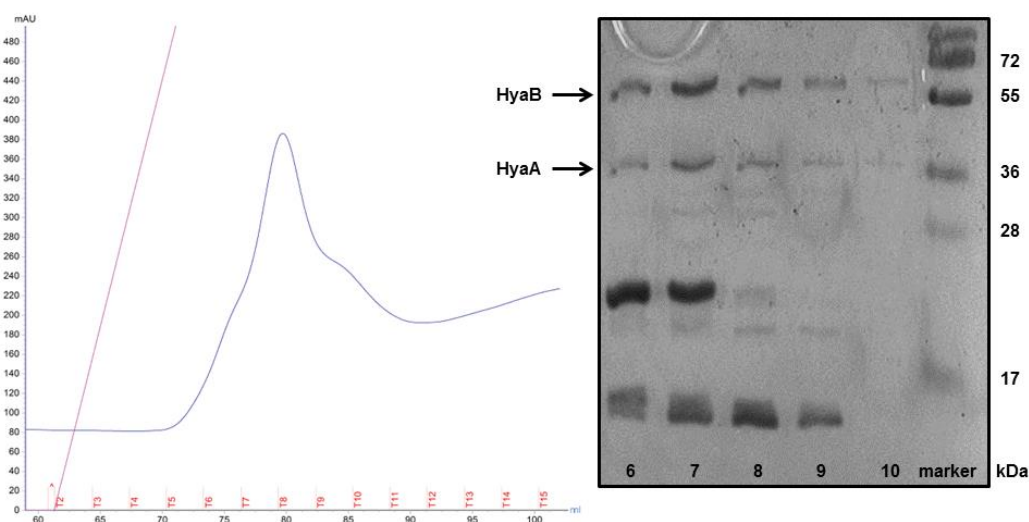
Figure 6.14. Typical elution profile shown for protein isolated from LAF003 and SDS-PAGE of fractions 6 to 10

Fractions containing hydrogenase were pooled, dialysed into buffer C (pH 7.3, 20 mM Tris, 150 mM NaCl) and concentrated into ~ 500 µl samples. This was done for all strains and SDS-PAGE analysis of protein isolated from each strain is shown in Figure 6.15.
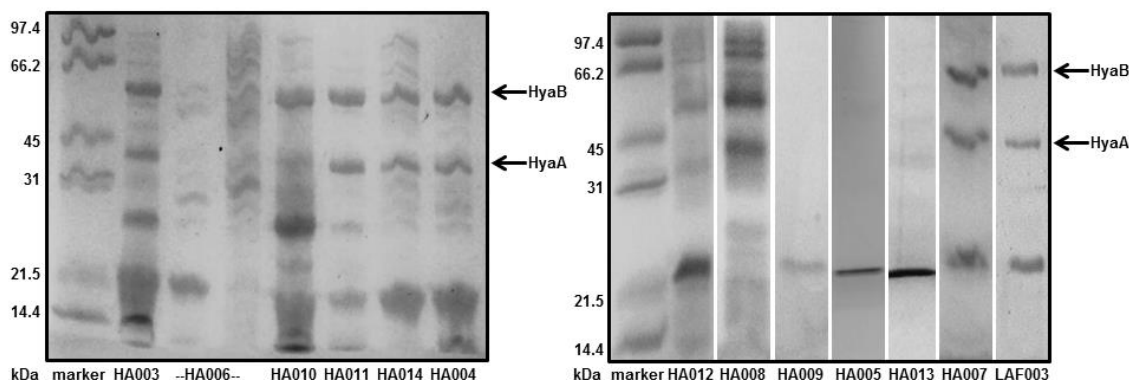
Figure 6.15 SDS-PAGE analysis of concentrated samples of protein isolated from strains LAF003 and HA003 to HA0014. Bands expected from the small (HyaA) and large (HyaB) subunits of *E. coli* hydrogenase-1 are indicated.

Strains HA005, HA009 and HA0013 seemed to produce no hydrogenase at all. Strains HA006, HA008, HA010 and HA012 gave poor purification results and isolated protein bands in SDS-PAGE analysis did not well match those expected for *E. coli* hydrogenase-1. As this initial purification for screening purposes was only conducted once, these observations are not fully conclusive and repeat purifications would need to be conducted to prove that these strains do not produce structurally intact hydrogenase.

Protein purified from strains LAF003, HA003, HA004, HA007, HA011 and HA014 contained bands matching those expected for *E. coli* hydrogenase-1 in SDS-PAGE analysis. For all these strains SDS-PAGE revealed that the purified protein also contained other bands, particularly of lower molecular weight. To further purify the samples and remove the contaminant proteins of differing molecular weight, size-exclusion chromatography (gel filtration) was performed on the samples (Chapter 3.7.4). Smaller samples were purified on a Superdex 200 10/30 column (GE Healthcare) and larger samples on a Superdex 200 16/600 column (GE Healthcare). The elution profile and associated SDS-PAGE analysis of fractions is shown for a 1.5 ml sample of protein purified from strain LAF003 (Figure 6.16).
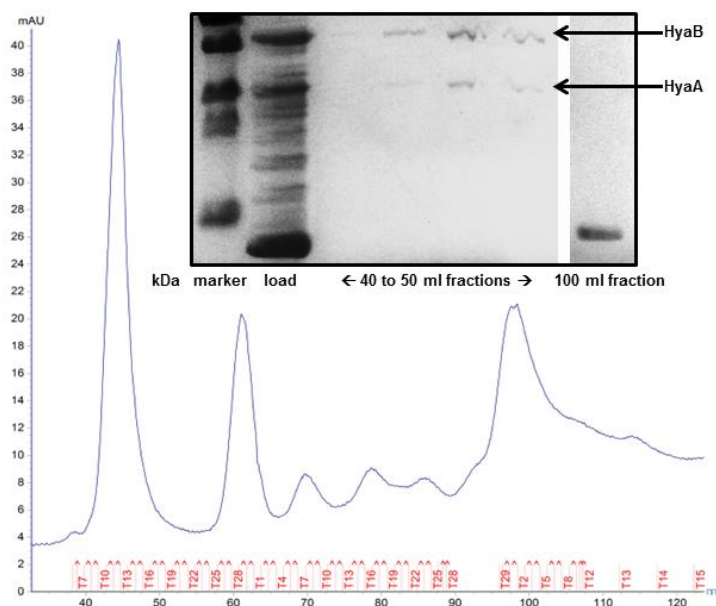
Figure 6.16 Elution profile and associated SDS-PAGE analysis of a 1.5 ml sample of protein purified from strain LAF003 eluted from a Superdex 200 16/600 column at 0.7 ml min^{-1} in buffer C.

The first peak of protein eluted from the column contains protein purely corresponding to the small (HyaA) and large subunit (HyaB) of *E. coli* hydrogenase-1. Later fractions contain the contaminating proteins of lower molecular weight. Fractions containing pure hydrogenase were pooled and concentrated to ~ 0.25 – 1 mg ml^{-1} samples. Protein concentrations were measured by Bradford assay (Chapter 3.7.6). SDS-PAGE analysis of concentrated samples of hydrogenase from size exclusion chromatography of protein purified from strains HA003, HA004, HA011, HA014, LAF003 and HA007 is shown in Figure 6.17.
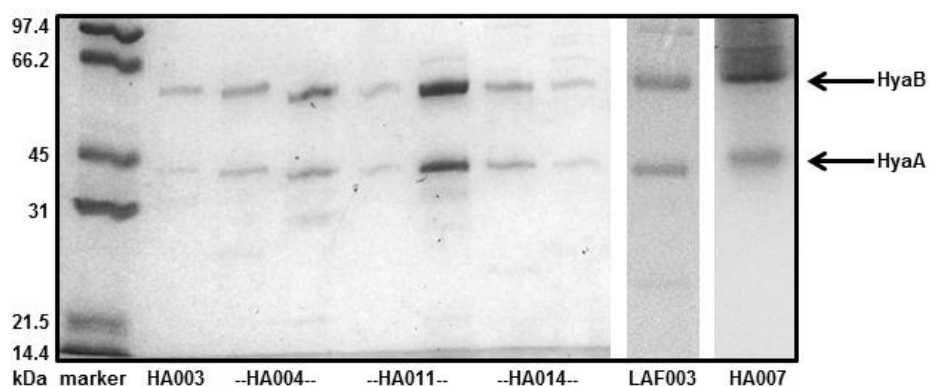
Figure 6.17 SDS-PAGE of concentrated samples of hydrogenase purified from strains HA003, HA004, HA011, HA014, LAF003 and HA007, following size exclusion chromatography.

Protein puried from HA007 was not completely pure, even following gel filtration. Hydrogenase samples purified from strains LAF003 (wild-type), HA003 (E28Q HyaB), HA004 (R193L HyaA), HA011 (K189N HyaA) and HA014 (Y191E HyaA) were extremely pure following gel filtration. The hydrogen production and oxidation activity of these hydrogenase-1 variants was tested with protein film electrochemistry (Chapter 1.3.2). K189N (HyaA) and Y191E (HyaA) were found to be be indistinguishable from wild-type. E28Q (HyaB) was catalytically inactive and R193L (HyaA) displayed increased bias towards hydrogen production and a lower overpotential for onset of hydrogen oxidation, compared to wild-type. As two variants with the desired characteristics for electrochemical studies (Chapter 7) were found, no further investigation of the other variants was carried out. The initial screening of protein purified from 12 – 16 litre cultures of the variant strains is summarised (Table 6.2).

Table 6.2 Summary of the screening of protein purified from variant strains

Strain	Mutation	Screening
LAF003	Wild type	Pure and active hydrogenase
HA003	E28Q (HyaB)	Pure but inactive hydrogenase
HA004	R193L (HyaA)	Pure and active hydrogenase with enhanced bias towards H_2 production and reduced overpotential for H_2 oxidation
HA005	R193E (HyaA)	No evidence of hydrogenase
HA006	R185L (HyaA)	Poor purification (protein bands at incorrect molecular weight)
HA007	H187C (HyaA)	Impure hydrogenase after gel filtration
HA008	H187G (HyaA)	Poor purification (protein bands at incorrect molecular weight)
HA009	H187S (HyaA)	No evidence of hydrogenase
HA010	K189H (HyaA)	Poor purification (protein bands at incorrect molecular weight)
HA011	K189N (HyaA)	Pure and active hydrogenase (indistinguishable from wild-type)
HA012	C190G (HyaA)	Poor purification (protein bands at incorrect molecular weight)
HA013	C190H (HyaA)	No evidence of hydrogenase
HA014	Y191E (HyaA)	Pure and active hydrogenase (indistinguishable from wild-type)

Hydrogenase variants with the desired characteristics have been produced by strains HA003 and HA004. These two variant hydrogenases of interest and native (from LAF003) were then produced on a large scale with multiple 36 litre preparations, yielding ~ 3.3 g of cells per litre of culture. Stepped imidazole concentrations between 0.05 M and 1 M were used to elute the solubilised protein from the HiTrap Ni-affinity column, in order to improve the purity of the collected fractions. An example of this for protein purified from LAF003 is shown in Figure 6.18.
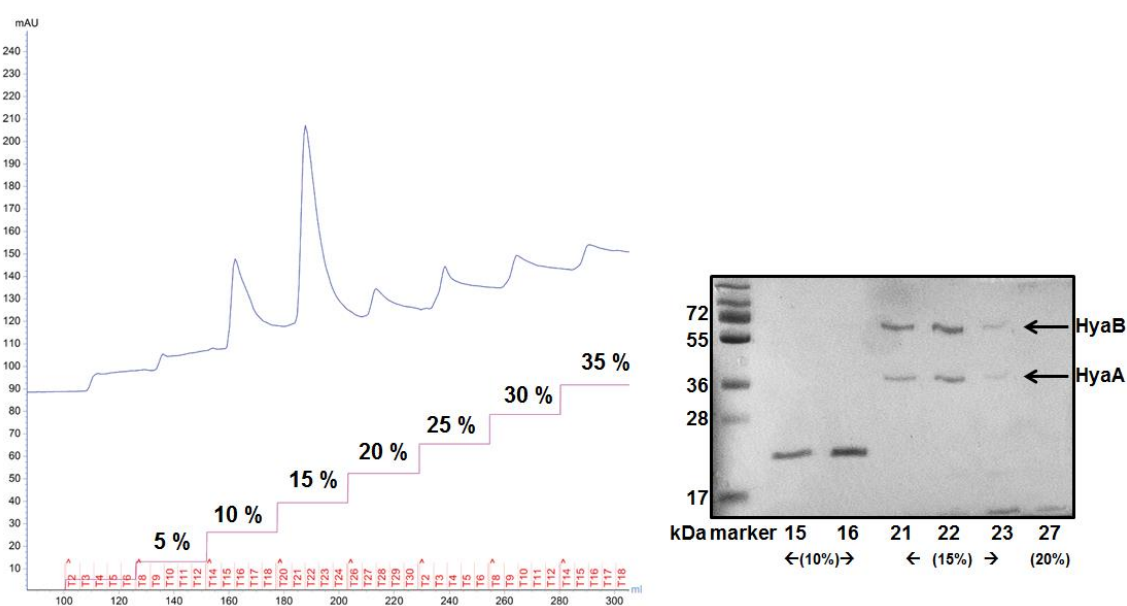
Figure 6.18 Stepped imidazole elution from 5% to 35% Buffer B (pH 7.3, 20 mM Tris, 150 mM NaCl, 1 M imidazole) for protein isolated from LAF003.

Fractions containing pure hydrogenase were pooled and concentrated. Final sample purity was confirmed by SDS-PAGE (Figure 6.19) and protein concentrations measured by Bradford assay (Chapter 3.7.6). The main contaminant that elutes at lower imidazole concentration was shown to be the well-known Ni-column contaminant cyclic amp receptor protein by mass spectrometry (Tech Facility, University of York).
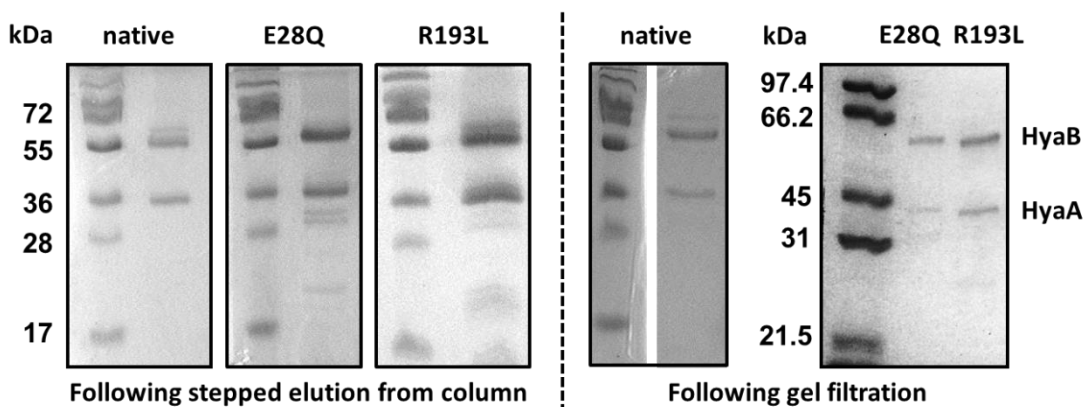
Figure 6.19 SDS-PAGE analysis of hydrogenase samples following stepped imidazole elution from a HiTrap Ni-affinity column and following gel filtration.

Yields were ~ 0.01 mg of hydrogenase per gram of cells for LAF003 and HA004 and slightly less for HA003. For EPR samples the protein was then dialysed into buffer D (pH 7, 50 mM HEPES, 50 mM dibasic sodium phosphate, 150 mM NaCl, 30% v/v glycerol), so that the buffer would maintain its pH at the cryogenic temperatures used in EPR studies. For all assay and electrochemical experiments the protein was further purified by size exclusion chromatography and absolute purity confirmed by SDS-PAGE (Figure 6.19). All samples were stored at −80°C. Studies conducted on native, E28Q (HyaB) and R193L (HyaA) *E. coli* hydrogenase-1 are detailed in Chapter 7.

References

1. Lubitz, W., et al., *Hydrogenases.* Chemical Reviews, 2014. **114**(8): p. 4081-4148.

2. Vignais, P.M. and B. Billoud, *Occurrence, classification, and biological function of hydrogenases: an overview.* Chemical Reviews, 2007. **107**(10): p. 4206-4272.

3. Vignais, P.M., B. Billoud, and J. Meyer, *Classification and phylogeny of hydrogenases.* FEMS microbiology reviews, 2001. **25**(4): p. 455-501.

4. Volbeda, A., et al., *X-ray crystallographic and computational studies of the O2-tolerant [NiFe]-hydrogenase 1 from Escherichia coli.* Proceedings of the National Academy of Sciences, 2012. **109**(14): p. 5305-5310.

5. Volbeda, A., et al., *Crystal structure of the O 2-tolerant membrane-bound hydrogenase 1 from Escherichia coli in complex with its cognate cytochrome b.* Structure, 2013. **21**(1): p. 184-190.

6. Lukey, M.J., et al., *How Escherichia coli is equipped to oxidize hydrogen under different redox conditions.* Journal of Biological Chemistry, 2010. **285**(6): p. 3928-3938.

7. Lukey, M.J., et al., *Oxygen-tolerant [NiFe]-hydrogenases: the individual and collective importance of supernumerary cysteines at the proximal Fe-S cluster.* Journal of the American Chemical Society, 2011. **133**(42): p. 16881-16892.

8. Fritsch, J., O. Lenz, and B. Friedrich, *Structure, function and biosynthesis of O2-tolerant hydrogenases.* Nature Reviews Microbiology, 2013. **11**(2): p. 106-114.

9. Wait, A.F., et al., *Characteristics of enzyme-based hydrogen fuel cells using an oxygen-tolerant hydrogenase as the anodic catalyst.* The Journal of Physical Chemistry C, 2010. **114**(27): p. 12003-12009.

10. Xu, L. and F.A. Armstrong, *Pushing the limits for enzyme-based membrane-less hydrogen fuel cells–achieving useful power and stability.* RSC Advances, 2015. **5**(5): p. 3649-3656.

11. Wang, Y., T.F. Esterle, and F.A. Armstrong, *Electrocatalysis by H 2–O 2 membrane-free fuel cell enzymes in aqueous microenvironments confined by an ionic liquid.* RSC Advances, 2016. **6**(50): p. 44129-44134.

12. Mersch, D., et al., *Wiring of photosystem II to hydrogenase for photoelectrochemical water splitting.* Journal of the American Chemical Society, 2015. **137**(26): p. 8541-8549.

13. Bachmeier, A. and F. Armstrong, *Solar-driven proton and carbon dioxide reduction to fuels—lessons from metalloenzymes.* Current opinion in chemical biology, 2015. **25**: p. 141-151.

14. Woolerton, T.W., et al., *Enzymes and bio-inspired electrocatalysts in solar fuel devices.* Energy & Environmental Science, 2012. **5**(6): p. 7470-7490.

15. Murphy, B.J., F. Sargent, and F.A. Armstrong, *Transforming an oxygen-tolerant [NiFe] uptake hydrogenase into a proficient, reversible hydrogen producer.* Energy & Environmental Science, 2014. **7**(4): p. 1426-1433.

16. Flanagan, L.A. and A. Parkin, *Electrochemical insights into the mechanism of NiFe membrane-bound hydrogenases.* Biochemical Society Transactions, 2016. **44**(1): p. 315-328.

17. Wombwell, C., C.A. Caputo, and E. Reisner, *[NiFeSe]-Hydrogenase Chemistry.* Accounts of chemical research, 2015. **48**(11): p. 2858-2865.

18. Parkin, A., et al., *The difference a Se makes? Oxygen-tolerant hydrogen production by the [NiFeSe]-hydrogenase from Desulfomicrobium baculatum.* Journal of the American Chemical Society, 2008. **130**(40): p. 13410-13416.

19. Reisner, E., J.C. Fontecilla-Camps, and F.A. Armstrong, *Catalytic electrochemistry of a [NiFeSe]-hydrogenase on TiO2 and demonstration of its suitability for visible-light driven H 2 production.* Chemical Communications, 2009. (5): p. 550-552.

20. Hexter, S.V., et al., *Electrocatalytic mechanism of reversible hydrogen cycling by enzymes and distinctions between the major classes of hydrogenases.* Proceedings of the National Academy of Sciences, 2012. **109**(29): p. 11516-11521.

21. Hexter, S.V., T.F. Esterle, and F.A. Armstrong, *A unified model for surface electrocatalysis based on observations with enzymes.* Physical Chemistry Chemical Physics, 2014. **16**(24): p. 11822-11833.

22. Dubini, A., et al., *How bacteria get energy from hydrogen: a genetic analysis of periplasmic hydrogen oxidation in Escherichia coli.* International Journal of Hydrogen Energy, 2002. **27**(11): p. 1413-1420.

23. Forzi, L. and R.G. Sawers, *Maturation of [NiFe]-hydrogenases in Escherichia coli.* Biometals, 2007. **20**(3-4): p. 565-578.

24. Casalot, L. and M. Rousset, *Maturation of the [NiFe] hydrogenases.* Trends in microbiology, 2001. **9**(5): p. 228-237.

25. Zhang, J.W., et al., *A role for SlyD in the Escherichia coli hydrogenase biosynthetic pathway.* Journal of Biological Chemistry, 2005. **280**(6): p. 4360-4366.

26. Flanagan, L.A., et al., *Re-engineering a NiFe hydrogenase to increase the H 2 production bias while maintaining native levels of O 2 tolerance.* Chemical Communications, 2016. **52**(58): p.9133-9136.

27. Evans, R.M., et al., *Principles of sustained enzymatic hydrogen oxidation in the presence of oxygen–the crucial influence of high potential Fe–S clusters in the electron relay of [NiFe]-hydrogenases.* Journal of the American Chemical Society, 2013. **135**(7): p. 2694-2707.

28. Evans, R.M., et al., *Mechanism of hydrogen activation by [NiFe] hydrogenases.* Nature chemical biology, 2016. **12**(1): p. 46-50.

29. Dementin, S., et al., *A glutamate is the essential proton transfer gate during the catalytic cycle of the [NiFe] hydrogenase.* Journal of Biological Chemistry, 2004. **279**(11): p. 10508-10513.

30. De Lacey, A.L., et al., *FTIR spectroelectrochemical study of the activation and inactivation processes of [NiFe] hydrogenases: effects of solvent isotope replacement and site-directed mutagenesis.* JBIC Journal of Biological Inorganic Chemistry, 2004. **9**(5): p. 636-642.

31. Greene, B.L., et al., *Glutamate Gated Proton-Coupled Electron Transfer Activity of a [NiFe]-Hydrogenase.* Journal of the American Chemical Society, 2016. **138**(39): p. 13013-13021.

32. Dementin, S., et al., *Changing the ligation of the distal [4Fe4S] cluster in NiFe hydrogenase impairs inter-and intramolecular electron transfers.* Journal of the American Chemical Society, 2006. **128**(15): p. 5209-5218.

33. Marshall, N.M., et al., *Rationally tuning the reduction potential of a single cupredoxin beyond the natural range.* Nature, 2009. **462**(7269): p. 113-116.

34. Hosseinzadeh, P., et al., *Design of a single protein that spans the entire 2-V range of physiological redox potentials.* Proceedings of the National Academy of Sciences, 2016. **113**(2): p. 262-267.

35. Lin, I.-J., et al., *Changes in hydrogen-bond strengths explain reduction potentials in 10 rubredoxin variants.* Proceedings of the National Academy of Sciences of the United States of America, 2005. **102**(41): p. 14581-14586.

36. Zuris, J.A., et al., *Engineering the redox potential over a wide range within a new class of FeS proteins.* Journal of the American Chemical Society, 2010. **132**(38): p. 13120-13122.

37. Kolling, D.J., et al., *Atomic resolution structures of rieske iron-sulfur protein: role of hydrogen bonds in tuning the redox potential of iron-sulfur clusters.* Structure, 2007. **15**(1): p. 29-38.

38. Denke, E., et al., *Alteration of the midpoint potential and catalytic activity of the Rieske iron-sulfur protein by changes of amino acids forming hydrogen bonds to the iron-sulfur cluster.* Journal of Biological Chemistry, 1998. **273**(15): p. 9085-9093.

39. Chen, K., et al., *Azotobacter vinelandii Ferredoxin IA sequence and structure comparison approach to alteration of [4Fe-4S] 2+/+ reduction potential.* Journal of Biological Chemistry, 2002. **277**(7): p. 5603-5610.

40. Chen, K., et al., *Alteration of the Reduction Potential of the [4Fe-4S] 2+/+ Cluster of Azotobacter vinelandii Ferredoxin I.* Journal of Biological Chemistry, 1999. **274**(51): p. 36479-36487.

41. Shen, B., et al., *Azotobacter vinelandii ferredoxin I. Alteration of individual surface charges and the [4FE-4S] 2+/+ cluster reduction potential.* Journal of Biological Chemistry, 1994. **269**(11): p. 8564-8575.

42. Heermann, R., T. Zeppenfeld, and K. Jung, *Simple generation of site-directed point mutations in the Escherichia coli chromosome using Red®/ET® Recombination.* Microbial cell factories, 2008. **7**(1): p. 1.

Chapter 7

Control of Catalytic Bias and Overpotential by the Electron Entry/exit Site in a [NiFe]-hydrogenase

Declaration

I designed the research with Dr Alison Parkin (University of York). I performed all the molecular biology, with the advice and initial aid of Lindsey Flanagan (University of York), and all the protein purification, with the advice and initial aid of Julia Walton (University of York). All other research and analysis was performed by myself, aside from the data optimisation done by Dr Martin Robinson and Prof. David Gavaghan (University of Oxford) and EPR measurements performed by John Wright and Dr Maxie Roessler (Queen Mary University of London). Darrell Elton (La Trobe University) and Prof. Alan Bond (Monash University) provided the FTacV instrumentation. Prof. Alan Bond also advised on data analysis. I wrote the complete first draft of the paper, and alongside Dr Alison Parkin revised this to include contributions from all the other authors, and thus generate the final version.

Signed   Dr Alison Parkin

Signed   Dr Martin Robinson

Reference:

This paper is not published but has been submitted to the journal Nature Chemical Biology.

Control of Catalytic Bias and Overpotential by the Electron Entry/exit Site in a [NiFe]-hydrogenase

Hope Adamson[1], Martin Robinson[2], John J. Wright[3], Lindsey A. Flanagan[1], Julia Walton[1], Darrell Elton[4], David J. Gavaghan[2], Alan M. Bond[5], Maxie M. Roessler[3], and Alison Parkin[1,*]

[1] Department of Chemistry, University of York, Heslington, York, YO10 5DD, UK

[2] Department of Computer Science, University of Oxford, Oxford, OX1 3QD, UK

[3] School of Biological and Chemical Sciences, Queen Mary University of London, Mile End Road, London, E1 4NS, UK

[4] Department of Engineering, School of Engineering and Mathematical Sciences, La Trobe University, Melbourne, Victoria 3086, Australia

[5] School of Chemistry, Monash University, Clayton, Victoria 3800, Australia

Abstract

The redox chemistry of the electron entry/exit site in *Escherichia coli* hydrogenase-1 is shown to play a vital role in tuning biocatalysis. Inspired by Nature, we generate a HyaA-R193L variant to disrupt a proposed Arg-His cation-π interaction in the secondary coordination sphere of the outermost, "distal", iron-sulfur cluster. This re-wires the enzyme, enhancing the relative rate of H_2 production and the thermodynamic efficiency of H_2 oxidation catalysis. On the basis of Fourier transformed alternating current voltammetry (FTacV) measurements, we ascribe these changes in catalysis to a shift in the distal $[Fe_4S_4]^{2+/1+}$ redox potential. By probing this previously experimentally intractable redox process, we substantiate theoretical mechanistic models which ascribe catalytic overpotential and bias to the difference between the distal $[Fe_4S_4]^{2+/1+}$ redox potential and that of the $2H^+/H_2$ substrate couple. Thus metalloenzyme chemistry is shown to be controlled by the ligand field of an electron transfer site distant from the catalytic center.

Introduction

Hydrogenases are remarkable biological catalysts, with the ability to interconvert H_2, protons and electrons ($H_2 \leftrightarrows 2H^+ + 2e^-$) at efficiencies

comparable to platinum, but using abundant-metal active sites of iron or nickel and iron(1). These enzymes are therefore studied with the hope of both understanding microbial metabolism and discovering sustainable catalysts to underpin a H_2-energy economy. The O_2-tolerant membrane-bound [NiFe]-hydrogenases (MBHs), capable of sustained catalysis in O_2, have garnered the most significant interest. Re-programming the reactivity of such [NiFe]-hydrogenases is desirable because there is not a naturally occurring enzyme that is both active in O_2 and capable of high efficiency catalysis and rapid H_2-production. This is particularly clear in catalytic protein film voltammetry experiments, in which hydrogenase is adsorbed onto the surface of an electrode and catalytic current is measured as a function of potential, fingerprinting both the catalytic bias (ratio of H_2 oxidation to H_2 production current) and the potential at which catalysis commences (Figure 1)(2). The [NiFe]-hydrogenases which are ideal bidirectional H_2 electro-catalysts, displaying high H_2 production and oxidation turnover rates, are inactivated by O_2 (O_2 sensitive, e.g. *Escherichia coli* hydrogenase-2)(2-4). Conversely, the O_2-tolerant MBHs are poor H_2-producing catalysts and require an additional thermodynamic driving force (overpotential) to initiate H_2 oxidation at pH > 5, e.g. *Escherichia coli* hydrogenase-1 (*E. coli* Hyd-1)(2-4). Therefore, despite [NiFe]-hydrogenases being naturally expressed by photosynthetic microbes, sustained solar water-splitting to yield H_2 is impossible using native enzymes(5), and a molecular understanding of the factors which control catalytic bias and overpotential is required.

Crystal structures have been resolved for four O_2-tolerant MBHs, including the subject of this study, *E. coli* Hyd-1(6-11). The electron entry/exit site is the "distal" $[Fe_4S_4]$ cluster which sits at the end of a chain of three iron-sulfur clusters that span the small (approx. 30 kDa) protein subunit and transfer electrons between the surface of the protein and the bimetallic NiFe H_2-activating site that is buried in the large (approx. 60 kDa) protein subunit (Figure 1)(6-11). Soluble and membrane-bound O_2-sensitive [NiFe]-hydrogenases have this same overall structure(12-15), in particular, the NiFe centers are identical, and the surrounding architecture is remarkably similar. A fully conserved large subunit Glu is found close to the NiFe center in all structures (Figure 1), and replacement with a non-acidic residue disables catalysis in a number of [NiFe]-hydrogenases(16-18), suggesting a highly conserved proton transfer relay and

mechanism for active site chemistry. Therefore the NiFe site is unlikely to be the control center for differences in the H_2-reactivity of O_2-tolerant and O_2-sensitive [NiFe]-hydrogenases, in contrast with classical models of enzyme catalysis, which ascribe substrate reactivity and energetics solely to the local environment of the active site.
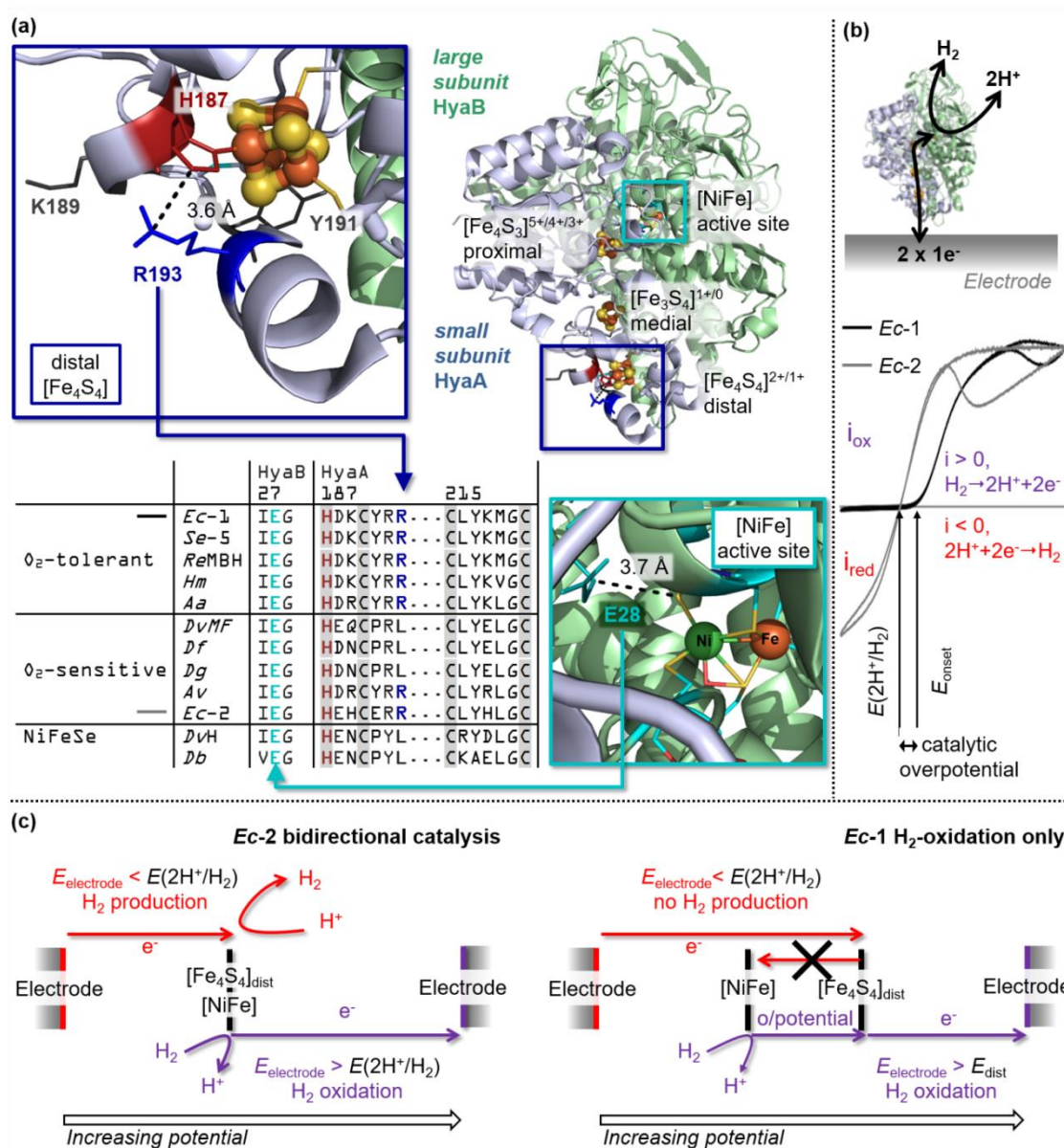
Figure 1 (a) *E. coli* **hydrogenase-1 structure (PDB 5A4I) with detail of position of HyaB-E28 relative to active site and HyaA-H187, HyaA-R193, HyaA-K189 and HyaA-Y191 relative to the distal cluster**. The sequence alignment (*E. coli* Hyd-1 numbering) highlights the conserved nature of E28 in the HyaB protein in *E. coli* Hyd-1 (*Ec*-1), *Salmonella enterica* Hyd-5 (*Se*-5), *Ralstonia eutropha* MBH (*Re*MBH), *Hydrogenovibrio marinus* (*Hm*), *Aquifex aeolicus* (*Aa*), *Desulfovibrio vulgaris* Miyazaki F (*Dv*MF), *Desulfovibrio fructosovorans* (*Df*), *Desulfovibrio gigas* (*Dg*), *Allochromatium vinosum* (*Av*), *E. coli* Hyd-2 (*Ec*-2), *Desulfovibrio vulgaris* Hildenborough (*Dv*H) and *Desulfomicrobium baculatum* (*Db*) NiFe or NiFeSe hydrogenases. Also indicated are the distal cluster ligands (grey shading) with dark red text highlighting HyaA-H187 and dark blue text highlighting HyaA-R193. **(b) Cartoon depiction of enzyme on electrode, and resultant comparative direct current voltammogram traces for either an O_2**

tolerant hydrogenase (*Ec*-1) or an O₂ sensitive hydrogenase (*Ec*-2) at pH > 5 and under a H₂ atmosphere. The difference in catalytic bias is quantified by the ratio of oxidation current, i_{ox}, to reduction current, i_{red}. The onset potential of H₂ oxidation catalysis, E_{onset}, coincides with the reduction potential for the proton/H₂ couple ($E(2H^+/H_2)$) for an O₂ sensitive hydrogenase, but there is an overpotential requirement for O₂-tolerant hydrogenases. **(c) Cartoon depiction of distal cluster control over catalytic bias and overpotential**

A unique $[Fe_4S_3]$ proximal cluster is required for O₂-tolerance in MBHs(7-11, 19, 20), and along with the $[Fe_3S_4]$ medial cluster(21), these centers provide electrons for the reduction of inhibitory O₂ to water at the NiFe site, indicating that iron sulfur cluster chemistry can control active site reactivity. However, in variants with diminished O₂-tolerance due to proximal and medial cluster ligand changes, there is no change in the catalytic reversibility of the enzyme(11, 19-21). Instead, an electrocatalytic model by Hexter *et al* proposes that both the catalytic bias and overpotential of multicenter redox enzymes are controlled by the redox potential of the electron entry/exit site; the distal cluster in [NiFe]-hydrogenases(4, 22). Decoding to what extent the redox potential of one electron transfer center can control catalytic reversibility and efficiency is important because hydrogenases are just one example of a large class of electron-relay containing "wired" metalloenzymes that redox-activate notoriously stable small molecules like N₂, H₂O and CO₂.

The simple conclusion of the Hexter model is that complete catalytic reversibility is predicted when the potential of the distal cluster $[Fe_4S_4]^{2+/1+}$ redox transition, E_{dist}, matches that of the substrate product couple, $E(2H^+/H_2)$(4, 22). A mismatch in potentials results in catalytic bias and a concurrent overpotential, for reduction when $E_{dist} < E(2H^+/H_2)$, or oxidation when $E_{dist} > E(2H^+/H_2)$(4, 22). Thus, it is theorized that at pH > 5 the essentially unidirectional H₂-oxidising O₂-tolerant MBHs have more positive E_{dist} values, less closely matched to $E(2H^+/H_2)$ than the bidirectional O₂-sensitive [NiFe]-hydrogenases. When $E_{dist} \gg E(2H^+/H_2)$ the distal cluster effectively acts as a diode; electrons can only flow out of the enzyme (prohibiting H₂ production) and H₂ oxidation can only commence once the distal cluster is oxidized, giving a catalytic overpotential controlled by E_{dist} (Figure 1)(4, 22). The enhanced catalytic reversibility of *E. coli* Hyd-1 at pH < 5 is interpreted as evidence that the potentials of E_{dist} and $E(2H^+/H_2)$ converge at low pH(23). In contrast, based on their more complex electrocatalytic model of hydrogenase activity, Leger and co-workers suggest that E_{dist} will only influence the catalytic reversibility, not completely control it, due to the different nature of the rate limiting steps in H₂ production and

oxidation and the effects of intramolecular electron transfer(24, 25). Comparison of the two models is not possible because there is no experimental measurement of E_{dist} for *E. coli* Hyd-1(26), and there have been no [NiFe]-hydrogenase distal cluster variants with a re-tuned E_{dist}.

There is a wealth of literature describing how re-tuning the non-covalent interactions of residues in the second coordination sphere of protein electron-transfer centers can have a substantial impact on the redox potential(27, 28). In many O_2 sensitive [NiFe]-hydrogenases, a Leu residue sits at the apex of the helix between the surface of the protein and the distal cluster His ligand (Figure 1 and Supplementary Figure 1)(12-15). In contrast, sequence comparisons and structural analyses reveal that in all O_2-tolerant hydrogenases(6-11), a conserved Arg occupies this position, and it is close enough to the distal cluster His ligand for a cation-π interaction to persist (Cζ to Nτ from 3.3 to 3.7 Å), i.e. there should be an electrostatic attraction between the π electron system of His and the positively charged Arg side chain (Figure 1 and Supplementary Figure 2)(29, 30). Such interactions have recently been identified as playing a vital role in tuning protein redox chemistry involving Trp residues(31-34), and we explore how an *E. coli* Hyd-1 small subunit Arg-193 to Leu amino acid exchange (HyaA-R193L) impacts E_{dist}, and what the associated catalytic changes are. First coordination sphere ligands are not investigated as the only previous study on distal cluster variants of a [NiFe]-hydrogenase showed that in the O_2-sensitive *Desulfovibrio fructosovorans* enzyme, changing the Fe-ligating His residue to a Gly or Cys had a strikingly deleterious effect on catalysis (H_2 oxidation activity decreased by at least 97%)(35). Recent density functional theory calculations suggest that this is because electrons pass between the outer surface of the protein and the distal cluster via a precise molecular route which includes the His ligand(36, 37). Variants HyaA-K189N and HyaA-Y191E, which mimic differences in this surface-to-histidine route in O_2-tolerant and O_2-sensitive [NiFe]-hydrogenases (Figure 1), are generated to investigate the potential role of residues along this route in tuning E_{dist}.

EPR measurements do not provide a measure of E_{dist} for the genetically tractable enzyme *E. coli* Hyd-1 because the distal center is EPR-silent or -invisible in the oxidized $[Fe_4S_4]^{2+}$ and reduced $[Fe_4S_4]^{1+}$ states, respectively(26). Traditional direct-current voltammetry measurements cannot be used to probe

E_{dist} because such experiments require non-catalytic conditions(38), but protons cannot be excluded from aqueous solutions, and O_2-tolerant hydrogenases cannot be fully inhibited by CO(3). Computational modelling of the protein structure cannot provide a value for E_{dist} via direct calculation because the assignment of the electronic levels in iron sulfur clusters is extremely challenging, and such estimates are normally calibrated against unambiguous experimental data(39). Therefore, in order to provide the first measure of E_{dist} we use large amplitude Fourier transformed alternating current voltammetry(40) (FTacV) to probe a hydrogenase for the first time.

In FTacV a large amplitude sine wave of frequency f is applied to a voltage sweep and the measured current output is Fourier transformed into the frequency domain to give an aperiodic direct current (dc) component and harmonic signals at multiples of the input frequency (f, $2f$ etc.). Individual harmonics are band selected and inverse Fourier transformed back to the time domain(40-42). This is advantageous because in one experiment an FTacV measurement of a redox enzyme and substrate can simultaneously quantify (i) the catalytic current (via the aperiodic dc component), and (ii) non-catalytic, reversible electron-transfer processes, such as the distal cluster redox transition $[Fe_4S_4]^{2+/1+}$ via the capacitance-free high harmonic current(42). Thus, unlike traditional voltammetry techniques, in FTacV catalytic current does not mask non-catalytic current and we describe how this allows us to quantify turnover rates. Complementary EPR experiments probe the redox chemistry of iron-sulfur sites not interrogated via FTacV. We detail the mechanism of how the single HyaA-R193L amino acid exchange enhances bias towards H_2 production and reduces the H_2 oxidation overpotential for an O_2-tolerant [NiFe]-hydrogenase, while retaining the enzyme's catalytic activity in the presence of O_2.

Results

Separate Resolution of Hydrogenase Catalytic and Non-Catalytic Processes by FTacV

The aperiodic dc and 6th harmonic ac components of high frequency (144 Hz) and large amplitude (150 mV) FTacV conducted on as-isolated *E. coli* Hyd-1 adsorbed on a graphite electrode are shown in Figure 2, along with enzyme-

free "blank" control data. For native enzyme the aperiodic dc component is analogous to previous direct current voltammetry (dcV) studies, thus at pH 4.0 negative current corresponding to H_2 production (H^+ reduction) catalysis is detectable under 100% N_2 but under 100% H_2 only positive current from H_2 oxidation catalysis is measured(3, 6, 19, 21, 23, 43). The high harmonic signals from the same experiments (displayed as current magnitude plots for the 6th harmonic in Figure 2) are insensitive to the presence of H_2, indicating that the FTacV technique has enabled the simultaneous and separate measurement of non-catalytic electron-transfer in the high harmonics, *and* catalytic current in the aperiodic dc component. (For clarity, only the 6th harmonic is depicted in Figure 2, but harmonics 4-7 all provide a background-free measurement of non-catalytic enzyme redox chemistry, Supplementary Figure 3.) FTacV conducted at higher pH shows a negative shift in the potential of the high harmonic signal and the expected drop in H_2 production current in the aperiodic dc component (Supplementary Figure 4). The amplitude of the sine wave utilized in FTacV affects the apparent onset potential of catalysis in the aperiodic dc component(44) (Supplementary Figure 5), so catalytic overpotential values are assessed in separate dcV experiments described later.
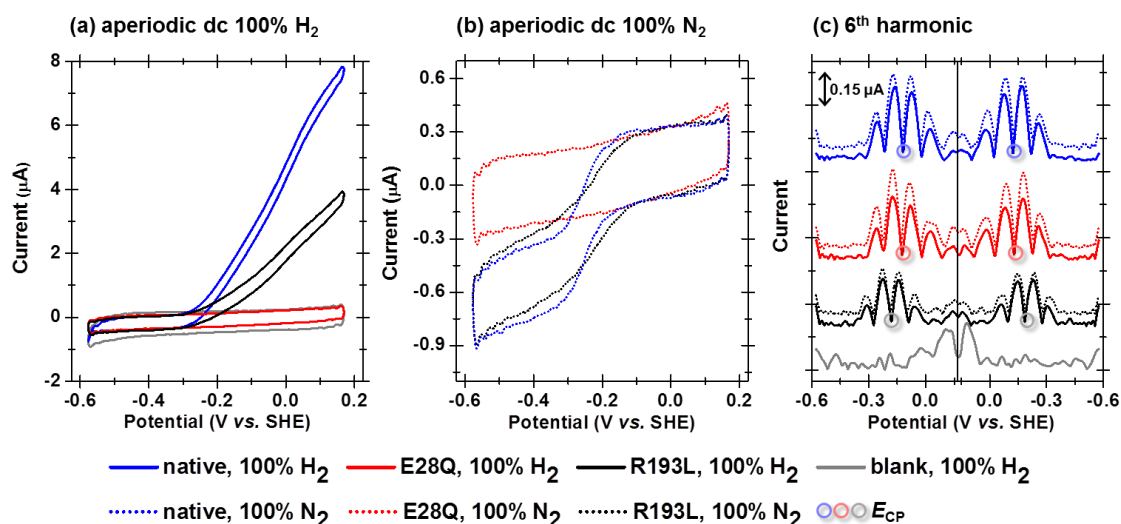
Figure 2 FTacV of *E. coli* hydrogenase-1 at frequency = 144 Hz, amplitude = 150mV and scan rate = 27.94 mV s^{−1}. (a) and (b) Aperiodic dc component of forward and reverse scan shown as cyclic voltammogram. (b) 6th harmonic components of forward and reverse scan. Datasets offset for clarity, and color code as indicated, where "blank" refers to an enzyme-free control experiment. Other experimental conditions: pH 4.0, 2000 rpm, 25°C.

To experimentally corroborate the separate resolution of catalytic and non-catalytic redox processes in 144 Hz FTacV of as-isolated native Hyd-1, a

catalytically disabled HyaB-E28Q variant was generated, with the fully conserved proton transfer residue close to the NiFe center (Figure 1) replaced by a non-acidic residue, as first described for *D. fructosovorans* [NiFe]-hydrogenase(18). The structural integrity of the medial and proximal clusters of HyaB-E28Q was confirmed by EPR measurements (Supplementary Figures 6 and 7), and the catalytic inactivity established via H_2 oxidation dye assays (Supplementary Figure 8). The aperiodic dc component of 144 Hz FTacV of as-isolated HyaB-E28Q further validates the catalytic inactivity, since there is no discernable H_2 production current under 100% N_2 or oxidation current under 100% H_2, at pH 4.0 (Figure 2) or higher pH (Supplementary Figure 9). In contrast, the 6th harmonic of 144 Hz FTacV measurements of HyaB-E28Q and native Hyd-1 are almost identical under both 100% N_2 and H_2 (Figure 2 and Supplementary Figure 9), confirming that such high frequency harmonics provide a measure of purely non-catalytic hydrogenase electron-transfer current.

Lower frequency (9Hz) FTacV measurements do not provide this full separation of catalytic and non-catalytic current. The 6th harmonic of an 8.98 Hz FTacV measurement of native Hyd-1 is sensitive to H_2 (Supplementary Figure 10) and no longer matches that of catalytically inactive HyaB-E28Q (supplementary Figure 11), indicating a catalytic component to the high harmonic current(44). Theoretical simulations have previously predicted that for a sufficiently rapid surface confined catalytic process, FTacV will be unable to fully deconvolute current contributions from reversible electron transfer and substrate turnover(44). To ensure that our maximum experimental frequency of 144 Hz is always fast enough to generate catalysis-free high harmonic current, as-isolated rather than fully activated Hyd-1 is used for all electrochemical experiments in this study. The catalytic current is lower for as-isolated Hyd-1 because following aerobic purification a proportion of the hydrogenase molecules contain catalytically inactivated Ni-sites, which only recover activity upon prolonged (> 12 hours) exposure to H_2 (Supplementary Figure 8)(3, 19, 21).

Assignment of the High Harmonic Signal to Distal Cluster Redox Chemistry

An automated parameter optimization procedure can be used to determine the values that give the best fit between a model redox reaction and high harmonic

FTacV data measured at a frequency of less than 9 Hz(41). The 8.88 Hz FTacV measurements of HyaB-E28Q are uncomplicated by any catalytic reactions, and were therefore simulated using such a protocol, resulting in a good fit between the experimental data and a model reversible one-electron redox reaction (electron transfer rate, k^0, fixed at 10^4 s^{-1}) (Figure 3). This yields a measure of the total amount of protein on the electrode, M = 0.195 pmol. Dispersion has been shown to be important in previous models of hydrogenase electrocatalysis(4, 22, 24, 25, 45) and this is incorporated into the simulation with a Gaussian distribution in the reversible potential of the redox process, E_{rev}(46). The best fit potential values are average E_{rev} = −123 mV, and standard deviation = 31 mV. Optimization of a zero-dispersion reversible one-electron model does not provide a good fit to the experimental data (Supplementary Figure 12).
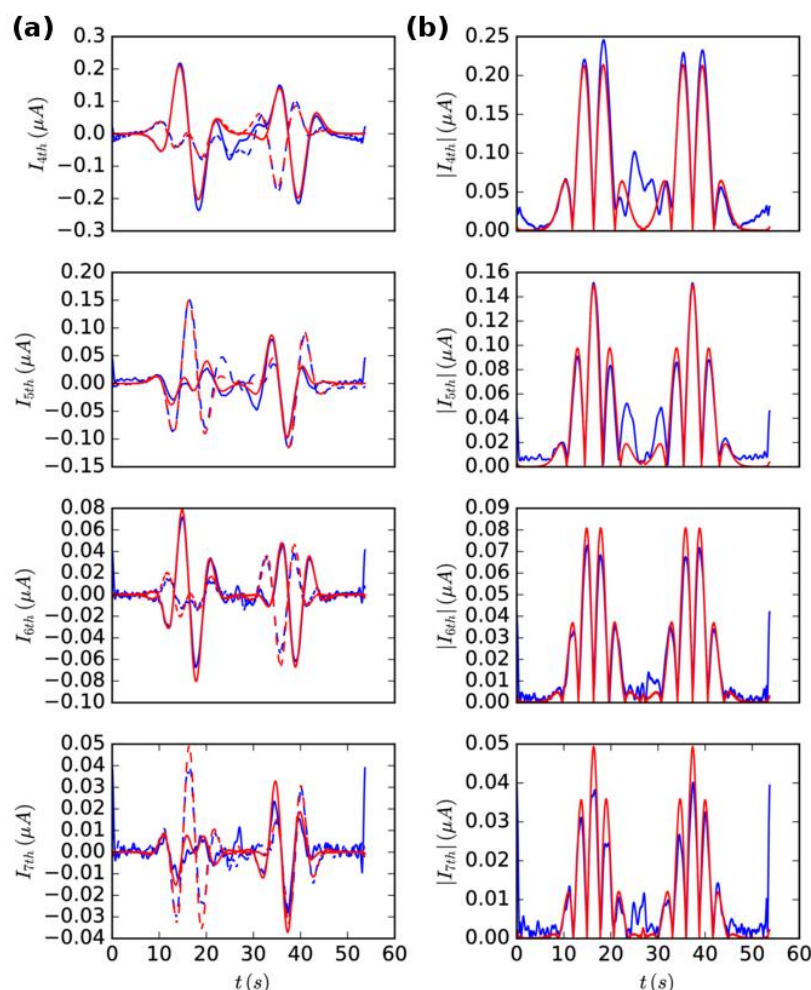
Figure 3 Simulation of HyaB-E28Q FTacV. Overlay of 4th to 7th harmonic components of 8.88 Hz FTacV experimental measurement of HyaB-E28Q (blue) and parameter optimized reversible one-electron reaction simulation (red), as detailed in the text. (a) Plots show the real (solid lines) and imaginary (dashed lines) components used in the parameter optimization procedure. Each

plot was obtained by (i) filtering out the positive frequencies of each harmonic in the frequency domain, (ii) frequency-shifting these down to a center frequency of zero, and then (iii) taking the inverse Fourier transform. (b) The absolute current magnitudes which result from taking the magnitude of each harmonic signal in (a). Other experimental conditions: amplitude = 150 mV, scan rate = 27.94 mV s^{-1}, pH 4.0, 100 % H_2 atmosphere, 2000 rpm, 25°C, uncompensated resistance (R_u) = 20 Ω. Simulation parameters: phase = −0.0327, average E_{rev} = −0.123 V with std dev = 0.031 V, Γ = 6.5 pmol cm^{-2}.

Except for a scalar increase in magnitude, FTacV measurements of HyaB-E28Q at frequencies greater than 8.88 Hz yield 6th harmonic signals with a very similar current response, indicating that the same redox process is under interrogation (Supplementary Figure 13). The center point potential of the 144 Hz high harmonic signals, E_{CP} (the potential of the minimum and maximum current in the center of the even and odd harmonic signals, respectively), corresponds to the simulation derived average redox potential E_{rev} (Figures 2 and 3). Therefore E_{CP}, derived from simple inspection of the 144 Hz FTacV data, is used as a measure of the midpoint potential of the one-electron transfer redox reaction ascribed as giving rise to the non-catalytic current. Since the 144 Hz FTacV high harmonics of native Hyd-1 and HyaB-E28Q are almost identical (Figure 2) the same E_{CP} analysis is applied to high frequency measurements of native Hyd-1. Between pH 3 and 7 the E_{CP} of native Hyd-1 and HyaB-E28Q remain essentially indistinguishable, decreasing as a function of pH, with a gradient of −18 mV pH^{-1} (Supplementary Figure 14 and Supplementary Table 1).

Since the 144 Hz FTacV high harmonic signal of as-isolated native Hyd-1 is insensitive to H_2 and carbon monoxide, an inhibitor which is known to bind at the active site of [NiFe] hydrogenases[1, 3] (Supplementary Figure 15), it is unlikely that this current arises from Ni-based redox chemistry. Comparison of E_{CP} values with the published potentials of E. coli Hyd-1 active site Ni redox transitions[21, 47, 48] validates this assignment, indicating that the non-catalytic FTacV current must instead arise from iron-sulfur cluster chemistry (Supplementary Table 2 and associated text).

For native Hyd-1 at pH 7.0 the EPR-titration determined midpoint potentials of the proximal and medial iron-sulfur cluster redox transitions are positive (Supplementary Figure 16 and Supplementary Table 3) whilst E_{CP} = −176 ± 3 mV (Supplementary Table 1). This suggests that it is the EPR-invisible[26] distal cluster redox transition, $[Fe_4S_4]^{2+/1+}$, under interrogation in the 144 Hz FTacV high harmonics. We cannot measure across a higher potential window in

an attempt to also observe current from the medial and proximal cluster redox transitions because the graphite electrode surface ceases to be non-reactive, with Faradaic responses attributed to quinone reactivity(49) observed in enzyme-free "blank" high harmonic FTacV measurements (Supplementary Figure 17).

A HyaA-R193L variant was designed to disrupt the putative cation-π interaction between Arg-193 and the distal cluster His-ligand of *E. coli* Hyd-1 (Figure 1). The 144 Hz FTacV 6th harmonic of HyaA-R193L is insensitive to H$_2$ and retains the same shape as native Hyd-1 and HyaB-E28Q (Figure 2 and Supplementary Figure 9), suggesting that a one-electron non-catalytic redox reaction is again measured. However, as a result of this amino acid exchange, across the pH range 3 to 7 the E_{CP} shifts by approx. −60 mV relative to native Hyd-1 and HyaB-E28Q (Figure 2 and Supplementary Figures 9 and 14). We interpret this as further evidence that the distal cluster $[Fe_4S_4]^{2+/1+}$ transition is under interrogation and from this point it is assumed that E_{CP} values are equivalent to E_{dist}.

Relating the Distal Cluster Potential to Catalytic Bias and Overpotential

Having determined that FTacV permits measurement of E_{dist}, and generated a variant with a tuned E_{dist}, we now compare the catalytic activity of native Hyd-1 and HyaA-R193L to explore the role of the distal cluster in controlling catalytic bias and overpotential in [NiFe]-hydrogenases. A visual inspection of the aperiodic dc component of pH 4.0 144 Hz FTacV (Figure 2) suggests that HyaA-R193L is less biased towards H$_2$ oxidation than native Hyd-1. Under 100% N$_2$ the maximum H$_2$ production currents of native Hyd-1 and HyaA-R193L are similar, but under 100% H$_2$ the H$_2$-oxidation current of HyaA-R193L is significantly lower.

A quantitative measure of the changes in turnover rates that lead to a change in catalytic bias can only be obtained via knowledge of the number of active moles of enzyme on the electrode, M_{active}. This parameter is normally unmeasurable in dcV of O$_2$-tolerant MBHs(2, 43). FTacV permits estimation of M_{active}, and we do so based on $i_{max}^{144\,Hz}{}_{6th}$ the maximum current magnitude of the 144 Hz FTacV 6th harmonic. Simulation of 8.88 Hz FTacV of HyaB-E28Q quantified the total amount of hydrogenase on the electrode as M = 0.195 pmol (Figure 3), and when this same protein film was interrogated at 144 Hz, $i_{max}^{144\,Hz}{}_{6th}$= 0.285 µA

(Supplementary Figure 13). For a reversible one-electron reaction the harmonic current magnitude scales linearly with M(44), so it is extrapolated that $M(mol) \approx 6.8 \times 10^{-7} \times i_{max}^{144\,Hz}{}_{6th}$ for all variants. Since as-isolated enzyme is interrogated, some hydrogenase molecules are inactive and $M \neq M_{active}$. Dye assay data indicates that following overnight incubation in H_2, activity increases by a scalar factor of approx. 3 for both native Hyd-1 and HyaA-R193L, and so it is estimated that $M_{active} \approx \frac{M}{3}$ (Supplementary Figure 8).

The turnover rate, k_{H_2}, can thus be calculated from a single 144 Hz FTacV measurement (Figure 2) using the equation $k_{H_2} = \frac{i_{cat}}{2M_{active}\text{F}}$, where F is the Faraday constant.(38) Averaging the catalytic current measured at a certain potential in the forward and back sweep of the aperiodic dc component yields i_{cat}, while M_{active} is estimated from the 6th harmonic. Analysis of repeat experiments conducted at pH 4.0, 25 °C and under 100% H_2 quantifies H_2 oxidation turnover rates at +150 mV of 510, 790 and 750 s^{-1} for native Hyd-1 and 390, 320 and 190 s^{-1} for HyaA-R193L. Similarly, H_2 production rates at −550 mV, pH 4.0, 25 °C and under 100% N_2 are measured as 45, 51 and 48 s^{-1} for native Hyd-1 and 75, 60 and 57 s^{-1} for HyaA-R193L. There is significant variability in the absolute turnover rates extracted, which can be attributed to error in our quantification of M_{active}, but the analysis suggests that HyaA-R193L is more biased towards H_2 production catalysis than native enzyme due to both an increase in H_2 production rate and a decrease in H_2 oxidation rate.

Catalytic onset potentials are quantified via dcV experiments (Figure 4). At pH 3.0 and under 1% H_2 both native Hyd-1 and HyaA-R193L have zero overpotential requirement, since both oxidative and reductive catalysis commence at the potential of E(2H$^+$/H$_2$) (Figure 4a). Since the catalysis is reversible an absolute measure of catalytic bias can be obtained. The ratios of the H_2 oxidation current at +0.13 V and H$^+$ reduction current at −0.37 V (both taken from the average of the forward and back dcV sweep) are 3.2 ± 0.2 for native Hyd-1 and 1.1 ± 0.2 for HyaA-R193L (± indicates standard error of three repeats). The change in bias cannot be attributed to changes in the Michaelis constant (K$_M$) or the inhibition constant (K$_I$) for H_2 (Supplementary Figure 18 and Supplementary Table 4), suggesting that it is the lowering of E_{dist} that has led to a concomitant shift in catalytic bias towards H_2 production in HyaA-

R193L. Dye assay measurements of activated enzyme using methylene blue as the electron acceptor ($E_{m, pH\ 3}$ ~ + 0.14 V) indicate that at pH 3.0 the H_2 oxidation turnover rate of native Hyd-1 is approx. 1.3 times that of HyaA-R193L (Supplementary Figure 8). To give the measured change in catalytic bias the H_2 production turnover rate of HyaA-R193L would thus need to exceed that of native Hyd-1 under these conditions, supporting the conclusions of the FTacV catalytic rate analysis.
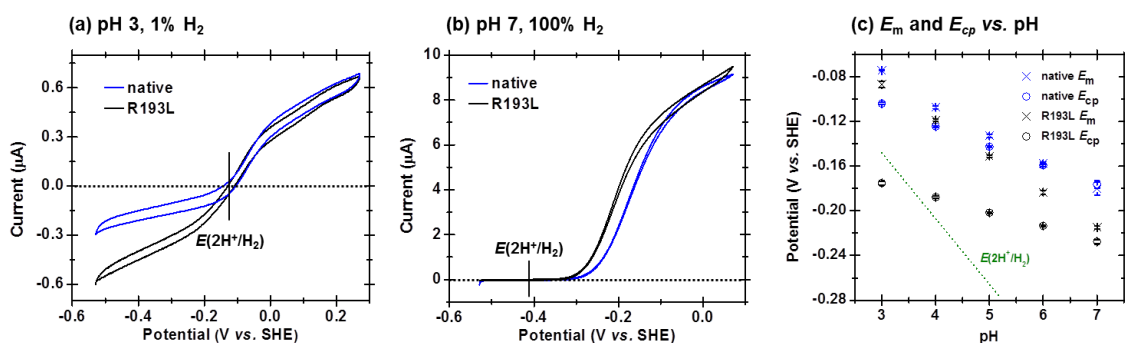
Figure 4 Comparison of the catalytic bias and overpotential requirement of native Hyd-1 and HyaA-R193L (a) dcV experiment to emphasize increased bias towards H_2 production of *E. coli* hydrogenase-1 HyaA-R193L variant relative to native enzyme, (b) dcV experiment to highlight the decreased catalytic overpotential of HyaA-R193L relative to native Hyd-1. Other experimental conditions: scan rate = 5 mV s^{-1}, 25°C, 5000 rpm, pH and gas atmosphere as indicated. (c) pH dependence of the H_2-independent 144 Hz FTacV determined 6th harmonic E_{CP}, E_m from dcV experiments conducted in 10% H_2, and the Nernstian determined $E(2H^+/H_2)$ value at 10% H_2. Error bars show standard error of at least three repeats.

At pH 7.0 and under 100 % H_2 both native Hyd-1 and HyaA-R193L are unidirectional, H_2 oxidation-only catalysts (Figure 4b). Both enzymes have an overpotential requirement for H_2 oxidation, since catalysis does not commence until a potential significantly higher than $E(2H^+/H_2)$. The onset of catalysis is clearly shifted to lower potential for HyaA-R193L, making it a more thermodynamically efficient H_2 oxidation catalyst than native Hyd-1, and confirming a relationship between E_{dist} and catalytic overpotential.

To quantify the impact of pH on the onset potential of H_2 oxidation catalysis, dcV experiments in which native Hyd-1 and variant HyaA-R193L had similar maximum oxidative currents were analyzed under 10% H_2. The onset potential is compared by characterizing a catalytic potential E_m, the potential of the maxima in a first derivative di_{avg}/dE vs E plot, where i_{avg} is the average of the forward and back current. Defining this parameter also facilitates comparison between E_{dist} and the potential of H_2 oxidation catalysis. As shown in Figure 4c, at pH 3.0 both native Hyd-1 and HyaA-R193L are thermodynamically optimized

catalysts with similar E_m values close to $E(2H^+/H_2)$. Thus, the difference in E_{dist} values does not apparently impact on the thermodynamic efficiency of catalysis under these conditions. As the pH increases from 3.0 to 7.0 both native and variant enzyme gain an overpotential requirement but the E_m of HyaA-R193L becomes increasingly more negative than that of native Hyd-1, suggesting that the difference in E_{dist} values has a significant impact on the overpotential requirement for H_2 oxidation under conditions of irreversible catalysis at high pH.

Further Impact of the HyaA-R193L Amino Acid Exchange

Relative to native enzyme, the catalytic profile of HyaA-R193L has been tuned towards that of an O_2-sensitive [NiFe]-hydrogenase, with enhanced bias towards H_2 production and decreased H_2 oxidation overpotential. To examine if O_2-tolerance has been maintained following this amino acid exchange, inhibition of H_2 oxidation by 3 % O_2 in 3 % H_2 was quantified using chronoamperometry at −0.029 V, pH 6.0 and 25°C (Supplementary Figure 19). HyaA-R193L is O_2-tolerant but this tolerance is slightly impaired relative to native Hyd-1; for HyaA-R193L approx. 60% of initial oxidation activity is sustained in 3 % O_2 / 3% H_2 and approx. 85% of original activity is rapidly recovered when the O_2 is removed, for native Hyd-1 approx. 75% activity is sustained and approx. 95% is recovered.

There is also a small difference between HyaA-R193L and native Hyd-1 in the reversible anaerobic formation of the Ni-B (Ni(III)-OH) inactivated state at positive potential. Formation of the Ni-B state was achieved via a 1,000 s hold at + 0.451 V and reactivation was driven by a 0.25 mV s^{-1} linear sweep to low potential, under 10 % H_2 at 25°C (Supplementary Figure 20). A qualitative measure of the thermodynamics and kinetics of Ni-B reactivation is given by E_{switch}, the potential at which the recovering catalytic current increases most rapidly (potential of the first derivative minima), in the sweep to low potential[50]. HyaA-R193L has a marginally (< 10 mV) more negative E_{switch} than native Hyd-1 across the pH range 4.0 to 8.0 (Supplementary Figure 20), indicating slightly slower activation kinetics and/or a slightly more negative Ni-B reduction potential[50]. This difference in E_{switch} is less than the 15 to 30 mV difference in E_m (potential of the first derivative maxima), observed in the same the experiments (Supplementary Figure 20).

These changes in anaerobic inactivation and O_2 tolerance could be linked to the more negative E_{dist} of HyaA-R193L, but such changes have previously been related to modifications of the proximal and medial clusters in *E. coli* Hyd-1(19, 21). EPR titrations at pH 7.0 reveal that the midpoint potentials associated with the medial cluster $[3Fe4S]^{1+/0}$ and proximal cluster $[Fe_4S_3]^{5+/4+}$ redox transitions are more negative in HyaA-R193L than native Hyd-1, decreased by 109 mV and 41 mV, respectively (Table 1 and Supplementary Figures 21 and 22). Thus, re-tuning the distal cluster potential also impacts the medial and proximal cluster potentials, indicating a highly-convoluted structure-function relationship.

Table 1: EPR determined iron sulfur cluster midpoint potentials at pH 7.0. Errors were estimated by using signal intensities at different field positons (*g* values) arising from the same species.

Redox transition	Native *E. coli* Hyd-1	HyaA-R193L
Proximal $[Fe_4S_3]^{5+/4+}$	211 mV (± 15)	170 mV (± 15)
Medial $[Fe_3S_4]^{1+/0}$	212 mV (± 30)	103 mV (± 30)
Proximal $[Fe_4S_3]^{4+/3+}$	4 mV (± 15)	-4 mV (± 15)

Distal Cluster Variants HyaA-K189N, HyaA-Y191E and HyaA-R193E

The variants HyaA-K189N and HyaA-Y191E have the same distal cluster redox potential as native Hyd-1, as quantified by E_{CP}, despite these residues also being in the vicinity of the distal cluster and the amino acid exchanges being inspired by differences between O_2-tolerant MBHs and O_2-sensitive [NiFe]-hydrogenases (Figure 1 and Supplementary Figures 23 and 24). The catalytic activity of both variants is also unchanged compared to native enzyme (Supplementary Figures 25 and 26). Attempts were also made to generate a HyaA-R193E variant, to investigate if a distal cluster with even more negative potential would result from replacing the positively charged Arg residue with a negatively charged Glu. However, growth and protein purification from the relevant *E. coli* mutant did not yield this Hyd-1 variant, suggesting that this amino acid exchange has a deleterious impact on the structural integrity of the enzyme (Supplementary Figure 27).

Discussion

Using *E. coli* Hyd-1, we prove that the bias and overpotential of the $2H^+/H_2$ interconversion that takes place at the buried NiFe active site of a hydrogenase

can be controlled by E_{dist}, the redox potential of the distal cluster electron entry/exit site approx. 30 Å away(4, 22-25). The previously elusive parameter E_{dist} is measured using high frequency, high harmonic FTacV measurements, and manipulated via an R193 to L amino acid exchange that is based on the first proposal of a His-mediated cation-π interaction tuning the redox chemistry of a FeS cluster. Engineering E_{dist} to a more negative potential enhanced the bias towards H_2 production and reduced the overpotential for H_2 oxidation, whilst almost native levels of O_2-tolerance were retained. [NiFe]-hydrogenase H_2 production activity is important since these enzymes naturally occur in photosynthetic microbes which could be engineered for sustained solar H_2 output if a blueprint can be found for designing O_2-functioning, H_2 producing biocatalysts(5). Decreasing the overpotential in [NiFe]-hydrogenase H_2 oxidation would also improve the thermodynamic efficiency of fuel cell and NAD(P)H recycling devices which use these enzymes instead of Pt.

Whether studying synthetic H_2-catalysts or hydrogenases, the ubiquitous presence of protons in aqueous solution makes the electrochemical deconvolution of catalytic and non-catalytic redox processes a non-trivial problem because the catalytic current is usually at least one order of magnitude larger than the non-catalytic current. FTacV is therefore a powerful technique because it permits the simultaneous and separate measurement of electron transfer (in the high harmonics) and H_2-catalysis (in the aperiodic dc component) from a single experiment, elucidating mechanistic insight into catalytic control by underlying electron transfer. We have shown, however, that this is only possible in sufficiently high frequency measurements. Simulation of the non-catalytic FTacV response quantifies the amount of catalyst on the electrode and therefore enables turnover rates to be estimated from the simultaneously measured catalytic response. Future work will focus on developing the experimental and parameter-optimization simulation procedure to much higher frequency, such that fully activated enzyme and even faster catalysts can be interrogated.

Cation- π interactions between a positively charged amino acid side chain and the π-system of an aromatic side chain are well-documented in structural biology but much less commonly considered in the tuning of protein redox sites (29). In all O_2-tolerant MBH crystal structures an Arg residue points at the distal

cluster His ligand with close enough proximity for a cation-π interaction to exist.(6-11) Replacement of the positive Arg residue with a neutral Leu, found in many O_2-sensitive [NiFe]-hydrogenases(12-15), results in an FTacV determined E_{dist} approx. 60 mV more negative in HyaA-R193L than in native *E. coli* Hyd-1, across the pH range 3.0 to 7.0. Thus, removal of the putative electrostatic cation-π interaction has increased the thermodynamic driving force required to reduce the distal cluster. This can be rationalized by considering that the cation-π interaction serves to withdraw electron density from the cluster in the native enzyme, stabilizing the reduced state. Therefore, cation-π interactions should be considered alongside other electrostatic, hydrogen bonding and hydrophobic interactions in the tuning of protein redox site reduction potentials by secondary coordination sphere effects.

The R193 to L amino acid exchange does not appear to influence the protonation state of His-187 since E_{dist} values of both HyaA-R193L and native Hyd-1 display relatively flat pH-potential profiles of −13 mV pH^{-1} and −18 mV pH^{-1}, respectively, over the pH range 3.0 to 7.0. This indicates that across this pH window, electron transfer in/out of the cluster is only weakly coupled to proton transfer, i.e. the protonation state of the His ligand is not affected by redox state changes in either native or variant enzyme. This compares with Rieske [Fe_2S_2] clusters that often have a strong pH-potential dependence only above pH 7, once the oxidized cluster histidine pKa is exceeded and reduction is coupled to protonation of imidazolate histidine ligands(51).

The weak pH dependence of E_{dist} contrasts with the −59 mV pH^{-1} dependence of the equilibrium potential for the H_2 redox couple, $E(2H^+/H_2)$. So, as predicted by Murphy *et al*(23), the two parameters converge at low pH and a concurrent enhancement in the catalytic reversibility of Hyd-1 is observed. The more negative E_{dist} of HyaA-R193L leads to a further shift in bias towards H_2-production, confirming the relationship between E_{dist} and catalytic bias anticipated by the electrocatalytic models of Hexter *et al*(4, 22). However, this simple model is not entirely validated since it predicts that when E_{dist} is more negative than $E(2H^+/H_2)$ a catalytic bias towards H_2 production will be observed(4, 22). Under conditions of pH 3.0 and 1% H_2 HyaA-R193L is equally active towards H_2 oxidation and H_2 production despite E_{dist} = −175 ± 2 mV < $E(2H^+/H_2)$ = −118 mV (Figure 4). Thus, although the catalytic bias is

demonstrably influenced by the distal cluster potential, further factors must control this important catalytic property. This conclusion is supported by previous studies showing that mutation of amino acid residues distant from the distal cluster can alter the catalytic bias, but not overpotential, of [NiFe]-hydrogenases(5, 43). The simple Hexter model implicitly assumes that the distal cluster controls both oxidative and reductive catalysis but our pH 4.0 FTacV rates analyses indicate that the HyaA-R193L amino acid exchange results in much larger decrease in H_2-oxidation rate than increase in H_2-production rate. Thus, enzyme wiring appears to play a more vital role in controlling H_2 oxidation than H_2 production. This supports the more complex electrocatalytic models of Leger and coworkers, which suggest that while electron transfer is rate limiting in H_2 oxidation, the rate of H_2 production catalysis is significantly limited by slow H_2 release from the active site(24, 25). Although the simple Hexter model has provided an excellent blueprint for substantially re-tuning the catalytic bias of Hyd-1, if the rate of H_2 production is to be further enhanced, large subunit changes which impact the rate of H_2 release from the active site may be required.

The electrocatalytic models of both Hexter et al(4, 22) and Leger and co-workers(24) predict a relationship between bias and overpotential, which is observed for native Hyd-1 and HyaA-R193L. As the bias towards H_2 oxidation increases with pH, the overpotential increases, as measured here by the difference between the catalytic potential E_m and the equilibrium potential of the H_2 redox couple $E(2H^+/H_2)$. At pH > 5 the bias is so great that catalysis is essentially irreversible and there is a significant overpotential requirement for H_2 oxidation. At pH 6.0 and 7.0 the E_m of native Hyd-1 matches the distal cluster potential E_{dist} and the more negative E_{dist} of HyaA-R193L coincides with a more negative E_m and reduced overpotential requirement. This is in agreement with the Hexter model of electrocatalysis, which predicts that the overpotential requirement for H_2 oxidation is governed by E_{dist} and as such its tuning to lower potential has engineered improved thermodynamic efficiency under conditions of irreversible H_2 oxidation catalysis (4, 22). At lower pH where catalysis becomes reversible, the E_m of native Hyd-1 diverges to a slightly higher potential than E_{dist} and the E_m of HyaA-R193L converges with that of native Hyd-1, despite the significantly more negative E_{dist} of the variant. Thus, E_{dist} is

not in total control of the exact catalytic potential under conditions of reversible catalysis. The results are in accordance with the electrocatalytic models of Leger and co-workers(24), which predict no simple relation between the catalytic potential and that of a relay site, due to the relative rates of other processes in the enzyme such as intramolecular electron transfer, which are specifically avoided in the Hexter model for the sake of simplicity (4, 22).

In addition to lowering E_{dist} the amino acid exchange in HyaA-R193L also lowers the medial and proximal iron-sulfur cluster potentials. The fact that the redox potential of one center in an electron transfer relay influences the redox potential of other centers is a well observed phenomenon that has been reported for other [NiFe]-hydrogenase variants(5, 35, 43). Accounting for this interdependency further complicates attempts to model metalloenzyme chemistry, and as such we cannot deconvolute whether changes in E_{dist} directly result in all the changes in enzyme reactivity, or if there are more complex interdependencies occurring. However, it must be acknowledged that in previous studies of purified [NiFe]-hydrogenases the potentials of the medial and proximal clusters have not had any significant impact on catalytic bias or overpotential, highlighting a crucial importance of the distal cluster modification in tuning these properties(19-21). The slightly diminished O_2-tolerance of HyaA-R193L could be attributed to the lower potential medial and proximal clusters being less able to provide an electron for O_2 reduction as has been previously observed(19, 21), but the lower potential distal cluster may also have an impact.

Although variants HyaA-K189N and HyaA-Y191E were indistinguishable from native Hyd-1, there must be residues in addition to R193 that play an important role in tuning E_{dist} and by extension the catalytic reversibility of [NiFe]-hydrogenases. All O_2-sensitive [NiFe]-hydrogenases have E_{dist} values of approx. −0.3 V at pH 7, irrespective of whether there is an Arg or Leu neighboring the distal cluster(35, 38, 52). Further, exchanging the Arg for Leu in Hyd-1 does not result in the E_{dist} or −60 mV pH^{-1} gradient reported for *D. gigas* O_2-sensitive [NiFe]-hydrogenase, which has a Leu at this position(52) and the catalytic reversibility is not enhanced to the level of O_2-sensitive [NiFe]-hydrogenases. Furthermore, although we identify E_{dist} as controlling the overpotential requirement of irreversible H_2 oxidation, we conclude that E_{dist} only

influences the catalytic bias and the full mechanism of enhanced H_2 production in O_2-sensitive [NiFe]-hydrogenases requires elucidation.

Nitrogenase, carbon monoxide dehydrogenase and photosystem II enzymes also convert small molecules into their redox activated and chemically useful counterparts (nitrogen to ammonia, carbon dioxide to carbon monoxide and water to oxygen, respectively) and contain a relay of redox-active centers that wire the outer surface of the protein to the "buried" active sites. FTacV should be considered a very useful tool for probing such systems and exploring how the electron transfer centers may control catalysis in these redox-enzymes. Ultimately, the inclusion of a molecular wire may be found to be an important design principle for synthetic multi-electron redox catalysts, which typically lack such additional redox centers.

Acknowledgments

Author Contributions

HA and AP designed the molecular biology and electrochemistry experiments and HA carried out the work with technical assistance from LAF and JW. MR, AMB and DJG designed the simulation approach and MR carried out the work. JJW and MMR designed the EPR experiments with input from HA and AP, and JJW carried out the work. Data analysis was performed by HA, MR and JJW. The paper was mainly written by HA and AP with valuable contributions from all other authors.

Competing Financial Interests Statement

The authors declare no competing financial interests.

Methods

Molecular Biology

All native and variant Hyd-1 enzymes were produced from W3110-derived *E. coli* K-12 strain LAF003 and variant strains. Strain LAF003 has an engineered *hyaA*(*his₇*)*BCDEF* operon to produce "wild-type" *E. coli* hydrogenase-1 with a polyhistidine tag at the C terminus of the small subunit(43). Five variant strains, carrying chromosomal *hyaB*(E28Q), *hyaA*(R193L), *hyaA*(R193E), *hyaA*(K189N) and *hyaA*(Y191E) mutations were derived from LAF003 using the "Counter-Selection BAC Modification Kit" (Cambio) and the protocol detailed previously(43). Briefly, the *rpsL*-neo cassette was inserted into an appropriate region of *hyaB* or *hyaA* of strain LAF003 to generate strains HA001 and HA002, respectively. The cassette was swapped out of HA001 by linear DNA (HyaBE28Qdsfrag), to give strain HA003 encoding a chromosomal E28Q mutation in *hyaB*. The cassette was swapped out of HA002 by linear DNA to give strains HA004, HA005, HA011 and HA014 encoding chromosomal mutations R193L, R193E, K189N or Y191E, respectively, in *hyaA*. All mutations were confirmed by sequencing (GATC Biotech). Details of all strains, oligonucleotide primers, plasmids and linear DNA used in this study are given in Supplementary Tables 5-8.

Protein production and purification

All strains were grown and proteins produced using a very similar protocol to that detailed previously(43). Briefly, strains were cultured anaerobically, harvested at stationary phase, lysed by osmotic shock then sonication and solubilized overnight by addition of 3% TritonX-100. Solubilized protein was purified by adding 50 mM imidazole and loading onto a 5 mL HiTrap Ni affinity column (GE Healthcare) that had been equilibrated in 20mM Tris, 150 mM NaCl, 50 mM imidazole, pH 7.3. Protein was eluted from the column using step changes in imidazole, up to a maximum concentration of 1 M, with all other buffer components unchanged. Fractions containing hydrogenase were confirmed by SDS-PAGE, pooled, and then dialyzed in a 20 mM Tris, 150 mM NaCl, pH 7.3 buffer overnight at 4°C using 6-8 kDa MWCO dialysis tubing (Fisher). Protein was concentrated using a 50 kDa MWCO Vivaspin centrifugal concentrator (GE Healthcare), and purity was confirmed by SDS-PAGE (Supplementary Figures 28 and 29).

For EPR samples the protein was then dialyzed in 50 mM HEPES, 50 mM dibasic sodium phosphate, 150 mM NaCl, 30% v/v glycerol, pH 7.0 using a 3.5 kDa MWCO Slide-A-Lyzer cassette (ThermoFisher).

For all assay and electrochemical experiments the protein was further purified by gel filtration on a Superdex 200 10/30 column (GE Healthcare) equilibrated in 20 mM Tris, 150 mM NaCl, pH 7.3. Fractions containing completely pure hydrogenase were confirmed by SDS-PAGE, pooled and concentrated using a 50 kDa MWCO Vivaspin centrifugal concentrator (GE Healthcare). Final sample purity was confirmed by SDS-PAGE (Supplementary Figures 28 and 29) and protein concentrations were measured by Bradford assay.

Protein Film Electrochemistry

All electrochemical experiments (dcV and FTacV) were performed in an anaerobic glovebox (University of York, Department of Chemistry, Mechanical Workshop). A three-electrode set-up of platinum counter, pyrolytic graphite edge (PGE) working electrode (geometric surface area 0.03 cm^2) and saturated calomel electrode (SCE) reference electrode was used, with a conversion factor of E(V vs SHE) = E (V vs SCE) + 0.241. All electrodes were contained in a water-jacketed and gas-tight glass cell containing mixed buffer of 15 mM each of MES, CHES, HEPES, TAPS and Na acetate, and 2 M NaCl. The temperature was controlled to 25°C by a water circulator and the atmosphere regulated by 100 scc min^{-1} flow of gas (BOC) of a certain composition by mass flow controllers (Sierra instruments).

To prepare an enzyme film the PGE surface was abraded with P1200 sandpaper (Norton) and then 0.5 µL of 0.25–1.5 mg ml^{-1} protein applied to the electrode surface for ~30 s, before excess enzyme was removed with a stream of water (Pur1te, 7.4 MΩ·cm). An Origatrod rotator (Origalys) was used to rotate the working electrode at 2000–5000 rpm to ensure mass transport of substrate or product was not rate limiting to catalysis. Direct current cyclic voltammetry and chronoamperometry measurements were performed with an Ivium CompactStat potentiostat. All Fourier Transformed ac Voltammetry was performed using the custom-made instrumentation described previously(40). Impedance was measured at potentials devoid of Faradaic current and a simple RC circuit model was used to calculate the uncompensated resistance value used in simulations.

Simulations

Simulations were performed using a protocol based on those previously described in Morris et. al.(46) and Adamson et al(41). We assumed a Langmuir isotherm and any proton transfer accompanying electron transfer is reversible, with the equilibrium constants associated with protonation incorporated into E_{rev}. The one-electron transfer process for HyaB-E28Q was modelled using two surface confined species A and B, with reactions

$$A + e^- \leftrightarrows B$$
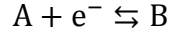
We use the Butler-Volmer theory for the forward k_{red} and backwards k_{ox} reaction rates. If θ is the proportion of species A on the surface, then the rate of change in time of θ is given by

$$\frac{d\theta}{dt} = k_0(1-\theta)\exp\left((1-\alpha)\frac{F}{RT}[E_r(t)-E_0]\right) - k_0\theta\exp\left(-\frac{\alpha F}{RT}[E_r(t)-E_0]\right) \quad (1)$$

where $E_r(t) = E(t) - R_u I_{tot}(t)$ is the input applied potential $E(t)$ minus the potential due to uncompensated resistance R_u as reflected in the Ohmic (IR_u) drop.

The total current I_{tot} is the addition of capacitive and Faradaic terms, and is given by

$$I_{tot}(t) = C_{dl}(1 + C_{dl1}E_r(t) + C_{dl2}E_r^2(t) + C_{dl3}E_r^3(t))\frac{dE_r}{dt} + FS\Gamma\frac{d\theta}{dt}, \quad (2)$$

where the capacitive current is given by a third order polynomial in $E_r(t)$. The input potential $E(t)$ is the sum of dc (E_{dc}) and ac contributions

$$E(t) = E_{dc}(t) + \Delta E\sin(\omega t + \eta)$$

where ΔE is the amplitude of the sine wave of frequency ω ($\omega = 2\pi f$, where f is frequency in Hz) and phase η. The dc contribution is given by a forward and backwards linear sweep with scan rate v, starting potential E_{start} and reverse potential $E_{reverse}$,

$$E_{dc}(t) = \begin{cases} E_{start} + vt, & \text{for } 0 \leq t < t_r \\ E_{reverse} - v(t-t_r), & \text{for } t_r \leq t \end{cases}$$

$$t_r = \frac{E_{reverse} - E_{start}}{v}.$$

We solve (1) and (2) by discretizing the time derivative with an implicit Euler method, and solve the resulting non-linear equation using the Newton-Raphson method as implemented in the Boost C++ library (https://www.boost.org).

To include the effects of thermodynamic and kinetic dispersion, we write the total current as a function of E_0 and k_0, i.e. $I_{\text{tot}}(t, E_0, k_0)$, and calculate the expected value of I_{tot} given probability distributions $\rho(E_0)$ and $\rho(k_0)$,

$$\overline{I_{\text{tot}}}(t) = \iint\limits_{E_0, k_0} I_{\text{tot}}(t, E_0, k_0)\, \rho(E_0)\rho(k_0)dE_0 dk_0,$$

where $\rho(E_0)$ is a normal distribution with mean $\overline{E_0}$ and standard deviation σ_E, and $\rho(k_0)$ is a log-normal distribution with location parameter μ_k and scale parameter σ_k. Given the cumulative distributions $F(E_0)$ and $F(k_0)$ corresponding to $\rho(E_0)$ and $\rho(k_0)$, and mapping functions $\alpha_E = F(E_0)$ and $\alpha_k = F(k_0)$, we can map this integral, over an infinite domain, into the finite domain $0 \leq \alpha_E, \alpha_k < 1$,

$$\overline{I_{\text{tot}}}(t) = \iint\limits_{\alpha_E, \alpha_k} I_{\text{tot}}\big(t, F^{-1}(\alpha_E), F^{-1}(\alpha_k)\big)\, d\alpha_E d\alpha_k.$$

To numerically evaluate the integral, we chose a set of quadrature points using the Sobol quasi-random sequence, which generates a low discrepancy pseudo-random sequence of N points over $0 \leq \alpha_E, \alpha_k < 1$, with quadrature weights equal to $1/N$. The integral thus becomes

$$\overline{I_{\text{tot}}}(t) = \frac{1}{N}\sum_i^N I_{\text{tot}}\left(t, F^{-1}(\alpha_E^i), F^{-1}(\alpha_k^i)\right).$$

Through numerical experiments we have determined that the accuracy of this integral converges sufficiently with $N \geq 128$ points.

We fit the capacitive parameters $(C_{\text{dl}}, C_{\text{dl1}}, C_{\text{dl2}}, C_{\text{dl3}})$ and ac signal frequency ω, by minimizing an objective function $\mathcal{L}_c$ based on the time domain data that is devoid of any significant influence of the Faradaic current. If $I_e(t)$ is the experimental data, then $\mathcal{L}_c$ is given by

$$\mathcal{L}_c^2 = \sum_{j=1}^N \begin{cases} 0 & \text{for } t_l \leq t_j - nt_p < t_h, \\ [\overline{I_{\text{tot}}}(t_j) - I_e(t_j)]^2 & \text{otherwise,} \end{cases}$$

where n is any integer and

$$t_l = \frac{1}{5}(\epsilon_{\text{reverse}} - \epsilon_{\text{start}}),$$

$$t_h = \frac{4}{5}(\epsilon_{\text{reverse}} - \epsilon_{\text{start}}),$$

$$t_p = \epsilon_{\text{reverse}} - \epsilon_{\text{start}}.$$

We fit the Faradaic parameters (i.e. E_0 and k_0 if no dispersion is added; or $\overline{E_0}$, σ_E, μ_k and σ_k with both thermodynamic and kinetic dispersion) and the phase η, by using an objective function $\mathcal{L}_f$ based on the harmonics $n = n_0 \ldots n_M$ of the Fourier transformed simulated and experimental data ($f_{\text{tot}}(\omega)$ and $f_e(\omega)$, respectively).

$$\mathcal{L}_f = \sqrt{\sum_k^N |w(\omega_k)(f_{tot}(\omega_k) - f_e(\omega_k))|^2},$$

$$w(\omega_k) = \sum_{n=n_0}^{n_M} w_n(\omega_k),$$

where w_n is the Kaiser window centered on the n-th harmonic. In order to mitigate any inaccuracies in the polynomial model for the capacitive current, we use only higher order harmonics ($n_0 = 4$), which are background-free. The upper harmonic used was $n_M = 8$, as harmonics greater than the 8th were dominated by measurement noise.

EPR

EPR titrations were performed as detailed previously(43). Briefly, 100-200 µL of enzyme solution in pH 7.0 buffer (above) was transferred to a custom electrochemical cell with a platinum working electrode and Ag/AgCl reference electrode (DRIREF-2, WPI) inside a Braun UniLab-plus glovebox ($O_2 < 0.5$ ppm, N_2 atmosphere). The following redox mediators were added at 25 µM (native Hyd-1 and HyaB-E28Q) or 40 µM (HyaA-R139L): phenazine methosulfate, 1,4-naphthoquinone, methylene blue, indigotrisulfonate, 2-hydroxy-1,4- naphthoquinone, benzyl viologen, and methyl viologen. In addition, 40 µM anthraquinine-2-sulfonate was added to the HyaA-R139L sample. Each hydrogenase sample was titrated by the addition of small aliquots of potassium

ferricyanide or sodium dithionite until the desired potential was achieved, at which stage 9 µL samples were transferred to quartz EPR tubes (1.6 mm O.D., Wilmad) and flash frozen in ethanol cooled externally using a dry-ice/acetone bath.

EPR measurements were performed on a X/Q-band Bruker Elexsys E580 Spectrometer (Bruker BioSpin GmbH, Germany) equipped with a closed-cycle cryostat (Cryogenic Ltd, UK) and an X-band split-ring resonator module with 2 mm sample access (ER 4118X-MS2, Bruker) operated in continuous-wave mode. All measurements were conducted at 20 K with 2 mW power, 100 kHz modulation frequency and 1.0 mT modulation amplitude. In order to determine reduction potentials of the EPR-visible clusters, signal intensities were monitored as a function of potential ("Nernst plots" in Figures S16 and S21, right). The proximal $[Fe_4S_3]^{5+/4+}$ signal intensity was plotted using the difference in peak heights at g = 1.981 and 1.970, with the maximum intensity scaled to 1. The $[Fe_4S_3]^{4+/3+}$ intensities were taken from the height of the EPR signal at g = 1.892 – 1.871. The intensity of the medial $[Fe_3S_4]^{1+}$ cluster EPR signal (that decreased at high potentials due to magnetic coupling with $[4Fe-3S]^{5+}$) was monitored using g = 2.025 – 1.981 (native Hyd-1) or g = 2.059 – 2.025 (HyaA-R193L). The reduction potential of the medial cluster $[3Fe-4S]^{+/0}$ transition was determined as described in Roessler et. al(26). The double integral of the EPR spectrum from the most oxidized sample was normalized to two spins per enzyme molecule to account for the fully oxidized medial and proximal clusters. The percentage of signal arising from the medial cluster was then determined by subtraction of the percentage of signal arising from the proximal cluster (established from its reduction potential). Signal intensities from the medial $[3Fe-4S]^+$ signal were then scaled according to the percentage reduction of the cluster.

References

1. Lubitz W, Ogata H, Rüdiger O, & Reijerse E (2014) Hydrogenases. *Chem. Rev.* 114(8):4081-4148.

2. Flanagan Lindsey A & Parkin A (2016) Electrochemical insights into the mechanism of NiFe membrane-bound hydrogenases. *Biochem. Soc. Trans.* 44(1):315-328.

3. Lukey MJ*, et al.* (2010) How *Escherichia coli* Is Equipped to Oxidize Hydrogen under Different Redox Conditions. *J. Biol. Chem.* 285(6):3928-3938.

4. Hexter SV, Grey F, Happe T, Climent V, & Armstrong FA (2012) Electrocatalytic mechanism of reversible hydrogen cycling by enzymes and distinctions between the major classes of hydrogenases. *Proc. Natl. Acad. Sci. U.S.A.* 109(29):11516-11521.

5. Raleiras P*, et al.* (2016) Turning around the electron flow in an uptake hydrogenase. EPR spectroscopy and *in vivo* activity of a designed mutant in HupSL from *Nostoc punctiforme*. *Energy Environ. Sci.* 9(2):581-594.

6. Evans RM*, et al.* (2016) Mechanism of hydrogen activation by [NiFe] hydrogenases. *Nat. Chem. Biol.* 12(1):46-50.

7. Fritsch J*, et al.* (2011) The crystal structure of an oxygen-tolerant hydrogenase uncovers a novel iron-sulphur centre. *Nature* 479(7372):249-252.

8. Shomura Y, Yoon K-S, Nishihara H, & Higuchi Y (2011) Structural basis for a [4Fe-3S] cluster in the oxygen-tolerant membrane-bound [NiFe]-hydrogenase. *Nature* 479(7372):253-256.

9. Volbeda A*, et al.* (2012) X-ray crystallographic and computational studies of the O_2-tolerant [NiFe]-hydrogenase 1 from *Escherichia coli*. *Proc. Natl. Acad. Sci. U.S.A.* 109(14):5305-5310.

10. Bowman L*, et al.* (2014) How the structure of the large subunit controls function in an oxygen-tolerant [NiFe]-hydrogenase. *Biochem. J.* 458(3):449-458.

11. Frielingsdorf S*, et al.* (2014) Reversible [4Fe-3S] cluster morphing in an O_2-tolerant [NiFe] hydrogenase. *Nat. Chem. Biol.* 10(5):378-385.

12. Volbeda A*, et al.* (1995) Crystal structure of the nickel-iron hydrogenase from *Desulfovibrio gigas*. *Nature* 373(6515):580-587.

13. Rousset M*, et al.* (1998) [3Fe-4S] to [4Fe-4S] cluster conversion in *Desulfovibrio fructosovorans* [NiFe] hydrogenase by site-directed mutagenesis. *Proc. Natl. Acad. Sci. U.S.A.* 95(20):11625-11630.

14. Ogata H, Kellers P, & Lubitz W (2010) The Crystal Structure of the [NiFe] Hydrogenase from the Photosynthetic Bacterium *Allochromatium vinosum*: Characterization of the Oxidized Enzyme (Ni-A State). *J. Mol. Biol.* 402(2):428-444.

15. Ogata H, Nishikawa K, & Lubitz W (2015) Hydrogens detected by subatomic resolution protein crystallography in a [NiFe] hydrogenase. *Nature* 520(7548):571-574.

16. Gebler A*, et al.* (2007) Impact of alterations near the [NiFe] active site on the function of the H_2 sensor from *Ralstonia eutropha*. *FEBS J.* 274(1):74-85.

17. Greene BL, Vansuch GE, Wu C-H, Adams MWW, & Dyer RB (2016) Glutamate Gated Proton-Coupled Electron Transfer Activity of a [NiFe]-Hydrogenase. *J. Am. Chem. Soc.*

18. Dementin S*, et al.* (2004) A Glutamate Is the Essential Proton Transfer Gate during the Catalytic Cycle of the [NiFe] Hydrogenase. *J. Biol. Chem.* 279(11):10508-10513.

19. Lukey MJ*, et al.* (2011) Oxygen-Tolerant [NiFe]-Hydrogenases: The Individual and Collective Importance of Supernumerary Cysteines at the Proximal Fe-S Cluster. *J. Am. Chem. Soc.* 133(42):16881-16892.

20. Goris T*, et al.* (2011) A unique iron-sulfur cluster is crucial for oxygen tolerance of a [NiFe]-hydrogenase. *Nat. Chem. Biol.* 7(5):310-318.

21. Evans RM*, et al.* (2013) Principles of Sustained Enzymatic Hydrogen Oxidation in the Presence of Oxygen – The Crucial Influence of High Potential Fe–S Clusters in the Electron Relay of [NiFe]-Hydrogenases. *J. Am. Chem. Soc.* 135(7):2694-2707.

22. Hexter SV, Esterle TF, & Armstrong FA (2014) A unified model for surface electrocatalysis based on observations with enzymes. *Phys. Chem. Chem. Phys.* 16(24):11822-11833.

23. Murphy BJ, Sargent F, & Armstrong FA (2014) Transforming an oxygen-tolerant [NiFe] uptake hydrogenase into a proficient, reversible hydrogen producer. *Energy Environ. Sci.* 7(4):1426-1433.

24. Fourmond V, *et al.* (2013) Steady-State Catalytic Wave-Shapes for 2-Electron Reversible Electrocatalysts and Enzymes. *J. Am. Chem. Soc.* 135(10):3926-3938.

25. Abou Hamdan A, *et al.* (2012) Understanding and Tuning the Catalytic Bias of Hydrogenase. *J. Am. Chem. Soc.* 134(20):8368-8371.

26. Roessler MM, Evans RM, Davies RA, Harmer J, & Armstrong FA (2012) EPR Spectroscopic Studies of the Fe–S Clusters in the O_2-Tolerant [NiFe]-Hydrogenase Hyd-1 from *Escherichia coli* and Characterization of the Unique [4Fe–3S] Cluster by HYSCORE. *J. Am. Chem. Soc.* 134(37):15581-15594.

27. Marshall NM, *et al.* (2009) Rationally tuning the reduction potential of a single cupredoxin beyond the natural range. *Nature* 462(7269):113-116.

28. Stephens PJ, Jollie DR, & Warshel A (1996) Protein Control of Redox Potentials of Iron−Sulfur Proteins. *Chem. Rev.* 96(7):2491-2514.

29. Mahadevi AS & Sastry GN (2013) Cation−π Interaction: Its Role and Relevance in Chemistry, Biology, and Material Science. *Chem. Rev.* 113(3):2100-2138.

30. Liao S-M, Du Q-S, Meng J-Z, Pang Z-W, & Huang R-B (2013) The multiple roles of histidine in protein interactions. *Chem. Cent. J.* 7(1):44.

31. Kobayashi K, Mizuno M, Fujikawa M, & Mizutani Y (2011) Protein Conformational Changes of the Oxidative Stress Sensor, SoxR, upon Redox Changes of the [2Fe–2S] Cluster Probed with Ultraviolet Resonance Raman Spectroscopy. *Biochem.* 50(44):9468-9474.

32. Yorita H, *et al.* (2008) Evidence for the Cation−π Interaction between Cu^{2+} and Tryptophan. *J. Am. Chem. Soc.* 130(46):15266-15267.

33. Xue Y, *et al.* (2008) Cu(I) recognition via cation-p and methionine interactions in CusF. *Nat. Chem. Biol.* 4(2):107-109.

34. Sibert R, *et al.* (2007) Proton-Coupled Electron Transfer in a Biomimetic Peptide as a Model of Enzyme Regulatory Mechanisms. *J. Am. Chem. Soc.* 129(14):4393-4400.

35. Dementin S, *et al.* (2006) Changing the Ligation of the Distal [4Fe4S] Cluster in NiFe Hydrogenase Impairs Inter- and Intramolecular Electron Transfers. *J. Am. Chem. Soc.* 128(15):5209-5218.

36. Petrenko A & Stein M (2017) Distal [FeS]-Cluster Coordination in [NiFe]-Hydrogenase Facilitates Intermolecular Electron Transfer. *Int. J. Mol. Sci.* 18(1):100.

37. Petrenko A & Stein M (2015) Rates and Routes of Electron Transfer of [NiFe]-Hydrogenase in an Enzymatic Fuel Cell. *J. Phys. Chem. B* 119(43):13870-13882.

38. Pershad HR*, et al.* (1999) Catalytic Electron Transport in *Chromatium vinosum* [NiFe]-Hydrogenase: Application of Voltammetry in Detecting Redox-Active Centers and Establishing That Hydrogen Oxidation Is Very Fast Even at Potentials Close to the Reversible H^+/H_2 Value. *Biochem.* 38(28):8992-8999.

39. Sharma S, Sivalingam K, Neese F, & ChanGarnet K-L (2014) Low-energy spectrum of iron–sulfur clusters directly from many-particle quantum mechanics. *Nat. Chem.* 6(10):927-933.

40. Bond AM*, et al.* (2015) An integrated instrumental and theoretical approach to quantitative electrode kinetic studies based on large amplitude Fourier transformed a.c. voltammetry: A mini review. *Electrochem. Commun.* 57:78-83.

41. Adamson H*, et al.* (2017) Analysis of HypD Disulfide Redox Chemistry via Optimization of Fourier Transformed ac Voltammetric Data. *Anal. Chem.* 89(3):1565–1573.

42. Adamson H*, et al.* (2015) Electrochemical evidence that pyranopterin redox chemistry controls the catalysis of YedY, a mononuclear Mo enzyme. *Proc. Natl. Acad. Sci. U.S.A.* 112(47):14506-14511.

43. Flanagan LA, Wright JJ, Roessler MM, Moir JW, & Parkin A (2016) Re-engineering a NiFe hydrogenase to increase the H_2 production bias while maintaining native levels of O_2 tolerance. *Chem. Commun.* 52(58):9133-9136.

44. Zhang J & Bond AM (2007) Theoretical studies of large amplitude alternating current voltammetry for a reversible surface-confined electron transfer process coupled to a pseudo first-order electrocatalytic process. *J. Electroanal. Chem.* 600(1):23-34.

45. Léger C, Jones AK, Albracht SPJ, & Armstrong FA (2002) Effect of a Dispersion of Interfacial Electron Transfer Rates on Steady State

Catalytic Electron Transport in [NiFe]-hydrogenase and Other Enzymes. *J. Phys. Chem. B* 106(50):13058-13063.

46. Morris GP*, et al.* (2015) Theoretical Analysis of the Relative Significance of Thermodynamic and Kinetic Dispersion in the dc and ac Voltammetry of Surface-Confined Molecules. *Langmuir* 31(17):4996-5004.

47. Hidalgo R, Ash PA, Healy AJ, & Vincent KA (2015) Infrared Spectroscopy During Electrocatalytic Turnover Reveals the Ni-L Active Site State During H_2 Oxidation by a NiFe Hydrogenase. *Angew. Chem. Int. Ed.* 54(24):7110-7113.

48. Murphy BJ*, et al.* (2015) Discovery of Dark pH-Dependent H^+ Migration in a [NiFe]-Hydrogenase and Its Mechanistic Relevance: Mobilizing the Hydrido Ligand of the Ni-C Intermediate. *J. Am. Chem. Soc.* 137(26):8484-8489.

49. Lu M & Compton RG (2014) Voltammetric pH sensor based on an edge plane pyrolytic graphite electrode. *Analyst* 139(10):2397-2403.

50. Fourmond V, Infossi P, Giudici-Orticoni M-Trs, Bertrand P, & Léger C (2010) "Two-step" chronoamperometric method for studying the anaerobic inactivation of an oxygen tolerant NiFe hydrogenase. *Journal of the American Chemical Society* 132(13):4848-4857.

51. Zu Y*, et al.* (2003) Reduction potentials of Rieske clusters: importance of the coupling between oxidation state and histidine protonation state. *Biochemistry* 42(42):12400-12408.

52. Cammack R, Patil DS, Hatchikian EC, & Fernández VM (1987) Nickel and iron-sulphur centres in *Desulfovibrio gigas* hydrogenase: ESR spectra, redox properties and interactions. *Biochim. Biophys. Acta, Protein Struct. Mol. Enzymol.* 912(1):98-109.

Supplementary Information for "Control of Catalytic Bias and Overpotential by the Electron Entry/exit Site in a [NiFe]-hydrogenase"

Hope Adamson[1], Martin Robinson[2], John J. Wright[3], Lindsey A. Flanagan[1], Julia Walton[1], Darrell Elton[4], David J. Gavaghan[2], Alan M. Bond[5], Maxie M. Roessler[3], and Alison Parkin[1,*]

[1] Department of Chemistry, University of York, Heslington, York, YO10 5DD, UK

[2] Department of Computer Science, University of Oxford, Oxford, OX1 3QD, UK

[3] School of Biological and Chemical Sciences, Queen Mary University of London, Mile End Road, London, E1 4NS, UK

[4] Department of Engineering, School of Engineering and Mathematical Sciences, La Trobe University, Melbourne, Victoria 3086, Australia
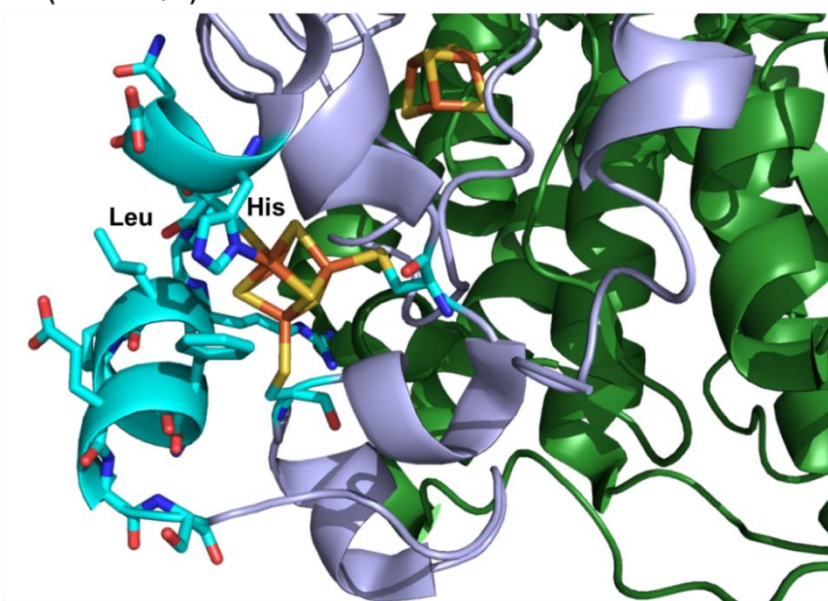
[5] School of Chemistry, Monash University, Clayton, Victoria 3800, Australia

1. The relative locations of Arg at the distal cluster of *E. coli* Hyd-1, an O₂ tolerant hydrogenase, and Leu at the distal cluster of *Desulfovibrio fructosovorans* O₂ sensitive [NiFe] hydrogenase

Ec Hyd-1 (PDB 3UQY)
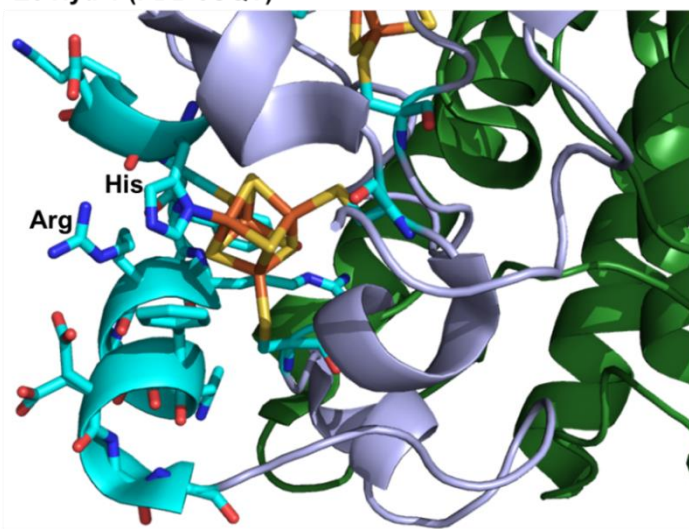
Df (PDB 1YQW)

Supplementary Figure 1: The position of Arg-193 in the small subunit of *E. coli* Hyd-1 and the location of the equivalently-positioned Leu-190 in *Desulfovibrio fructosovorans*. Light blue cartoon indicates the small subunit and green cartoon indicates the large subunit. Line colors: yellow indicates sulfur, orange-red indicates Fe, bright blue indicates carbon, dark blue indicates nitrogen and bright red indicates oxygen. Abbreviations are *E. coli* Hyd-1 (*Ec* Hyd-1), *Desulfovibrio fructosovorans* [NiFe]-hydrogenase (*Df*). The residues along the bright blue helix in the *Df* structure form part of the electron transfer route that DFT calculation indicate conducts electrons between the protein surface and the distal cluster, His184-Asn186-Cys187-Pro188-Arg189-Leu190-Pro191-His192-Phe193-Glue194-Ala195-Ser196 (1, 2). The equivalent residues are also indicated on the *Ec* structure, His187-Asn188-Lys189-Cys190-Tyr191-Arg192-Arg193-Ala194-His195-Phe196-Asp197-Ala198-Gly199.

2. Distance between distal cluster histidine ligand and arginine in hydrogenase crystal structures

Ec Hyd-1 H₂ reduced (PDB 3UQY)
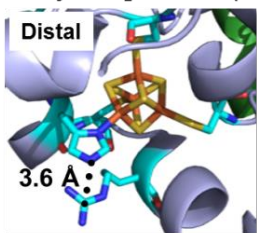
Ec Hyd-1 K₃Fe(CN)₆ oxidized (PDB 3USC)
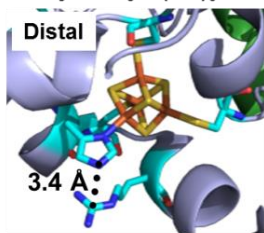
Sal Hyd-5 oxidized, as-isolated (PDB 4C3O)
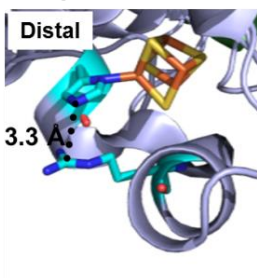
Re MBH H₂ reduced (PDB 3RGW)
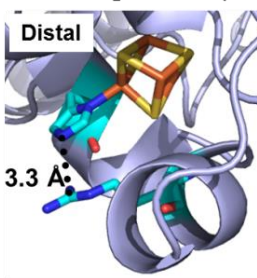
Re MBH oxidized state 3 (PDB 4TTT)
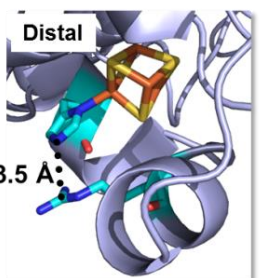
Hm H₂ reduced (PDB 3AYX)
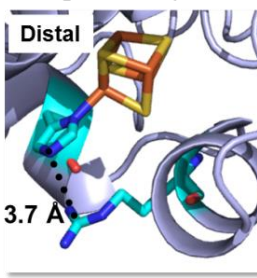
Hm K₃Fe(CN)₆ oxidized (PDB 3AYY)
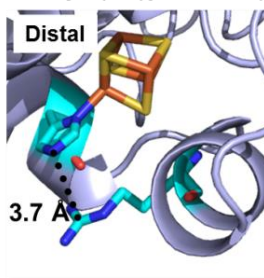
Supplementary Figure 2: Pymol determined distance measurements between N^τ ($N^{\delta 1}$ or ND1) of the distal cluster His ligand and C^ζ of the neighboring Arg of O$_2$-tolerant [NiFe]-hydrogenases. Light blue cartoon indicates the small subunit and green cartoon indicates the large subunit. Line colors: yellow indicates sulfur, orange-red indicates Fe, bright blue indicates carbon, dark blue indicates nitrogen and bright red indicates oxygen. Abbreviations are *E. coli* Hyd-1 (*Ec* Hyd-1), *Salmonella enterica* Hyd-5 (*Sal* Hyd-5), *Ralstonia eutropha* membrane bound hydrogenase (*Re* MBH), *Hydrogenovibrio marinus* [NiFe]-hydrogenase (*Hm*).

3. 4th to 7th harmonics of 144 Hz FTacV measurement of native Hyd-1
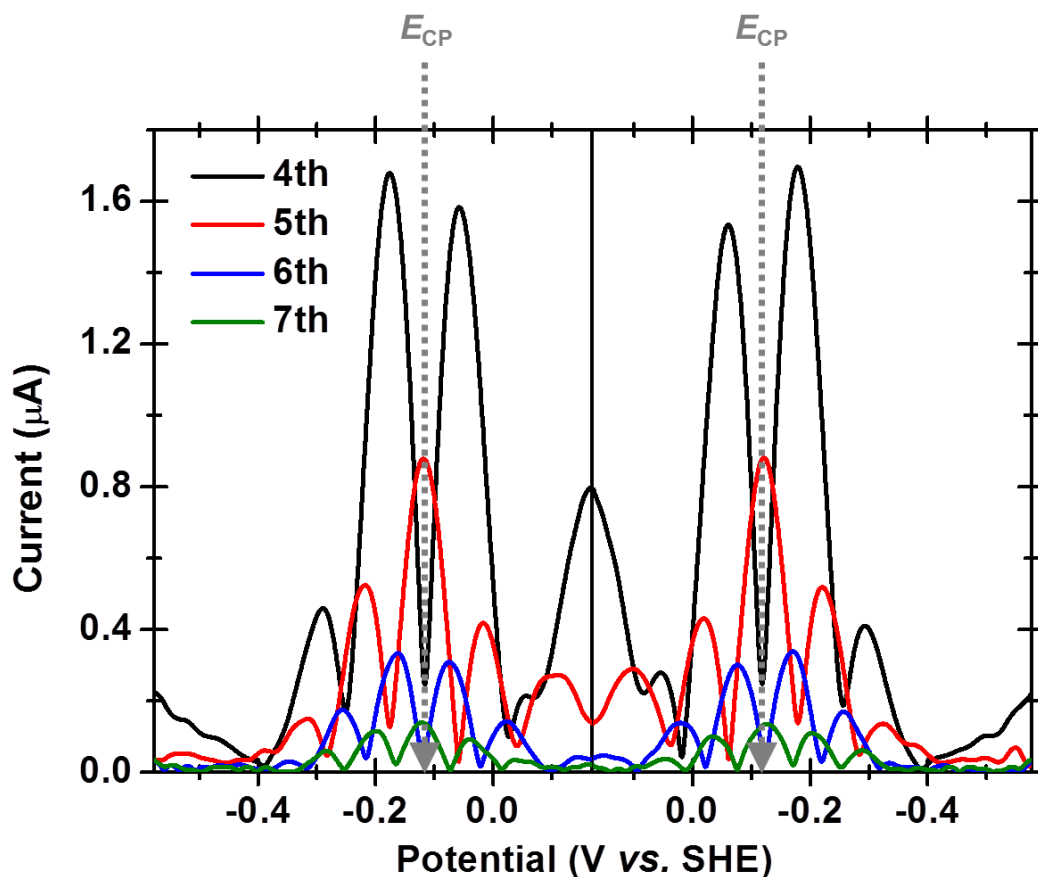
Supplementary Figure 3: 4th to 7th harmonics from FTacV of native _E. coli_ hydrogenase-1 at frequency = 144 Hz, amplitude = 150 mV and scan rate = 27.94 mV s⁻¹. Other experimental conditions: pH 4.0, 2000 rpm, 25°C, 100% H_2.

Note that E_{CP} denotes the center point of the redox process observed in the high harmonic measurements.

4. Impact of pH on native Hyd-1 FTacV data

(a) aperiodic dc, 100% H$_2$

(b) 6th harmonic, 100% H$_2$

(c) aperiodic dc, 100% N$_2$

(d) 6th harmonic, 100% N$_2$
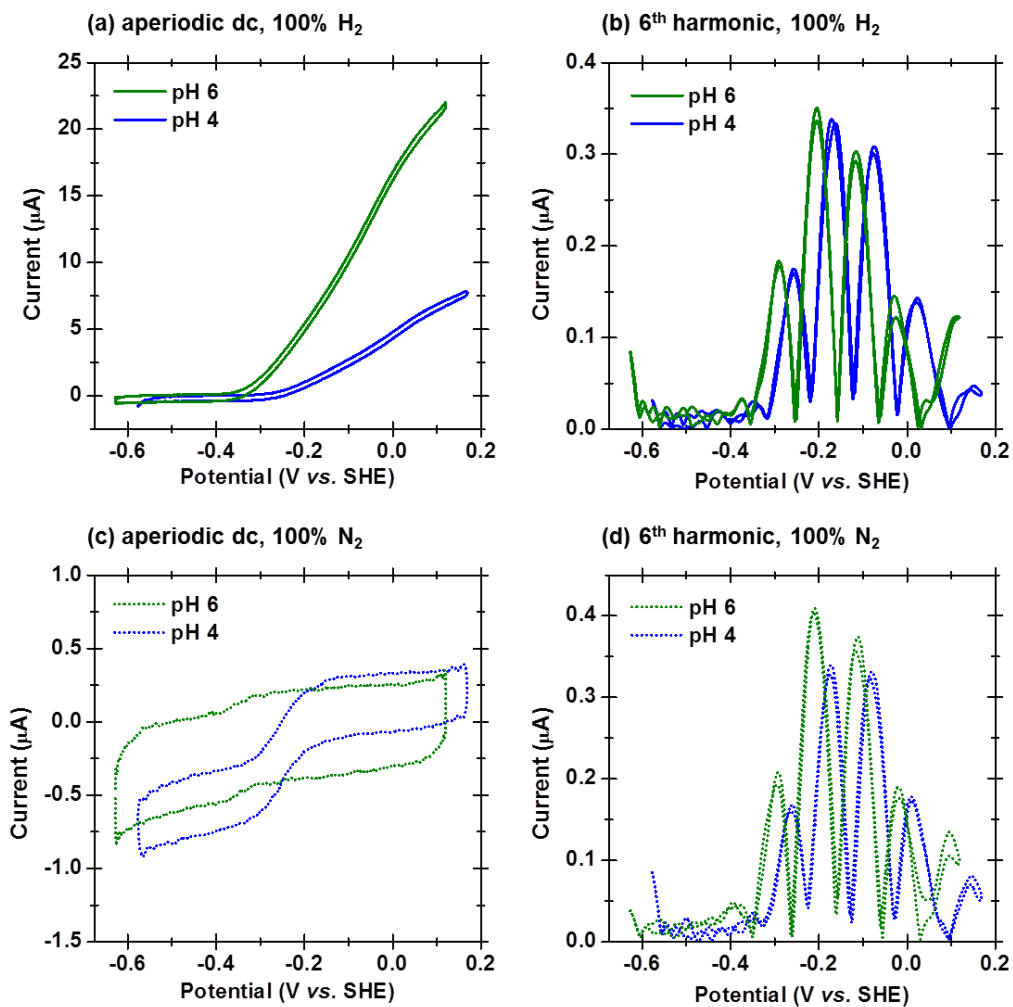
Supplementary Figure 4: Overlay of aperiodic dc component and 6th harmonic of 144 Hz FTacV measurement of native *E. coli* hydrogenase-1 at pH 6 and 4. Other experimental conditions: amplitude = 150 mV, scan rate = 27.94 mV s^{-1}, 2000 rpm, 25°C, pH and gas atmosphere as indicated.

5. Impact of amplitude on apparent onset potential in FTacV
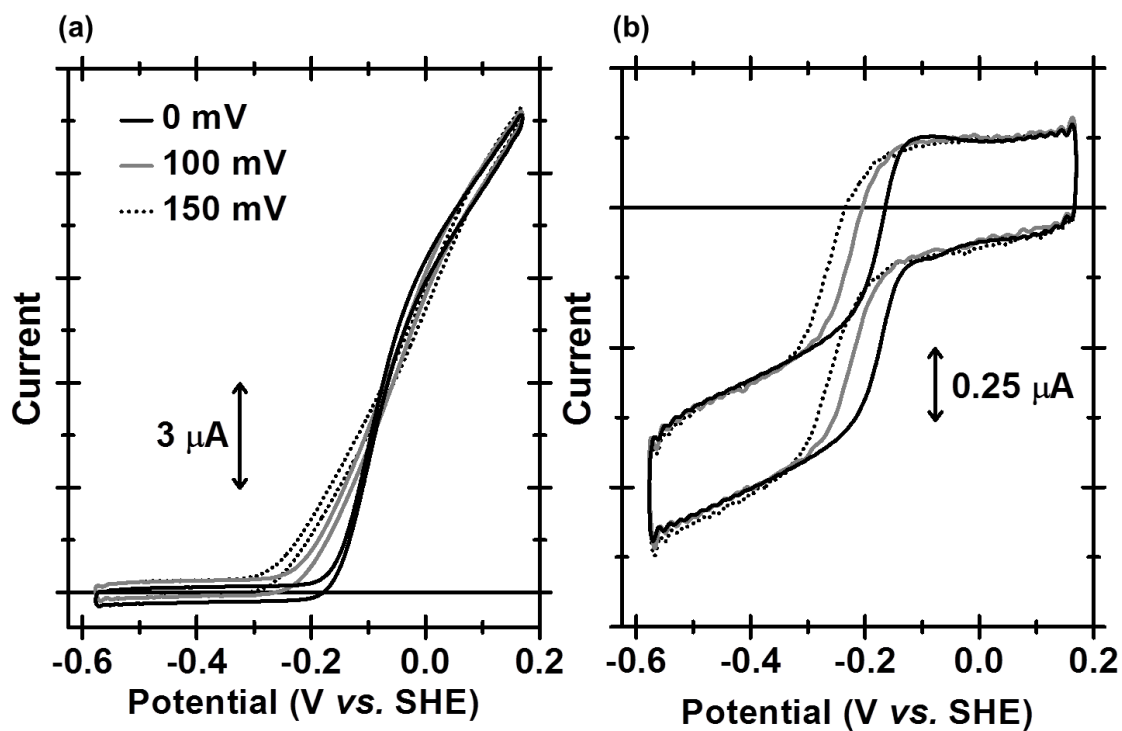
Supplementary Figure 5: Aperiodic-dc component of FTacV of native _E. coli_ hydrogenase-1 at frequency = 144 Hz, scan rate = 27.94 mV s^{-1} and varying amplitudes in (a) 100% H_2 atmosphere (b) 100% N_2 atmosphere. Measurements with amplitude = 0 mV shown in black solid line, 100 mV shown in grey solid line and 150 mV shown in black dotted line. Other experimental conditions: pH 4.0, 2000 rpm, 25°C.

6. EPR spectroscopy confirms structural integrity of the HyaB-E28Q Hyd-1 variant

100 µL of 25 µM HyaB-E28Q was titrated and EPR measurements were carried out as described in the Online Methods.
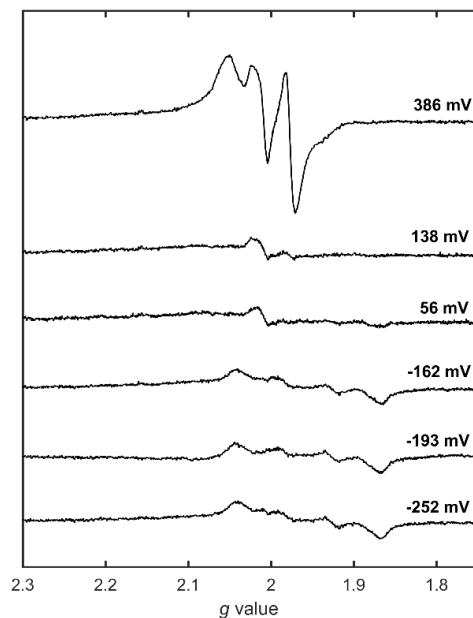
Supplementary Figure 6: X-band continuous-wave EPR spectra resulting from the redox titration of HyaB-E28Q Hyd-1 at pH 7.0.
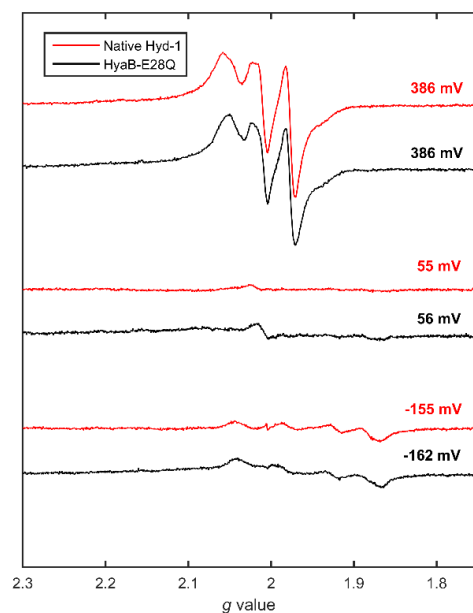
Supplementary Figure 7: Comparison between the EPR spectra of HyaB-E28Q Hyd-1 and native Hyd-1 at pH 7.0. Equivalent concentrations (25 µM) of native Hyd-1 and HyaB-E28Q recorded under the same measurement conditions. See Supplementary Figure 16 for a full titration of native Hyd-1.

7. H$_2$ oxidation dye assay data

Rates of hydrogen oxidation were measured by monitoring the reduction of 25 μM methylene blue at 626 nm (ε = 28 mM^{-1} cm^{-1}) by ~ 3 nM hydrogenase, in 2 mL of H$_2$ saturated mixed buffer (15 mM each of MES, CHES, HEPES, TAPS and Na acetate, 0.1 M NaCl) at pH 3 or pH 6 and room temperature. All assays were performed in a 3 mL cuvette and the solution constantly stirred by a magnetic bead and stirrer plate. All measurements were taken in an anaerobic glovebox (University of York Department of Chemistry Mechanical Workshop) using an LED spectrophotometer (Department of Chemistry Electronic Workshops, University of York), according to the protocol detailed previously (3). Measurements were performed on "as-isolated" samples and "H$_2$-activated" samples, which had been activated overnight in a 100% H$_2$ atmosphere. Quoted apparent turnover rates are the average maximum initial rates taken from three repeat experiments.
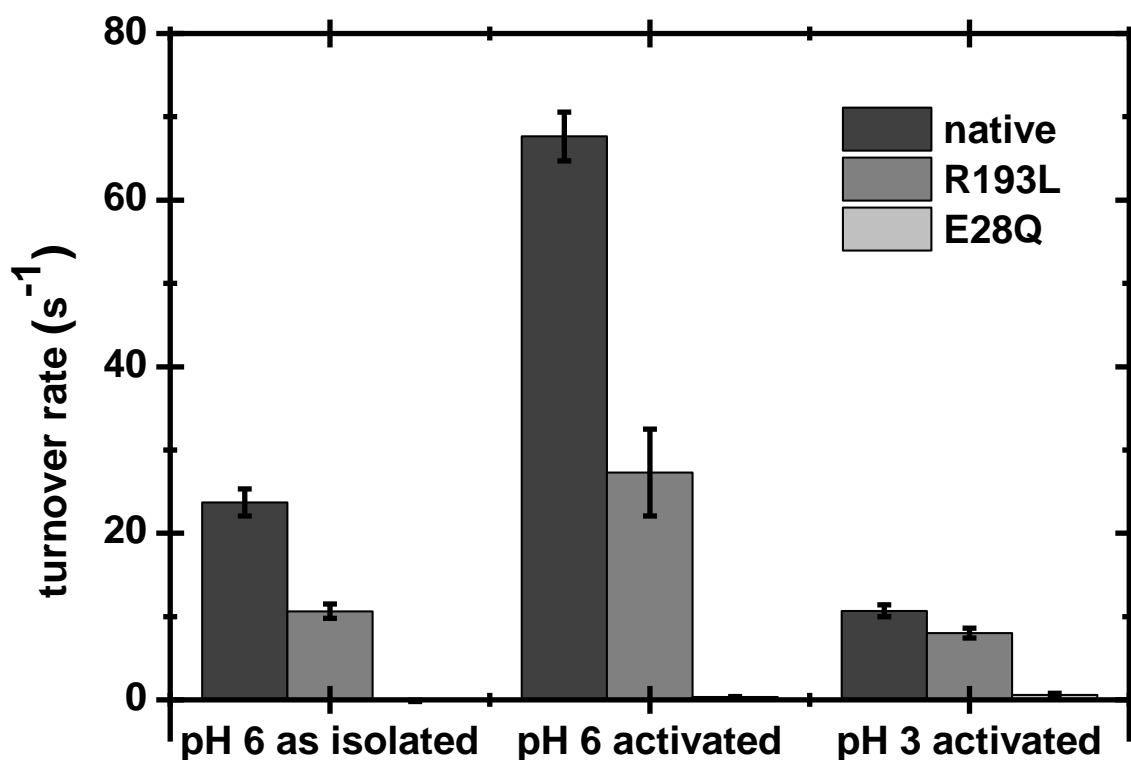
Supplementary Figure 8: Turnover rates of hydrogen oxidation by *E.coli* hydrogenase-1. Determined by dye assays using methylene blue as an electron acceptor. Activated enzyme had been incubated in a 100% H$_2$ atmosphere overnight. Error bars indicate standard error or at least three repeats. Other experimental conditions: room temperature.

8. pH 6, 144 Hz FTacV data for native Hyd-1 and variants HyaB-E28Q and HyaA-R193L
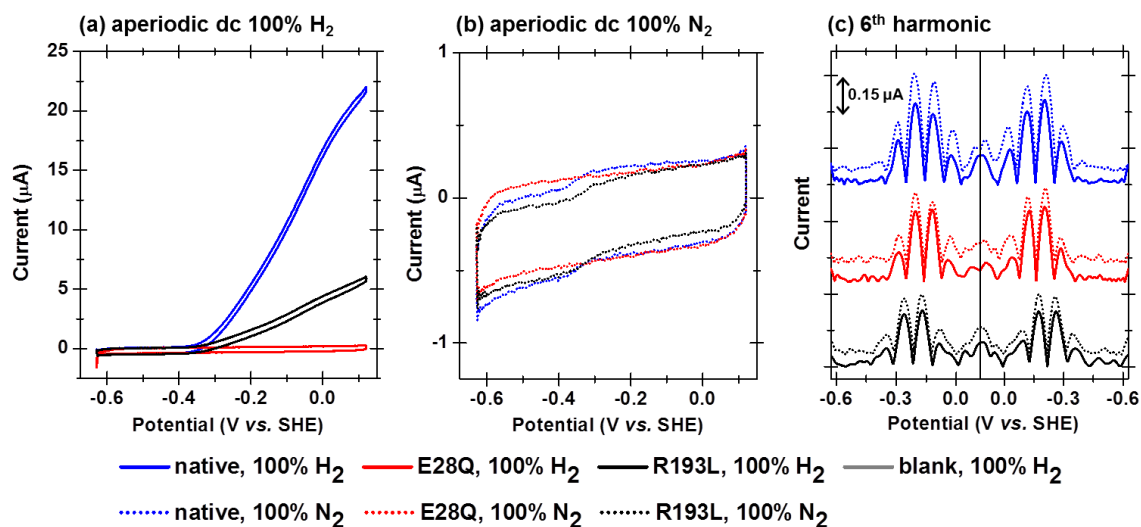
Supplementary Figure 9: 144 Hz FTacV measurement of native *E. coli* hydrogenase-1 and variants HyaB-E28Q and HyaA-R193L at pH 6. Other experimental conditions: amplitude = 150 mV, scan rate = 27.94 mV s^{-1}, 2000 rpm, 25°C, gas atmosphere as indicated.

9. Impact of H_2 concentration on low frequency FTacV

Higher electrode rotation rates provide an increased hydrodynamic flux of H_2 saturated buffer to the electrode surface, therefore effectively increasing the concentration of H_2.

(a)

(b)
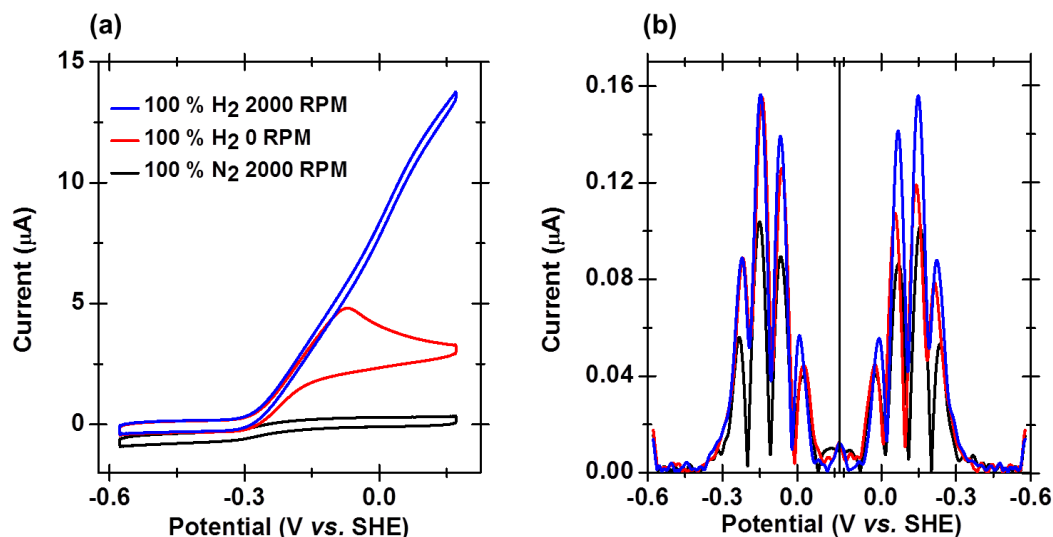
Supplementary Figure 10: 8.98 Hz FTacV of native *E. coli* hydrogenase-1 under different gas and rotation rate conditions, as indicated. (a) Aperiodic-dc component of forward and reverse scan shown as cyclic voltammogram. (b) 6th harmonic components of forward and reverse scan. Other experimental conditions: amplitude = 150 mV, scan rate = 27.94 mV s^{-1}, pH 4.0, 25°C

(a)

(b)
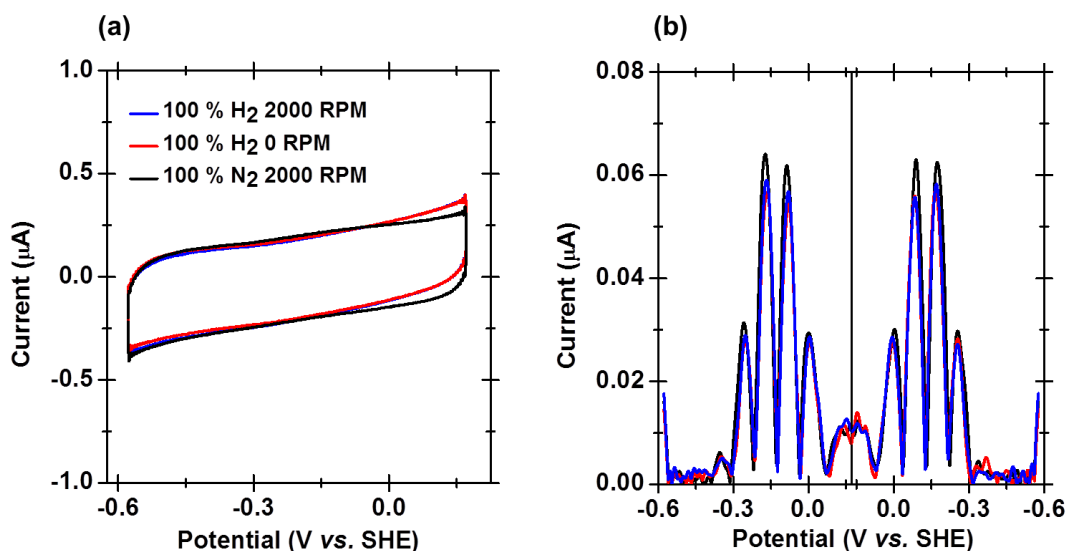
Supplementary Figure 11: 8.88 Hz FTacV of HyaB-E28Q *E. coli* hydrogenase-1 under different gas and rotation rate conditions, as indicated. (a) Aperiodic-dc component of forward and reverse scan shown as cyclic voltammogram. (b) 6th harmonic components of forward and reverse scan. Other experimental conditions: amplitude = 150 mV, scan rate = 27.94 mV s^{-1}, pH 4.0, 25°C.

.**10. Poor fits to experimental data are achieved by parameter optimization of a zero-dispersion reversible one-electron transfer model**
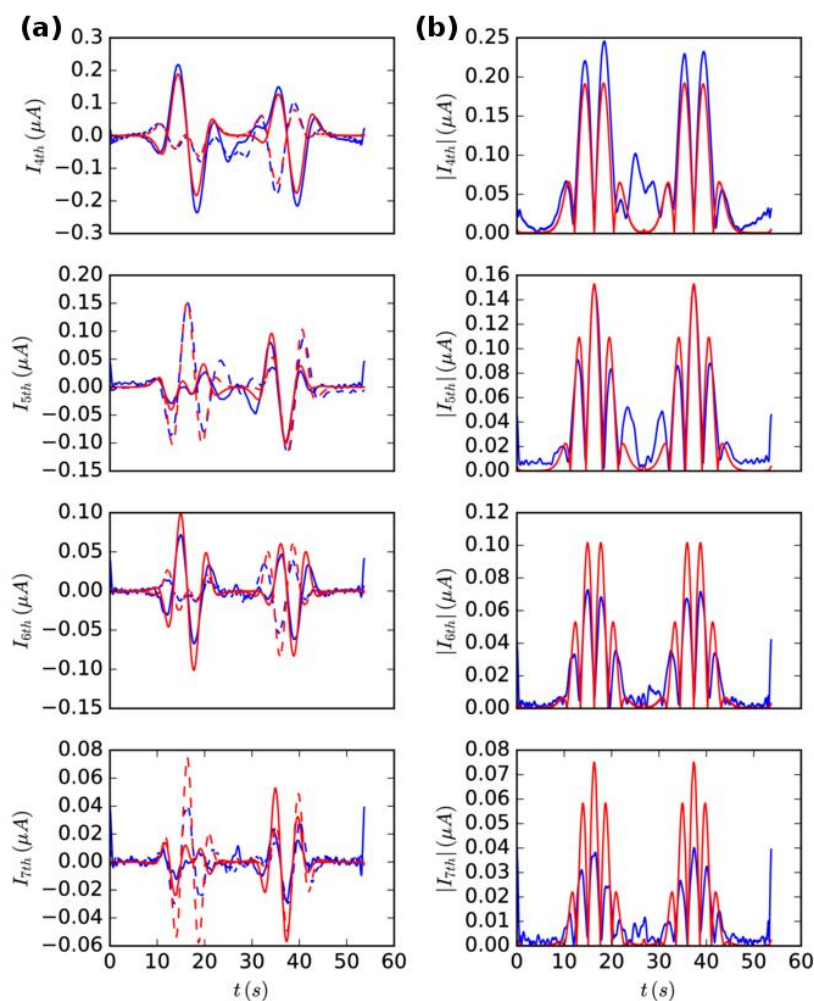
Supplementary Figure 12: Overlay of 4th to 7th harmonic components of 8.88 Hz FTacV experimental measurement of HyaB-E28Q (blue) and data-optimized reversible one-electron reaction simulation with zero dispersion (red). (a) Plots show the real (solid lines) and imaginary (dashed lines) components. (b) The absolute current magnitudes. Other experimental conditions: amplitude = 150 mV, scan rate = 27.94 mV s^{-1}, pH 4.0, 100% H$_2$ atmosphere, 2000 rpm, 25°C, uncompensated resistance (R$_u$) = 20 Ω. Simulation parameters: phase = -0.0340, E_{rev} = -123 mV, and Γ = 4.1 pmol cm^{-2}.

11. Impact of FTacV frequency on the 6th harmonic signal of HyaB-E28Q
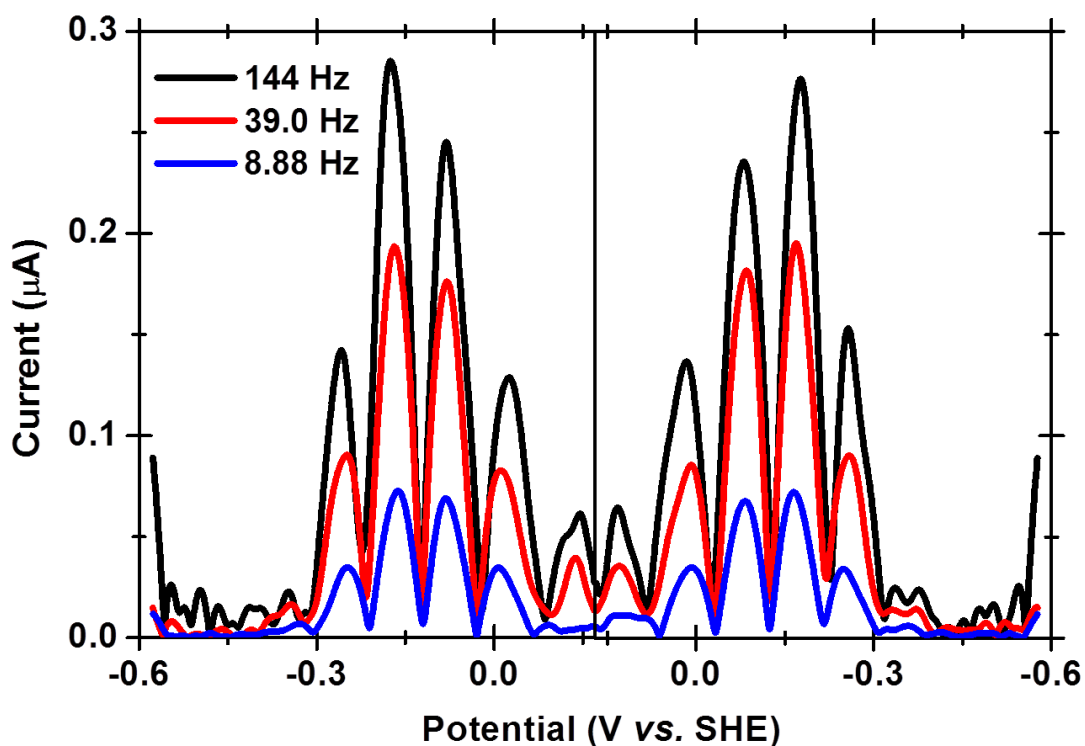
Supplementary Figure 13: Comparison of 6th harmonic components of HyaB-E28Q FTacV measurements made at different frequency. 8.88 Hz (blue) 39.0 Hz (red) and 144 Hz (black) Other experimental conditions: amplitude = 150 mV, scan rate = 27.94 mV s^{-1}, pH 4.0, 100% H$_2$ atmosphere, 2000 rpm, 25°C

12. E_{CP} as a function of pH

Change in center point potential of high harmonic signal (E_{CP}) as a function of pH
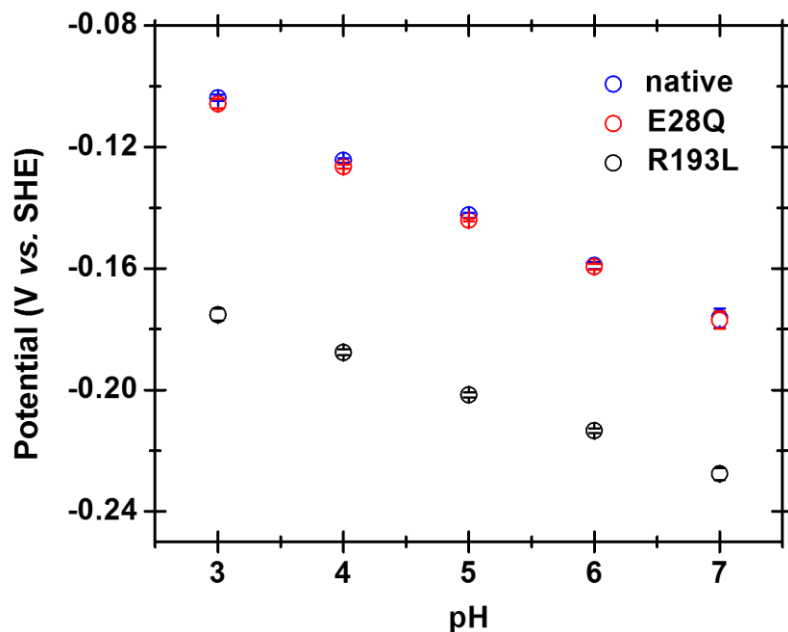
Supplementary Figure 14: E_{CP} as a function of pH for native *E. coli* hydrogenase-1 and variants HyaB-E28Q and HyaA-R193L. Data extracted from 6th harmonic signals of FTacV experiments conducted at frequency = 144 Hz, amplitude = 150 mV, scan rate = 27.94 mV s^{-1}, 2000 rpm, 25°C. Error bars show standard error of at least three repeats.

Supplementary Table 1: Values of data plotted in Supplementary Figure 14. Values quoted ± standard error of at least three repeats.

pH	E_{CP} (mV *vs.* SHE)		
	Native Hyd-1	HyaB-E28Q	HyaA-R193L
3	−104 ± 1	−106 ± 1	−175 ± 2
4	−124 ± 1	−126 ± 1	−188 ± 1
5	−142 ± 1	−144 ± 1	−202 ± 1
6	−159 ± 1	−159 ± 1	−213 ± 1
7	−176 ± 3	−177 ± 3	−228 ± 2

13. High harmonic signals of 144 Hz FTacV measurement of native enzyme are insensitive to carbon monoxide

(a)   **(b)**
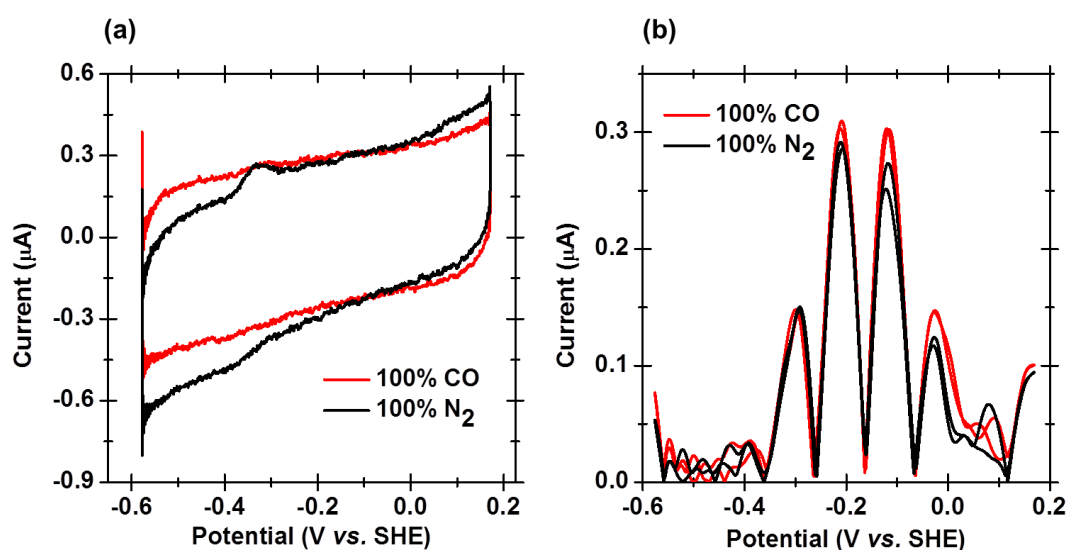
Supplementary Figure 15: Overlay of (a) aperiodic dc component and (b) 6th harmonic of 144 Hz FTacV measurement of native *E. coli* hydrogenase-1 under gas atmospheres of either 100% CO or 100% N$_2$. Other experimental conditions: amplitude = 150 mV, scan rate = 27.94 mV s^{-1}, 0 rpm, 25°C, pH 6.0.

Under 100% N$_2$ the small peak in positive current is attributed to the enzyme re-oxidizing the hydrogen it produces due to proton reduction catalysis.

14. Comparison of E_{CP} and the published potentials of *E. coli* Hyd-1 active site Ni redox transitions

For both native Hyd-1 and HyaB-E28Q, E_{CP} has a pH dependence of −18 mV pH^{-1}, and a value of −159 ± 1 mV at pH 6.0 (Supplementary Table 1). In contrast, the reported midpoint potentials associated with the reversible one-electron inactivation/reactivation transitions of the Ni center are much more positive (Supplementary Table 2)(4-8). At lower potential, the apparent midpoint potential value associated with conversion of the Ni from the [Ni-SI] state to the [Ni-C/Ni-L] state is closer to E_{CP} (Supplementary Table 2), but the –50 mV pH^{-1} gradient derived from FTIR titrations is significantly greater than that observed for E_{CP}(4-6). Finally, E_{CP} is too positive to be attributed to the [Ni-C/Ni-L]-to-[Ni-R] redox transition (Supplementary Table 2). Differences between the FTIR and EPR Ni literature redox potentials are attributed to the fact that native Hyd-1 was used in FTIR experiments but to avoid spin-coupling issues the EPR titrations used a HyaAC19GC120G proximal cluster variant(4-8).

Supplementary Table 2: Midpoint potentials associated with the redox transitions of the Ni center of *E. coli* Hyd-1.

Redox transition	pH 6 midpoint potentials	
	EPR(4,7,8)	FTIR(5,6)
[Ni-A]/[Ni-SI]	+45 mV	-
[Ni-B]/[Ni-SI]	+130 mV	0 mV
[Ni-SI]/[Ni-C/Ni-L]	−100 mV	−150 mV
[Ni-C/Ni-L]/[Ni-R]	−247 mV	−220 mV

15. Native Hyd-1 EPR titration

An EPR redox titration and analysis was performed with 200 µL of 25 µM native Hyd-1 as outlined in the Online Methods.
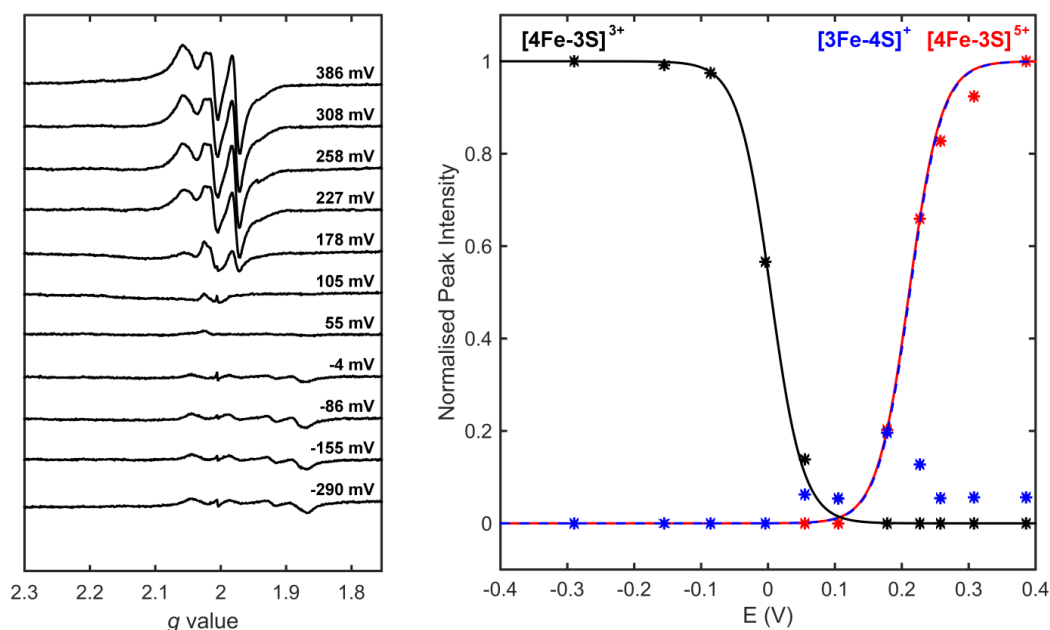
Supplementary Figure 16: EPR redox titration of native Hyd-1 at pH 7.0. (Left) X-band continuous-wave EPR spectra of different titration samples, and (right) "Nernst plot" of signal intensities of the EPR-active species as a function of potential. Solid lines show the best fit of the peak intensities (asterisks) to the one-electron Nernst equation for each redox couple.

Supplementary Table 3: EPR determined iron sulfur cluster midpoint potentials. Errors were estimated by using signal intensities at different field positons (*g* values) arising from the same species.

Redox transition	Native *E. coli* Hyd-1, literature(9)	Native *E. coli* Hyd-1, this study
Proximal $[Fe_4S_3]^{5+/4+}$	230 mV (± 15)	211 mV (± 15)
Medial $[Fe_3S_4]^{1+/0}$	190 mV (± 30)	212 mV (± 30)
Proximal $[Fe_4S_3]^{4+/3+}$	30 mV (± 30)	4 mV (± 15)

16. Enzyme-free FTacV control experiments reveal an electrode-based redox process at positive potential
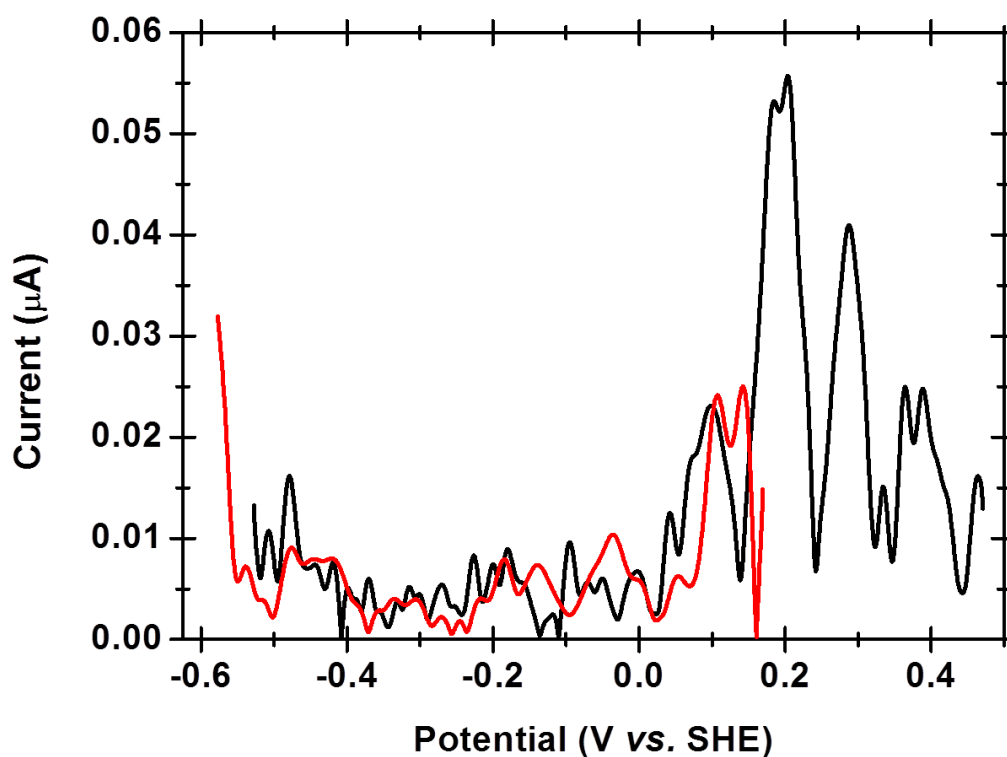
Supplementary Figure 17: 6th harmonic of enzyme free control FTacV measurement to positive potentials. Red line: frequency = 8.98 Hz, scan rate = 27.94 mV s^{-1}; black line: frequency = 8.96 Hz, scan rate = 18.63 mV s^{-1}. Other experimental conditions: amplitude = 150 mV, 100% N_2 atmosphere, 0 rpm, 25°C, pH 4.0.

17. Comparison of native Hyd-1 and HyaA-R193L under different $p(H_2)$

Experimental data used to extract Michaelis constants for H_2, K_M, and inhibition constant, K_I (3,7).
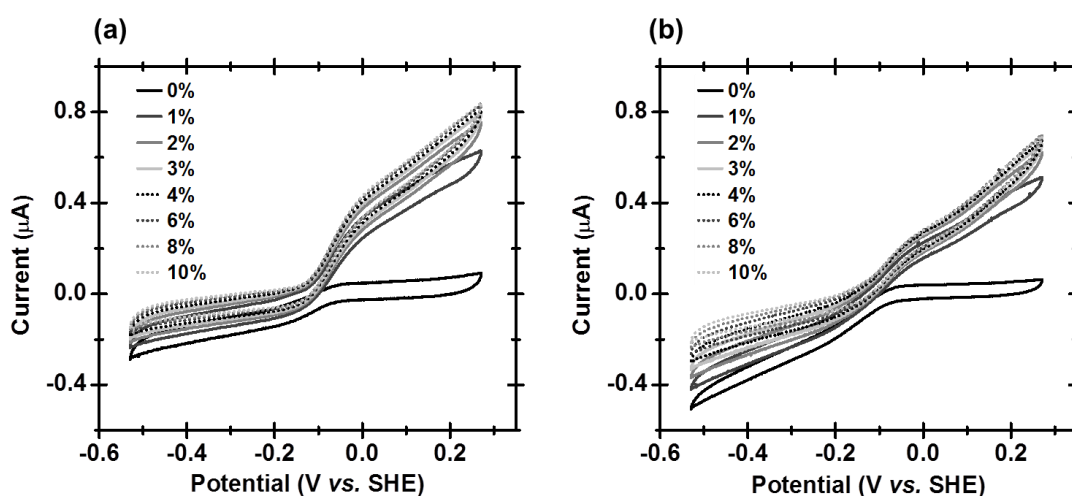
Supplementary Figure 18: 5 mV s^{-1} dcV at pH 3.0 from 1 to 10 % H_2 for (A) native and (B) R193L Hyd-1. Other experimental conditions: 5000 rpm, 25°C.

Using the data shown in Supplementary Figure 18, K_M was calculated by taking the average current at +0.13 V (average of forward and reverse sweep) for each H_2 concentration, and fitting to the Michaelis Menton equation using a least squares linear regression analysis. Apparent K_I was calculated by taking the average current at −0.37 V (average of forward and reverse sweep) for each H_2 concentration, dividing by the current in 0% H_2 and plotting against [H_2]. Apparent $K_I(H_2)$ given by 1/gradient(3,7).

Supplementary Table 4: K_M and K_I values (average ± standard error of 3 repeats) extracted from analysis of experiments like those shown in Supplementary Figure 18.

	native	R193L
K_M at +0.13 V / µM	3.5 ± 0.4	2.4 ± 0.5
K_I at -0.37 V / µM	40 ± 3	41 ± 4

18. Comparing oxygen tolerance of native Hyd-1 and HyaA-R193L

(a)

(b)
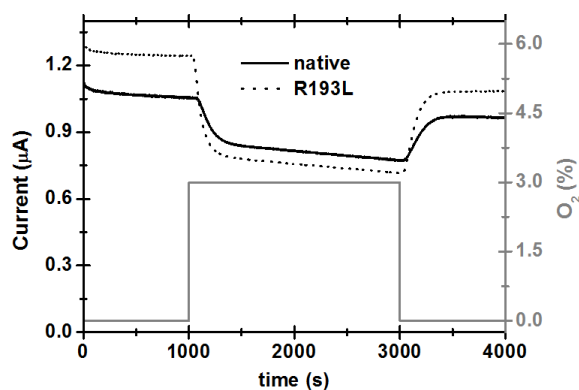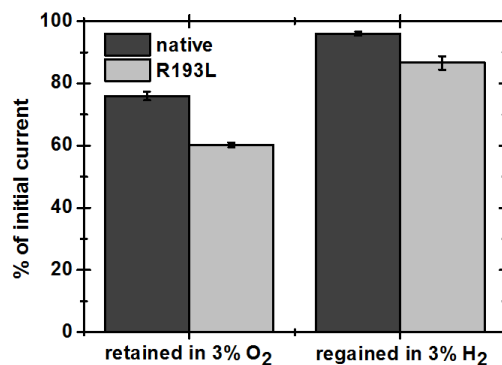
Supplementary Figure 19: Comparison of O$_2$ tolerance of native and HyaA-R193L *E. coli* hydrogenase-1. (a) Chronoamperometry at −0.029 V in 3% H$_2$ and indicated level of O$_2$. (b) Comparison of what % of initial current (measured at 500 s) was retained at 2000 s, in presence of 3% O$_2$, and recovered at 3500 s, following removal of O$_2$, for data corrected for "film loss" (enzyme desoprtion)(10). Error bars indicate standard error of three repeats. Other conditions: pH 6, 5000 rpm, 25°C.

19. pH dependence of E_{switch} and E_m for native Hyd-1 and HyaA-R193L

(a)

(b)
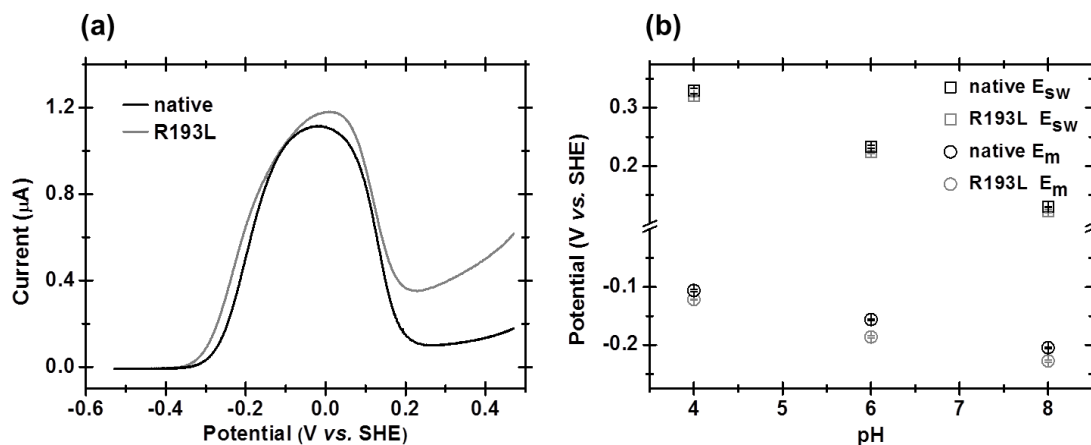
Supplementary Figure 20: (a) 0.25 mV s^{-1} dcV from +0.471 V to −0.529 V measured at pH 8 following a potential poise at +0.471 V for 1000 s. (b) pH dependence of E_m and E_{sw} calculated from experiments such as that shown in (a). The potential of the maxima in a first derivative plot of the voltammogram data is termed E_m, and reports on the onset voltage of catalysis. The potential of the minima in the first derivatve plot is termed E_{switch} and reports on the reactivation process(11). Error bars indicate the standard error of three repeats. Other conditions: 5000 rpm, 10% H_2 atmosphere, 25°C.

20. HyaA-R193L EPR

The redox titration and analysis was performed with 200 µL of 40 µM R193L Hyd-1 as outlined in the Online Methods.
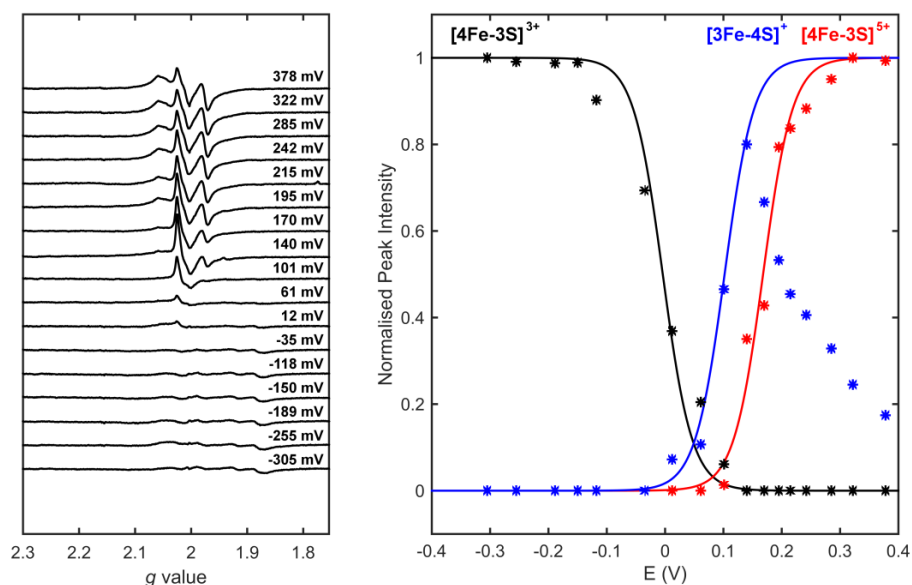

Supplementary Figure 21: EPR redox titration of HyaA-R193L at pH 7.0. (Left) X-band continuous-wave EPR spectra of different titration samples, and (right) "Nernst plot" of signal intensities of the EPR-active species as a function of potential. Solid lines in the Nernst plot show the best fit of the peak intensities (asterisks) to the one-electron Nernst equation for each redox couple.
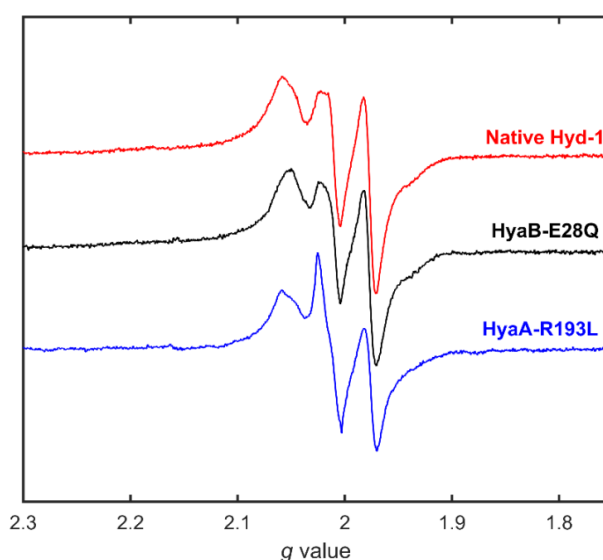
Supplementary Figure 22: Comparison of EPR spectra of native Hyd-1, HyaB-E28Q and HyaA-R193L variants at high potential. Native Hyd-1 (25 µM, +386 mV), HyaB-E28Q (25 µM, +386 mV) and HyaA-R193L (40 µM, +378 mV) are compared. Identical measurement conditions except that the HyaA-R193L data was recorded with a larger incremental step between data points.

21. Variants HyaA-K189N and HyaA-Y191E have the same FTacV and dcV profile as native Hyd-1
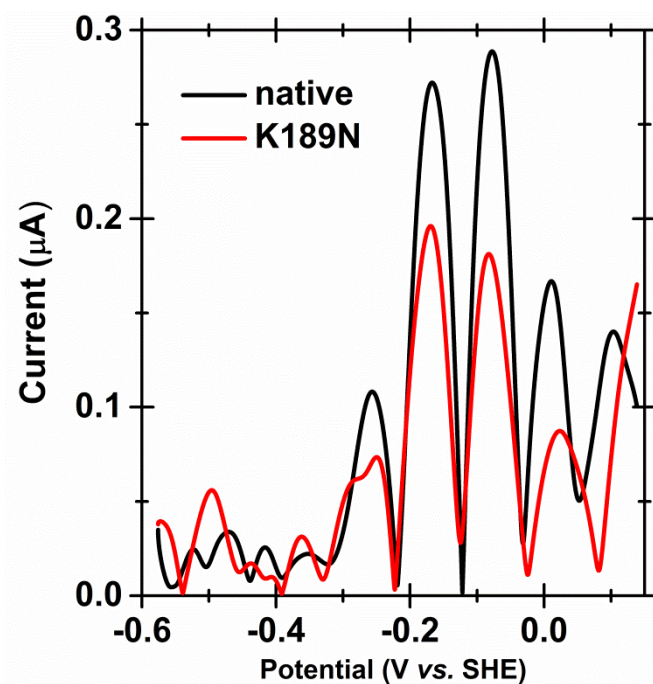
Supplementary Figure 23: 6th harmonic of FTacV measurements of native *E. coli* Hyd-1 (black line) and variant HyaA-K189N (red line). Frequency = 218.95 Hz, scan rate = 27.94 mV s^{-1}, amplitude = 150 mV, 100% N$_2$ atmosphere, 0 rpm, 25°C, pH 4.0.
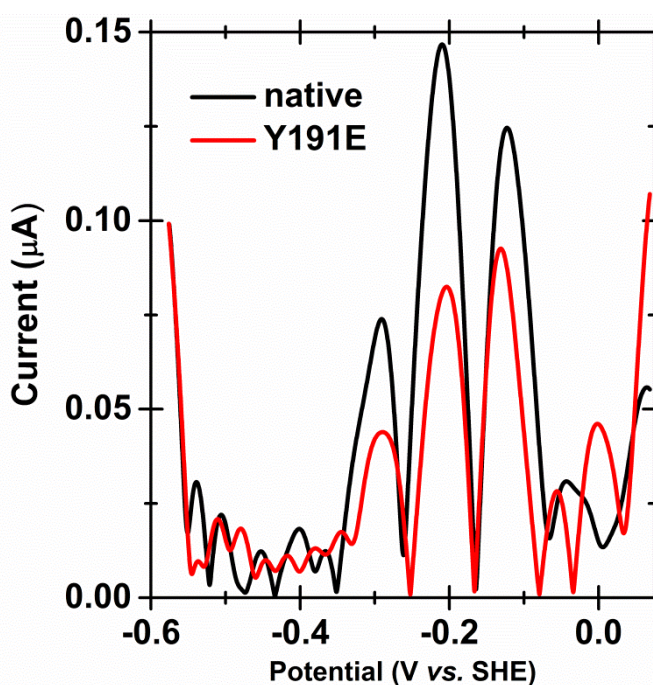
Supplementary Figure 24: 6th harmonic of FTacV measurements of native *E. coli* Hyd-1 (black line) and variant HyaA-Y191E (red line). Frequency = 88.98 Hz, scan rate = 27.94 mV s^{-1}, amplitude = 150 mV, 100% N$_2$ atmosphere, 0 rpm, 25°C, pH 6.0.
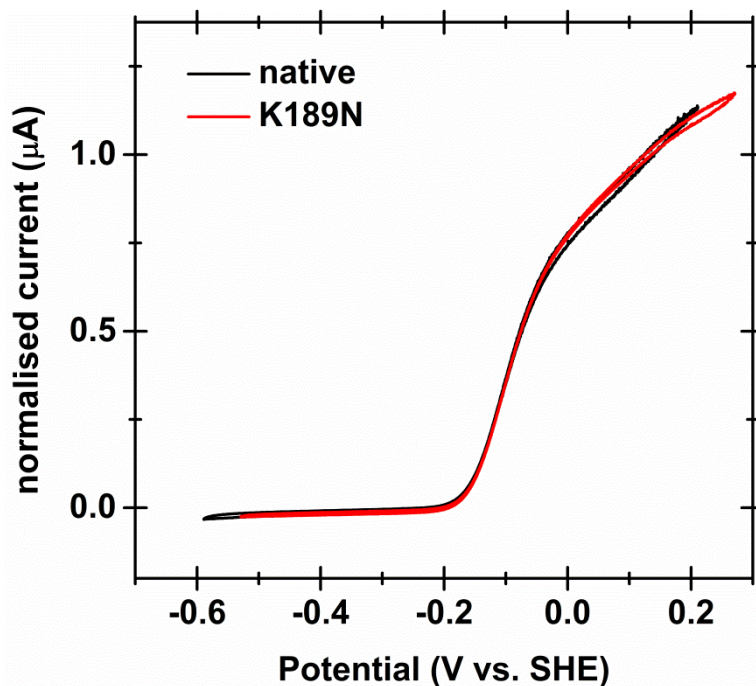
Supplementary Figure 25: dcV comparison of native *E. coli* Hyd-1 (black line) and variant HyaA-K189N (red line). Current is normalized to the average current measured at +0.13 V vs SHE. Scan rate = 5 mV s^{-1}, 10% H_2 atmosphere, 5000 rpm, 25°C, pH 4.0.
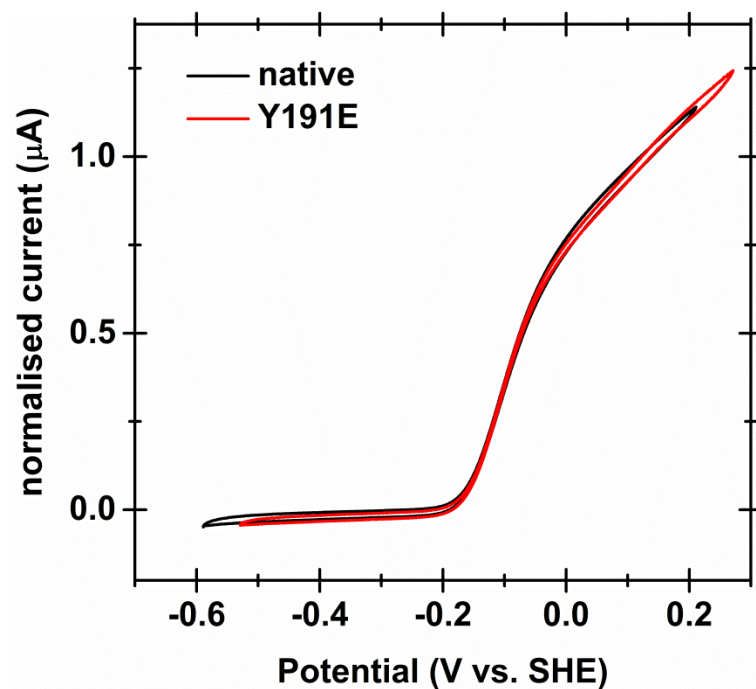
Supplementary Figure 26: dcV comparison of native *E. coli* Hyd-1 (black line) and variant HyaA-Y191E (red line). Current is normalized to the average current measured at +0.13 V vs SHE. Scan rate = 5 mVs^{-1}, 10% H_2 atmosphere, 5000 rpm, 25°C, pH 4.0.

22. HyaA-R193L amino acid exchange does not yield isolable protein
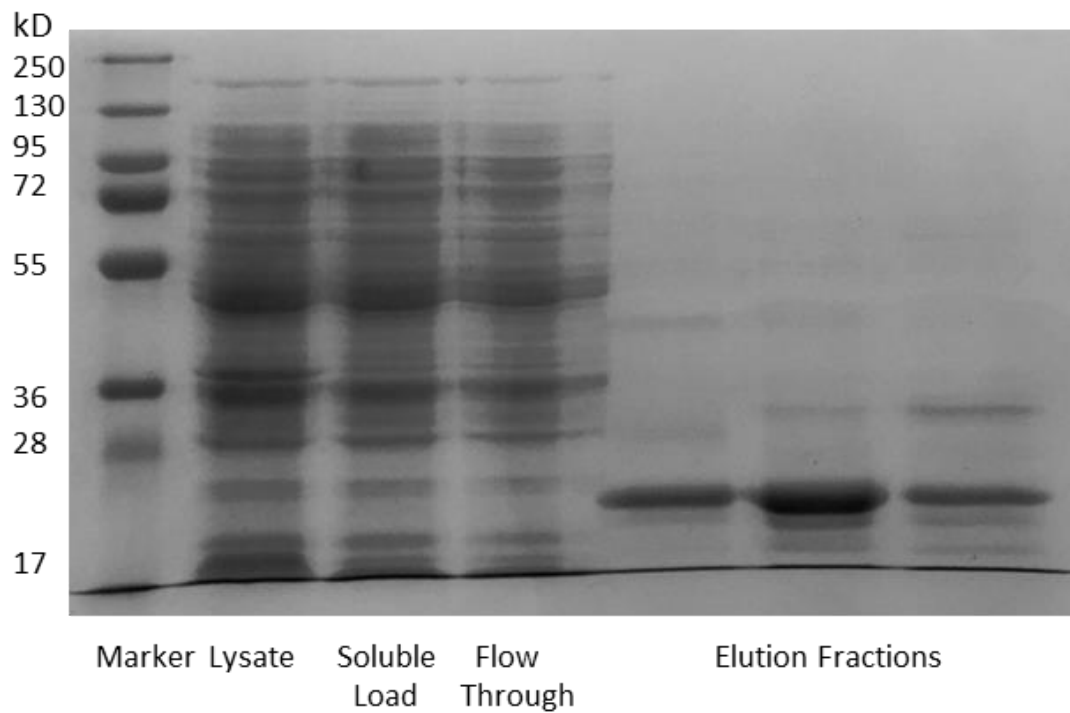
Supplementary Figure 27: Denaturing SDS-PAGE following attempt to purify the HyaA-R193E hydrogenase variant. In the elution fractions, eluted directly from the HiTrap column, the largest protein bands correspond to a cyclic AMP receptor protein (identified by mass spec of a trypsin digested gel band), with insignificant hydrogenase protein.

23. Molecular biology experimental methods

Supplementary Table 5: Plasmids used in this study

Plasmid Name	Plasmid Function	Source
pRed/ET	Red/ET expression plasmid, which confers ampicillin resistance and encodes the proteins for recombination	Gene Bridges – Quick and easy *E. coli* gene deletion kit

Supplementary Table 6: Oligonucleotide primers used in this study

Primer Name	Primer Function	Primer sequence (5'-3')	Source
hyaB_E28Q_neo_sense	cassette homology arm	CCATCAATAATGCCGGACGCCGC CTGGTGGTCGACCCGATTACGC GCATCGGCCTGGTGATGATGGC GGGATCG	Sigma
hyaB_E28Q_neo_antisense	cassette homology arm	TTGGTGATCACATTCTGATCGTTA ATATTCACTTCGCAGCGCATGTG GCCTTGTCAGAAGAACTCGTCAA GAAGGCG	Sigma
hyaB_E28Q_olap_sense	To make hyaBE28Qdsfrag	CCATCAATAATGCCGGACGCCGC CTGGTGGTCGACCCGATTACGC GCATCCAAGGCCAC	Sigma
hyaB_E28Q_olap_antisense	To make hyaBE28Qdsfrag	TTGGTGATCACATTCTGATCGTTA ATATTCACTTCGCAGCGCATGTG GCCTTGGATGCG	Sigma
hyaA_K189_neo_sense	cassette homology arm	TCGACAGAATGGGCCGTCCGCT GATGTTCTATGGTCAGCGAATCC ACGATGGCCTGGTGATGATGGC GGGATCG	IDT
hyaA_K189_neo_antisense	cassette homology arm	TCCCAACTCTGGACGAACTCTCC GGCGTCGAAGTGGGCGCGGCGA TAGCATTTTCAGAAGAACTCGTC AAGAAGGCG	IDT
hyaA_R193L_	To make	GCCGTCCGCTGATGTTCTATGGT	IDT

olap_sense	hyaAR193Ld sfrag	CAGCGAATCCACGATAAATGCTA TCGCCTCGCCCAC	
hyaA_R193L_ olap_antisens e	To make hyaAR193Ld sfrag	GCAGCGTCATCATCCCAACTCTG GACGAACTCTCCGGCGTCGAAG TGGGCGAGGCGATA	IDT
hyaA_R193E_ olap_sense	To make hyaA_R193E _dsfrag	GCCGTCCGCTGATGTTCTATGGT CAGCGAATCCACGATAAATGCTA TCGCGAGGCCCAC	IDT
hyaA_R193E_ olap_antisens e	To make hyaA_R193E _dsfrag	GCAGCGTCATCATCCCAACTCTG GACGAACTCTCCGGCGTCGAAG TGGGCCTCGCGATA	IDT
hyaA_K189N_ olap_sense	To make hyaA_K189N _dsfrag	TCGACAGAATGGGCCGTCCGCT GATGTTCTATGGTCAGCGAATCC ACGATAATTGCTAT	IDT
hyaA_K189N_ olap_antisens e	To make hyaA_K189N _dsfrag	TCCCAACTCTGGACGAACTCTCC GGCGTCGAAGTGGGCGCGGCGA TAGCAATTATCGTG	IDT
hyaA_Y191E_ olap_sense	To make hyaA_Y191E _dsfrag	GAATGGGCCGTCCGCTGATGTTC TATGGTCAGCGAATCCACGATAA ATGCGAGCGCCGC	IDT
hyaA_Y191E_ olap_antisens e	To make hyaA_Y191E _dsfrag	TCATCATCCCAACTCTGGACGAA CTCTCCGGCGTCGAAGTGGGCG CGGCGCTCGCATTT	IDT

Supplementary Table 7: Linear DNA used in this study

Linear DNA	DNA Description and Function	Source
rpsL-neo template	PCR template for generating a rspL-neomycin (kanamycin) counter-selection/selection cassette.	Gene Bridges – Counter selection BAC modification kit
hyaBE28Qneo	*rpsL-neo* cassette flanked by homology arms, used to introduce the cassette at the E28 position of *hyaB*	This work
hyaBE28Qdsfr	Non-selectable DNA used to swap out the	This work

ag	cassette and introduce the E28Q mutation to *hyaB*	
hyaAK189neo	rspL-neo cassette flanked by homology arms, used to introduce the cassette at the K189 position of *hyaA*	This work
hyaA_R193L_ dsfrag	Non-selectable DNA used to swap out the cassette and introduce the R193L mutation to *hyaA*	This work
hyaA_R193E_ dsfrag	Non-selectable DNA used to swap out the cassette and introduce the R193E mutation to *hyaA*	This work
hyaA_K189N_ dsfrag	Non-selectable DNA used to swap out the cassette and introduce the K189N mutation to *hyaA*	This work
hyaA_Y191E_ dsfrag	Non-selectable DNA used to swap out the cassette and introduce the Y191E mutation to *hyaA*	This work

Supplementary Table 8: *E. coli* strains used in this study

Strain name	Strain Genotype and Description	Source / Reference
LAF003	F⁻ lambda⁻ *IN(rrnD-rrnE)1 rph-1 rpsL150 hyaA(histag) (StrepR)* "native" strain encoding hydrogenase-1 with a polyhistidine tag at the C terminus of the small subunit	(3)
HA001	F⁻ lambda⁻ *IN(rrnD-rrnE)1 rph-1 rpsL150 hyaA(histag) hyaB(E28Q):rpsL-neo (KanR StrepS)* Derived from LAF003, with *rpsL-neo* cassette inserted at position E28 of *hyaB*	This work
HA002	F⁻ lambda⁻ *IN(rrnD-rrnE)1 rph-1 rpsL150 hyaA(histag)(K189):rpsL-neo (KanR StrepS)* Derived from LAF003, with *rpsL-neo* cassette inserted at position K189 of *hyaA*	This work
HA003	F⁻ lambda⁻ *IN(rrnD-rrnE)1 rph-1 rpsL150 hyaA(histag) hyaBE28Q (StrepR)*	This work

	Strain encoding hydrogenase-1 with a polyhistidine tag at the C terminus of the small subunit and an E28Q mutation in the large subunit (by a codon change in *hyaB* of the chromosome of LAF003)	
HA004	F⁻ lambda⁻ *IN(rrnD-rrnE)1 rph-1 rpsL150 hyaAR193L(histag) (StrepR)* Strain encoding hydrogenase-1 with a polyhistidine tag at the C terminus of the small subunit and a R193L mutation in the small subunit (by a codon change in *hyaA* of the chromosome of LAF003)	This work
HA005	F⁻ lambda⁻ *IN(rrnD-rrnE)1 rph-1 rpsL150 hyaAR193E(histag) (StrepR)* Strain encoding hydrogenase-1 with a polyhistidine tag at the C terminus of the small subunit and a R193E mutation in the small subunit (by a codon change in *hyaA* of the chromosome of LAF-003)	This work
HA011	F⁻ lambda⁻ *IN(rrnD-rrnE)1 rph-1 rpsL150 hyaAK189N (histag) (StrepR)* Strain encoding hydrogenase-1 with a polyhistidine tag at the C terminus of the small subunit and a K189N mutation in the small subunit (by a codon change in *hyaA* of the chromosome of LAF003)	This work
HA014	F⁻ lambda⁻ *IN(rrnD-rrnE)1 rph-1 rpsL150 hyaAY191E (histag) (StrepR)* Strain encoding hydrogenase-1 with a polyhistidine tag at the C terminus of the small subunit and a Y191E mutation in the small subunit (by a codon change in *hyaA* of the chromosome of LAF003)	This work

24. SDS-PAGE
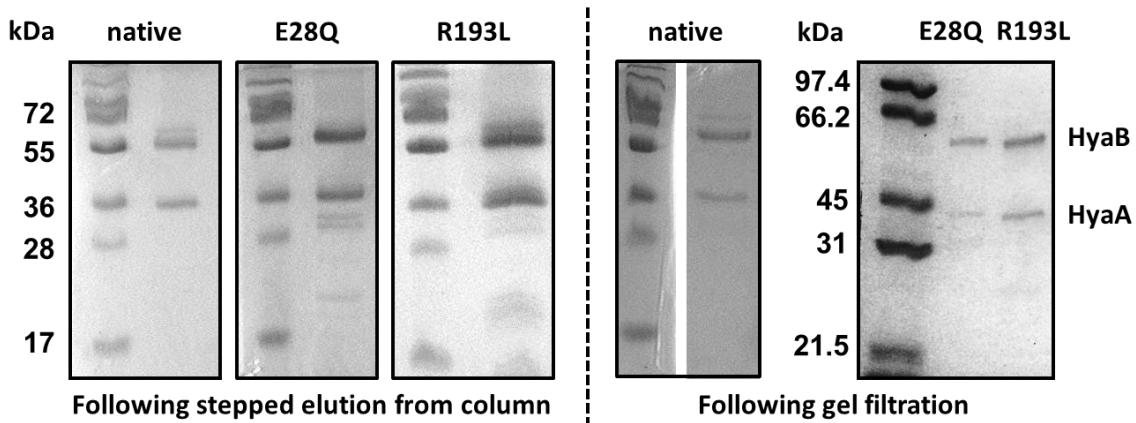
Supplementary Figure 28: Denaturing SDS-PAGE of native, HyaB-E28Q and HyaA-R193L hydrogenase samples post HiTrap column (left) and post gel filtration (right). Protein bands corresponding to the expected mass of the large (HyaB) and small (HyaA) subunit are observed and indicated.
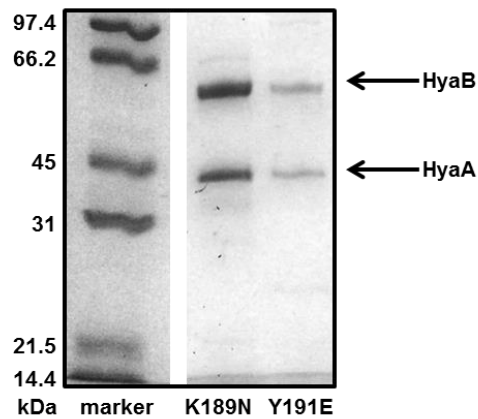
Supplementary Figure 29: Denaturing SDS-PAGE of HyaA-K189N and HyaA-Y191E hydrogenase samples post gel filtration. Protein bands corresponding to the expected mass of the large (HyaB) and small (HyaA) subunit are observed and indicated.

References

1   Petrenko A & Stein M (2015) Rates and Routes of Electron Transfer of [NiFe]-Hydrogenase in an Enzymatic Fuel Cell. *J. Phys. Chem. B* 119:13870-13882.

2   Petrenko A & Stein M (2017) Distal [FeS]-Cluster Coordination in [NiFe]-Hydrogenase Facilitates Intermolecular Electron Transfer. *Int. J. Mol. Sci.* 18:100.

3   Flanagan LA, Wright JJ, Roessler MM, Moir JW & Parkin A (2016) Re-engineering a NiFe hydrogenase to increase the H_2 production bias while maintaining native levels of O_2 tolerance. *Chem. Commun.* 52: 9133-9136.

4   Evans R M, *et al.* (2013) Principles of Sustained Enzymatic Hydrogen Oxidation in the Presence of Oxygen – The Crucial Influence of High Potential Fe–S Clusters in the Electron Relay of [NiFe]-Hydrogenases. *J. Am. Chem. Soc.* 135:2694-2707.

5   Hidalgo R, Ash PA, Healy AJ & Vincent K A (2015) Infrared Spectroscopy During Electrocatalytic Turnover Reveals the Ni-L Active Site State During H_2 Oxidation by a NiFe Hydrogenase. *Angew. Chem. Int. Ed.* 54:7110-7113.

6   Murphy BJ, *et al.* (2015) Discovery of Dark pH-Dependent H^+ Migration in a [NiFe]-Hydrogenase and Its Mechanistic Relevance: Mobilizing the Hydrido Ligand of the Ni-C Intermediate. *J. Am. Chem. Soc.* 137:8484-8489.

7   Lukey MJ, *et al.* (2010) How *Escherichia coli* Is Equipped to Oxidize Hydrogen under Different Redox Conditions. *J. Biol. Chem.* 285:3928-3938.

8   Lukey MJ, *et al.* (2011) Oxygen-Tolerant [NiFe]-Hydrogenases: The Individual and Collective Importance of Supernumerary Cysteines at the Proximal Fe-S Cluster. *J. Am. Chem. Soc.* 133:16881-16892.

9   Roessler MM, Evans RM, Davies RA, Harmer J & Armstrong FA (2012) EPR Spectroscopic Studies of the Fe–S Clusters in the O_2-Tolerant [NiFe]-Hydrogenase Hyd-1 from *Escherichia coli* and Characterization of the Unique [4Fe–3S] Cluster by HYSCORE. *J. Am. Chem. Soc.* 134: 15581-15594.

10   Fourmond V, *et al.* (2009) Correcting for Electrocatalyst Desorption and Inactivation in Chronoamperometry Experiments. *Anal. Chem.* 81:2962-2968.

11   Fourmond V, Infossi P, Giudici-Orticoni MT, Bertrand P & Léger C (2010) "Two-Step" Chronoamperometric Method for Studying the Anaerobic Inactivation of an Oxygen Tolerant NiFe Hydrogenase. *J. Am. Chem. Soc.* 132:4848-4857.

Chapter 8

Conclusions and perspectives

8.1 Conclusion

This utility of PF-FTacV in characterising previously ambiguous aspects of biological redox chemistry has been thoroughly demonstrated in this thesis. PFE is now a well-established technique in the dynamic study of redox proteins and has been particularly useful in understanding catalytic mechanisms. A major drawback in a number of PFE studies has been the inability to measure "non-turnover" electron transfer from redox centres with an enzyme, even when amplified catalytic currents can be measured. This prevents analysis of the redox centres and how they may control catalysis, whilst precluding quantification of the electrode surface coverage of enzyme and measurement of turnover rates from the associated catalytic current. This is largely due to the dominance of the large background electrode capacitance current over the small "non-turnover" Faradaic current. This thesis has showcased the particular ability of FTacV to separately resolve the Faradaic current of interest from the background capacitive current in the higher and lower harmonics, respectively, and exploited this to provide vastly enhanced signal quality compared to conventional dcV. This thesis has utilised higher amplitudes (ΔE) and minimised uncompensated solution resistance (R_u) compared to previous studies to maximise the enhancement in signal quality. This has enabled exquisite analysis of redox processes that are much harder to observe and analyse with conventional dcV methods and provided valuable information for spectroscopically elusive sites unable to be studied by redox titration (Chapter 4 and 7). This thesis shows, for the first time, that the enhancement in signal quality with FTacV is such that even processes that are invisible with dcV (i.e. the Faradaic current is swamped by the background) are well defined by background-free high harmonic FTacV measurements (Chapter 5).

This thesis has also harnessed the power of FTacV to simultaneously measure and resolve catalytic and electron transfer current in the aperiodic dc and high harmonic components, respectively. The dual time domains of dc sweep and ac perturbation enable this resolution, which is just not possible with the single time domain of dcV. This had been shown and theoretically proven over a decade ago, but had not since been capitalised on. This thesis has measured electron transfer properties in the presence of substrate, which has the potential to affect redox sites, and is not usually possible with dcV. This has been used to show

how underlying electron transfer events can control catalytic activity (Chapter 4 and 7). This property of FTacV was particularly useful in the study of hydrogenases (Chapter 7). The ubiquitous presence of protons in solution and inability to fully inhibit catalysis with carbon monoxide meant that it was impossible to measure non-turnover electron transfer signals with dcV, as they were obscured by catalytic current. In the case of rather fast catalysis by hydrogenases it was shown that true separation of catalytic and electron transfer current could only be achieved using high frequency measurements. Measurement of underlying electron transfer processes has also enabled estimation of enzyme surface coverages concomitantly with catalytic current, so enzyme turnover rates have been quantified (Chapter 4 and 7). Even when the electron transfer process is visible by dcV enabling surface coverage estimation, this must be done in a separate substrate free measurement and so the simultaneous FTacV measurement utilised here is more useful.

Quantification of the kinetics, thermodynamics and mechanism of protein electron transfer reactions by simulations of FTacV responses has also been explored and utilised in this thesis. Chapter 4 showed that heuristic simulations using MECSim software could be used to accurately simulate high harmonic responses, quantifying kinetic and thermodynamic parameters and enabling discrimination between different mechanisms. However, the heuristic simulation process was prohibitively time-consuming and inadequacies in theory experiment comparisons remained, thought to be largely due to enzyme dispersion on the electrode. An efficient two-step multi-parameter optimisation procedure was developed and implemented by Dr. Martin Robinson (University of Oxford) and introduced in Chapter 5. Dr. Martin Robinson also introduced enzyme dispersion to the parameter optimisation and this enabled more accurate modelling in Chapter 7.

The described developments in the application of FTacV to PFE have been used in concert with spectroscopic, biochemical and molecular biology techniques to understand previously elusive aspects of redox chemistry in three enzymes. Chapter 4 provided electrochemical evidence that spectroscopically elusive two-electron redox chemistry ascribed to the pyranopterin ligand controls catalysis of substrate mimics in the molybdoenzyme YedY. This settled an uncertainty in how YedY, capable of only one-electron molybdenum

chemistry, can catalyse two-electron reactions usually achieved by Mo(IV)/Mo(VI) conversions in other molybdoenzymes. Chapter 5 quantified thermodynamic, kinetic and mechanistic aspects of a previously uncharacterised cysteine disulphide redox reaction in hydrogenase maturation protein HypD, evidencing its proposed redox role in reductive insertion of cyanide ligands into the hydrogenase active site. Chapter 7 uses FTacV and variants described in Chapter 6 to prove that the potential of the spectroscopically silent distal FeS cluster electron entry / exit site exerts significant control over the crucial catalytic properties of overpotential and catalytic bias in a [NiFe]-hydrogenase. This had been proposed in a recent model but not yet experimentally proven. Enhanced bias towards H_2 production and decreased catalytic overpotential for H_2 oxidation could thus be engineered into a [NiFe]-hydrogenase by reducing the distal cluster potential. This highlighted that redox centres distant from the active site must not be ignored as crucial catalytic tuning sites in protein engineering or synthetic catalysts, which typically lack additional electron transfer centres.

8.2   Perspectives

Although automated data-optimisation procedures enabled more efficient simulation of FTacV data, they could only be implemented for low frequency measurements and so the greater kinetic resolution provided by high frequencies could not be harnessed using this simulation methodology. It is hoped that the high frequency measurements of HypD provided in Chapter 5, Additional Material, can be used in the development of data-optimisation procedures for high frequency FTacV data. This will enable quantification of faster electron transfer rates, discrimination of faster chemical steps and better measurement of kinetic dispersion of enzymes. It is extremely quick to make FTacV measurements that have the potential to unravel all the kinetic, thermodynamic and mechanistic parameters of a redox reaction. However, the development of simulation procedures that can analyse such data as quickly as they are taken is required.

FTacV is able to enhance non-turnover electron transfer signal quality but in some cases insufficient enzyme coverage on the electrode precludes analysis, even using sensitive FTacV measurements. The work in this thesis has relied upon electroactive enzyme adsorption to a pyrolytic graphite edge electrode but

not all proteins will absorb in this way or by other common techniques such as on a SAM on a gold electrode, within a polymer matrix or on nanostructured materials. For PF-FTacV to be utilised more freely on redox proteins robust enzyme-electrode attachment strategies need to be developed. A generic method able to be employed to many systems would be the most useful. Perhaps the most promising strategy would be to introduce a tag to both the protein and the electrode, such that they can be covalently linked to secure the protein in an electroactive configuration on the electrode surface.

In this thesis FTacV measurements have been useful in characterising spectroscopically elusive redox sites. However, the lack of structural information afforded by FTacV limits its utility and confidence in conclusions drawn. It is vital to perform FTacV in concert with other techniques, in order to verify the interrogated redox site. This thesis has utilised spectroscopy (Chapter 4 and Chapter 7), biochemical tests (Chapter 5) and enzyme variants (Chapter 7) for this purpose, but still some uncertainties have remained. Integration of QCM-D, SEIRA and FTIR measurements concurrently with PFE have been developed which provide side by side structural and electrochemical analysis. Incorporation of this into PF-FTacV studies would be advantageous.

This thesis used FTacV to propose that novel pyranopterin redox chemistry controlled catalysis of substrate mimics by molybdoenzyme YedY. YedY is now known to be a methionine sulfoxide reductase and it will be interesting to see if these conclusions are valid for the true substrate and of physiological relevance.[27, 28] The redox activity of HypD has been proven in this thesis but it remains to be elucidated if it is involved in the incorporation of CO into the active site of [NiFe]-hydrogenases. Understanding this maturation mechanism will require biochemical rather than electrochemical studies. The distal cluster of the [NiFe]-hydrogenase *E. coli* Hyd-1, which is distant from the active site, has been shown to influence the crucial catalytic properties of overpotential and bias and it is hoped that this mechanistic insight can guide engineering strategies for H_2 catalysis. However, it is clear that further factors control hydrogen production rates and elucidation of the mechanism of this control will be valuable in research towards sustainable H_2 production technologies.

Overall, just as it has improved NMR and IR studies, introduction of the Fourier transform to voltammetry delivers significant advantages in terms of signal

enhancement, separation of background, catalytic and electron transfer current, and kinetic, thermodynamic and mechanistic insight. It is hoped that mechanistic understanding of biological redox reactions that underpin a breadth of crucial life processes .can be characterised by implementing the experimental and analytical advances in PF-FTacV made in this thesis. Inspiration for chemical, biomedical and future energy technologies can be taken from the exquisitely optimised examples of Nature.

Abbreviations

Aa	*Aquifex aeolicus*
ac	alternating current
ALS	amyotrophic lateral sclerosis
AMP	adenosine monophosphate
Arg	arginine
Asn	asparagine
Asp	aspartic acid
ATP	adenosine triphosphate
Av	*Allochromatium vinosum*
bp	base pair
BSA	bovine serum albumin
CHES	N-Cyclohexyl-2-aminoethanesulfonic acid
CMA-ES	Covariance Matrix Adaptation Evolution Strategy
CoM	Coenzyme M
Cys	cysteine
Db	*Desulfomicrobium baculatum*
dc	direct current
dcV	direct current voltammetry
Df	*Desulfovibrio fructosovorans*
DFT	density functional theory
dFT	discrete Fourier transform
Dg	*Desulfovibrio gigas*

DMSO	dimethyl sulfoxide
DNA	deoxyribonucleic acid
DPV	differential pulse voltammetry
*Dv*H	*Desulfovibrio vulgaris* Hildenborough
*Dv*MF	*Desulfovibrio vulgaris* Miyazaki F
E. coli	*Escherichia coli*
Ec	*Escherichia coli*
Ec1	*Escherichia coli* Hyd-1
Ec2	*Escherichia coli* Hyd-2
EDTA	ethylenediaminetetraacetic acid
EPR	electron paramagnetic resonance
FAD	flavin adenine dinucleotide
FMN	flavin mononucleotide
FT	Fourier transform
FTacV	Fourier Transformed ac Voltammetry
FTIR	Fourier transform infrared spectroscopy
Glu	glutamic acid
HEPES	4-(2-hydroxyethyl)-1-piperazineethanesulfonic acid
His	histidine
Hm	*Hydrogenovibrio marinus*
Hp	*Helicobacter pylori*
Hyd-1	hydrogenase-1
iFT	inverse Fourier transform
IR	infrared

kanR	kanamycin resistant
kb	kilobase
LB	lysogeny broth
LED	light emitting diode
Leu	leucine
MBH	membrane bound hydrogenase
MCD	magnetic circular dichroism
MES	2-(N-morpholino)ethanesulfonic acid
MOPS	3-(N-morpholino)propanesulfonic acid
MWCO	molecular weight cut-off
NADP	nicotinamide adenine dinucleotide phosphate
NEM	N-Ethylmaleimide
NMR	nuclear magnetic resonance
ODE	ordinary differential equation
PAGE	polyacrylamide gel electrophoresis
PCR	polymerase chain reaction
PF-dcV	protein film direct current voltammetry
PFE	protein film electrochemistry
PF-FTacV	protein film Fourier transformed ac voltammetry
PGE	pyrolytic graphite edge
PQQ	pyrroloquinoline quinone
QM/MM	quantum mechanics / molecular mechanics
Re	*Ralstonia eutropha*
RR	Resonance Raman

SCE	saturated calomel electrode
SDS	sodium dodecyl sulfate
Se	*Salmonella enterica*
SHE	standard hydrogen electrode
SIERA	surface enhanced infrared absorption
std dev	standard deviation
strepR	streptomycin resistant
SWV	Square-wave voltammetry
T. kodakarensis	*Thermococcus kodakarensis*
TAE	Tris-acetate-EDTA
TAPS	Tris(hydroxymethyl)methyl]-3-aminopropanesulfonic acid
Tk	*Thermococcus kodakaraensis*
TMAO	trimethylamine N-oxide
Tris	tris(hydroxymethyl)aminomethane
Trp	tryptophan
UV-vis	ultraviolet visible
XAS	X-ray absorption spectroscopy

References

The integrative Chapters 1, 2, 3 and 8 are referenced here. The results Chapters 4 to 7 are referenced individually within each chapter.

1.	Seravalli, J. and S.W. Ragsdale, *Expanding the biological periodic table.* Chemistry & biology, 2010. **17**(8): p. 793-794.

2.	Maret, W., *The metals in the biological periodic system of the elements: Concepts and conjectures.* International journal of molecular sciences, 2016. **17**(1): p. 66.

3.	Prabhulkar, S., et al., *Engineered proteins: redox properties and their applications.* Antioxidants & redox signaling, 2012. **17**(12): p. 1796-1822.

4.	Winkler, J.R. and H.B. Gray, *Electron flow through metalloproteins.* Chemical reviews, 2013. **114**(7): p. 3369-3380.

5.	Gray, H.B. and J.R. Winkler, *Electron flow through metalloproteins.* Biochimica et Biophysica Acta (BBA)-Bioenergetics, 2010. **1797**(9): p. 1563-1572.

6.	Atkins, P., *Shriver and Atkins' inorganic chemistry.* 2010: Oxford University Press, USA.

7.	Kaim, W., B. Schwederski, and A. Klein, *Bioinorganic Chemistry-- Inorganic Elements in the Chemistry of Life: An Introduction and Guide.* 2013: John Wiley & Sons.

8.	Bryant, D.A. and N.-U. Frigaard, *Prokaryotic photosynthesis and phototrophy illuminated.* Trends in microbiology, 2006. **14**(11): p. 488-496.

9.	Lambers, H., F.S. Chapin III, and T.L. Pons, *Photosynthesis*, in *Plant physiological ecology*. 2008, Springer. p. 11-99.

10.	Blankenship, R.E., *Molecular mechanisms of photosynthesis*. 2013: John Wiley & Sons.

11.	McConnell, I., G. Li, and G.W. Brudvig, *Energy conversion in natural and artificial photosynthesis.* Chemistry & biology, 2010. **17**(5): p. 434-447.

12.	Armstrong, F.A., *Why did Nature choose manganese to make oxygen?* Philosophical Transactions of the Royal Society of London B: Biological Sciences, 2008. **363**(1494): p. 1263-1270.

13.	Barber, J., *Crystal structure of the oxygen-evolving complex of photosystem II.* Inorganic chemistry, 2008. **47**(6): p. 1700-1710.

14. Raymond, J. and R.E. Blankenship, *The origin of the oxygen-evolving complex.* Coordination chemistry reviews, 2008. **252**(3): p. 377-383.

15. Rich, P., *The molecular machinery of Keilin's respiratory chain.* Biochemical Society Transactions, 2003. **31**(6): p. 1095-1105.

16. Nicholls, D.G. and S. Ferguson, *Bioenergetics.* 2013: Academic Press.

17. Yoshida, M., E. Muneyuki, and T. Hisabori, *ATP synthase—a marvellous rotary engine of the cell.* Nature Reviews Molecular Cell Biology, 2001. **2**(9): p. 669-677.

18. Richardson, D.J., *Bacterial respiration: a flexible process for a changing environment.* Microbiology, 2000. **146**(3): p. 551-571.

19. Sawers, G., *The hydrogenases and formate dehydrogenases of Escherichia coli.* Antonie Van Leeuwenhoek, 1994. **66**(1-3): p. 57-88.

20. Sigel, A., H. Sigel, and R.K. Sigel, *The ubiquitous roles of cytochrome P450 proteins: metal ions in life sciences.* Vol. 10. 2007: John Wiley & Sons.

21. Gruber, K. and C. Kratky, *Cobalamin-Dependent Methionine Synthase.* Handbook of Metalloproteins, 2001.

22. Hille, R., J. Hall, and P. Basu, *The mononuclear molybdenum enzymes.* Chemical reviews, 2014. **114**(7): p. 3963-4038.

23. Winterbourn, C.C. and M.B. Hampton, *Thiol chemistry and specificity in redox signaling.* Free Radical Biology and Medicine, 2008. **45**(5): p. 549-561.

24. Paulsen, C.E. and K.S. Carroll, *Cysteine-mediated redox signaling: chemistry, biology, and tools for discovery.* Chemical reviews, 2013. **113**(7): p. 4633-4679.

25. Crack, J., J. Green, and A.J. Thomson, *Mechanism of oxygen sensing by the bacterial transcription factor fumarate-nitrate reduction (FNR).* Journal of Biological Chemistry, 2004. **279**(10): p. 9278-9286.

26. Stripp, S.T., et al., *HypD is the scaffold protein for Fe-(CN) 2CO cofactor assembly in [NiFe]-hydrogenase maturation.* Biochemistry, 2013. **52**(19): p. 3289-3296.

27. Tarrago, L., et al., *Monitoring methionine sulfoxide with stereospecific mechanism-based fluorescent sensors.* Nature chemical biology, 2015. **11**(5): p. 332-338.

28.   Gennaris, A., et al., *Repairing oxidized proteins in the bacterial envelope using respiratory chain electrons.* Nature, 2015. **528**(7582): p. 409-412.

29.   Rouault, T.A., *Iron-sulfur proteins hiding in plain sight.* Nature chemical biology, 2015. **11**(7): p. 442-445.

30.   Bertini, I., *Biological inorganic chemistry: structure and reactivity*. 2007: University Science Books.

31.   Roat-Malone, R.M., *Bioinorganic chemistry: a short course.* 2007: John Wiley & Sons.

32.   Winter, J.M. and B.S. Moore, *Exploring the chemistry and biology of vanadium-dependent haloperoxidases.* Journal of Biological Chemistry, 2009. **284**(28): p. 18577-18581.

33.   Eady, R.R., *Current status of structure function relationships of vanadium nitrogenase.* Coordination Chemistry Reviews, 2003. **237**(1): p. 23-30.

34.   Yocum, C.F. and V.L. Pecoraro, *Recent advances in the understanding of the biological chemistry of manganese.* Current opinion in chemical biology, 1999. **3**(2): p. 182-187.

35.   Reddy, K.H., *Bioinorganic chemistry.* 2007: New Age International.

36.   Bak, D.W. and S.J. Elliott, *Alternative FeS cluster ligands: tuning redox potentials and chemistry.* Current opinion in chemical biology, 2014. **19**: p. 50-58.

37.   Berg, J.M. and S. Lippard, *Principles of bioinorganic chemistry.* Mill Valley, 1994.

38.   Jensen, K.P., *Iron–sulfur clusters: Why iron?* Journal of inorganic biochemistry, 2006. **100**(8): p. 1436-1439.

39.   Bruschi, M. and F. Guerlesquin, *Structure, function and evolution of bacterial ferredoxins.* FEMS Microbiology Letters, 1988. **54**(2): p. 155-175.

40.   Lubitz, W., et al., *Hydrogenases.* Chemical reviews, 2014. **114**(8): p. 4081-4148.

41.   Hexter, S.V., et al., *Electrocatalytic mechanism of reversible hydrogen cycling by enzymes and distinctions between the major classes of hydrogenases.* Proceedings of the National Academy of Sciences, 2012. **109**(29): p. 11516-11521.

42. Hexter, S.V., T.F. Esterle, and F.A. Armstrong, *A unified model for surface electrocatalysis based on observations with enzymes.* Physical Chemistry Chemical Physics, 2014. **16**(24): p. 11822-11833.

43. Kubas, G.J., *Fundamentals of H2 binding and reactivity on transition metals underlying hydrogenase function and H2 production and storage.* Chemical reviews, 2007. **107**(10): p. 4152-4205.

44. Sigel, A. and R.K. Sigel, *Metal-carbon bonds in enzymes and cofactors*. Vol. 6. 2009: Royal Society of Chemistry.

45. Kobayashi, M. and S. Shimizu, *Cobalt proteins.* European Journal of Biochemistry, 1999. **261**(1): p. 1-9.

46. Ragsdale, S.W., *Nickel-based enzyme systems.* Journal of Biological Chemistry, 2009. **284**(28): p. 18571-18575.

47. Ragsdale, S.W., *Nickel Enzymes & Cofactors.* Encyclopedia of inorganic chemistry, 2005.

48. Solomon, E.I., et al., *Copper active sites in biology.* Chemical reviews, 2014. **114**(7): p. 3659-3853.

49. Iwata, S., et al., *Structure at 2.8 A resolution of cytochrome c oxidase from Paracoccus denitrificans.* Nature, 1995. **376**(6542): p. 660-668.

50. Kosman, D.J., *Multicopper oxidases: a workshop on copper coordination chemistry, electron transfer, and metallophysiology.* JBIC Journal of Biological Inorganic Chemistry, 2010. **15**(1): p. 15-28.

51. Hoffman, B.M., et al., *Mechanism of nitrogen fixation by nitrogenase: the next stage.* Chemical reviews, 2014. **114**(8): p. 4041-4062.

52. Joosten, V. and W.J. van Berkel, *Flavoenzymes.* Current opinion in chemical biology, 2007. **11**(2): p. 195-202.

53. Davidson, V.L., *Electron transfer in quinoproteins.* Archives of biochemistry and biophysics, 2004. **428**(1): p. 32-40.

54. Zouni, A., et al., *Crystal structure of photosystem II from Synechococcus elongatus at 3.8 Å resolution.* Nature, 2001. **409**(6821): p. 739-743.

55. Westerlund, K., et al., *Exploring amino-acid radical chemistry: protein engineering and de novo design.* Biochimica et Biophysica Acta (BBA)-Bioenergetics, 2005. **1707**(1): p. 103-116.

56. Cheng, Z., et al., *Reactivity of thioredoxin as a protein thiol-disulfide oxidoreductase.* Chemical reviews, 2011. **111**(9): p. 5768-5783.

57.   Luo, X. and J.J. Davis, *Electrical biosensors and the label free detection of protein disease biomarkers.* Chemical Society Reviews, 2013. **42**(13): p. 5944-5962.

58.   Wang, J., *Electrochemical glucose biosensors.* Chemical reviews, 2008. **108**(2): p. 814-825.

59.   Bullen, R.A., et al., *Biofuel cells and their development.* Biosensors and Bioelectronics, 2006. **21**(11): p. 2015-2045.

60.   Xu, L. and F.A. Armstrong, *Optimizing the power of enzyme-based membrane-less hydrogen fuel cells for hydrogen-rich H 2–air mixtures.* Energy & Environmental Science, 2013. **6**(7): p. 2166-2171.

61.   Mano, N., et al., *Oxygen is electroreduced to water on a "wired" enzyme electrode at a lesser overpotential than on platinum.* Journal of the American Chemical Society, 2003. **125**(50): p. 15290-15291.

62.   Bachmeier, A., B. Siritanaratkul, and F.A. Armstrong, *Enzymes as Exploratory Catalysts in Artificial Photosynthesis*, in *From Molecules to Materials.* 2015, Springer. p. 99-123.

63.   Lubitz, W., E.J. Reijerse, and J. Messinger, *Solar water-splitting into H 2 and O 2: design principles of photosystem II and hydrogenases.* Energy & Environmental Science, 2008. **1**(1): p. 15-31.

64.   Bachmeier, A. and F. Armstrong, *Solar-driven proton and carbon dioxide reduction to fuels—lessons from metalloenzymes.* Current opinion in chemical biology, 2015. **25**: p. 141-151.

65.   Bowman, L., et al., *Biosynthesis of Salmonella enterica [NiFe]-hydrogenase-5: probing the roles of system-specific accessory proteins.* JBIC Journal of Biological Inorganic Chemistry, 2016. **21**(7): p. 865-873.

66.   Martinez, C.A. and S.G. Rupashinghe, *Cytochrome P450 bioreactors in the pharmaceutical industry: challenges and opportunities.* Current topics in medicinal chemistry, 2013. **13**(12): p. 1470-1490.

67.   Maier, R., et al., *Respiratory hydrogen use by Salmonella enterica serovar Typhimurium is essential for virulence.* Infection and immunity, 2004. **72**(11): p. 6294-6299.

68.   Fontecilla-Camps, J.C. and Y. Nicolet, *Metallo-proteins.* 2014: Springer.

69.   Kendrew, J.C., et al., *A three-dimensional model of the myoglobin molecule obtained by x-ray analysis.* Nature, 1958. **181**(4610): p. 662-666.

70. Kendrew, J. and M. Perutz, *X-ray studies of compounds of biological interest.* Annual review of biochemistry, 1957. **26**(1): p. 327-372.

71. Bowman, S.E., J. Bridwell-Rabb, and C.L. Drennan, *Metalloprotein crystallography: More than a structure.* Accounts of chemical research, 2016. **49**(4): p. 695-702.

72. Volbeda, A., *X-Ray Crystallographic Studies of Metalloproteins.* Metalloproteins: Methods and Protocols, 2014: p. 189-206.

73. Blomberg, M.R., et al., *Quantum chemical studies of mechanisms for metalloenzymes.* Chemical reviews, 2014. **114**(7): p. 3601-3658.

74. Clémancey, M., et al., *Mössbauer Spectroscopy.* Metalloproteins: Methods and Protocols, 2014: p. 153-170.

75. Martinho, M. and E. Münck, *57Fe Mössbauer Spectroscopy in Chemistry and Biology.* Physical Inorganic Chemistry: Principles, Methods, and Models, 2010: p. 39-67.

76. Ward, J., et al., *X-Ray Absorption Spectroscopy of Metalloproteins.* Metalloproteins: Methods and Protocols, 2014: p. 171-187.

77. McMaster, J. and V.S. Oganesyan, *Magnetic circular dichroism spectroscopy as a probe of the structures of the metal sites in metalloproteins.* Current opinion in structural biology, 2010. **20**(5): p. 615-622.

78. Bradley, J.M., J.N. Butt, and M.R. Cheesman, *Electrochemical titrations and reaction time courses monitored in situ by magnetic circular dichroism spectroscopy.* Analytical biochemistry, 2011. **419**(2): p. 110-116.

79. Vincent, K.A., *Triggered infrared spectroscopy for investigating metalloprotein chemistry.* Philosophical Transactions of the Royal Society of London A: Mathematical, Physical and Engineering Sciences, 2010. **368**(1924): p. 3713-3731.

80. Gutiérrez-Sanz, O., O. Rüdiger, and A.L. De Lacey, *FTIR Spectroscopy of Metalloproteins.* Metalloproteins: Methods and Protocols, 2014: p. 95-106.

81. Oladepo, S.A., et al., *UV resonance Raman investigations of peptide and protein structure and dynamics.* Chemical reviews, 2012. **112**(5): p. 2604-2628.

82. Siebert, E., et al., *Resonance Raman spectroscopy as a tool to monitor the active site of hydrogenases.* Angewandte Chemie International Edition, 2013. **52**(19): p. 5162-5165.

83. Gambarelli, S. and V. Maurel, *Study of Metalloproteins Using Continuous Wave Electron Paramagnetic Resonance (EPR).* Metalloproteins: Methods and Protocols, 2014: p. 139-151.

84. Bertini, I., et al., *Perspectives in paramagnetic NMR of metalloproteins.* Dalton Transactions, 2008(29): p. 3782-3790.

85. Li, H. and H. Sun, *NMR studies of metalloproteins*, in *NMR of Proteins and Small Biomolecules.* 2011, Springer. p. 69-98.

86. Winkler, J.R., et al., *Electron-transfer kinetics of pentaammineruthenium (III)(histidine-33)-ferricytochrome c. Measurement of the rate of intramolecular electron transfer between redox centers separated by 15. ANG. in a protein.* Journal of the American Chemical Society, 1982. **104**(21): p. 5798-5800.

87. Winkler, J.R. and H.B. Gray, *Long-range electron tunneling.* Journal of the American Chemical Society, 2014. **136**(8): p. 2930-2939.

88. Shih, C., et al., *Tryptophan-accelerated electron flow through proteins.* Science, 2008. **320**(5884): p. 1760-1762.

89. Léger, C. and P. Bertrand, *Direct electrochemistry of redox enzymes as a tool for mechanistic studies.* Chemical reviews, 2008. **108**(7): p. 2379-2438.

90. Blanford, C.F., *The birth of protein electrochemistry.* Chemical Communications, 2013. **49**(95): p. 11130-11132.

91. Kuwana, T. and W.R. Heineman, *Spectroelectrochemical studies of stoichiometry, energetics, and kinetics of heme proteins: cytochrome c and cytochrome c oxidase.* Bioelectrochemistry and Bioenergetics, 1974. **1**(3-4): p. 389-406.

92. Eddowes, M.J. and H.A.O. Hill, *Novel method for the investigation of the electrochemistry of metalloproteins: cytochrome c.* Journal of the Chemical Society, Chemical Communications, 1977(21): p. 771b-772.

93. Yeh, P. and T. Kuwana, *Reversible electrode reaction of cytochrome c.* Chemistry Letters, 1977. **6**(10): p. 1145-1148.

94. Allen, P.M., et al., *Surface modifiers for the promotion of direct electrochemistry of cytochrome c.* Journal of electroanalytical chemistry and interfacial electrochemistry, 1984. **178**(1): p. 69-86.

95. Armstrong, F.A., H.A.O. Hill, and N.J. Walton, *Direct electrochemistry of redox proteins.* Accounts of Chemical Research, 1988. **21**(11): p. 407-413.

96. Armstrong, F.A., H.A. Heering, and J. Hirst, *Reaction of complex metalloproteins studied by protein-film voltammetry.* Chemical Society Reviews, 1997. **26**(3): p. 169-179.

97. Gulaboski, R., et al., *Protein film voltammetry: electrochemical enzymatic spectroscopy. A review on recent progress.* Journal of Solid State Electrochemistry, 2012. **16**(7): p. 2315-2328.

98. Evans, R.M. and F.A. Armstrong, *Electrochemistry of Metalloproteins: Protein Film Electrochemistry for the Study of E. coli [NiFe]-Hydrogenase-1.* Metalloproteins: Methods and Protocols, 2014: p. 73-94.

99. Bard, A.J. and L.R. Faulkner, *Electrochemical Methods: Fundamentals and Applications.* 2000: Wiley.

100. Fisher, A.C., *Electrode Dynamics.* 1996: Oxford University Press.

101. Léger, C., et al., *Enzyme electrokinetics: using protein film voltammetry to investigate redox enzymes and their mechanisms.* Biochemistry, 2003. **42**(29): p. 8653-8662.

102. Armstrong, F.A., *Recent developments in dynamic electrochemical studies of adsorbed enzymes and their active sites.* Current opinion in chemical biology, 2005. **9**(2): p. 110-117.

103. Flanagan, L.A. and A. Parkin, *Electrochemical insights into the mechanism of NiFe membrane-bound hydrogenases.* Biochemical Society Transactions, 2016. **44**(1): p. 315-328.

104. Heering, H.A., J. Hirst, and F.A. Armstrong, *Interpreting the catalytic voltammetry of electroactive enzymes adsorbed on electrodes.* The Journal of Physical Chemistry B, 1998. **102**(35): p. 6889-6902.

105. Sucheta, A., et al., *Reversible electrochemistry of fumarate reductase immobilized on an electrode surface. Direct voltammetric observations of redox centers and their participation in rapid catalytic electron transport.* Biochemistry, 1993. **32**(20): p. 5455-5465.

106. Léger, C., et al., *Electron flow in multicenter enzymes: Theory, applications, and consequences on the natural design of redox chains.* Journal of the American Chemical Society, 2006. **128**(1): p. 180-187.

107. Léger, C., et al., *Enzyme electrokinetics: energetics of succinate oxidation by fumarate reductase and succinate dehydrogenase.* Biochemistry, 2001. **40**(37): p. 11234-11245.

108. Jones, A.K., et al., *Enzyme electrokinetics: electrochemical studies of the anaerobic interconversions between active and inactive states of Allochromatium vinosum [NiFe]-hydrogenase.* Journal of the American Chemical Society, 2003. **125**(28): p. 8505-8514.

109. Heffron, K., et al., *Determination of an optimal potential window for catalysis by E. coli dimethyl sulfoxide reductase and hypothesis on the role of Mo (V) in the reaction pathway.* Biochemistry, 2001. **40**(10): p. 3117-3126.

110. Léger, C., et al., *Effect of a dispersion of interfacial electron transfer rates on steady state catalytic electron transport in [NiFe]-hydrogenase and other enzymes.* The Journal of Physical Chemistry B, 2002. **106**(50): p. 13058-13063.

111. Hirst, J., *Elucidating the mechanisms of coupled electron transfer and catalytic reactions by protein film voltammetry.* Biochimica et Biophysica Acta (BBA)-Bioenergetics, 2006. **1757**(4): p. 225-239.

112. Butt, J., *Voltammetry of Adsorbed Proteins*, in *Encyclopedia of Applied Electrochemistry*, G. Kreysa, K.-i. Ota, and R.F. Savinell, Editors. 2014, Springer New York: New York, NY. p. 2103-2109.

113. Armstrong, F.A. and J. Hirst, *Reversibility and efficiency in electrocatalytic energy conversion and lessons from enzymes.* Proceedings of the National Academy of Sciences, 2011. **108**(34): p. 14049-14054.

114. Pershad, H.R., et al., *Catalytic electron transport in Chromatium vinosum [NiFe]-hydrogenase: application of voltammetry in detecting redox-active centers and establishing that hydrogen oxidation is very fast even at potentials close to the reversible H+/H2 value.* Biochemistry, 1999. **38**(28): p. 8992-8999.

115. Jones, A.K., et al., *Interruption and time-resolution of catalysis by a flavoenzyme using fast scan protein film voltammetry.* Journal of the American Chemical Society, 2000. **122**(27): p. 6494-6495.

116. Morris, G.P., et al., *Theoretical analysis of the relative significance of thermodynamic and kinetic dispersion in the dc and ac voltammetry of surface-confined molecules.* Langmuir, 2015. **31**(17): p. 4996-5004.

117. Hirst, J. and F.A. Armstrong, *Fast-scan cyclic voltammetry of protein films on pyrolytic graphite edge electrodes: characteristics of electron exchange.* Analytical chemistry, 1998. **70**(23): p. 5062-5071.

118. Armstrong, F.A., et al., *Fast voltammetric studies of the kinetics and energetics of coupled electron-transfer reactions in proteins.* Faraday discussions, 2000. **116**: p. 191-203.

119. Ash, P.A. and K.A. Vincent, *Spectroscopic analysis of immobilised redox enzymes under direct electrochemical control.* Chemical Communications, 2012. **48**(10): p. 1400-1409.

120. Guo, S., et al., *Fourier transform large-amplitude alternating current cyclic voltammetry of surface-bound azurin.* Analytical chemistry, 2004. **76**(1): p. 166-177.

121. Jeuken, L.J., J.P. McEvoy, and F.A. Armstrong, *Insights into gated electron-transfer kinetics at the electrode-protein interface: a square wave voltammetry study of the blue copper protein azurin.* The Journal of Physical Chemistry B, 2002. **106**(9): p. 2304-2313.

122. Smith, E.T. and B. Feinberg, *Redox properties of several bacterial ferredoxins using square wave voltammetry.* Journal of Biological Chemistry, 1990. **265**(24): p. 14371-14376.

123. Scholz, F., *Electroanalytical Methods: Guide to Experiments and Applications*. 2013: Springer Berlin Heidelberg.

124. Wang, J., *Analytical Electrochemistry*. 2006: Wiley.

125. Mirceski, V., S. Komorsky-Lovric, and M. Lovric, *Square-Wave Voltammetry: Theory and Application*. 2007: Springer Berlin Heidelberg.

126. Bond, A.M., et al., *Fundamental and second harmonic alternating current cyclic voltammetric theory and experimental results for simple electrode reactions involving solution-soluble redox couples.* Analytical Chemistry, 1976. **48**(6): p. 872-883.

127. Bond, A.M., et al., *Changing the look of voltammetry.* Analytical chemistry, 2005. **77**(9): p. 186 A-195 A.

128. Gavaghan, D. and A. Bond, *A complete numerical simulation of the techniques of alternating current linear sweep and cyclic voltammetry: analysis of a reversible process by conventional and fast Fourier transform methods.* Journal of Electroanalytical Chemistry, 2000. **480**(1): p. 133-149.

129. Honeychurch, M.J. and A.M. Bond, *Numerical simulation of Fourier transform alternating current linear sweep voltammetry of surface bound molecules.* Journal of Electroanalytical Chemistry, 2002. **529**(1): p. 3-11.

130. Engblom, S.O., J.C. Myland, and K.B. Oldham, *Must ac voltammetry employ small signals?* Journal of Electroanalytical Chemistry, 2000. **480**(1): p. 120-132.

131. Si-Xuan, G., B. Alan M, and Z. Jie, *Fourier Transformed Large Amplitude Alternating Current Voltammetry: Principles and Applications.* Review of Polarography, 2015. **61**(1): p. 21-32.

132. Bond, A.M., et al., *An integrated instrumental and theoretical approach to quantitative electrode kinetic studies based on large amplitude Fourier transformed ac voltammetry: A mini review.* Electrochemistry Communications, 2015. **57**: p. 78-83.

133. Házì, J., et al., *Microcomputer-based instrumentation for multi-frequency Fourier transform alternating current (admittance and impedance) voltammetry.* Journal of Electroanalytical Chemistry, 1997. **437**(1): p. 1-15.

134. Bond, A.M., et al., *Characterization of nonlinear background components in voltammetry by use of large amplitude periodic perturbations and Fourier transform analysis.* Analytical chemistry, 2009. **81**(21): p. 8801-8808.

135. Mashkina, E.A., A.N. Simonov, and A.M. Bond, *Optimisation of windowing for harmonic recovery in large-amplitude Fourier transformed ac voltammetry.* Journal of Electroanalytical Chemistry, 2014. **732**: p. 86-92.

136. Zhang, J. and A.M. Bond, *Theoretical studies of large amplitude alternating current voltammetry for a reversible surface-confined electron*

transfer process coupled to a pseudo first-order electrocatalytic process. Journal of Electroanalytical Chemistry, 2007. **600**(1): p. 23-34.

137. Oldham, K.B., et al., *The aperiodic current, and its semiintegral, in reversible ac voltammetry: Theory and experiment.* Journal of Electroanalytical Chemistry, 2014. **719**: p. 113-121.

138. Zhang, J., et al., *Large-amplitude Fourier transformed high-harmonic alternating current cyclic voltammetry: kinetic discrimination of interfering Faradaic processes at glassy carbon and at boron-doped diamond electrodes.* Analytical chemistry, 2004. **76**(13): p. 3619-3629.

139. Fleming, B.D., et al., *Separation of electron-transfer and coupled chemical reaction components of biocatalytic processes using Fourier transform ac voltammetry.* Analytical chemistry, 2005. **77**(11): p. 3502-3510.

140. Kennedy, G.F., A.M. Bond, and A.N. Simonov, *Modelling ac voltammetry with MECSim: facilitating simulation-experiment comparisons.* Current Opinion in Electrochemistry, 2017. **1**(1): p140-147.

141. Rudolph, M., D.P. Reddy, and S.W. Feldberg, *A simulator for cyclic voltammetric responses.* Analytical chemistry, 1994. **66**(10): p. 589A-600A.

142. Mashkina, E. and A.M. Bond, *Implementation of a statistically supported heuristic approach to alternating current voltammetric harmonic component analysis: re-evaluation of the macrodisk glassy carbon electrode kinetics for oxidation of ferrocene in acetonitrile.* Analytical chemistry, 2011. **83**(5): p. 1791-1799.

143. Mashkina, E., et al., *Estimation of electrode kinetic and uncompensated resistance parameters and insights into their significance using Fourier transformed ac voltammetry and e-science software tools.* Journal of Electroanalytical Chemistry, 2013. **690**: p. 104-110.

144. Enticott, C., et al. *Electrochemical parameter optimization using scientific workflows.* in *e-Science (e-Science), 2010 IEEE Sixth International Conference on.* 2010. IEEE.

145. Peachey, T., et al., *Leveraging e-Science infrastructure for electrochemical research.* Philosophical Transactions of the Royal Society of London A: Mathematical, Physical and Engineering Sciences, 2011. **369**(1949): p. 3336-3352.

146. Simonov, A.N., et al., *New insights into the analysis of the electrode kinetics of flavin adenine dinucleotide redox center of glucose oxidase immobilized on carbon electrodes.* Langmuir, 2014. **30**(11): p. 3264-3273.

147. Morris, G.P., et al., *A comparison of fully automated methods of data analysis and computer assisted heuristic methods in an electrode kinetic study of the pathologically variable [Fe (CN) 6] 3–/4–process by AC voltammetry.* Analytical chemistry, 2013. **85**(24): p. 11780-11787.

148. Simonov, A.N., et al., *Multiparameter Estimation in Voltammetry When an Electron Transfer Process Is Coupled to a Chemical Reaction.* Analytical chemistry, 2016. **88**(9): p. 4724-4732.

149. Jeuken, L.J. and F.A. Armstrong, *Electrochemical origin of hysteresis in the electron-transfer reactions of adsorbed proteins: contrasting behavior of the "blue" copper protein, azurin, adsorbed on pyrolytic graphite and modified gold electrodes.* The Journal of Physical Chemistry B, 2001. **105**(22): p. 5271-5282.

150. Rooney, M.B., et al., *A thin-film electrochemical study of the" blue" copper proteins, auracyanin A and auracyanin B, from the photosynthetic bacterium Chloroflexus aurantiacus: the reduction potential as a function of pH.* JBIC Journal of Biological Inorganic Chemistry, 2003. **8**(3): p. 306-317.

151. Zhang, J., et al., *Novel kinetic and background current selectivity in the even harmonic components of Fourier transformed square-wave voltammograms of surface-confined azurin.* The Journal of Physical Chemistry B, 2005. **109**(18): p. 8935-8947.

152. Fleming, B.D., et al., *Application of power spectra patterns in Fourier transform square wave voltammetry to evaluate electrode kinetics of surface-confined proteins.* Analytical chemistry, 2006. **78**(9): p. 2948-2956.

153. Fleming, B.D., et al., *Detailed analysis of the electron-transfer properties of azurin adsorbed on graphite electrodes using dc and large-amplitude Fourier transformed ac voltammetry.* Analytical chemistry, 2007. **79**(17): p. 6515-6526.

154. Lee, C.-Y., et al., *Systematic evaluation of electrode kinetics and impact of surface heterogeneity for surface-confined proteins using analysis of*

harmonic components available in sinusoidal large-amplitude Fourier transformed ac voltammetry. Analytica chimica acta, 2009. **652**(1): p. 205-214.

155. Fleming, B.D., et al., *The electrochemistry of a heme-containing enzyme, CYP199A2, adsorbed directly onto a pyrolytic graphite electrode.* Journal of Electroanalytical Chemistry, 2007. **611**(1): p. 149-154.

156. Simonov, A.N., et al., *Mechanistic scrutiny identifies a kinetic role for cytochrome b5 regulation of human cytochrome P450c17 (CYP17A1, P450 17A1).* PloS one, 2015. **10**(11): p. e0141252.

157. Lee, C.-Y. and A.M. Bond, *A comparison of the higher order harmonic components derived from large-amplitude Fourier transformed ac voltammetry of myoglobin and heme in DDAB Films at a pyrolytic graphite electrode.* Langmuir, 2010. **26**(7): p. 5243-5253.

158. Lee, C.-Y., et al., *Theoretical and experimental investigation of surface-confined two-center metalloproteins by large-amplitude Fourier transformed ac voltammetry.* Journal of electroanalytical chemistry, 2011. **656**(1): p. 293-303.

159. Stevenson, G.P., et al., *Theoretical analysis of the two-electron transfer reaction and experimental studies with surface-confined cytochrome c peroxidase using large-amplitude Fourier transformed AC voltammetry.* Langmuir, 2012. **28**(25): p. 9864-9877.

160. Atkins, P. and J. de Paula, *Physical Chemistry.* 2007: W. H. Freeman.

161. Brett, C.M.A. and A.M.O. Brett, *Electroanalysis.* 1998: Oxford Universisty Press.

162. Marcus, R.A., *On the theory of oxidation-reduction reactions involving electron transfer. I.* The Journal of Chemical Physics, 1956. **24**(5): p. 966-978.

163. Marcus, R.A., *Electron transfer reactions in chemistry. Theory and experiment.* Reviews of Modern Physics, 1993. **65**(3): p. 599.

164. Miller, J., L. Calcaterra, and G. Closs, *Intramolecular long-distance electron transfer in radical anions. The effects of free energy and solvent on the reaction rates.* Journal of the American Chemical Society, 1984. **106**(10): p. 3047-3049.

165. Zeng, Y., et al., *Simple formula for Marcus–Hush–Chidsey kinetics.* Journal of Electroanalytical Chemistry, 2014. **735**: p. 77-83.

166. Henstridge, M.C., et al., *Marcus–Hush–Chidsey theory of electron transfer applied to voltammetry: A review.* Electrochimica Acta, 2012. **84**: p. 12-20.

167. Feldberg, S.W., *Implications of Marcus− Hush Theory for Steady-State Heterogeneous Electron Transfer at an Inlaid Disk Electrode.* Analytical chemistry, 2010. **82**(12): p. 5176-5183.

168. CHIDSEY, C.E.D., *Free Energy and Temperature Dependence of Electron Transfer at the Metal-Electrolyte Interface.* Science, 1991. **251**(4996): p. 919-922.

169. Royea, W.J., et al., *A comparison between interfacial electron-transfer rate constants at metallic and graphite electrodes.* The Journal of Physical Chemistry B, 2006. **110**(39): p. 19433-19442.

170. Giese, B., M. Graber, and M. Cordes, *Electron transfer in peptides and proteins.* Current opinion in chemical biology, 2008. **12**(6): p. 755-759.

171. Blumberger, J., *Recent advances in the theory and molecular simulation of biological electron transfer reactions.* Chemical reviews, 2015. **115**(20): p. 11191-11238.

172. Hopfield, J., *Electron transfer between biological molecules by thermally activated tunneling.* Proceedings of the National Academy of Sciences, 1974. **71**(9): p. 3640-3644.

173. Moser, C.C., et al., *Nature of biological electron transfer.* Nature, 1992. **355**(6363): p. 796-802.

174. Page, C.C., et al., *Natural engineering principles of electron tunnelling in biological oxidation–reduction.* Nature, 1999. **402**(6757): p. 47-52.

175. Beratan, D.N., J.N. Onuchic, and J. Hopfield, *Electron tunneling through covalent and noncovalent pathways in proteins.* The Journal of chemical physics, 1987. **86**(8): p. 4488-4498.

176. Beratan, D., J. Betts, and J. Onuchic, *Protein electron transfer rates set by the bridging secondary and tertiary structure.* Science, 1991. **252**(5010): p. 1285-1288.

177. Beratan, D.N., et al., *Charge transfer in dynamical biosystems, or the treachery of (static) images.* Accounts of chemical research, 2014. **48**(2): p. 474-481.

178. Zhang, Y., et al., *Biological charge transfer via flickering resonance.* Proceedings of the National Academy of Sciences, 2014. **111**(28): p. 10049-10054.

179. Johnson, K.A. and R.S. Goody, *The original Michaelis constant: translation of the 1913 Michaelis–Menten paper.* Biochemistry, 2011. **50**(39): p. 8264-8269.

180. Michaelis, L. and M.L. Menten, *Die kinetik der invertinwirkung.* Biochem. z, 1913. **49**(333-369): p. 352.

181. Laviron, E., *General expression of the linear potential sweep voltammogram in the case of diffusionless electrochemical systems.* Journal of Electroanalytical Chemistry and Interfacial Electrochemistry, 1979. **101**(1): p. 19-28.

182. Gonzalez, J., M. Lopez-Tenes, and A. Molina, *Non-Nernstian Two-Electron Transfer Reactions for Immobilized Molecules: A Theoretical Study in Cyclic Voltammetry.* The Journal of Physical Chemistry C, 2013. **117**(10): p. 5208-5220.

183. Laviron, E., *Theoretical study of a 1e, 1H+ surface electrochemical reaction (four-member square scheme) when the protonation reactions are at equilibrium.* Journal of Electroanalytical Chemistry and Interfacial Electrochemistry, 1980. **109**(1-3): p. 57-67.

184. Jeuken, L.J., et al., *The pH-dependent redox inactivation of amicyanin from Paracoccus versutus as studied by rapid protein-film voltammetry.* JBIC Journal of Biological Inorganic Chemistry, 2002. **7**(1-2): p. 94-100.

185. Zhang, Z. and J.F. Rusling, *Electron transfer between myoglobin and electrodes in thin films of phosphatidylcholines and dihexadecylphosphate.* Biophysical chemistry, 1997. **63**(2): p. 133-146.

186. Salverda, J.M., et al., *Fluorescent cyclic voltammetry of immobilized azurin: direct observation of thermodynamic and kinetic heterogeneity.* Angewandte Chemie International Edition, 2010. **49**(33): p. 5776-5779.

187. Limoges, B.t. and J.-M. Savéant, *Catalysis by immobilized redox enzymes. Diagnosis of inactivation and reactivation effects through odd cyclic voltammetric responses.* Journal of Electroanalytical Chemistry, 2004. **562**(1): p. 43-52.

188. Fourmond, V., et al., *Steady-state catalytic wave-shapes for 2-electron reversible electrocatalysts and enzymes.* Journal of the American Chemical Society, 2013. **135**(10): p. 3926-3938.

189. Elliott, S.J., et al., *Detection and interpretation of redox potential optima in the catalytic activity of enzymes.* Biochimica et Biophysica Acta (BBA)-Bioenergetics, 2002. **1555**(1): p. 54-59.

190. Fourmond, V., et al., *"Two-step" chronoamperometric method for studying the anaerobic inactivation of an oxygen tolerant NiFe hydrogenase.* Journal of the American Chemical Society, 2010. **132**(13): p. 4848-4857.

191. Sivia, D.S. and S.G. Rawlings, *Foundations of Science Mathematics.* 1999: OUP Oxford.

192. Sundararajan, D., *The Discrete Fourier Transform: Theory, Algorithms and Applications.* 2001: World Scientific.

193. Rao, K.R., D.N. Kim, and J.J. Hwang, *Fast Fourier Transform - Algorithms and Applications.* 2011: Springer Netherlands.

194. Cooley, J.W. and J.W. Tukey, *An algorithm for the machine calculation of complex Fourier series.* Mathematics of computation, 1965. **19**(90): p. 297-301.

195. Wright, J.J., et al., *small-volume potentiometric titrations: EPR investigations of Fe-S cluster N2 in mitochondrial complex I.* Journal of inorganic biochemistry, 2016. **162**: p.201-206.

196. Flanagan, L.A., et al., *Re-engineering a NiFe hydrogenase to increase the H 2 production bias while maintaining native levels of O 2 tolerance.* Chemical Communications, 2016. **52**(58): p.9133-9136.

197. Loschi, L., et al., *Structural and biochemical identification of a novel bacterial oxidoreductase.* Journal of Biological Chemistry, 2004. **279**(48): p. 50391-50400.

198. Brokx, S.J., et al., *Characterization of an Escherichia coli sulfite oxidase homologue reveals the role of a conserved active site cysteine in assembly and function.* Biochemistry, 2005. **44**(30): p. 10339-10348.